Experimental study of the interaction between RF antennas and the edge plasma of a tokamak

Martin Kubic

▶ To cite this version:

Martin Kubic. Experimental study of the interaction between RF antennas and the edge plasma of a tokamak. Other [cond-mat.other]. Université de Lorraine, 2013. English. NNT : 2013LORR0220 . tel-01750516

HAL Id: tel-01750516

https://hal.univ-lorraine.fr/tel-01750516

Submitted on 29 Mar 2018

Collegium Sciences et Technologies École doctorale EMMA

ETUDE EXPÉRIMENTALE D'INTERACTIONS ENTRE ANTENNES HF ET PLASMA PÉRIPHÉRIQUE D'UN TOKAMAK

THÈSE

Prèsentée et soutenue publiquement le 23.10. 2013
pour l'obtention du titre de

Docteur de l'Université de Lorraine
(Physique)
par

Martin KUBIČ

Prof. Michel Vergnat	Président du jury	Université de Lorraine
Prof. Jean-Marie Noterdaeme	Rapporteur	Universiteit de Ghent
Prof. Roman Schrittwieser	Rapporteur	Université de Innsbruck
Dr. Dirk Van Eester	Examinateur	Ecole Royale Militaire
Dr. Vojtěch Svoboda	Examinateur	Czech Technical University
Prof. Stéphane Heuraux	Directeur de thèse	Université de Lorraine
Dr. James P. Gunn	Responsable CEA	Commissariat a l'Énergie Atomique

Commissariat à l'Énergie Atomique et aux énergies alternatives
Direction des Sciences de la Matière
Institut de Recherche sur la Fusion par confinement Magnétique
Service Intégration Plasma Paroi

Etude expérimental d'interactions entre antennes HF et plasma périphérique d'un tokamak

Les antennes en opération dans la gamme de fréquence cyclotron ionique (FCI) représentent un moyen utile pour chauffer du plasma dans les tokamaks et autres plasmas de fusion. Ces systèmes de chauffage sont amenés a jouer un rôle important dans le projet ITER. L'objectif du chauffage FCI est d'injecter une onde électromagnétique jusqu'à cour du plasma ou l'onde est absorbée. Conjointement avec le chauffage souhaité, les interactions parasites avec le bord du plasma et de la limite des matériaux apparaissent. Plusieurs de ces effets délétères sont causés par la formation de la Radio-Fréquence (RF) des gaines. L'objectif de cette thèse est d'étudier, principalement de façon expérimentale, les modifications du plasma de bord ≪ scrape-off layer (SOL) ≫ causées par les effets non-linéaires des gaines RF. Cela se fait en utilisant les sondes électrostatiques (de Langmuir, "Retarded Field Analyser" (RFA), tunnel). Ces sondes sont reliées magnétiquement a une FCI antenne en puissance. De plus, depuis le printemps 2011, l'une des trois FCI antennes dans le tokamak Tore Supra est équipée d'un nouveau type d'écran de Faraday (FS). Les résultats des simulations RF du nouvel écran de Faraday (FS), comportant barres d' écran non connectées a la partie centrale de l'antenne et des bords de boîte en dents de requin, modifie considérablement la distribution de courant sur la face avant de l'antenne. Ces nouveautés devaient réduire théoriquement le potentiel et les champs électriques RF, sachant que la composante de la densité de courant parallèle aux lignes de champ magnétique est a l'origine de la génération de RF gaines via l'excitation du mode lent. Nous étudions les effets d'un nouvel écran de Faraday en comparaison avec la conception conventionnelle. Les effets sur les champs RF induisant les modifications de la SOL sont étudiés. Ceci est étudié pour différentes configurations du plasma et des antennes avec des études paramétriques en fonction du déséquilibre entre les émetteurs de l'antenne, de la puissance injectée et de la densité SOL. De plus, l'influence des gaines RF sur les mesures du potentiel de la gaine avec le RFA sont analysées. Cette étude s'effectue à l'aide d'un code 1D basé sur le modèle cinétique ≪ particle-in-cell ≫. Ces simulations ont montré que la RFA est capable de mesurer de manière fiable le potentiel gaine, toutefois cela reste limité pour les fréquences de plasma ionique ω_{pi} proche de la fréquence injectée ω_{rf}. Par contre, pour des conditions réelles du SOL ($\omega_{pi} > \omega_{rf}$), quand RFA est magnétiquement connectée à la structure de l'antenne RF, il est fortement sous-estimé. Une autre méthode pour étudier les effets RF gaines est proposée. Il consiste à utiliser un élargissement de la fonction de distribution des ions pour prouver l'existence de champs électriques RF dans la gaine. Enfin, les mesures de RFA dans Tore Supra indiquent que les potentiels RF se propagent au moins jusqu'à de 12m de l'antenne le long de lignes de champ magnétiques.

Mots clé: plasma, sonde de Langmuir, antenne ICRF, gaine

Motivation principale

Pour atteindre les conditions pour l'ignition, le plasma à l'intérieur d'un réacteur thermo-nucléaire doit être chauffé au delà de la température critique. Les antennes opérationnelles dans le bande de la fréquence cyclotronique ionique sont un outil utile dans le chauffage de tokamaks. Ca va aussi jouer un rôle important dans le projet d'un réacteur thermonucléaire international - ITER. L'objectif du chauffage HF est lancer une onde rapide dans le cour du plasma ou l'onde est absorbée. La physique de la propagation d'une onde dans le milieu ionisé impose que les antennes soient installées en contact ou proche du plasma sachant que les ondes sont évanescentes. Par contre, il y aussi des interactions indésirables avec le bord du plasma et les matériaux.

Plusieurs de ces effets non-désirés sont causés par la présence des gaines radio-fréquence (RF). Si le champ magnétique n'est pas aligné parfaitement avec la structure d'antenne, l'onde lente va être excitée. Puis, il y aura une interaction avec la surface d'un matériel. Le champ électrique parallèle de l'onde lente conduit le RF potentiel qui oscille jusqu'à atteindre quelques cents volts entre les points limites d'un tube du flux magnétique ouverte. La réaction naturelle de la gaine est de rectifier le RF voltage qui oscille en produisant le potentiel continu dit DC. Par conséquence, les ions accélérés, à travers cette forte variation de potentiel DC, causent plusieurs interactions antenne-bord indésirables. En autre le "sputtering" induisant la génération des impuretés, le transport convectif et les forts flux de chaleur localisés aux points de connexion de la ligne de champ sur la paroi ou la structure d'antenne. De plus, la charge différentielle des tubes de flux adjacents induit de la convection de particules dit E × B à travers de la ligne de champs. Cette convection de particules via les cellules convectives a la tendance à modifier le profil poloïdal de la densité avant l'antenne. Néanmoins, pour une fonctionnalité pérenne des antennes en cas de chocs à haute puissance, les interactions indésirables doivent être minimisées. Pour parvenir à la suppression de ces effets indésirables, il est nécessaire d'étudier et de comprendre les phénomènes physiques qui se produisent dans le voisinage de la structure face au plasma, et en particulier à proximité de l'antenne.

Jusqu'à récemment, les effets des gaines RF ont été principalement étudiés dans le voisinage de l'antenne. Ils ont été estimés en utilisant l'approximation des champs émis dans le vide pour déterminer la tension gaine en intégrant la composante parallèle du champ électrique entre les deux points de contact du champ magnétique avec la paroi conductrice. Chaque ligne de champ magnétique interceptée par la surface métallique peut être considérée comme un tube de flux le long de laquelle le potentiel oscille à la fréquence RF et est longitudinalement constant. Une telle situation est équivalent à un modèle double sonde. Dans ce cas, un courant négatif est recueilli sur l'antenne alimenté FCI, alors qu'un courant positif est collecté par la sonde de Langmuir reliée magnétiquement comme cela est observé expérimentalement sur Tore Supra.

Les études d'un concept alternatif d'écran ont été lancées suit problèmes de chauffage et puis disponibilité d'un écran Faraday avec une conception conventionnelle installé sur Tore Supra. La motivation principale d'amélioration d'une écran Faraday a été de réduire les forts flux localisés que sont crées pendant le fonctionnement simultané des chauffages LH et FCI. Ces opérations conduisent à des points chauds dit "hot spots" sur le bord de l'écran de Faraday. Il y avait aussi une motivation d'augmenter la capacité de refroidissement du nouvel écran. En conséquence, la réduction des charges thermiques ainsi que du cycle de fatigue va autoriser le fonctionnement même pour des décharges en haute puissance. En plus, la motivation a été de réduire les potentiels de RF sur les lignes de champ ouverte et de qualifier le nouvel écran pour ITER. Pour atteindre la diminution de ces effets de bords indésirables, il est nécessaire d'investiguer et comprendre les phénomènes physiques que se produisent proche de composante face au plasma; et en particulière, proche de l'antenne FCI.

L'objectif de cette thèse est d'étudier des effets d'interaction entre le plasma du bord et FCI antenne en puissance. L'étude expérimentale est réalisée en utilisant les sondes de Langmuir. Ces sondes sont connectées par lignes magnétiques à l'antenne. Le travail se concentre sur le suivi des variations des paramètres de plasma de bord- densité du plasma, température d'un électron, gaine potentiel et l'écoulement parallèle induit par la présence d'une antenne active.

Note personnelle

Les obligations de l'école de formation doctorale EMMA demande que le manuscrit de thèse comporte un résumé en français de 30 pages de la thèse. Alors, dans ce manuscrit de la thèse vous allez trouver la partie suivante en français. L'auteur de la thèse permet de souligner que la langue française est pour lui une langue étrangère. Il a fait un effort de traduire ces pages mais il n'a pas étudié le français avant de venir en France. Il est alors très recommandé dans la lecture de se concentrer à la partie anglaise du manuscrit. Cela vous garantira une bien meilleure compréhension du travail présenté.

Résumé élargi

Contexte énergétique

L'énergie est nécessaire pour le développement de la société. Elle est présente dans tous les domaines de tous les la vie quotidienne, ainsi que les transactions économiques et les politiques publiques. Le moteur le plus important dans la demande d'énergie est l'être humain lui-même. Il y a actuellement environ 7 milliards personnes vivant sur la Terre (et continue d'augmenter). Comme la société humaine évolue, les besoins de la production d'énergie augmentent. Avant de commencer la discussion sur la consommation d'énergie mondiale, il est nécessaire de comprendre l'ampleur du problème. Unités telles que les terawatts, joules et BTU (unité thermique britannique) apportent la confusion le sujet difficile. Pour aider à résoudre ce problème, un nouveau terme a été assimilé - un ≪ mile cube de pétrole ≫ (CMO). Cette unité exprime la consommation mondiale annuelle de pétrole. Nous pouvons utiliser l'énergie contenue dans un mile cube de pétrole en tant qu'unité pour représenter visuellement l'énergie de tout autres sources: le charbon, le gaz naturel, biomasse, nucléaire, hydroélectrique, solaire, éolienne et géothermique. L'utilisation mondiale d'énergie dans les unités de CMO nous permet plus facilement de débattre et d'évaluer notre progrès. Au prix actuel, à un mile cube de pétrole coute environ \$2 trillions. Chaque année, le monde consomme environ 3CMO d'énergie (1 CMO de l'huile, 0,8 du charbon, 0,6 du gaz naturel et environ 0,2 chacune des bois, hydraulique et nucléaire) et les prévisions disent que pour être à 9CMO dans 50 années en fonction de la conservation et de l'efficacité de gagner de l'énergie.

En regardant sur les futures prévisions, la consommation mondiale d'énergie primaire devrait croître de 1,6% p.a. au cours de la période de 2010 à 2030, ajoutant 39% à consommation mondiale d'ici 2030. Il est intéressant de remarquer que la quasi-totalité (96%) de la croissance est régie par des non-membres de l'OECD. En 2030, la consommation d'énergie non membres de l'OECD devrait à 69% au-dessus du niveau de 2010. Le développement économique des pays non-OECD crée un appétit pour l'énergie qui ne peut pas être satisfaite en augmentant tous les carburants. La croissance de la consommation mondiale d'énergie est de plus en plus satisfaite par des combustibles non fossiles. Un effort important est payé pour augmenter le ratio des sources d'énergie renouvelables.

Cela se justifie par l'intérêt international pour réduire la pollution de CO_2 et contribuer à protéger l'environnement. Cependant, centrales thermiques au charbon fournit encore une fraction importante de la production totale d'énergie. Par exemple, si nous voulions remplacer l'utilisation du charbon tout le monde par des sources non carbonées, il faudrait à construire chaque année pour les 50 prochaines années, soit 32 nouveaux 1GW centrales nucléaires, 10 000 de 3.2 MW de nouvelles moulins à vent, ou 6.4 millions de nouvelles maisons de 5kW photovoltaiques.

La fusion nucléaire

Les réactions de fusion donnent la puissance aux étoiles. Dans les étoiles, le combustible de fusion est détenu par la forte force gravitationnelle. Il faut beaucoup d'énergie pour forcer les noyaux de fusionner, même en cas d'élément le plus léger, l'hydrogène. Mais la fusion des noyaux plus légers, ce qui crée un noyau plus lourd et un neutron libre, généralement libère plus d'énergie qu'il faut pour les forcer ensemble. L'énergie libérée dans la plupart des réactions nucléaires est beaucoup plus grande que celle des réactions chimiques. C'est car l'énergie de liaison qui maintient un noyau ensemble est beaucoup plus grande que l'énergie de maintien les électrons autour du noyau. Par exemple, l'énergie d'ionisation gagnée par la jonction d'un électron vers un noyau d'hydrogène est - 13,6 eV - moins d'un millionième de 17 MeV relâché en cas de réaction du deutérium-tritium. Toute la production d'énergie dans les réactions nucléaires est basée sur les différences d'énergie de liaison nucléaire. Cette différence de masse correspond à l'énergie de liaison nucléaire selon Einstein masse-énergie relation $\mathrm{E} = \Delta\mathrm{mc}^2$.

Il y a deux façons d'obtenir de l'énergie nucléaire. En transformant les noyaux lourds dans les noyaux d'une taille moyenne - cela se fait par la fission. Ou, par la fusion de noyaux légers en noyaux plus lourds. Faire cela d'une manière contrôlée a été l'objectif de recherche sur la fusion depuis environ 40 ans. L'énergie libérée par nucléon est de l'ordre de 1 MeV pour les réactions de fission et de l'ordre de quelques MeV pour les réactions de fusion. Cette est de 6-7 ordres de grandeur au-dessus d'énergie typique dans les réactions chimiques, ce qui explique l'efficacité et le risque potentiel de l'énergie nucléaire.

Pour être un candidat pour un système de production d'énergie, le combustible de fusion doit aussi être suffisamment abondante et facilement accessible afin de rendre la production d'énergie économiquement rentable. Le deutérium est naturellement présent dans les océans. Le rapport entre le deutérium et la présence d'hydrogène est d'environ 1/6420. Par exemple, un litre d'eau de mer contient la même quantité d'énergie que trois cents litres d'essence. Compte tenu de la quantité totale d'eau dans les océans, le poids de deutérium est estimé à $\sim$ 4.613 tonnes! Le deutérium peut être récupéré par électrolyse de l'eau, par l'intermédiaire la distillation de l'hydrogène liquide, ou en utilisant différentes techniques d'adsorption chimique. L'énergie libérée par une tonne de deutérium est d'environ 250 · 1015 J. Le deutérium contenu dans l'eau de mer donne donc 3,6 · 1011 TW d'énergie consommée sur un an. Mais nous avons mentionné plutôt que la consommation d'énergie est aujourd'hui 3CMO. Utilisation de conversion d'unité, 1CMO = 1,6 · 1020 J, la consommation mondiale annuelle est 15TW. Cela signifie que l'énergie contenue dans l'eau de mer serait suffisant pour plusieurs milliards d'années. Par exemple, dans le cadre de réacteur de fusion, il est prévu qu'il y aura moins de 1g de carburant à un instant quelconque dans la chambre à vide. Il est prévu, que les futures centrales de fusion aura besoin d'environ 250 kg de carburant par an (la moitié du deutérium, dont la moitié du tritium). Le deutérium est concentré dans les fins industrielles, scientifiques et militaires que l'eau lourde de l'eau ordinaire. Lourd l'eau a été largement utilisée comme modérateur de neutrons dans les réacteurs canadiens à eau lourde. La partie du combustible tritium est plus problématique, car il n'y a pas de source importante naturelle. Le tritium est un isotope instable radioactif avec une demi-vie de 12,3 ans. Inventaire mondial pour le tritium est actuellement d'environ vingt kilos. Par conséquent, le tritium est très cher - $30 000 / g. Par contre, une deuxième source de tritium existe: le tritium peut être produit avec réactions nucléaires des neutrons issus de la réaction DT et de lithium.

Le combustible de fusion ultime sera donc le deutérium et le lithium. Ce dernier est aussi très abondant et répandu dans la croute terrestre et même l'eau de mer contient une concentration moyenne d'environ 0,15 ppm de lithium. Si la fusion était de fournir de l'électricité pour le monde entier, les réserves connues de lithium vont durer au moins mille ans. Contrairement aux réactions de particules chargées, ces réactions neutroniques ne nécessitent pas des températures élevées. Dans un réacteur de fusion deutérium-tritium, le tritium sera donc élevé dans une couverture contenant du lithium entourant le récipient thermonucléaire. En raison des propriétés radioactives de tritium, les dispositifs de fusion de nos jours utilisent principalement des réactions DD. Quelques concepts complets décrits ci-dessus avec des réactions DT et couvertures lithium seront utilisées dans réacteur thermonucléaire expérimental international (ITER), qui est opération est prévue pour 2020. L'impulsion purement inductif conduit a une durée de décharge nominale de 400 s . Au cours de ces 400s environ 0,4g de tritium sera utilisé pour les réactions de fusion. Mais pour le premier prototype de centrale à fusion (DEMO), environ 300g de tritium seront nécessaires par jour pour produire 800 MW d'énergie électrique. Par conséquent, la question de la faisabilité du concept tritigène jouera un rôle crucial.

Ignition

Pour initier la fusion nucléaire, il est nécessaire de mettre ensemble et si proche des noyaux de certains atomes légers pour surmonter les fortes forces électrostatiques répulsives et de permettre d'agir la force nucléaire. En raison du ≪ quantum mechanical tunneling ≫ effet tunnel, la réaction D-T se produit aux énergies inférieures qu'il faut pour surmonter la barrière de Coulomb. Comme un plasma D-T est chauffé par des sources d'énergie externes à des conditions de chauffage thermonucléaires l'α- particules fournit une fraction croissante de la puissance totale de chauffage. Lorsque les conditions de confinement adéquates seraient fournies, on atteint un point ou la température du plasma pourrait être maintenue contre les pertes d'énergie uniquement par des particules α-chauffage - l'allumage. La condition pour l'allumage peut être exprimée en soi-disant critère de Lawson (ou triple produit) ce qui donne pour la réaction DT:

$$n\tau_E > \frac{12}{\langle \sigma v \rangle} \frac{T}{E_\alpha} \tag{1}$$

C'est une forme très pratique pour la condition d'allumage, car il fait ressortir clairement les exigences sur le temps de la densité, la température et l'accouchement.

Fusion par confinement magnétique

Ce travail est exclusivement un sujet appartenant à la fusion par confinement magnétique, ou les grands principes sont expliqués. Le concept principal pour atteindre la fusion thermonucléaire sur Terre est de confiner un plasma. Le plasma est constitué de noyaux atomiques légers et des électrons dans une configuration de champ magnétique. Le plasma thermique peut atteindre des conditions nécessaires pour atteindre un bilan énergétique positif. La force de Lorentz induit une trajectoire hélicoïdale des particules chargées (orbite de Larmor) le long des lignes de champ magnétique. Le champ magnétique est donc susceptible de restreindre le mouvement des particules perpendiculairement au champ magnétique. Mais ce n'est pas d'empêcher les particules de se déplacer le long du champ magnétique. Cet effet sert de base pour tous les systèmes de confinement magnétique. Il est nécessaire de fermer les deux bords ensemble pour éviter des pertes à partir des bords. Pour une seule particule dans un dispositif toroïdal, le confinement est parfait. Malheureusement, dans la réalité, les collisions de particules, la dérive, la turbulence conduisent au transport des particules et de l'énergie au travers de la bouteille magnétique.

Tokamak

Un tokamak est un dispositif toroïdal dans lequel le champ magnétique poloïdal est créé par une courant toroïdal circulant à travers le plasma. Un fort champ magnétique toroïdal est généré par un système de bobine de champ toroïdal. Le courant toroïdal est induit par l'effet de transformateur. Le plasma se sert d'un enroulement secondaire du transformateur, tandis que le primaire est enroulé sur le cour central. La géométrie du plasma toroïdal conduit à deux forces de cerceaux, qui sont à la fois dans le sens d'élargir la bague de plasma. La première de ces forces résulte de la tendance naturelle d'une boucle de courant à se développer dans un effort visant à abaisser son énergie magnétique. La seconde force est la résultante de la somme des forces centrifuges et grad-B rencontrées par les particules individuelles au cours de leur mouvement le long des lignes de champ. Si le champ appliqué vertical est spatialement non uniforme et augmente avec le rayon principal, le plasma se trouve verticalement instable. Pour éviter cette séparation de charge, il est nécessaire de tordre les lignes de champ magnétique par d'autres composantes du champ magnétique. Puis, les lignes de champ simples cartographier les surfaces de flux dits. Sur ces surfaces de flux, le plasma de transport est rapide, car il est toujours parallèle à B, et donc les paramètres du plasma sont généralement constants sur une surface donnée de flux. La position de ces surfaces de flux est généralement décrite par l'angle ϕ toroïdal, le rayon r et l'angle mineur poloïdal θ. Le paramètre définissant le nombre de fois doit déplacement des particules toroïdale pour revenir au même point en projection poloïdal est appelé facteur de sécurité q et peut être exprimée comme

$$q(r) = \frac{r}{R}\frac{B_T}{B_p} \tag{2}$$

ou r est la distance radiale à partir de l'axe magnétique, R est le rayon du plasma principal, et B_T, B_p est le champ magnétique poloïdal et toroïdal, respectivement. Dans le but d'augmenter la pression du plasma, le plasma est poussé au maximum du côté extérieur élevé, ce qui crée un plasma en forme de D, c'est à dire ayant un allongement et triangularité.

Pour amorcer la réaction de fusion, certaine procédure doit être suivie. La premiere étape consiste à nettoyer la chambre des impuretés par cuisson. Les impuretés risquent de contaminer le plasma et par plasma processus d'irradiation refroidir. Par ailleurs, des pistes de cuisson à la libération de prisonnières espèces hydrogénoides (dégazage) des deux surfaces proches et les couches co-déposés. Particules libérées sont constamment pompée à basse pression (pression de fonctionnement typique de plasma sur Tore Supra est de l'ordre de 10^{-5}Pa). La procédure de chambre de cuisson prend habituellement quelques jours (ou semaines) à de grosses machines et doit être faite avant la campagne expérimentale. Lors de la cuisson, le système d'eau de refroidissement fournit de l'eau à haute température et de pression pour augmenter la température des composants en cuve. Température de cuisson typique est supérieure à 200°C. Une fois que la chambre est propre et prête pour le plasma, de puissants aimants qui permettent de limiter et de contrôler le plasma sont allumés. En même temps, à faible densité de combustible gazeux est introduit dans l'enceinte à vide par un système d'injection de gaz. Puis un courant électrique est appliqué au système qui amène le gaz à décomposer électriquement, obtenir plasma ionisé et forme. Dans le cas d'ITER, le plasma est prévu pour le démarrage sur le côté haut champ avec une configuration de section transversale circulaire. Dans le but d'augmenter la pression du plasma, le plasma change de forme en forme de D en tant que le courant de plasma est accéléré. Appliquée de l'extérieur un champ magnétique horizontal peut ensuite être utilisé pour maintenir le plasma centré. Dans tous les tokamaks modernes le contrôle de la position horizontale et verticale est obtenus par feedback systèmes. La combinaison des champs ci-dessus peut générer une configuration tokamak équilibre. Une fois le plasma formé, un ravitaillement additionnel continu en carburant (mélange D-T) est nécessaire pour maintenir l'état d'équilibre. Dans la phase finale du pulse, d'alimentation en carburant est réduite pour parvenir une lente descente de l'énergie de fusion. Le courant de plasma est incliné vers le bas pour mettre fin à la décharge.

Chauffage du plasma

Pour atteindre les conditions pour un plasma en combustion, il est nécessaire de chauffer le plasma à des températures extrêmes de l'ordre de centaines de millions de degrés Kelvin. Pour ce faire, des méthodes de chauffage efficaces sont nécessaires. Aussi le confinement du plasma et son contrôle sont nécessaires pour maintenir la densité et pour minimaliser les pertes de chaleur. Comme mentionné ci-dessus, dans les tokamaks, le plasma est vu comme un enroulement secondaire d'un transformateur de conduite et un grand courant. En raison d'une résistance au plasma finie, elle peut être chauffée via l'effet Joule. Malheureusement, la résistance du plasma est très faible et diminue avec la température ce qui ne permette pas d'arriver aux conditions d'auto-entretien des conditions de fusion. Depuis l'unité de résistance électrique est l'Ohm, cette méthode se réfère à un chauffage ohmique.

Chauffage à la fréquence cyclotronique ionique: chauffage dans la gamme de fréquences cyclotron ionique repose sur le mouvement circulaire des particules chargées perpendiculairement la ligne de champ. La fréquence de l'oscillation est donnée uniquement par la charge et la masse de la particule, et la force du champ magnétique. Par conséquent, si une onde électromagnétique est lancée avec une fréquence similaire à la fréquence des particules dans le coeur du plasma, l'écho d'onde avec le mouvement des particules perpendiculaires et chauffe le plasma.

Injection du faisceau neutre: Cette technique est basée sur l'injection des faisceaux énergétiques d'atomes neutres dans le plasma ohmique pré chauffé. Que le faisceau pénêtre dans le plasma, les atomes s'ionisent et sont donc en conséquence capturés dans le champ magnétique du tokamak. Étant donné que ces nouveaux ions sont beaucoup plus rapides par rapport aux particules du plasma moyennes, ils transfèrent une partie de leur énergie au plasma via les collisions causant l'augmentation de la vitesse moyenne des particules.

Lower hybrid current drive: Génération de courant par ondes sur le mode hybride-bas: Bien qu'il existe de nombreuses autres fréquences de résonance dans le plasma du tokamak, il a été constaté expérimentalement que certains d'entre eux sont inefficaces ou qu'ils ne peuvent tout simplement pas pénétrer à la région de plasma. Cependant, il existe une fréquence comprise entre hybride d'électrons et d'ions fréquence de résonance. Cela joue un rôle dans la génération de courant du au fait que le champ d'ondes électriques est parallèle aux lignes de champ magnétiques. Les électrons avec un peu plus lentes vitesses thermiques peuvent ≪surfer≫ sur le potentiel électrique de façon résonante et ainsi augmenter leur vitesse dans la direction de l'onde. Bien sur, un effet inverse se produit pour accélérer les électrons. Heureusement, il s'avère qu'il y a plus d'électrons lents que de rapides dans la distribution de vitesse thermique.

Le Tokamak "Tore Supra"

Tore Supra (TS) est un grand tokamak avec une section circulaire de plasma section (grand rayon $R = 2{,}4$m et rayon mineur $a = 0{,}7$m) dont la dernière surface magnétique fermée (DSMF) est défini par son intersection avec le fond limiteur toroïdal ou avec le moteur d'antenne de protection limiteur (APL). Le plasmatique maximale actuelle et le champ magnétique toroïdal sont $I_p < 1{,}5$mA et $B_T < 4$T, respectivement. Principales caractéristiques de TS sont ses supraconducteurs toroïdaux sur le terrain (TF) bobines et sa paroi activement refroidie en premier. En total, il y a 18 bobines supraconductrices TF qui sont refroidis par des super-fluide, il à une température de 1.8K environ. Tore Supra est le seul tokamak entièrement équipée par le refroidissement actif des composantes en face du plasma. Le refroidissement est fourni par une boucle d'eau à haute pression avec une température d'environ 200°C , vitesse d'écoulement de 10 ms^{-1}, et la pression de 40 bars. Cela rend le tokamak TS, avec son chauffage d'appoint et des capacités d'entraînement actuelles (9 MW de FCI et 7 MW de puissance de la LH), une machine idéale pour l'étude des décharges de plasma longues.

Le but de Tore Supra est d'obtenir de longues décharges stationnaires, répondant ainsi à deux questions principales: la non-inductive génération actuelle et la chaleur continue et l'élimination des particules. Le programme de physique a donc deux principaux axes de recherche, complétés par des études sur la stabilité magnethydrodynamic, la turbulence et du transport. Le programme de physique de première concerne l'interaction des champs électromagnétiques (inférieure hybride et cyclotronique ionique) vagues avec le plasma chaud central. Tout ou partie du courant de plasma peut être généré de cette façon, de manière à contrôler le profil de densité de courant. Il s'agit d'une contribution importante à la notion de ≪tokamak avancé ≫. En 1996, des progrès notables ont été réalisés, permettant des décharges totalement non-inductives sur une période de 75s à obtenir. Le programme de physique concerne aussi le plasma de bord et de son interaction avec la première paroi. Par ailleurs, dans le cadre du projet ITER, le plasma a une nouvelle forme en D avec une configuration divertor tungstene complète. Cette amélioration est vue comme une importante mise à niveau Tore Supra - WEST projet (acronyme de l'Environnement W en régime permanent Tokamak). Avec cette mise à jour majeure, Tore Supra servira de banc d'essai pour tester les composants face au plasma d'ITER.

Physique de bord du plasma

Un enjeu majeur dans la conception et la construction d'un réacteur de fusion nucléaire avec un plasma confiné par champ magnétique est l'interaction du plasma chaud avec les composants matériels d'un tel dispositif. D'une part, les composants face au plasma représentent un puits pour l'énergie et des particules émises par le plasma. Le bombardement de particules du matériau peut provoquer le dégagement des atomes de paroi et d'atomes de carburant préalablement bloqués qui à son tour peut entrer dans le plasma. La contamination du plasma par des impuretés libérées de la structure de l'enceinte est l'un des principaux problèmes causés par l'interaction plasma paroi processus conduisant à un rayonnement de plasma et le refroidissement du plasma. Un problème supplémentaire est la dégradation de la structure du matériau par le bombardement de particules et le flux d'énergie élevée. Cela pourrait à son tour limiter la durée de vie des composants face au plasma de façon significative. Ces problèmes doivent être résolus sous la contrainte que la puissance générée doit passer à travers les composantes de l'enceinte à un certain endroit. Le mur peut en outre agir comme un réservoir pour les isotopes à combustible à hydrogène conduisant à une source incontrôlable supplémentaire d'atomes, ce qui peut causer des problèmes dans le maintien des conditions de décharge fixes. En outre, la rétention du tritium dans le mur doit être limitée à respecter les contraintes de radiation et de sécurité.

Interactions plasma-surface

En effet, le confinement du plasma dans les tokamaks fils n'est pas parfait à de nombreuses interactions indésirables de plasma avec les matériaux environnants. En conséquence, les impuretés matérielles sont libérées dans le plasma confiné. Les impuretés présentes un certain nombre de problèmes dans les tokamaks. Principal inconvénient d'avoir impuretés dans le plasma est la perte de puissance radiative due à l'ionisation complète de l'atome d'impureté qui à son tour refroidit plasma. Ceci est particulièrement important pour les machines fonctionnant avec du tungstène qui a un numéro atomique élevé. Deuxième point important est la dilution de carburant due aux électrons découplés. Par conséquent, il est nécessaire de maintenir le plasma propre par cuisson de la cuve de nettoyage par des décharges luminescentes. Il existe plusieurs façons du matériau du mur peuvent être introduites dans le plasma telles que le recyclage, la pulvérisation cathodique, évaporation ou arc.

Le transport des particules dans le plasma entourant les murs est principalement causé par la diffusion du cour du plasma. Les particules chargées frappent à la surface solide ou ils sont neutralisés par l'ion-électron recombinaison. Une telle particule neutre nouvellement créée est libre d'agir du champ magnétique. Cela peut rentrer dans le plasma à nouveau jusqu'à ce qu'ils obtiennent ionisé par collisions électroniques. Ce processus est connu sous le nom ≪ recyclage ≫. Dans les tokamaks limiteur de particules recyclées entrer dans le plasma ionisé neutres et obtenir après avoir passé une fraction du rayon du plasma, alors que dans le divertor tokamaks l'ionisation pourrait avoir lieu près des plaques de neutralisation. Un autre processus qui s'impose fréquemment en raison de plasma paroi interactions est appelé ≪sputteting≫. Sputtering est un procédé au cours de laquelle les atomes de surface solide sont arrachés par l'impact des ions ou des atomes incidents. A côté de la production de l'impureté, le sputtering conduit aussi à la dégradation des matériaux et de l'érosion de surface. Nous distinguons deux types de sputtering: physiques et chimiques. Voyons d'abord décrire le sputtering physique. Si l'énergie cinétique de la particule incidente est suffisamment élevée pour dépasser l'énergie de liaison de surface, le sputtering se produit et un atome libéré de la matière. Par conséquent, le sputtering diminue le rendement de l'énergie de surface augmente de liaison et augmente avec l'énergie transférée à partir de la particule incidente à l'atome de matière. C'est l'un des principaux problèmes de chauffage cyclotronique ionique résonance. Le principal problème de l'utilisation de FCI est le fait qu'elle produit des tensions continues importantes dues à effet de rectification des gaines RF. En conséquence, l'énergie cinétique des ions accélérés à travers ces grands potentiels est augmentée ainsi que la vitesse de pulvérisation. En ce qui concerne chimique sputtering, l'atome d'incident peut interagissent avec les atomes du matériau et créer une molécule qui peut être facilement détaché de la surface. Réaction la plus courante de nos jours dans les tokamaks est la réaction entre les isotopes de l'hydrogène et de carbone. Dans l'autre cas, l'isotope de l'hydrogène présente une affinité chimique élevée aux matériaux des murs et est emprisonnée dans ceux-ci. Cette ≪rétention≫ phénomène pourrait être dangereux pour le fonctionnement du réacteur thermonucléaire car elle pourrait conduire à un cumul de tritium de la chambre du réacteur.

Transport des particules

Particules se déplacent non seulement le long des lignes de champ, mais peut se déplacer perpendiculairement aux lignes de champ magnétique principalement en raison du transport turbulent et les dérives. Dans la forme la plus simple, les principaux mécanismes qui peuvent être utilisés pour décrire le transport à travers les surfaces de flux sont des collisions entre les particules colombiens. Deux particules circulant le long de deux lignes de champ fermées peuvent en effet interagir via des forces électrostatiques et de la dérive sur les autres lignes de champ. Du point de vue classique, ces effets collisionnels peuvent être décrits comme un processus de diffusion car elle implique en quelque sorte une marche aléatoire. Le flux de particules à la surface transversale de flux est proportionnel au gradient de densité et le coefficient de diffusion locale $D_\perp^c$:

$$\Gamma_\perp = -D_\perp^c \nabla n \tag{3}$$

En réalité, le problème est plus complexe. La courbure de la géométrie toroïdale implique plus grande variété de processus de transport de collision par conséquent à l'inhomogénéité du champ magnétique. Cela conduit à la description néo-classique du transport. À bas régime collisionnel les trajectoires des particules sont déterminées par la géométrie toroïdale. Considérons une particule en orbite le long d'une ligne de champ magnétique connaît une variation de l'intensité du champ magnétique le long de la direction parallèle. Il y a une force magnétique $F = -\mu B$ qui pousse les particules provenant des régions de fort champ magnétique au plus basses. Si la vitesse parallèle d'une particule se déplaçant sur le côté bas du champ vers le côté haut du champ est faible, telle particule subit un effet de miroir magnétique et est réfléchie. La trajectoire résultante de particules piégées rappelle, dans la projection poloïdale, en forme de banane. Ces orbites plus grandes dans le régime de la banane permettre une plus grande diffusion par rapport à la description classique. Le transport dans le régime collisionnel est qualifié de régime Pfirsch-Schlüter. Dans le régime entre le régime fortement et faiblement collisionnel est appelée le plateau, dans lequel aucune dépendance en fonction la fréquence des collisions n'existe.

Bien que la description néo-classique des processus de diffusion retourne une valeur plus élevée que la diffusion de l'approche classique, le modèle n'est pas en mesure d'expliquer les coefficients de diffusion mesurés lors des expériences, en particulier au bord du plasma (écart de l'ordre de quelques ordres de grandeur). Historiquement, le coefficient de transport étonnamment élevé mesuré dans le plasma a reçu le qualificatif d'anormal puisque ni les théories classiques et néoclassiques ont réussi à prédire ces valeurs. On croit que l'amélioration de la diffusion est causée par la turbulence du plasma.

Face au plasma matériaux

Dans un réacteur de fusion, on peut trouver plusieurs éléments auxquels est confronté le plasma directement. La plus grande surface est constituée de la première paroi qui entoure la région de masse à plasma du tore. La forme du plasma peut être limitée par des limiteurs de supplémentaires pour protéger la paroi du vaisseau ou de l'équipement comme des antennes pour la radio-fréquence de chauffage ou l'optique de certains systèmes de diagnostic qui ne peuvent résister à des charges thermiques excessives. Enfin, les partie très importantes de composante face au plasma ; dans les dispositifs de fusion actuels et futurs, sont des plaques de divertor cibles. Dans une telle configuration ces plaques assurent la zone d'interaction plasma-surface principale.

Des lignes de champ magnétiques qui se trouvent sur une surface de flux qui ne fait contact avec un solide la surface sont appelées fermée, tandis que ceux qui passent à travers une surface solide sont appelés ouverte. La frontière de la région confinée est connue sous le nom de Dernière Surface Magnétique Fermé (DSMF) ou séparatrice (dans le cas de la configuration divertor), tandis que le terme de raclage hors couche (SOL) représente une région étroite de la largeur de seulement quelques cm, à l'extérieur de cette frontière. Le plasma de bord peut être compris comme étant la région ou le plasma est essentiellement séparé du plasma de coeur. La largeur de SOL peut alors être définie comme la distance radiale moyenne que particule se déplace au cours du temps de vol parallèle le long d'une longueur de connexion. Il y a deux façons par lesquelles la ligne de champ fermée dernière peut être limitée. Dans le cas le plus simple et historiquement l'option d'antérieure pour définir la région confinée était de 'limiter' en insérant un obstacle dans le plasma. Cet objet est appelé un limiteur. Flux d'impuretés importantes en provenance de matériau pulvérisé limiteur empêche la réalisation des plasmas chauds et propres. Par conséquent, une solution plus sophistiquée a été développée ; il y a environ 30 ans, en utilisant une modification des lignes de champ magnétique au bord du plasma. Dans le nouveau dessin, les lignes de champ du SOL sont incurvées vers une région dédiée ou l'échappement du plasma se termine en interagissant directement avec la paroi (les plaques cibles) ou avec une couche de gaz tampon. Cette configuration, appelée divertor, a prouvé dans les expériences d'être nettement plus avantageux, car il réduit de manière significative la contamination directe ≪ ligne de vue ≫ du plasma de base par des atomes d'impureté pulvérisée. Il permet également de parvenir à un H-mode ou une barrière de transport caractéristique bord conduit à un confinement de l'énergie améliorée.

Scrape-off layer

Le bord du plasma dans un plasma confiné magnétiquement est défini soit par une limite du matériau, soit par séparatrice magnétique dans le cas d'un plasma détourné. À l'intérieur de la limite, les surfaces magnétiques sont fermées. Dans la zone entre la limite et la surface de paroi, les lignes de champ coupent composants de matériels. Ces connexions jouent un rôle crucial en bordure physique des plasmas. L'échappement de particules et la fraction α-particule de la puissance sont couplées à une large mesure à travers cette région. Ils sont transférés vers les limiteurs ou des plaques divertor. Une telle situation est similaire à l'insertion d'une sonde mobile dans le SOL.

Des éléments de paroi qui se coupent le champ magnétique, servent en tant que puits de plasma parfaits. Elles imposent un écoulement dirigé le long des lignes de champ. Les tubes de flux générés à chaque élément de paroi sont remplies de plasma par perpendiculairement transport (diffusion, dérives). Nous avons mentionné dans les pages précédentes que le transport des particules à travers les privilèges de champ magnétique est assez complexe et pas encore pleinement compris. Des simulations basées sur le modèle de la diffusion dans les codes 2D reposent sur le coefficient de diffusion empiriquement ajusté $D(r, \theta)$. Cela rend les résultats de code en accord avec les observations expérimentales, mais toujours avec un succès limité. La meilleure approche consiste à utiliser des codes 3D avec soi transport turbulent uniforme, mais ils ont besoin d'énormes processeurs parallèles et ne sont pas adaptés pour la description analytique. Par conséquent, pour comprendre en fonction des caractéristiques de couche de bord, on peut utiliser le modèle heuristique simple.

Avec des estimations simples, nous pouvons maintenant caractériser certaines fonctions de base du SOL que l'épaisseur SOL et la variation de densité radiale. Pour cela, nous supposons simplement SOL avec la diffusion perpendiculaire comme source de particules. La caractéristique fondamentale du simple SOL est que la distance entre les DSMF et la première paroi est suffisamment grande. Pour cela la densité du plasma décroît naturellement à zéro. Dans les autres mots, toutes les particules chargées frappent le limiteur principal ou les plaques de déviation. Aucune ne frappe le mur en premier. Cependant, pour des raisons d'économie et de performance du plasma, les plasmas sont formés pour occuper le plus de volume de la chambre à vide que possible. En outre, tous les tokamaks ont limiteurs secondaires (limiteurs poloïdales, limiteurs de protection d'antenne, etc.) Par conséquent, une interaction significative avec le plasma SOL peut se produire. La structure simple SOL est perturbée conduisant à la formation d'un complexe SOL qui exige une analyse 3D. Parce que les tokamaks sont toroïdale symétrique, on peut traiter le transport à l'intérieur du SOL comme un problème de 2D: écoulement le long de la ligne de champ et la diffusion dans la direction radiale. En outre, en raison d'un faible épaisseur radiale du SOL par rapport au plasma petit rayon, on peut appliquer une géométrie plane et de redresser le SOL. Un tel modèle fournit alors l'épaisseur SOL comme

$$\lambda = \sqrt{\frac{D_{\perp} L}{c_s}} \tag{4}$$

La largeur du SOL typique pour le Tore Supra est de l'ordre de $\lambda \approx 2$ - 3cm. En dépit de fait que est un des résultats empiriques basées sur des mesures de SOL: λ, L, et c_s, il n'existe pas de dérivation du premier principe. On pense que le D efficace qui donne lieu à des longueurs de chute observée est due au transport turbulent. Il est important de noter que même dans l'approximation la relation SOL pour le plasma de bord est juste une estimation. La température, apparaissant dans la définition de la vitesse du son ion, n'est pas constante mais varie radialement sur cette région. Ayant maintenant en estimation de l'épaisseur SOL, nous aimerions savoir comment la densité varie radialement. Cette variation radiale de la densité à l'intérieur du plasma de bord peut être approchée à l'aide modèle 1D - calcul basé sur la conservation de la masse le long du tube de flux et les rendements

$$n(x) = n(0) \cdot e^{-x/\lambda} \tag{5}$$

Cependant, il faut être prudent lors de l'utilisation de ces expressions simples dues à des sources de particules à l'intérieur de cette région ou les dérives modifient le résultat. De plus, ces estimations 1D simples n'offrent qu'une base pour idée générale sur le plasma de bord, mais ne peut pas être utilisé pour les machines réelles qui exigent dans tous les cas des modèles 2D ou 3D.

Gaine

Dans les sections précédentes, nous avons décrit une région de plasma principal qui remplit la plupart de la chambre de tokamak. Mais, il y a aussi une autre région qui joue un rôle important dans la physique des plasmas bord - la gaine. La gaine est une région très mince qui apparaît spontanément entre le plasma et la surface solide. Ceci est causé par une différence importante dans la masse de l'électron et l'ion. Considérons maintenant plasma s'écoulant sur une surface neutre isolant. Parce que la vitesse des électrons est bien supérieure à ions, la surface reçoit un flux d'électrons plus élevé que le flux d'ions. À son tour, perturbe la condition imposée par l'égalité des flux ionique et électronique à la surface. La surface est chargée négativement en raison de l'accumulation d'électrons. Ce point conduit à une certaine répulsion des électrons à entrants et à l'attraction d'ions. Afin de préserver l'ambipolarité, un potentiel électrostatique est formé. Par conséquent, la gaine est définie comme le volume de plasma sur laquelle se produit la séparation de charge. La dimension caractéristique de la couche de gaine est déterminée par la longueur de Debye, qui peut être obtenu à partir de la solution de l'équation de Poisson

$$\frac{d^2\phi}{dx^2} = -\frac{e}{\epsilon_0}(n_i - n_e) \tag{6}$$

Aux autres fins, nous définissons une position de référence à l'entrée gaine, étiquetée comme se. Dans cette position, la neutralité tient quasiment encore mais commence à diverger comme se déplaçant à l'intérieur de la gaine. Nous supposons en outre que, dans ce potentiel, la densité d'ions est spatialement constante et électrons peuvent être décrits par l'équation de Boltzmann: $n_e(x) = n_{se}\, exp[e(\phi - \phi_{se})/kT_e]$. Nous supposons également que la température des ions est égale à zéro. La solution de l'équation de Poisson donne alors le critère de Bohm pour la vitesse de sortie de plasma et entrée dans la gaine

$$v_{se} \geq c_s \tag{7}$$

Dans le cadre du sujet de ce travail, nous sommes intéressés àa savoir la chute de potentiel $\Delta\phi$ qui naît sous l'action de la différence de mobilité ionique et électronique entre le plasma et une surface solide. Ici, nous supposons que la surface solide est isolée électriquement - flottant. La quantité $\Delta\phi$ est important pour la détermination du taux de pulvérisation ionique de la surface du solide, et le flux de chaleur à la surface du solide. La chute de potentiel dans la gaine de Debye peut être obtenue à partir de l'équation pour le débit total qui doit satisfaire $\Gamma_e = \Gamma_i$. L'utilisation du critère de Bohm permet de décrire la densité de flux d'ions à la cible que la densité de flux parallèle à la gaine d'entrée gaine supposer, sans aucune source. La chute de potentiel entre l'enveloppe de bord et la surface électriquement flottante est définie comme

$$\frac{e\Delta\phi}{kT_e} = 0.5\, ln\left[2\pi\frac{m_e}{m_i}(1+\frac{T_i}{T_e})\right] \tag{8}$$

Il est important de noter qu'il n'existe pas de dépendance à la densité du plasma. Grandeur de $\Delta\phi$ diminue avec l'augmentation de la température des ions rapport à électrons, et avec la diminution de la masse des ions. Pour un plasma de deutérium à l'équilibre thermique ou $T_e = T_i$, la chute de potentiel à travers la gaine est $\Delta\phi \approx -2,3kT_e/e$. Afin d'obtenir le total chute de potentiel, il faut ajouter la baisse qui se produit dans la pré-gaine. La chute de potentiel dans la pré-gaine est donnée par [ref]

$$\phi_{se} \equiv \phi(L) = -\frac{kT_e}{e}ln2 \approx -0.69\frac{kT_e}{e} \tag{9}$$

Par conséquent, la chute de potentiel à travers totale du pré-gaine et la gaine est $\approx 3\mathrm{T}_e$.

Sondes

Les sondes sont le diagnostic du plasma entrant en contact direct avec le plasma. Par conséquent, ils ne peuvent qu'être appliqués qu'au bord du plasma ou le flux de plasma reste acceptable et ne conduit pas à un échauffement excessif de la sonde. La forme la plus connue de la sonde est la sonde de Langmuir. Les sondes de Langmuir (LP) fournissent la température électronique et le diagnostic de la densité dans les conditions à froid (<50eV) et à faible densité des plasmas. La sonde se compose d'une électrode de métal léger - cylindrique, sphérique ou en forme de disque - plongeant dans le plasma. La gaine qui enveloppe la sonde protégé le plasma du potentiel de la sonde. L'essence même de la technique de sonde de Langmuir est de suivre le courant collecté par la sonde en fonction des variations de tension de la sonde. La dépendance actuelle sur la tension variable est généralement appelée caractéristique I-V. Le courant collecté par la sonde à partir du plasma est positif si la sonde de polarisation V est très négatif par rapport au potentiel plasma, V_p. Ensuite, le champ électrique autour de la sonde permettra d'éviter au maximum des électrons énergétiques d'atteindre la sonde. Cela conduit à une réduction effective de la mise à zéro de courant d'électrons. Le courant collecté par la sonde sera alors entièrement du aux ions positifs, puisque ceux-ci ne rencontre qu'un champ d'attraction. Ce courant est appelé I_{is} l'ions courant de saturation. Comme le potentiel appliqué à la sonde est augmenté, le nombre d'électrons qui est capable de surmonter le champ électrique répulsif et de contribuer à une augmentation exponentielle (si l'on suppose distribution de Boltzmann). Éventuellement le courant d'électrons est égal au produit-II, de telle sorte que le courant total est égal à zéro. A ce stade, le potentiel flottant V_f est atteint. Poursuite de la hausse de la polarisation sonde à V_p permet au courant d'électrons de totalement dominer le courant ionique. Au V_p, les électrons sont libres d'être collectés par la sonde. Tout accroissement supplémentaire de polarité, il suffit d'ajouter de l'énergie aux électrons, et non pas le courant consommé. Pas de courant supplémentaire est recueillie à stabiliser I_{es} ≪ électron-courant de saturation ≫. Notez que ce sont les caractéristiques idéales IV, ignorant les processus perturbateurs tels que le bombardement de la sonde par des électrons de haute énergie, des émissions d'électrons secondaires provenant de la sonde et la sonde enlever par gravure. En outre, de nombreuses sondes actives dans les plasmas de bord des dispositifs de fusion ne sont pas polarisées à de grandes tensions positives afin d'éviter la saturation partie des électrons et donc éviter que la sonde ne soit endommagée.

Pour décrire quantitativement la dépendance courant-tension, on peut utiliser la formule suivante

$$I = I_{sat}\, exp\left(\frac{V - V_f}{kT_e}\right), where \;\; I_{sat} = en_e c_s A_{col} \tag{10}$$

ou I est le courant collecté à la tête de la sonde, V est la tension de polarisation appliquée, est la saturation I_{sat} courant ionique et A_{col} est la zone de la sonde de collecte. La température des électrons est alors d'obtenir par un ajustement des moindres carrés de la partie exponentielle d'une caractéristique IV.

Tore Supra est équipé de deux sondes à pistons disques situés dans les ports supérieurs du navire situé à 40° et 160° toroïdale. Ils font des mouvements verticaux le long du cordon

R = 2,53m. La profondeur d'immersion maximale est de 0,46m en dessous de son point d'appui. Sonde est immergée dans la SOL avec la vitesse 1,5ms^{-1} qui est suffisamment assez vite pour éviter que la sonde ne soit détruite par l'accumulation d'énergie forte. Par l'utilisation intensive des boucles de rétroaction et l'intégration de plusieurs mesures de diagnostic, la fiabilité du système a atteint un niveau qui permet aux sondes pour être utilisée en routine, même en haute puissance, des décharges de longue durée.

Mach sonde

La plupart des sondes TS sont construits avec un arrangement type sonde de Mach. Les sondes de Mach sont constitués de deux sondes montées dos à dos, à une extrémité qui permet de recueillir des flux de particules chargées séparément le long des lignes de champ des deux côtés de la tète de sonde. En utilisant une théorie de Mach, on peut en déduire un écoulement parallèle dans la SOL. L'idée de base derrière une sonde de Mach, c'est que si le plasma circule, et qu'il existe une signature. Puis la parallèle densité de courant ionique mesuré sur chaque côté de la sonde polarisée négativement sera différent. Le courant mesuré sur le côté amont est plus grand que celle sur le côté aval. La théorie pour la sonde de Mach, supporte fluide ou cinétique, fournit une relation simple entre le rapport des courants d'ions collectés sur des côtés opposés de la sonde et la vitesse d'écoulement parallèle. La densité d'électrons calculée en prenant en compte le flux d'ions est ensuite

$$n_e = \frac{\sqrt{J_i^u J_i^d}}{0.35 e c_s} \quad avec \quad c_s = \frac{\sqrt{e(T_e + T_i)}}{m_i} \tag{11}$$

Les T_e et T_i sont la température d'électrons et d'ions, respectivement. Il est important de dire que, dans nos mesures d'une valeur moyenne de la température mesurée sur les deux côtés de la sonde est utilisée. Le nombre de Mach parallèle peut être dérivé à partir du modèle Hutchinson selon la formule suivante:

$$M_{||} = 0.4 \, ln \left(\frac{J_i^u}{J_i^d} \right) \tag{12}$$

Maintenant, avec la connaissance des résultats de théorie sonde Mach, nous pouvons introduire les deux sondes principales qui ont été utilisées pour l'étude de RF induite SOL modification. À savoir, la sonde tunnel est un retarding field analyzer.

Sonde Tunnel

La sonde tunnel est une sorte de sonde électrostatique utilisée pour les mesures dans la SOL. Il fournit des mesures simultanées de la température électronique, potentiel flottant et parallèle densité de courant ionique. La sonde tunnel utilisé dans ces expériences consiste en un tunnel creux en acier inoxydable de 3mm de diamêtre et 5mm de profondeur qui est fermé aà une extrémité électriquement isolée par une plaque de graphite. Le principal avantage de la sonde tunnel est sa forme concave. La sonde tunnel concave donne des mesures plus précises de T_e et que J_i conventionnels sondes convexes. Afin de mesurer correctement la densité de courant ionique, la surface efficace de collecte de la sonde doit être connue avec précision. Par exemple, la zone efficace d'un axe cylindrique de petit est plus grande que sa projection géométrique le long des lignes de champ provoqué par l'expansion de la gaine autour de la sonde aimantée. Ce domaine en pleine expansion électrique augmente la surface de collecte efficace. Par conséquent, le courant ionique ne sature pas pour une sonde convexe, alors qu'il sature parfaitement pour la sonde à effet tunnel. Comme le champ gaine électrique dépend fortement de la densité et de la température, il est possible que la zone de collecte réelle puisse différer de chaque côté de la sonde. Cela conduit à un certain nombre faussement déduit de la sonde de Mach. Ces problèmes sont éliminées pour sonde à effet tunnel cas, parce que la gaine se trouve à l'intérieur du tunnel. La gaine dans ce cas ne pas perturber les orbites ioniques entrants, et la surface effective de collecte de la sonde est presque exactement égale à sa projection géométrique le long des lignes de champ.

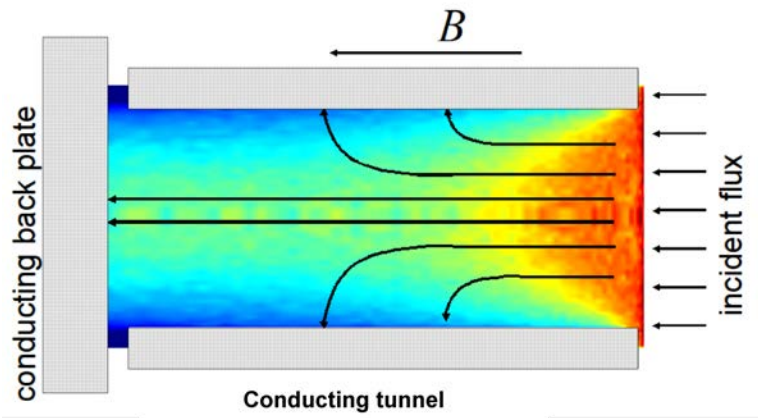

Figure 1: *Vue schématique de la sonde à effet tunnel. Le courant recueilli par chacun des trois conducteurs est surveillé séparément. Les trajectoires des ions centres directeurs sont indiqués par des flèches noires.*

Retarding field analyzer

En principe, retarding field analyzer peut mesurer directement le potentiel de gaine V_{sh} dans la SOL. La sonde RFA est constitué d'une fente d'entre (FE), deux grilles de sollicitation et un collecteur. La fente d'entre est polarisée négativement pour repousser la plupart des électrons thermiques. Les ions qui sont transmis à travers la fente d'entre sont retardés dans le champ électrique. Ce champ électrique est créé par une tension positive appliquée à balayage grille 1. Le collecteur doit recueillir seuls les ions. Par conséquent, il est nécessaire de repousser tous les électrons restants rapides qui sont passés par la fente d'entre. Ou ceux qui sont libérés par émission secondaire à l'intérieur de l'analyseur. Cela se fait en appliquant une tension négative sur la grille 2. Pour obtenir une caractéristique I-V de la sonde, on peut simplement tracer I_{col} collecteur de courant contre le balayage de tension sur la grille 1. Si V_{g1} est faible, I_{col} reste constante. Une fois la V_{g1} surmonte le potentiel de gaine, le signal sur le collecteur commence à diminuer de façon exponentielle.

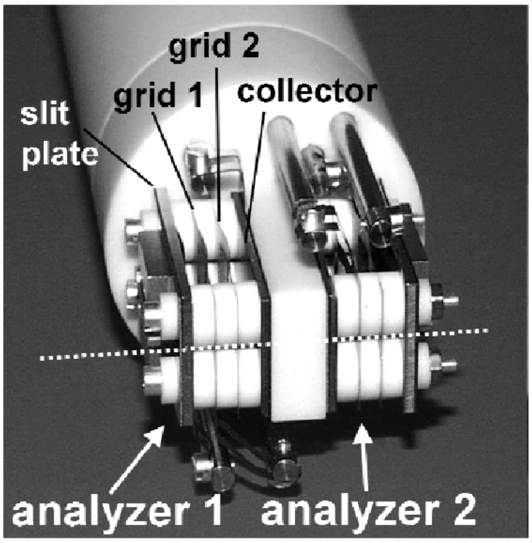

Figure 2: *Vue schématique des composants de RFA principale et le régime typique de polarisation utilisée pour les mesures de T_i et V_{sh}.*

Outre le potentiel gaine et la température des ions, la sonde RFA peut fournir également des informations sur la densité du plasma, la température électronique et le potentiel flottant. C'est fourni par une tension de balayage appliqué à la fente d'entre qui fonctionne alors comme une sonde de Langmuir. La tension de la FE varie seulement au cours de la phase, ou la grille 1 de tension est constante. Une fois la tension de FE est suffisamment négative pour repousser la plupart des électrons thermiques (typiquement -70 → -150V en fonction des conditions du plasma), la tension sur la grille 1 commence à augmenter jusqu'à la valeur maximale.

Modes de fonctionnement

La sonde de Langmuir peut fonctionner selon trois régimes différents en fonction du mode d'acquisition:

- Mode de balayage: Le potentiel appliqué à la sonde est balayé dans le temps, afin d'obtenir une caractéristique courant-tension. Une partie exponentielle de la caractéristique IV fournit des informations sur la température des électrons et le potentiel de la sonde flottante. La densité du plasma peut être dérivée directement de former la partie de saturation de la courbe d'ions.

- Mode flottant: Le courant collecté est fixé à zéro. Le potentiel de la sonde est imposé par l'interaction ambipolaire avec le plasma pour donner la masure du potentiel flottant.
- Régime de saturation: La tension de la sonde est fixée à une valeur fortement négative (-200V) pour collecter uniquement de courant qui est égal à la saturation de courant ionique.

Pour les mesures de TS standard, sans avoir besoin de haute résolution temporelle des données, le mode de balayage est suffisante avec un taux d'échantillonnage de 2 kHz. D'autre part, pour étude de la turbulence ou des fluctuations, il est plus pratique pour passer la sonde soit flottant ou mode de saturation en fonction du sujet d'intérêt.

CONCLUSION

L'objectif de cette thèse est d'étudier, principalement de manière expérimentale, les interactions entre la "scrape-off layer" et les antennes FCI lors de l'injection de puissance. Ces modifications induites par les ondes RF causent les variations du SOL et sont étudiées en utilisant les sondes de Langmuir. Une intention particulière porte sur l'étude des modifications des paramètres de la scrape-off lorsque qu'une antenne est active. L'évolution la densité du plasma, de la température électronique, du potentiel de gaine et de l'écoulement parallèle est suivie.

En particulier, on se concentre à la comparaison de l'influence SOL en utilisant deux différents types des écrans Faraday. Les expériences ont montré très clairement, contrairement aux prédictions théoriques, que le nouveau type d'écran de Faraday avec des barres en porte à faux et des ouvertures type créneau en haut et en bas de l'écran augmente significativement la magnitude du potentiel induit. Les potentiels mesurés par le nouvel écran sont généralement 5 fois plus élevés par rapport à l'écran précédent. Il et important de dire que pour 2MW de puissance de l'antenne, les potentiels mesurés peuvent dépasser 200V, même au milieu ou usuellement le minimum local est normalement observé. Ce désaccord signifie que notre compréhension de la génération RF potentiel n'est pas encore bien comprise. Il semble que le gros de ce désaccord est lié à l'évaluation du RF potentiel. De plus, le comportement de ce nouveau type de l'écran de Faraday n'est pas bien prédit ni par les simulations. Le code de calcule TOPICA a été utilisé qui calcule le potentiel tout simplement comme une intégrale du champ électrique le long de la ligne de champ. Les calculs ne sont pas en accord avec les observations expérimentales. Toutefois un défaut d'alignement a été constaté et nécessite de reprendre tous les calculs de champs proches.

En outre, les simulations prospectives sont actuellement en cours en utilisant les méthodes numériques des éléments finis utilisant le logiciel COMSOL basé sur la modélisation nommée SSWICH (Self-consistent Sheaths and Waves for Ion Cyclotron Heating). Ils prennent en compte de la condition aux limites de gaine. Ici, les simulations préliminaires montrent un bon accord avec nos mesures.

De plus, on a présenté la méthode de la reconstruction magnétique utilisée dans les calcules EFIT. Les calculs montrent que de forts potentiels sont bien induits poloïdalement au voisinage des coins de l'antenne mais radialement sont induits surtout sur les limiteurs latéraux. Cette différence dans la position radiale est attribuée au courant circulant sur l'écran de Faraday et autres courants se développant sur le structure d'antenne. Par conséquent, afin d'expliquer ce désaccord, les limiteurs latéraux ne peuvent pas être négligés dans le modèle, comme ils l'étaient dans les simulations TOPICA.

Une autre observation intéressante concerne la forte variation de l'écoulement parallèle dans les tubes de flux connectés à une antenne alimentée. Ça pourrait avoir une conséquence directe sur le transport des particules radiales. L'écoulement qui est entraîné par des bouffées de plasma, change de façon monotone dans la direction radiale dans la phase ohmique tandis que pendant la phase de FCI cet écoulement est fortement cisaillé. Dans le cas contraire avec l'écran précédent, le cisaillement n'est pas nul pour des densités élevées et est observé à différents angles poloïdaux. Nous avons montré avec une estimation simple que même une prise 100V de l'amplitude de tension peut être suffisante pour détruire les structures turbulentes à travers le SOL à la fraction de la vitesse du son d'ions. La formation de la barrière de transport local a été clairement observée au bord du profil de la densité caractérisé aussi par une forte baisse de la longueur de décroissance de la densité (facteur de 2 par rapport à 5mm). D'autre part, une telle diminution n'est pas observée dans le cas de l'ancien écran, même si un écoulement parallèle est fortement cisaillé ainsi. Cela pourrait impliquer un outil pour réduire un transport radial dans les tubes soumis à la RF. Toutefois, cela correspond à un défi, car ayant un rayon dévié à la paroi va nécessairement aller à l'accélération de particules sur la paroi résultant en sputtering, perte de chaleur etc. Cela arrive aussi avec FCI antenne elle-même. Toutefois, il serait intéressant de calculer si la réduction du transport radial s'étend eu-delà de la zone polarisée par l'antenne RF.

Comme il a été mentionné précédemment, les données de nos sondes sont évaluées par la théorie des sondes de Mach. Cette théorie permet de fournir une base qualitativement acceptable pour la plupart des scénarios de plasma. Mais sa validité en présence de tubes de flux polarisés qui sortent d'une antenne active vers la sonde est discutable à la base. Selon la théorie de la sonde Mach, ou la sonde est considérée comme un point dans l'espace, on s'attend à mesurer le même potentiel sur les deux côtés de la sonde. Mais nous avons montré que la différence entre les potentiels en amont aval peut varier de -100 à 100V. Premier cas se produit lorsque la sonde est reliée à la partie inférieure de l'émetteur. Ici les potentiels sont élevés (observée pour les deux types d'écrans). L'autre cas a été observé pour une grande puissance injectée d'une antenne FCI. Par conséquent, nos mesures indiquent que la sonde comme se comporte comme un petit limiteur et sa taille ne peut pas être négligée. Ce phénomène est associé à la structure complexe de courant radial. Les deux courants DC et RF sont en interaction avec les tubes de flux voisins. Des simulations en tenant compte de la contribution de ces courants transversaux sont basées sur le modèle de sonde double. Un saut de courant est oscillant (coté antenne) tandis que l'autre est flottant (coté sonde). Toutefois, dans le cadre de notre problème, un modèle numérique avec une sonde située au milieu entre deux bonds serait plus approprié. Mais sans doute il serait plus difficile à implémenter.

En ce qui concerne les mesures de la densité au bord, nous avons observé une asymétrie de haut en bas ou la densité est plus élevée au-dessus du plan médian. Cette variation poloïdale de la densité est attribuée aux cellules convectives E×B. Ceci est en bon accord avec la prédiction théorique. En plus, ces cellules convectives vont agir aussi dans le sens radial. Cela a été confirmé par l'analyse des images infrarouges des composants de l'écran de Faraday. Si la sonde est insérée dans la SOL, une augmentation soudaine / diminution de la température des barres de l'écran a été observée. Mais il est à préciser que l'écran lui-même est protégé par des limiteurs latéraux et cachés d' un centimètre derrière leur bord d'attaque. Ainsi, la ligne de champ ne touche pas la structure de l'écran directement. Il interagit par le biais des cellules convectives ExB. En outre, l'intensité du potentiel mesuré flottant semble être compatible avec le modèle de densité présentant une variation poloïdale. Ici, la plus faible densité mesurée au-dessous du plan médian du potentiel est une fonction fortement dépendante de la densité de plasma. D'après les observations expérimentales, soit avec l'ancien ou le nouvel écran, montre que 20% de changement dans la densité du plasma induit une variation d'un facteur de deux du potentiel flottant. Ça nous donne aussi un outil pour réduire ces forts potentiels.

Dans le dernier chapitre, nous avons étudié de façon théorique et expérimentale; des effets gaines RF sur les mesures gaine RFA potentiels. L'analyseur de champ retardé est couramment utilisé pour mesurer la température des ions dans le sol ou les électrons suprathermiques générés par l'antenne hybride basse. Mais son évaluation dans un environnement RF est toujours nécessaire. Nous avons montré par des simulations PIC 1D que la RFA ne peut pas mesurer le potentiel de gaine directement redressée. Mais il peut fournir une indication indirecte sur l'effet des gaines RF en raison de l'élargissement apparent de la fonction de distribution. Les mesures de RFA sont en bon accord avec la prédiction théorique. Ceci a été vérifié par l'observation d'une augmentation de ΔV à l'intérieur des zones perturbées. Le potentiel de gaine apparente mesurée par la RFA est encore bien en dessous de la moyenne en temps réel potentiel de gaine. Cela implique que les potentiels RF peuvent se propager sur de longues distances par rapport à l'antenne. Il convient de souligner que la dimension du domaine simulé dans le code PIC est négligeable par rapport aux 12m de longueur connexion expérimentale de la sonde mobile à l'antenne FCI. Cela démontre également la pertinence des résultats fournis par le code. Néanmoins, une évaluation plus détaillée de l'ampleur ΔV est nécessaire. Cela confirmera si elle est compatible avec la tension RF sur les limiteurs latéraux comme cela est prédit par les calculs.

La perspective future dans le domaine de cette thèse peut être discutée comme suit: On a montré que notre compréhension de la modification RF induite SOL est encore limitée à certains égards et conduit à ce poser des questions: en autre comment sont générés les potentiels RF? Pour bien le comprendre, différentes étapes sont nécessaires. Cela inclut un calcul 3D complet de la distribution du champ électrique autour de l'antenne avec des conditions aux limites appropriées. Également des limiteurs latéraux devraient être inclus. Les résultats expérimentaux peuvent être aussi discutés. Par exemple, un modèle interprétatif avancé des mesures de RFA dans les tubes de flux biaisées est nécessaire. Ceci pourrait être relié à l'élargissement de la fonction de distribution des ions avec le potentiel de gaine.

Contents

Experimental study of the interaction between RF antennas and the edge plasma of a tokamak

Antennas operating in the ion cyclotron range of frequency (ICRF) provide a useful tool for plasma heating in many tokamaks and are foreseen to play an important role in ITER. The goal of ICRF heating is to launch a fast wave into the plasma core where the wave is absorbed. However, in addition to the desired heating in the core plasma, spurious interactions with the plasma edge and material boundary are known to occur. Many of these deleterious effects are caused by the formation of radio-frequency (RF) sheaths. The aim of this thesis is to study, mainly experimentally, scrape-off layer (SOL) modifications caused by RF sheaths effects by means of Langmuir probes that are magnetically connected to a powered ICRH antenna. Moreover, since spring 2011, one of the three ICRH antennas in the Tore Supra tokamak is equipped with a new type of Faraday screen (FS). Results from RF simulations of the new Faraday screen suggest that the innovative structure with cantilevered bars and 'shark tooth' openings significantly changes the current flow pattern on the front of the antenna. This in turn reduces the RF potential and RF electrical field in particular parallel to the magnetic field lines which contributes to generating RF sheaths. Effects of the new FS operation, with comparison of the conventional FS design, on RF-induced SOL modifications are studied for different plasma and antenna configurations - scans of strap power ratio imbalance, injected power and SOL density. In addition to experimental work, the influence of RF sheaths on retarding field analyzer (RFA) measurements of sheath potential is investigated with one-dimensional particle-in-cell code. One-dimensional particle-in-cell simulations show that the RFA is able to measure reliably the sheath potential only for ion plasma frequencies ω_{pi} similar to RF cyclotron frequency ω_{rf}, while for the real SOL conditions ($\omega_{pi} > \omega_{rf}$), when the RFA is magnetically connected to RF region, it is strongly underestimated. An alternative method to investigate RF sheaths effects is proposed by using broadening of the ion distribution function as an evidence of the RF electric fields in the sheath. RFA measurements in Tore Supra indicate that RF potentials do indeed propagate from the antenna 12m along magnetic field lines.

Key words: plasma, Langmuir probe, ICRF antennas, sheath

Motivation

One of the conditions required to attain ignition in a thermonuclear fusion reactor is that the plasma must be heated to a critical temperature. Ion cyclotron resonance heating is presently employed for plasma heating in many tokamaks, and is foreseen to play an important role in the International Thermonuclear Experimental Reactor (ITER). The goal of ICRH heating is to launch a fast wave into the plasma core where the wave is absorbed. The physics of wave propagation in ionized media imposes that ICRH antennas have to be placed in close contact with the plasma, because the waves are evanescent in vacuum and for low densities typical of the scrape-off layer. However, in addition to the desired heating in the core plasma, spurious interactions with the plasma edge and material boundary are known to occur. Many of these deleterious effects are believed to be caused by the formation of radio-frequency sheaths. When an ICRH antenna is in operation, it excites, besides a fast wave responsible for ion heating, also a slow wave (SW) component which then interacts with the material boundary. The parallel electric field of the SW then drives an oscillating RF potential up to several hundred volts between the extremities of open magnetic flux tubes. The natural reaction of the sheath is to rectify the oscillating RF voltage by producing a dc potential due to the higher mobility of electrons with respect to that of ions. In consequence, ions accelerated across this high dc potential then cause many deleterious antenna-edge interactions, such as enhanced sputtering, impurity generation, and localized high heat fluxes at the field line extremities. In addition, the differential biasing of the nearby flux tubes gives arise RF-induced dc $\mathbf{E} \times \mathbf{B}$ particle convection transversally to the field lines. This particle convection which is realized via convective cells tends to modify the density pattern in front of the antenna. Nevertheless, for reliable antenna operation in high power long discharges, such spurious interactions should be minimized. To achieve the suppression of these unwanted side effects, it is necessary to investigate and understand physical phenomena that occur in the vicinity of the plasma facing components, and especially in the vicinity of ICRH antenna.

Until recently, rf sheaths effects were mainly studied in the vicinity of the antenna, and they were estimated using the vacuum field approximation to the sheath voltage as an integral of parallel electric field between the two contact points of the magnetic field whose conducting boundary. Each magnetic field line intercepted by a metallic surface can be considered as a flux tube along which the potential oscillates at the rf frequency and is longitudinally constant. Such a situation is equivalent to a double probe model and is known as thin flux tube approximation. In such case, negative current is collected on the powered ICRF antenna, while positive current is collected by magnetically connected Langmuir probe as is observed experimentally on Tore Supra (TS).

Problems of the heating of the Tore Supra conventional Faraday screen due to the above mentioned side effects and its operational consequences initiated studies on an alternative design. The primary motivation of the Faraday screen improvement was to reduce localized heat fluxes that arise especially during the combination of lower hybrid (LH) and ICRH operation leading to hot spots on the FS frame. Among other motivations of manufacturing the new FS were to increase its heat exhaust capability in order to reduce thermal loads and to withstand high power long discharge operation. A further motivation was to reduce the RF potentials on open field lines and to qualify new screen suitable for ITER.

The aim of this thesis is to investigate the interaction between the plasma edge and a powered ICRH antenna. The experimental study is made by means of reciprocating Langmuir probes that are magnetically connected to a powered antenna. One of the principal goals of this work was to systematically characterize modifications of scrape-off layer parameters (plasma density, electron temperature, sheath potential and parallel flow) due to a presence of active antenna, and especially, to focus on characterization of spatial structures and the effects of the various plasma and antenna configurations on them (density variation, power scan etc.).

Outline

The thesis is devoted to the experimental study of the interaction between antennas operating in the ion cyclotron range of frequencies and the edge plasma of a tokamak. Since the first use of ion cyclotron range of frequencies heating systems in magnetic fusion devices, the non-linear physics of waves in the plasma edge has received considerable attention. With the prospect of ITER, the topic has recently gained renewed interest especially due to side effects associated with ICRH that might play an important role in long discharges scenarios. The thesis is divided into seven chapters.

The first chapter presents basic ideas and physics of thermonuclear fusion and main technological concepts used to achieve a burning plasma. An introduction to magnetized plasma is given to explain how the charged particles can be trapped and separated from the surrounding environment. Particular attention is paid to explain the principles of tokamak devices and to present the Tore Supra tokamak on which this thesis was performed.

The second chapter attempts to provide a short review of the central ideas about edge plasma physics. A description of plasma configurations limited either by a limiter or a divertor is given. Moreover, derivations of fundamental scrape-off layer properties, such as Debye length or Bohm criterion, are highlighted. Finally, a brief summary of sheath physics is presented and the derivation of the potential drop across the sheath is provided.

The third part of the thesis is dedicated to Langmuir probes. At first, basic principles of the Langumir probe measurement technique are explained followed by the description of the operational principles and technical aspects of using probes on Tore Supra. In addition, a Mach probe theory described with a 1D fluid model is presented to derive an important tool for probe data interpretation, namely, how to evaluate the measured plasma density or parallel flow in the scrape-off layer. A detailed description of the operational principles of two probes used on Tore Supra, the tunnel probe (TP) and the retarding field analyzer, is provided with the emphasis on different modes of their operation. Considerable attention is given also to the real time feedback system whose proper functionality is necessary for the measurement of RF-induced SOL modifications.

The fourth chapter brings an overview of the main plasma heating methods in the ion cyclotron range of frequencies. A detailed look will be given to the physics of the formation of rf sheaths. A simple model is presented to demonstrate the sheath rectification effect. Afterwords, we will talk about the ICRH system used on Tore Supra tokamak. A description of two Faraday screen designs used on Tore Supra will be given to stress main operational consequences and the importance of manufacturing an improved screen. An example of the interactions between the screen and reciprocating Langmuir probe by means of infra-red images analysis is shown.

In the fifth chapter, we will focus on experimental observations that were made in order to characterize the RF-induced SOL modifications with emphasis on their spatial structures and the effects of the various plasma and antenna configurations on them. The results presented here were carried out during the 2009 and 2011 TS experimental campaigns during which Langmuir probe measurements were performed in $\sim$100 ICRH discharges. Several sessions dedicated to different aspects of antenna-SOL interactions were made such as: 2D radial-poloidal mapping, density and power scan or scan of strap power imbalance.

In addition to experimental measurements, the last two chapters are devoted to theoretical predictions based on code simulations. The modelling presented in the sixth chapter uses a 1D fluid code based on the exchange of rf and dc currents between neighbouring flux tubes working under the assumption of the flute hypothesis. The simulated dimension is the cross-field direction. We will deal with questions like whether or not are our probe measurements perturbing.

The final chapter of the thesis concerns the comparison of sheath potential measurements made by the RFA with theoretical modelling using a one-dimensional particle-in-cell code. In this case it is the parallel direction that is simulated. A discussion of whether or not the RFA can be used for reliable sheath potential measurements in rf perturbed zones is given. We will show that for real edge plasma conditions, the standard technique of sheath potential measurements is not applicable and an alternative method is proposed to investigate rf sheath rectification effects.

The necessary magnetic field line tracing technique that is used to map the measurements from a reciprocating probe at the top of the torus to an active ICRH antenna situated at the outboard mid-plane is presented in the appendix.

Chapter 1

Thermonuclear Fusion

1.1 Energy context

Almost all aspects of our daily life are associated with the transformation of one kind of energy to another. Every time we drive a car or use an electronic device, potential energy stored in chemical or nuclear bonds is dissipated irrevocably into the environment. As described by the second law of thermodynamics, this transformation of concentrated potential energy into diffuse heat is irreversible. Hence, in order to power our complex society, we must continuously seek and exploit new resources of stored energy. There are currently around 7 billion people living on the Earth (and still increasing) and every single one of them wants to improve his/her own well-being. As human society evolves the demand for energy increases accordingly. Before discussing global energy consumption, it is necessary to understand the scale of the problem. Over time, several different units have been established to express energy demand. The most recent one has been introduced by Hewitt Crane [Crane 10] and it is called a 'cubic mile of oil' (CMO). This unit expresses the world's annual consumption of oil. Because we Europeans are more familiar with SI units, we choose here to express energy units in terms of "cubic kilometre of oil" (1 CKO = 0.24 CMO). At today's prices, i.e. the beginning of 2013, one barrel of crude oil costs about \$94 (≈ €72.3). That makes about €0.6 trillion for one cubic km of oil. According to Forbes magazine, the annual world energy consumption was about 12CKO in 2010 [Carlson 10] and, if we wish to maintain a reasonable rate of average economic growth (of the order of 2% is considered healthy), it needs to rise up to 37CKO in 50 years.

A nice study concerning the world primary energy consumption has been recently made by the British Petrol [BP 12]. Based on their studies, we can expect the growth of the world primary energy consumption every year by 1.6% for next twenty years (Figure 1.1). As can be seen, this growth is driven mainly by non-OECD countries. Hence, in order to satisfy the world's energy requirements, it is necessary to expand the exploitation of all known energy sources. Over the last few years, increased attention has been paid

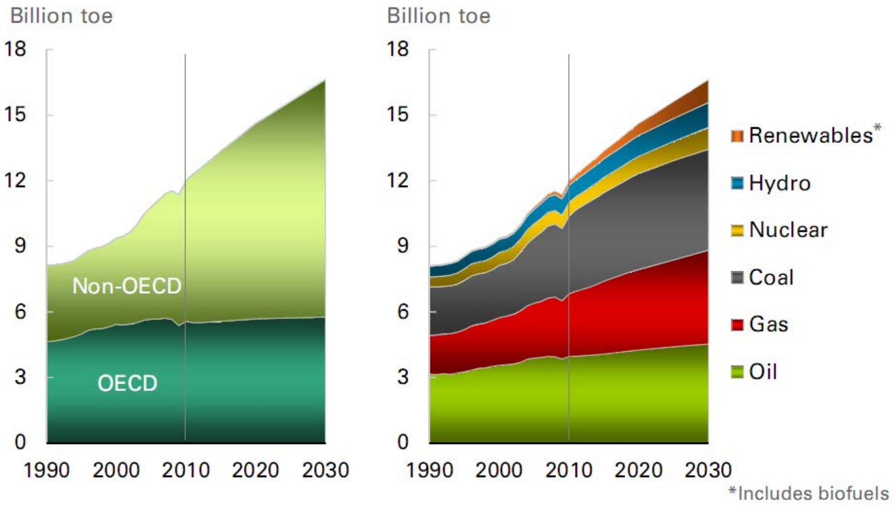

Figure 1.1: *Evolution of energy consumption for OECD and non-OECD countries (left) and as a function of the source (right). toe - tonne of oil equivalent: the amount of energy released by burning one tonne of crude oil - image courtesy British Petrol.*

especially to renewable sources of energy. Their main advantage is reduced pollution and hence reduced strain on our ecosystem. On the other hand, the density of total production capacity from renewable sources is low compared to coal or nuclear industry. For instance, if one would like to replace all existing coal power plants by non-carbon sources, it would be necessary to build each year for the next 50 years either 32 new 1GW nuclear plants, 10 000 new 3.2MW windmills, or to equip 6.4 million homes with 5kW solar panels.

As these numbers suggest, the energy demand cannot be provided solely by renewable energy sources. Building more nuclear power plants could be a solution, but there is still the question of the nuclear waste treatment. Moreover, after the recent accident in Fukushima due to a tsunami on March 11, 2011, public confidence in nuclear safety has decreased. However, nuclear processes are very efficient. From that point of view, the development of power production technology based on deuterium-tritium nuclear fusion reactions appears to be a promising solution for future energy demand requirements. Fusion offers important advantages: no carbon emissions, no air pollution, essentially unlimited fuel (on the time scale of human civilization), and is intrinsically safe. Despite the fact that a technological system providing substantial energy gain remains to be demonstrated, its enormous potential continues to motivate governments to fund nuclear fusion research. Fusion reactions are about four million times more energetic than chemical reactions such as the burning of coal, oil or gas. Moreover, fusion fuel is abundant because deuterium occurs naturally in oceans. The question of tritium is more challenging and it will be discussed more in the next section. There are very limited environmental risks in case of an accident and the mean lifetime of radioactive waste is limited to $\sim$300 years due to a radio-activation of the reactor walls by neutron bombardment. Due to a short decay time of the radioactive tritium (≈ 12.3 years), it is mainly the radioactive waste that determines the lifetime of fusion reactor structures. Contrary to a fission reactor, radioactive waste in a fusion reactor can be limited by a judicious choice of materials.

One of the main hurdles to the development of nuclear fusion reactors is their technological complexity. For example, to achieve a reliable control of the ITER machine, an extensive diagnostic system will be installed to evaluate and to optimize plasma performance. Moreover, many of these diagnostics (especially those dedicated to measurements of magnetic field or impurity production) has to be synchronized and controlled with real-time feedback systems. In addition, we still do not fully understand the behavior of the plasma during a fusion device operation (e.g. plasma wall interaction, helium ash removal, materials under neutron flux or turbulent transport). For instance, in the case of ITER, we will have to deal with conditions with which we have no experience, e.g. the level of neutral particle flux or the neutron flux will be respectively about 5, 10 times higher than we experience at current machines [ITER 12]. In the frame of this work, the proper operation of ICRH antennas without any side effects (e.g. generation of large potentials accelerating charged particles towards the walls and hence causing enhanced impurity production) has not yet been fully accomplished either. The main principles of the fusion concept are explained in the following parts.

1.2 Fusion principles

Fusion reactions power the stars and produce all of the light elements up to iron. Whereas the fusion of light elements in the stars releases energy, production of the heaviest elements absorbs energy, so that it can only take place in the extremely high-energy conditions of supernova explosions (Figure 1.2). But stars differ from prospective fusion reactors in three main aspects: confinement, efficiency of fusion reactions and radiative equilibrium. In stars, the fusion fuel is compressed to ignition by gravitational pressure. For stars like the sun, the dominant fusion process is the proton-proton fusion reaction. But this kind of reaction is not feasible in earth conditions due to the low cross-section $\sigma \approx 10^{-53} m^2$ [Atzeni 04]. Therefore, a more efficient reaction has to be considered, like the D-T reaction with maximal cross-section $\sigma = 5 \cdot 10^{-28} m^2$. Concerning the radiation, bremsstrahlung in a fusion reactor represents immediate plasma heat loss due to its long re-absorption mean free path which is well above the dimension of a fusion reactor. In stars, on the other hand, this re-absorption length is small compared with the star's size, so that radiation from the center diffuses slowly towards the photosphere [Boeur 08].

Any energy production from nuclear reactions is based on differences in the nuclear binding energy which is associated to a mass difference between the initial state and the final state. Figure 1.2 shows the nuclear binding energy per nucleon. It has been derived from measurements of the masses of the nuclei, that the masses of nuclei are always smaller than the sum of the free proton and neutron masses which constitute the nucleus. This mass difference corresponds to the nuclear binding energy according to Einstein's energy-mass relation $E = \Delta mc^2$. From Figure 1.2 it is clear that there are two ways of gaining nuclear energy:

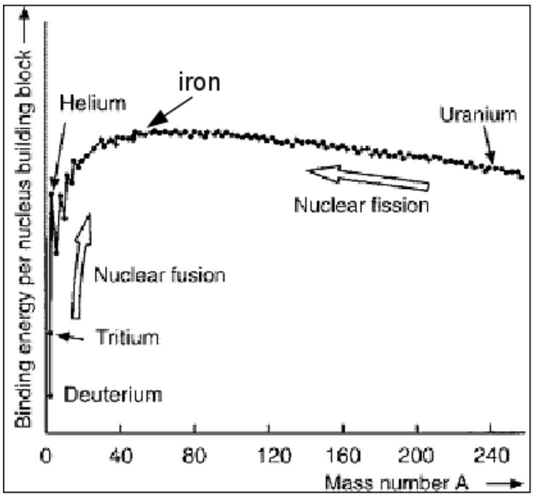

Figure 1.2: *Nuclear binding energy per nucleon as a function of the nucleon number A. Image courtesy - European Nuclear Society.*

1. By transforming heavy nuclei into medium-size nuclei: this is done by fission, e.g. of uranium.
2. By fusion of light nuclei into heavier ones: in particular the fusion of hydrogen isotopes into stable helium offers the highest energy release per mass unit. Doing this in a controlled manner has been the goal of fusion research for about 50 years.

The energy released per nucleon is of the order of 1 MeV for fission reactions and in the order of a few MeV for fusion reactions. This is 6-7 orders of magnitude above typical energy releases in chemical reactions (of the order of eV), which explains the effectiveness and potential hazard of nuclear power. Possible candidates for using fusion energy on earth are the following reactions:

$$\begin{array}{ccccccccc} D & + & D & \longrightarrow & {}^3He & + & n & + & 3.27 MeV \quad (50\%) \\ D & + & D & \longrightarrow & T & + & p & + & 4.03 MeV \quad (50\%) \\ D & + & {}^3He & \longrightarrow & {}^4He & + & p & + & 18.35 MeV \\ D & + & T & \longrightarrow & {}^4He & + & n & + & 17.59 MeV \end{array}$$

All the reaction cross sections plotted on Figure 1.3 show a steep increase with the relative energy, but the D-T reaction has by far the largest cross-section at the lowest energies.

This makes the D-T fusion process the most promising candidate for an energy-producing system. To be a candidate for an energy producing system, the fusion fuel (deuterium and tritium) has to be also sufficiently abundant and easily extractable in order to make energy production economically profitable. That is to say, the total cost of the fuel extraction, fabrication and utilization in the fusion reactor have to be much lower than profits from selling of produced electricity. Let us first discuss about the abundance of deuterium. Deuterium occurs naturally in oceans. The ratio between the deuterium and hydrogen occurrence is about 1/6420. For example, one litre of ocean water contains the same amount of energy as three hundred litres of gasoline. Given the total amount of water in the oceans, the weight of deuterium is estimated at $\sim 4.6^{13}$ tons! Deuterium can be recovered from water for example via electrolysis or via the distillation of liquid hydrogen. The energy released by one ton of deuterium is about $250 \cdot 10^{15}$J. The deuterium contained in the seawater therefore yields $3.6 \cdot 10^{11}$TW of power consumed over one year. But we mentioned earlier that nowadays energy consumption is 12CKO. Using unit conversion, $1\text{CKO} = 0.39 \cdot 10^{20}$J, the annual world power consumption is 15TW. That means, assuming the total available power of $3.6 \cdot 10^{11}$TW, the energy content in the seawater would be enough for 24 billion years. For example, in the scope of fusion reactor, it is planned that there will be less than 1g of fuel at any instant in the vacuum chamber. It is foreseen that future fusion power plants will need approximately 250kg of fuel per year (50% of deuterium and 50% of tritium) per fusion reactor. Deuterium is commonly used for industrial, scientific and military purposes as heavy water. On the other hand, the tritium part of the fuel is more problematic, because there is no sizeable natural source. Tritium is an unstable radioactive isotope with a half-life of 12.3 years. Global inventory for tritium is presently around 20kg. Therefore, tritium is very expensive - €23 000/g. Fortunately, a second source of tritium exists: tritium can be produced with nuclear reactions of the neutrons from the D-T reaction and lithium:

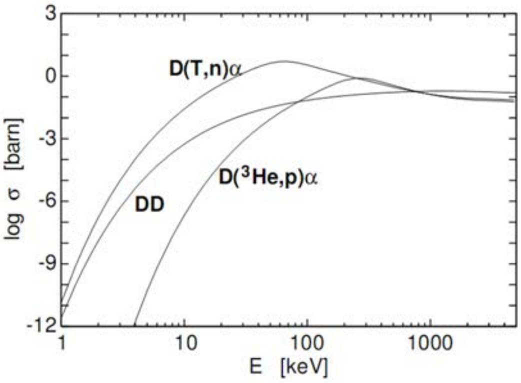

Figure 1.3: *Measured cross-sections for different fusion reactions as a function of the center of mass energy.*

$$\begin{array}{ccccc} n & + & ^6Li & \longrightarrow & ^4He+T & +4.8MeV \\ n & + & ^7Li & \longrightarrow & ^4He+T+n & -2.5MeV \end{array}$$

The ultimate fusion fuel will thus be deuterium and lithium. The latter is also very abundant and widespread in the earth's crust and even ocean water contains an average concentration of about 0.15 ppm of lithium. If we consider a situation that the fusion was to be the only source of electricity for the whole world, than it is estimated that known reserves of lithium would be sufficient for at least one thousand years. In contrast to charged particle reactions, these neutron reactions do not require high temperatures because the activation of ^{6}Li is possible with neutrons of any energy. However, the neutron problem is not totally eliminated through the above solution because not all neutrons will fuse with the lithium. Instead, they will fuse with other parts of the reactor which will lead to induced radioactivity. In a deuterium-tritium fusion reactor, the tritium will therefore be bred in a lithium-containing blanket surrounding the thermonuclear vessel. However, all today's tokamaks are principally operated for research and development purposes. Their main goal is to study magnetohydrodynamic properties of confined plasma, plasma-wall interactions, operational scenarios etc. Moreover, using tritium requires to obey strict radio-protection rules (like respecting annual dozes received by reactor staff) which would make experimentation difficult. Only JET and TFTR tokamaks attempted a D-T mixture [Hawryluk 02]. D-T reactions and lithium blankets will be used in ITER whose operation is planned for 2020 [ITER 12]. The typical discharge length planned for ITER will be about 400s. Assuming total fusion power of P_{fus} = 500-700MW, we can estimate the tritium consumption rate $\dot{m}$.

$$P_{fus} = \frac{E_{fus}}{t}N = \frac{E_{fus}mN_A}{tM} \quad \Rightarrow \quad \dot{m} = \frac{PM}{E_{fus}N_A} \approx 1mg/s \tag{1.1}$$

where E_{fus} is the energy released by D-T reaction in joules, N is the number of tritium atoms, M is the molar mass of tritium and N_A is the Avogadro number. The tritium consumption rate is then approximately 1mg/s yielding in total consumption of 0.4g of tritium per ITER discharge. But for the first prototype fusion power plant (DEMO), about 300g of tritium will be required per day, corresponding to fusion power of 1.95GW, to produce 800 MW of electrical power. Therefore, the issue of the feasibility of tritium breeding concept will play a crucial role. An overview of tritium fuel cycle in ITER and DEMO can be found in [Tanabe 12].

1.3 Ignition

To initiate nuclear fusion it is necessary to force together positively charged nuclei of specific light atoms by providing them such a kinetic energy to reach a point at which the strong repulsive electrostatic forces are overcome by the attractive nuclear force. Because of quantum mechanical tunnelling, the D-T reaction occurs at energies somewhat less than that required to overcome the Coulomb barrier. As a D-T plasma is heated by external power sources to thermonuclear conditions, the α-particle heating provides an increasing fraction of the total heating power. When adequate confinement conditions are provided, a point is reached where the plasma temperature might be maintained against the energy losses solely by α-particle heating. This point is called ignition. The applied external heating then can be switched off and the plasma temperature T is sustained by internal heating only. An important power loss affecting power balance in a fusion reactor is that due to radiation. There are in fact several types of radiation losses that can occur: line radiation due to impurities, cyclotron radiation due to particle motion in a magnetic field, and bremsstrahlung radiation due to Coulomb collisions. Among these, bremsstrahlung radiation usually produces the largest losses. Putting in equality the α-particle heating per unit volume $P_\alpha = \frac{1}{4}n^2 \langle \sigma v \rangle E_\alpha$ and the power losses $P_L = \frac{3nT}{\tau_E}$, the requirement for the plasma to burn in a self-sustaining way, can be written as

$$n\tau_E > \frac{12}{\langle \sigma v \rangle} \frac{T}{E_\alpha} \tag{1.2}$$

where n is plasma density, τ_E is energy confinement time, which is a ratio of total energy of plasma and total power loss, respectively, $\langle \sigma v \rangle$ is reaction rate and E_α is energy of α-particle. Equation 1.2 defines an ignition condition for thermonuclear devices. The right-hand side (RHS) of inequality Equation (1.2) is a function of temperature only and it has a minimum close to $T = 30keV$ and the requirement for ignition at this temperature has to satisfy

$$n\tau_E > 1.5 \cdot 10^{20} m^{-3} s \tag{1.3}$$

It should be pointed out that this value is almost twice as high as the original Lawson criterion [Lawson 57] in which he neglected the α-particle heating and took instead the efficiency of the external power source (30%). Therefore, the original Lawson criterion provided a lower threshold for ignition ($> 0.6 \cdot 10^{20} m^{-3} s$). However, since τ_E is itself a function of temperature, the optimal value for reactor operation does not correspond to the temperature of the minimum of Eq. 1.2 and it is somewhat lower. An estimation can be made if a steady state situation is considered where the alpha power heating is sufficiently large to balance the combined Bremsstrahlung and thermal conduction losses, without the need for any external power:

$$P_\alpha = P_B + P_C \tag{1.4}$$

Equation (1.4) provides limits for the pressure, temperature and energy confinement time. Adopting power sources from [Freidberg 07], the ignition power balance condition can be

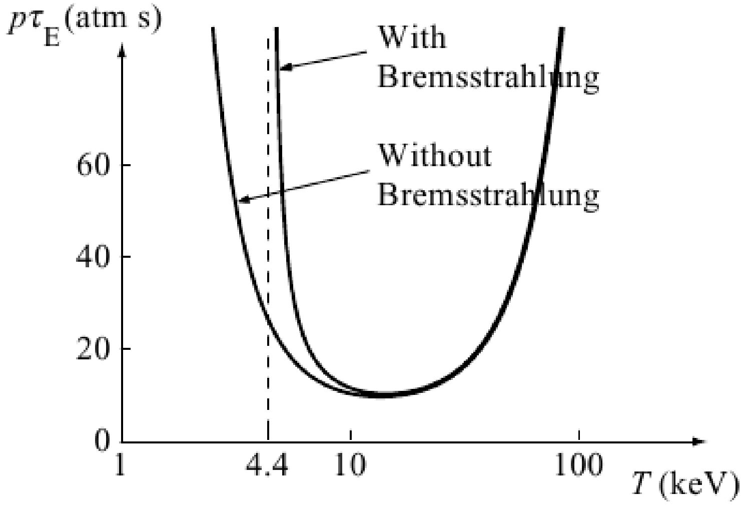

Figure 1.4: *Critical $p\tau_E$ for ignition as a function of temperature.*

visualized as on Figure 1.4. Figure 1.4 shows that for temperature about 15keV, plasma with an energy confinement time of 1 s, a pressure of about 8 atm is required for the plasma to be ignited. When neglecting the thermal conduction losses, the minimal temperature necessary for igniton yields T= 4.4keV.

The condition for ignition can be also expressed by the so-called triple product which gives for the D-T reaction:

$$nT\tau_E > 3 \cdot 10^{21} m^{-3} keVs \tag{1.5}$$

This formula gives a very useful relation for ignition that consists only of requirements on density, temperature and confinement time. The constant itself can vary in dependence on the profiles of n and T. The condition (1.5) is valid for flat profiles. For the purposes of the merit of the success of reaching burning conditions, one can use the power amplification factor Q. This factor is defined by the ratio of the produced thermonuclear power P_f to the provided heating power P_H, hence:

$$Q = \frac{P_f}{P_H} \tag{1.6}$$

Originally, ITER has been designed to reach ignition with no necessity of external sources, only with internal heating of produced α-particle from D-T reactions. The power amplification factor has been foreseen to be infinity. After re-evaluation of the ITER project, the new design is proposed to reach $Q = 10$ with external heating sources of 50-70MW. Concerning the future fusion power plants, this ratio is estimated to be about 80 rather than infinity, in order to have better control of reactor performance.

There are two ways how to reach ignition:

1. To maximize confinement time: the hot plasma is confined by strong magnetic fields leading to maximum densities of about $1.5 \cdot 10^{20} m^{-3}$, which is $2 \cdot 10^5$ times smaller

than the atom density of a gas under normal conditions. With these densities, the required energy confinement time is in the range of 2 to 4 seconds. This approach is the main line in fusion research today and it is called *'magnetic confinement fusion'*

2. The other extreme is to maximize the density. This can be done by strong, symmetric heating of a small D-T pellet. The heating can be done with lasers or particle beams and leads to ablation of some material causing implosion due to momentum conservation. It is clear that the energy confinement time is extremely short in this concept: it is the time required for the particles to leave the hot implosion center. The density required is about 1000 times the density of liquid D-T. Since it is the mass inertia which causes the finiteness of this time, this approach to fusion is often called *'inertial fusion'*.

This work is exclusively a topic belonging to magnetic confinement fusion, whose main principles are explained in the next sections.

1.4 Charged particle motion in a magnetic field

The idea of building a functional thermonuclear power plant that would supply mankind by electricity is more than 50 years old. Unfortunately, due to the technical difficulties (right choice of materials that have to withstand extreme temperatures together with their fabrication accuracy and degradation issue by irradiation etc.) and the complexity of the plasma behavior (MHD instabilities, turbulent transport, non-linearities in the scaling), this goal still has not yet been achieved [Braams 02]. The basic principle of achieving fusion reactions is to confine a plasma in a strong magnetic fields. The Lorentz force

$$\mathbf{F} = Q(\mathbf{E} + \mathbf{v} \times \mathbf{B}) \tag{1.7}$$

makes particle of charge Q and velocity v, to move in helical orbits (Larmor orbits) around magnetic field lines (Figure 1.5). The distance between the actual particle orbit and the magnetic field line is the Larmor radius r_L,

$$r_L = \frac{mv_\perp}{QB} \tag{1.8}$$

where m is the particle mass, and $v_\perp$ is its velocity in direction perpendicular to $\mathbf{B}$. Concerning typical ITER conditions with the average perpendicular velocity being roughly a thermal velocity $v_\perp \approx \sqrt{\frac{2kT}{m}}$, together with temperature necessary for burning plasma $T \approx 10keV$ in the magnetic field of 5.4T, the averaged Larmor radius for deuterium ions is in the order of few millimetres - $r_L \approx 2 \cdot 10^{-3}m$ and few tens of micrometers for electrons. Therefore, by varying the strength of magnetic field, we can obtain different level of freedom of perpendicular motion of particles gyrating around the field line in

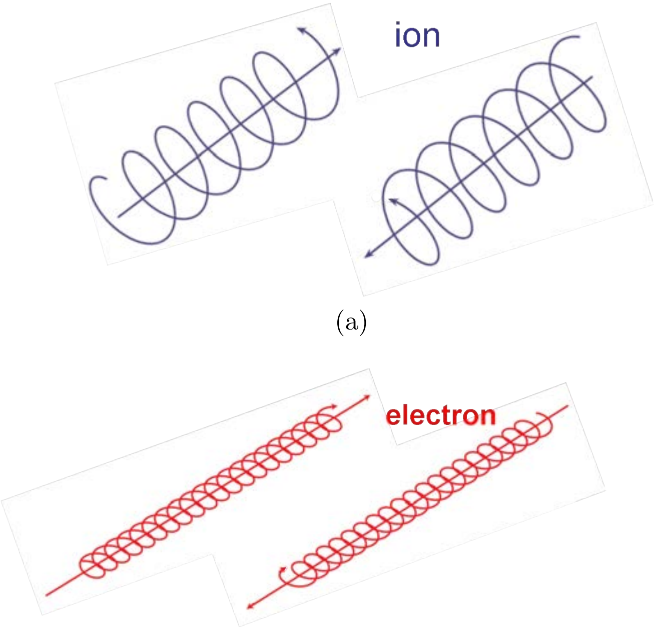

(a)

(b)

Figure 1.5: *Orientation of the gyration motion of ions and electrons in a magnetic field.*

homogeneous magnetic field, but cannot affect their movement along them. This effect of controlled charged particle motion serves as the basis for all magnetic confinement schemes. The idea is to create such geometric configuration whose extent is outlined by magnetic field that will confine hot plasma, and will keep it away from the walls of the chambers. Unfortunately, the particle confinement in a toroidal device is never perfect. In reality, particle collisions, guiding center drifts, turbulence or in the case of convective cells created in front of ICRH antenna by RF sheath rectification effects, lead to a cross-field transport of particles and energy. This is not the case of neutrons created during the fusion process. Neutron is a particle of free charge and therefore can escape the confined plasma with minimal loss of energy.

1.4.1 Cross-field drifts

The products of D-T fusion reactions are helium nuclei (α-particles) and neutrons. The first, also bound to the magnetic field lines, are supposed to transfer their energy to the thermal plasma by Coulomb collisions and thus sustain the fusion reaction. The latter, because they are not confined by the magnetic field, can leave the plasma directly and will be used to breed tritium from lithium and convert the fusion energy into heat. Knowledge of the cross-field drifts is important mainly from the plasma confinement point of view because some of them are responsible for plasma losses. In the scope of this thesis, the most important is the $\mathbf{E} \times \mathbf{B}$ drift that arises due to strong variations of the electromagnetic field around the antenna structure leading to a formation of strong currents. In many cases, we do not need to know detailed movement of a given particle in the magnetic field, but rather of its gyration center also called guiding-center. Let us consider a particle with mass m and charge Q gyrating in magnetic field around gyro-center described by vector $\mathbf{R}$. The equation of motion of the gyro-center can be written as [Kulhánek 08]:

$$m\ddot{\mathbf{R}} = \mathbf{F_{ext}} + Q\dot{\mathbf{R}} \times \mathbf{B} - \mu \nabla B; \quad , \quad \mu = \frac{mv_\perp^2}{2B} \tag{1.9}$$

where μ is the magnetic moment or the first adiabatic invariant. However, there are some important situations in which the magnetic moment is not invariant. One of them is cyclotron heating. If the wave electric field $\mathbf{E}$ oscillates close to the cyclotron frequency, the condition for adiabatic invariance is violated and heating is possible. In particular, the induced electric field rotates in phase with some of the particles and continuously increases their velocity in perpendicular direction. The external force $\mathbf{F_{ext}}$ on the right hand side of Equation (1.9) represents in general external forces acting on the particle movement such as gravitational or electric force. The last term on the RHS of Equation (1.9) is an effective force acting on the gyro-center. This force pushes particles from regions of high magnetic field to regions of lower magnetic field. It depends only on magnetic field strength, not the direction. The nature of this force gives the idea of building magnetic mirrors to trap particles. This mechanism is demonstrated on Figure 1.6. Let us consider a charged particle moving in a static, but spatially nonuniform magnetic field. The non-uniformity is such that the field strength varies in the direction of the field. If a particle moves in a slowly varying magnetic field, the angle of its gyro-motion will change accordingly with respect to the magnetic field lines. Let the α be an angle between the particles' velocity vector and the magnetic field vector (Figure 1.6). From the conservation of energy and adiabatic invariant it yields the mirror equation

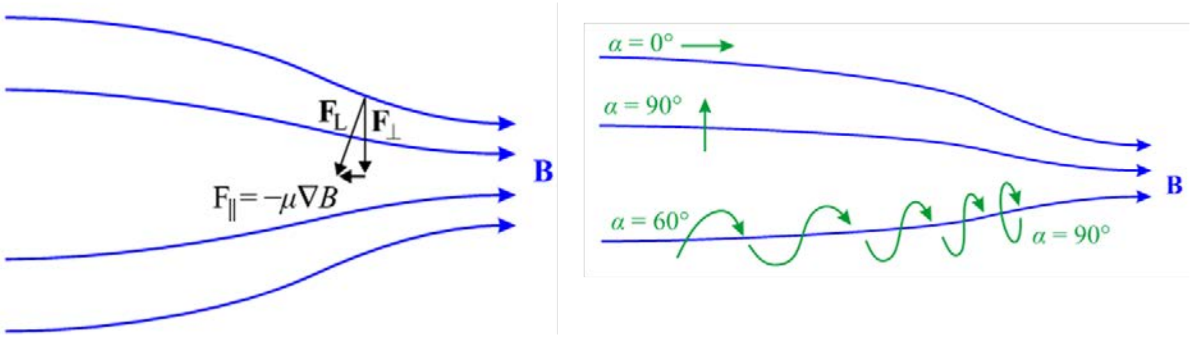

Figure 1.6: *Schematic of magnetic mirror principle.*

$$\frac{sin^2\alpha}{B} = const. \tag{1.10}$$

That is to say, if particle gyration is perpendicular to magnetic field ($\alpha = 90°$), particle will be reflected back. From Equation (1.10) also yields that any particle initially at the angle α at the field B will be reflected if the field increases to the critical value

$$B_c = \frac{B}{sin^2\alpha} \tag{1.11}$$

If the magnetic field is weaker than B_c, particles can escape. Unfortunately, the particle confinement at the ends characterised by a strong magnetic field is not perfect because there is always a finite fraction of particles that has a ratio of parallel to perpendicular velocity sufficient to overcome the mirror force. Therefore, in order to avoid losses from the ends, it is necessary to close both ends together by forming a closed configuration.

To obtain the drift equation, which describes the gyro-center motion perpendicular to magnetic field, one multiplies Equation (1.9) by $\times\mathbf{B}$:

$$\dot{\mathbf{R}} - \left(\dot{\mathbf{R}} \cdot \frac{\mathbf{B}}{B}\right)\frac{\mathbf{B}}{B} = \dot{\mathbf{R}}_{\perp} = \frac{\mathbf{F_{ext}} \times \mathbf{B} - \mu\nabla B \times \mathbf{B} - m\ddot{\mathbf{R}} \times \mathbf{B}}{QB^2} \tag{1.12}$$

Three main types of drift can occur corresponding to three terms on the RHS of Equation (1.12). First one is caused by the presence of another field (electric or gravitational). Second can be caused by the inhomogeneity of magnetic field leading to grad B drift. Last one might occur due to unequal motion of gyro-center generated by the curvature of magnetic field lines. In plasma, more than one drift usually acts at a time, because some of them lead to charge separation giving to rise an electric field and hence creating a drift in electric field.

- $\mathbf{E} \times \mathbf{B}$ drift: drift of charged particle in electromagnetic field. For $\mathbf{F} = \mathrm{Q}\mathbf{E}$

  $$\mathbf{v}_E = \frac{\mathbf{E} \times \mathbf{B}}{B^2} \tag{1.13}$$

  Drift velocity is independent of charge and mass, therefore electrons and ions drift in electric field in the same direction which is perpendicular both to electric and magnetic field.

- Gravitational drift: In combined gravitational field $\mathbf{F} = \mathrm{m}\mathbf{g}$ and magnetic field, there occurs drift with velocity

  $$\mathbf{v}_g = \frac{m\mathbf{g} \times \mathbf{B}}{QB^2} \tag{1.14}$$

  perpendicular both to gravitational and magnetic field. Its direction depends on charge of given particle and hence leads to generation of current due to charge separation.

- Grad B drift: is caused by magnetic field variation.

  $$\mathbf{v}_{\nabla B} = \frac{mv_\perp^2}{2Q}\frac{\mathbf{B}\times\nabla B}{B^3} \tag{1.15}$$

  This drift depends on particle charge and mass, and hence will lead to generation of electric current. Due to charge separation, an electric field is formed and as a consequence, $\mathbf{E}\times\mathbf{B}$ drift will appear as well.

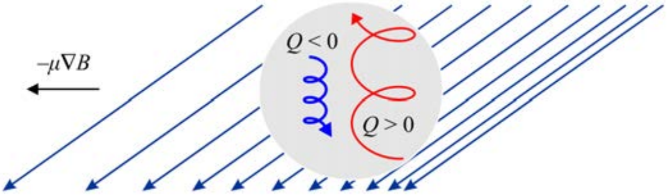

- Curvature drift: Particle moving around curved field line will be influenced by centrifugal force

  $$\mathbf{F} = -m\ddot{\mathbf{R}} = \frac{mv_\parallel^2}{R_k}\frac{\mathbf{R_k}}{R_k}$$

  where $\mathbf{R_k}$ is radius of field line curvature.

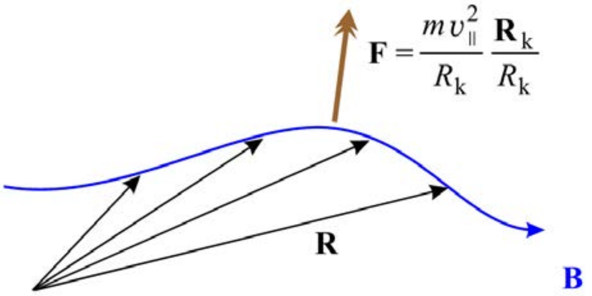

  Final drift yields

  $$\mathbf{v}_R = \frac{mv_\parallel^2}{QB^2}\frac{\mathbf{R_k}\times\mathbf{B}}{R_k} \tag{1.16}$$

As can be seen, motion of charged particles in electromagnetic field is rather complicated due to a presence of various drifts acting on them. Therefore, in order to design a successful fusion reactor, all above mentioned particle motions in the electromagnetic field have to be taken into account to avoid particle and energy losses. Through the last few decades were invented many magnetic configurations for applications to nuclear fusion [Braams 02]. Nowadays, the most viable concepts are the tokamak and the stellarator invented back in 1950's and they will be described in the following section.

1.5 Tokamak

A tokamak is a fusion device characterized mainly by two properties: strong toroidal magnetic field and large plasma current. In order to achieve equilibrium in which the plasma pressure is balanced by the magnetic forces, the toroidal field itself is not enough and has to be accompanied by additional poloidal field. This poloidal field is created mainly by the plasma current. The combination of both toroidal and poloidal magnetic field leads to a helical guiding center trajectories. Schematic view of a tokamak is shown on Figure 1.7. A tokamak is actually a big transformer where the plasma itself serves as a secondary winding, while the primary one is wound on a central core. Nevertheless, providing both toroidal and poloidal magnetic fields still does not ensure the equilibrium. The toroidal geometry of the plasma leads to two hoop forces, which are both in the direction to expand the plasma ring. The first of these forces results from the natural tendency of a current loop to expand in an effort to lower its magnetic energy. The second force is the resultant of the sum of centrifugal and grad-B forces experienced by the individual particles during their motion along the field lines [Weynants 06, Wesson 04]. According to Eq. (1.15), the variation of the magnetic field leads to the charge separation and consequently to the creation of an electric field that gives rise to E × B drift. To avoid this situation, it is necessary to twist the magnetic field lines by additional magnetic field components. Providing a vertical magnetic field that interacts with the toroidal current to give an inward force can compensate both these forces [Wesson 04]. Then, single field lines map out so-called flux surfaces. On these flux surfaces, plasma transport is much

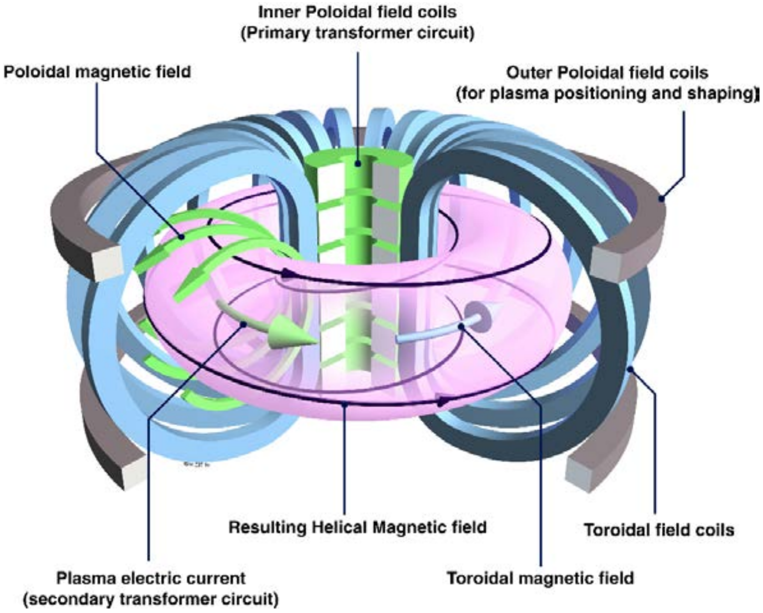

Figure 1.7: *Schematic view of a tokamak.*

faster in direction parallel to $\mathbf{B}$ compared to the perpendicular direction. Therefore, at the equilibrium, plasma parameters are usually constant on a given flux surface. Position on these flux surfaces is commonly described by the toroidal angle ϕ, the minor radius r and the poloidal angle θ (Figure 1.8). To characterize how many times a particle needs to circulate around the torus in order to return to the same position in poloidal projection, one can use the so-called safety factor q that is defined as

$$q(r) = \frac{r}{R}\frac{B_T}{B_p} \tag{1.17}$$

where r is the distance in radial direction from the magnetic axis, R is the major plasma radius, and B_T, B_p are the toroidal and poloidal magnetic fields, respectively.

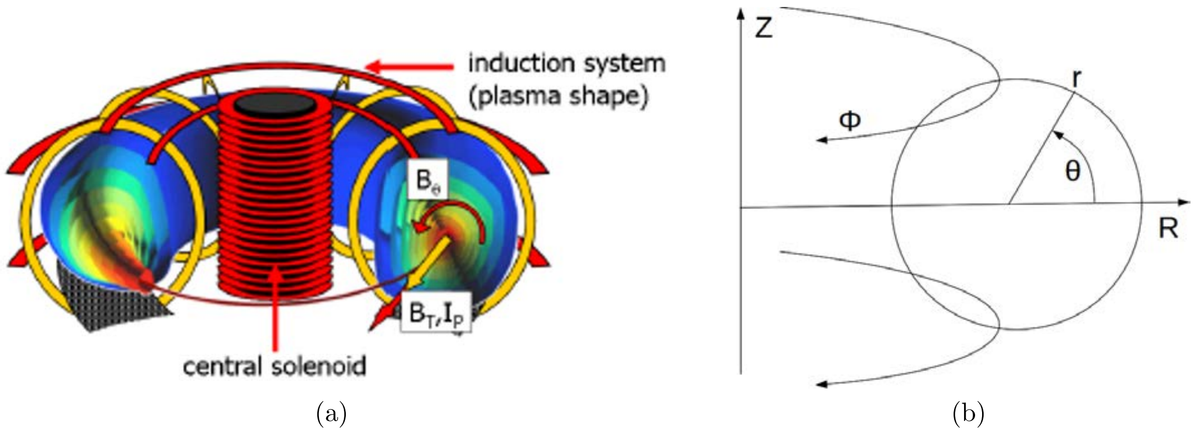

(a) (b)

Figure 1.8: *(a) Illustration of the magnetic configuration of Tore Supra : magnetic field coils (orange) create the toroidal magnetic field component. A central solenoid and a set of vertical magnetic field coils (red) create the poloidal magnetic field component and control the shape of the plasma. The resulting magnetic equilibrium consists of nested magnetic surfaces. (b) Coordinates system used to describe the geometry of flux surfaces in a tokamaks.*

Along with the tokamak concept, there exists another promising configuration that is based on confinement by strong magnetic field. This magnetic configuration is called a stellarator and was proposed by L. Sptizer in the 1950's. The advantage of this concept lies in the idea of not having a strong current flowing inside the plasma which reduces the free energy of such system. The necessary magnetic field is then provided by magnetic coils of complex shape that allow to create also a poloidal component of the field. This may be seen on the Figure 1.9 of the German stellarator project W7X [Wendelstein 7X], where the coils are represented in blue and the plasma in orange color [Hartmann 06]. Such a concept is very promising especially from the steady-state operation point of view. However, the complexity of the magnetic field coils design turns to be main factor causing the delay in the stellarator realization.

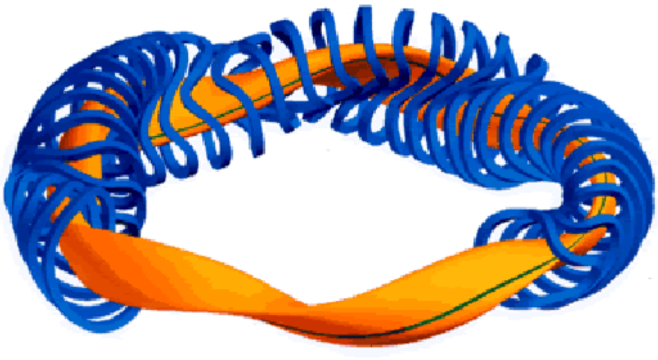

Figure 1.9: *Schematic view of a stellarator. Image courtesy - [Wendelstein 7X]*

1.6 Plasma heating

To reach conditions for burning plasma given by Equation (1.5), it is necessary to heat the plasma to extreme temperatures of the order of hundreds of millions of Kelvins. To achieve this, effective heating methods are required as well as the plasma confinement and control to maintain its density and to minimize heat losses. As mentioned above, in tokamaks, plasma serves as a secondary winding of a transformer driving a large current. Due to a finite plasma resistance R_p, it can be heated up via the Joule effect. Since the unit of electric resistance is the Ohm, this method is referred as *ohmic heating*. The plasma current is mainly an electron current and the plasma resistivity is caused by the collisions of the electrons with the ions. The ohmic heating is quite strong for low temperatures, but, because the plasma resistivity varies with plasma temperature as $T_e^{-3/2}$ [Wesson 04], it becomes less effective for hotter plasmas. On the other hand, the ohmic power is also proportional to the square of the plasma current I_p:

$$P_{OH} = R_p I_p^2 \tag{1.18}$$

Considering the dependence of plasma resistivity on T_e and relation given by Equation (1.18), it is not clear if the ohmic power increases with the plasma current. To find an answer, we need to relate T_e and I_p. But tokamak plasma is subject to turbulent transport that affects the temperature and density profiles. Therefore, one could obtain such a relation from scaling laws that provide an expression for the total energy content of the plasma W as a function of the various plasma parameters. In the ohmic regime, the reference ITER89 scaling law gives:

$$W_{OH} = 64 \cdot 10^3 M^{0.2} (10^{-6} I_p)^{0.8} R_0^{1.6} a^{0.6} \kappa^{0.5} (10^{-20} n)^{0.6} B_T^{0.35} \tag{1.19}$$

where M is isotopic mass, R_0 and a are plasma major and minor radii, respectively, κ is elongation[1] and n is the line-averaged plasma density. Now, if we consider the expression for total plasma energy content defined as

$$W_{OH} = \pi a^2 2\pi R_0 3nk_B T_{av} \tag{1.20}$$

we can compare it with Equation (1.19) resulting in

$$T_{av} = 64M^{0.2}(10^{-6}I_p)^{0.8}R_0^{0.6}a^{-1.4}\kappa^{0.5}(10^{-20}n)^{-0.4}B_T^{0.35} \tag{1.21}$$

Having finally the relation between plasma temperature and plasma current, we can answer our question. It is important to note that the energy confinement time τ_e

$$\tau_e(I_p) = \frac{W_{OH}}{P_{OH}} \propto \frac{I_p^{0.8}}{T_e^{-3/2}I_p^2} = \frac{I_p^{0.8}}{(I_p^{0.8})^{-3/2}I_p^2} = 1 \tag{1.22}$$

is independent of plasma current. However good the ohmic heating the machine disposes by, it is still insufficient to reach ignition. Moreover, the maximal current allowed in the plasma is limited by magnethydrodynamic stability requirements and beyond this limit discharge is ended by disruption. Therefore, additional heating systems have to be used to reach fusion burning conditions. The two principal heating methods are: injection of fast neutral particles and energy transfer via electromagnetic waves. The basic idea of neutral beam injection heating is to inject highly energetic particles into the plasma core where they can transfer their energy to the bulk plasma via collisions [Berkner 75, Hemsworth 09]. The need of electromagnetic waves in tokamak plasmas gives rise to many phenomena, predominantly caused by the RF sheath rectification (section 4.3) which is the main subject of this work. We will focus only on the heating by ion cyclotron waves. For more information about other methods of the plasma heating, the reader is referred to [Koch 00, Hoekzema 00].

1.6.1 Cyclotron Resonance Heating

Heating in the ion cyclotron range of frequencies relies on the circular motion of the charged particles around magnetic field lines. The cyclotron frequency corresponding to a circular motion in a plane perpendicular to the magnetic field line is proportional only to the electric charge Q and the mass m of the particle, and magnetic field strength B: $\omega_{ci} = QB/m$. Therefore, if an electromagnetic wave is launched with a frequency close to particles' frequency in the plasma core, the wave resonates with particle perpendicular motion increasing its Larmor radius linearly in time. This gained particle perpendicular energy is then redistributed to bulk plasma by collisions.

---

[1] Elongation is a plasma parameter that is related to the shape of plasma. It is defined as the ratio of the height of the plasma (measured from the mid-plane) and plasma minor radius.

Heating in ion cyclotron range of frequencies is a widely used technique for plasma heating and is routinely applied at all major tokamak such as JET, ASDEX-Upgrade or Tore Supra tokamak. It is also foreseen to play an important role in ITER with a total ICRH heating power of 20MW at frequencies of 40-55MHz. The typical parameters characterizing ICRF heating system are summarized in Table 1.1.

Frequency	f = 25-130MHz
Power	2MW / antenna strap
Voltage	10-50kV at the antenna
Antenna current	I_A = 1kA
RF electric field	20kV/m

Table 1.1: *Typical parameters for ICRF heating.*

With 12MW installed power at the generators, ion cyclotron resonance heating represents the main source of additional power at Tore Supra and, in the absence of high-power neutral beam injection, the only means to heat the ions. ICRF waves offer a large variety of applications, because of the many heating and current drive schemes, combined with active control of the ion species concentrations, the launched wave spectrum, and the resonance location. A detailed description of the heating in ion cyclotron resonance range of frequencies is given in chapter 4.

1.7 Tore Supra

Tore Supra is a large tokamak with a circular plasma cross-section (major radius $R = 2.4m$ and minor radius $a = 0.7m$) whose last closed flux surface is defined by its intersection with the bottom toroidal limiter or with the outboard antenna protection limiter (APL). The maximal plasma current and toroidal magnetic field are $I_p <$ 1.5MA and $B_T <$ 4T, respectively. Main features of TS are its superconducting toroidal field (TF) coils and its actively cooled first wall. In total, there are 18 superconducting TF coils which are cooled by super-fluid He at temperature of about 1.8K. Tore Supra is the only tokamak fully equipped with actively cooled plasma facing components[2]. The cooling is provided by a high pressure water loop with a temperature of about 200°C, flow speed of 10m·s^{-1}, and pressure of 40 bars. This makes the TS tokamak, together with its additional heating and current drive capabilities (9MW of ICRH and 7MW of LH power), an ideal machine for the study of long plasma discharges [Tore Supra].

---

[2] 98% of all surfaces in direct view of the plasma have water flowing in them, even the internal walls of the tall vertical ports.

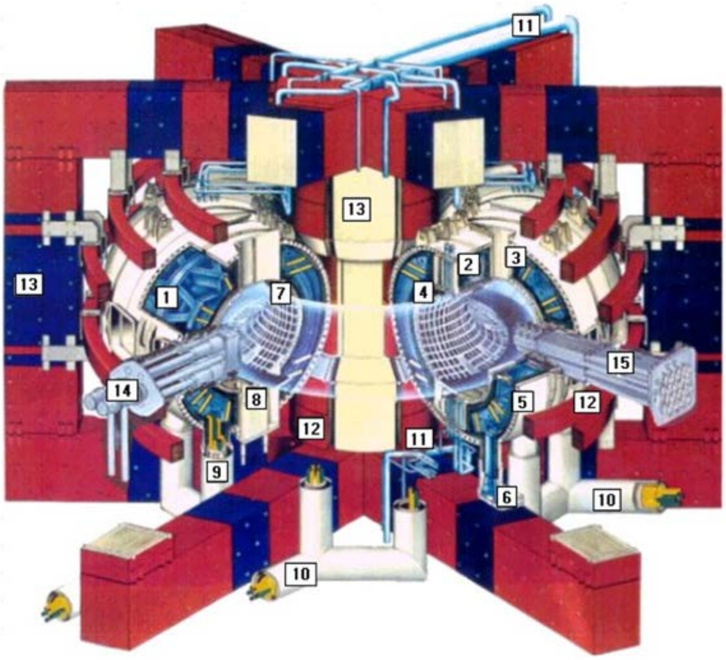

Figure 1.10: *Schematic of the Tore Supra tokamak.*

Plasma major radius	2.42m
Plasma minor radius	0.72m
Pulse length (inductive only)	30s
Toroidal magnetic field	< 4.5T
Plasma current	< 1.7MA
Volt-seconds to drive plasma current	15Vs
Total additional heating power	14MW

Table 1.2: *List of the main Tore Supra parametres.*

The first plasma was attained in Tore Supra in April 1988. Since that time the superconducting coils worked with no major failures. This represents a significant technological success and an important progress for the feasibility of the program of controlled thermonuclear fusion. In 1996 a record was reached with a plasma duration of two minutes with an induced current of almost 1 MA generated non inductively by 2.3MW of lower hybrid frequency waves (i.e. 280MJ of injected and extracted energy). This result was possible due to the actively cooled plasma facing components installed in the machine from the beginning. This result opened the way to the active control of steady state plasma discharges and the associated physics. The search for enhancement of performances has triggered new technological developments for plasma facing components (CIEL project) and non inductive current drive by electromagnetic waves (CIMES project). The new CIEL configuration was implemented in 2001 and the CIMES project is being progressively implemented. Thanks to the new CIEL configuration, a new world record was reached in 2003. A plasma discharge of 6.5 minutes was achieved with over 1000MJ of energy injected. The first step of improvement was the new LH antenna (plus steady state klystrons), which was installed in 2009 and a new Faraday screen [Mendes 09] installed on one of the three ICRF antennas in spring 2011.

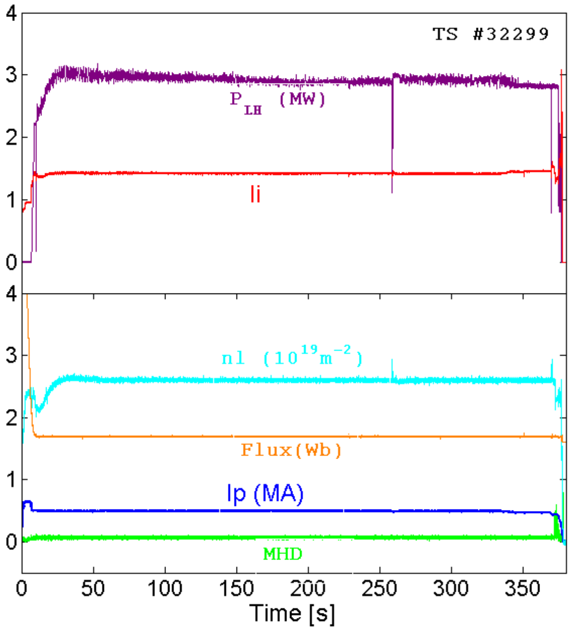

Figure 1.11: *The main plasma parameters profiles of the longest discharge ever reached on Tore Supra.*

The purpose of Tore Supra is to obtain long stationary discharges, thus addressing two major questions: non-inductive current generation and continuous heat and particle removal. The physics program therefore has two principal research orientations complemented by studies on magnethydrodynamic stability, turbulence, and transport. The first physics program concerns the interaction of electromagnetic (lower hybrid and ion cyclotron) waves with the hot central plasma. All or part of the plasma current can be generated in this manner, thus controlling the current density profile. This is an important contribution to the concept of an ‘advanced tokamak’. In 1996 notable progress was made, allowing totally non-inductive shots over a period of 75 s to be obtained. One of the main goals of TS tokamak for the year 2011 was to test new design of the Faraday screen which was installed on one of the ICRH antennas and to improve our understanding of the RF-SOL interactions. In the scope of this task, my duty was to study, mainly experimentally by means of reciprocating Langmuir probes, the phenomena of the interaction between the ICRH antennas with the plasma edge and to compare qualitatively the effects induced by the conventional and the new design of Faraday screen.

The second physics program concerns the edge plasma and its interaction with the first wall. Moreover, in the frame of ITER, a new D-shaped plasma with a full tungsten divertor configuration is being planned as a major Tore Supra upgrade - WEST project (acronym for **W** **E**nvironment in **S**teady-state **T**okamak) [Bucalossi 10]. With this major upgrade, Tore Supra will serve as a test bed for testing ITER plasma facing components. It is important to mention that all results that will be presented in this work were obtained only at Tore Supra tokamak characterized by a circular plasma cross section. An attempt was made to perform measurements also on ASDEX-Upgrade tokamak, but due to large noise in the measured data and hence impossibility to analyse them properly, these measurements are not presented here. Therefore, installation of a divertor on TS tokamak offers a great opportunity to improve our knowledge on the topic presented here.

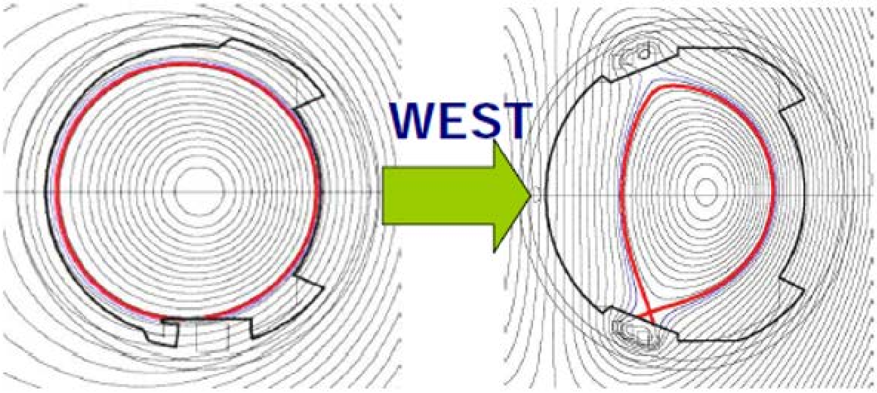

Figure 1.12: *Schematic of the divertor configuration planned for Tore Supra tokamak.*

Chapter 2

Edge Plasma Physics

2.1 Introduction

A major issue in the design and construction of a nuclear fusion reactor with magnetically confined plasma is the interaction of the hot plasma with the material components of such a device. On the one hand, the plasma facing vessel components represent a sink for energy and particles released by the plasma. The particle bombardment of the material surface may lead to the release of wall atoms and of previously trapped fuel atoms which in turn may enter the plasma. The contamination of the plasma by impurities released from the vessel structure is one of the main problems caused by plasma wall interaction processes leading to plasma radiation and hence plasma cooling. An additional problem is the degradation of the material structure by the particle bombardment and the high energy fluxes which in turn might limit the lifetime of the plasma facing components significantly. One of the sources of particle fluxes is a powered ICRH antenna itself [Bécoulet 02]. The large potentials induced due to RF sheath rectification effects cause the particles to accelerate significantly towards the surrounding materials. The wall may further act as a reservoir for the hydrogen fuel isotopes leading to an uncontrollable additional source of fuel atoms, which may cause problems in maintaining stationary discharge conditions. This is a problem of tritium which turned out to have a large affinity to carbon fibre components tokamak wall [Kaye 98]. To avoid that, ITER will have the first wall made of beryllium. Moreover, the retention of tritium in the wall must be limited to comply to radiation and safety constraints (the total tritium content within the vessel is in excess of 7,000 Curies, while dose rates approach 50 mRem/hr). In this chapter will be introduced plasma facing components and a heuristic model of the edge plasma region in contact with the walls, the so-called scrape-off layer, to understand its basic properties [Stangeby 00].

2.2 Plasma-surface interactions

The fact that plasma confinement in tokamaks is not perfect leads to particle fluxes to the walls causing there many unwanted interactions of plasma with surrounding materials. In addition, there are objects inside the tokamak chamber which are in direct contact with the plasma. One of such objects is an ICRH antenna. In order to ensure a good plasma-antenna coupling, one of the necessary conditions is to put antenna very close to the plasma. In the case of the Tore Supra tokamak, antennas are usually placed 1cm behind the main poloidal limiter. The necessity of antennas being placed very close to plasma imposes strong technological constraints on them (see chapter 4). As a result, material impurities are released into the confined plasma. Impurities present a number of problems in tokamaks. Main disadvantage of having heavy impurities in the plasma is the radiative power loss due to their ionization and excitation. Released electrons are then de-accelerated by collisions with bulk plasma, which in turn leads to the bremsstrahlung radiation that cools the plasma (this radiated power increases with Z_{eff}^2). This is especially important for machines operating with tungsten materials which have high atomic number. Second important issue is the fuel dilution due to stripped electrons. Therefore it is necessary to keep the plasma clean by baking the vessel and by cleaning it with glow discharges. There are several ways how the wall material can be introduced into the plasma such as recycling, sputtering, arcing or evaporating [Grisolia 00] (see Figure 2.1).

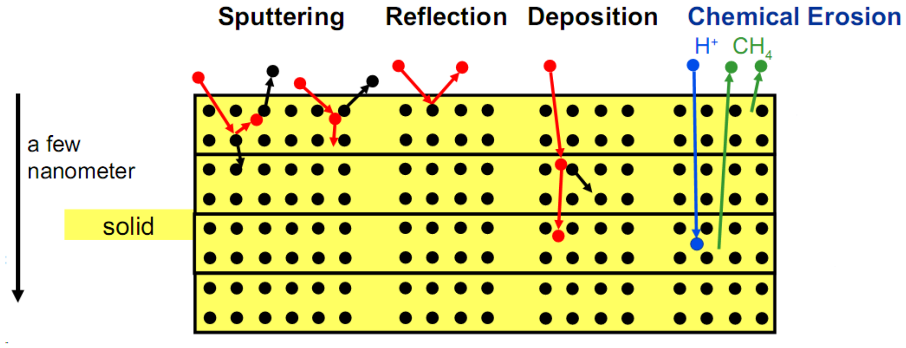

Figure 2.1: *Schematic of the main plasma-surface interactions.*

The particle transport to the vessel walls is primarily due to diffusion from the plasma core, but one of the sources is also represented by a powered ICRH antenna associated with the generation of rectified sheath potential [Colas 07b, D'Ippolito 91]. The charged particles then strike the solid surface where they are neutralized by ion-electron recombination. Such a newly created neutral particle, which is free of the action of magnetic forces, can re-enter the plasma again until it is ionized by electron collisions. This process is known as 'recycling'. Because the pulse length in most tokamaks is at least an order of magnitude larger than the particle replacement time, ions can hit material surface and re-enter plasma several times during the whole discharge. In limiter tokamaks the recycled particles enter the plasma as neutrals and get ionized after traversing a fraction of the plasma radius, while in the divertor tokamaks the ionization might take place near the targets.

Another process that arises frequently due to plasma wall interactions is called 'sputtering'. Sputtering is a process during which atoms of solid surface are removed by the impact of incident ions or atoms. This is the main problem of using ICRH because it generates large dc potentials due to the sheath rectification effect (see section 4.3). As a consequence, the kinetic energy of ions accelerated across these large potentials is increased above the sputtering threshold yielding in higher sputtering rate. Besides the impurity production, sputtering also leads to material degradation and surface erosion. We distinguish two types of sputtering: physical and chemical. Let us first describe chemical sputtering. Concerning chemical sputtering, the incident atom can interact with material atoms and create a molecule that can be easily detached from the surface. The most common reaction in nowadays tokamaks is the reaction between the hydrogen isotopes and carbon. In the other case, the hydrogen isotope exhibits high chemical affinity to the wall materials and is trapped there. This 'retention' phenomenon will be reduced in future reactors by the usage of Be and W materials which have less affinity for hydrogenic atoms. In the case of physical sputtering, the following situation can arise. If the kinetic energy of the incident particle is sufficiently high to exceed the surface binding energy, sputtering occurs and an atom is released from the material. Therefore, the sputtering yield decreases with increasing surface binding energy and increases with the energy transferred from the incident particle to the material atom. Enhanced sputtering and impurity generation by a powered ICRH antenna is one of the most deleterious side effects of ICRH. In order to mitigate these consequences, ICRH antennas are equipped with Faraday screens of sophisticated design in order to reduce current flow in the antenna structure and hence minimize the formation of large potentials. One of such sophisticated Faraday screen design was installed in 2011 on one of the three TS antennas and within this work we will study its impact on the scrape-off layer properties.

2.2.1 Particle transport

In this section will be treated the particle transport in the tokamak plasmas. Since plasma particles are in the ionized state, any particle transport can be actually considered as a electrical current. In order to be able to simulate a potential formed between a biased probe and a powered ICRH antenna, it is important to know how these currents flow not only in direction parallel to magnetic field (chapter 6), but most importantly also in the perpendicular direction. Particles move not only along magnetic field lines but can move perpendicularly to magnetic field lines mainly due to turbulent transport. In the plasma core, particle collisions are rare and hence core plasma is referred to collisionless plasma. In the simplest form, the main mechanisms that can be used to describe the transport across the flux surfaces at the plasma edge are Coulomb collisions between particles. Two particles circulating along two closed field lines can indeed interact via electrostatic forces causing their guiding centers to drift onto other field lines. From the classical point of view, these collisional effects can be described as a diffusion process since it implies somehow a random walk. The particle flux transversal to flux surface is proportional to the density gradient and the local diffusion coefficient $D_{\perp}^{c}$:

$$\Gamma_{\perp} = -D_{\perp}^{c} \nabla n \tag{2.1}$$

Following the idea of a random walk, the classical diffusion coefficient is simply determined by the collision frequency ν_c and the typical scale length, the Larmor radius, over which a collision displaces a particle transversely to the magnetic field

$$D_{\perp}^{c} = \nu_c r_L^2 \tag{2.2}$$

The collision frequency depends on the local density and temperature of the plasma as $\nu_c \propto nT^{-3/2}$, and varies typically from 1kHZ at the plasma center to tens of kHz at the plasma edge. Typical values of the classical diffusion coefficient at the edge are in the range of 10^{-4} to $10^{-2}\mathrm{m}^2\mathrm{s}^{-1}$ for deuterium ions. The first who tried to measure the diffusion coefficient in magnetic arcs was D. Bohm. According to his measurements, the empirical diffusion coefficient (characterising Bohm diffusion) is defined as:

$$D_{Bohm} = \frac{1}{16}\frac{kT}{eB} \tag{2.3}$$

which is significantly larger than the classical collisional estimate. It is now believed that the anomalously high diffusion rates observed in magnetized plasmas are due to a decorrelation process associated with plasma wave turbulence. It is important to understand these processes at the plasma edge also from the Langmuir probe measurement point of view in order to interpret correctly measured data and to apply right model describing probe behavior at the plasma edge. The curvature in torus geometry implies larger variety of collisional transport processes consequently to the magnetic field inhomogeneity. This leads to the neo-classical description of the transport. In the low collisional regime the trajectories of particles are determined by the toroidal geometry. Let us consider a particle orbiting along a magnetic field line experiencing a variation of the magnetic field strength along the parallel direction. As we mentioned earlier in the section 1.4, there is a magnetic force $F = -\mu B$ that pushes out particles from the regions of high magnetic field to lower ones. If the parallel velocity of a particle moving from the low field side towards the high field side is low, $v_{||} \leq \epsilon^{1/2} v_{\perp}$ with ϵ being inverse aspect ratio (i.e.

ratio between major plasma radius and minor plasma radius), such particle experiences a magnetic mirror effect and is reflected back. The resulting trajectory of trapped particles reminds, in the poloidal projection, banana shape. These larger orbits in banana regime allow a greater diffusion compared to the classical description. The transport in the highly collisional regime is called Pfirsch-Schlüter transport. The regime in between the low and high collisional regime is called the plateau in which there is no dependence on the collision frequency. The situation of different dependencies for the diffusion coefficient is summarized on Figure 2.2. Although the neo-classical description of the diffusion processes returns higher diffusion value than the classical approach, the model is not able to explain the diffusion coefficients measured during experiments, especially at the plasma edge (discrepancy of the order of few magnitudes). Historically, the unexpected high transport coefficient measured in the plasma received the adjective of anomalous since neither classical nor neoclassical theories were able to predict these values. It is believed that the enhancement of the diffusion is caused by plasma turbulence.

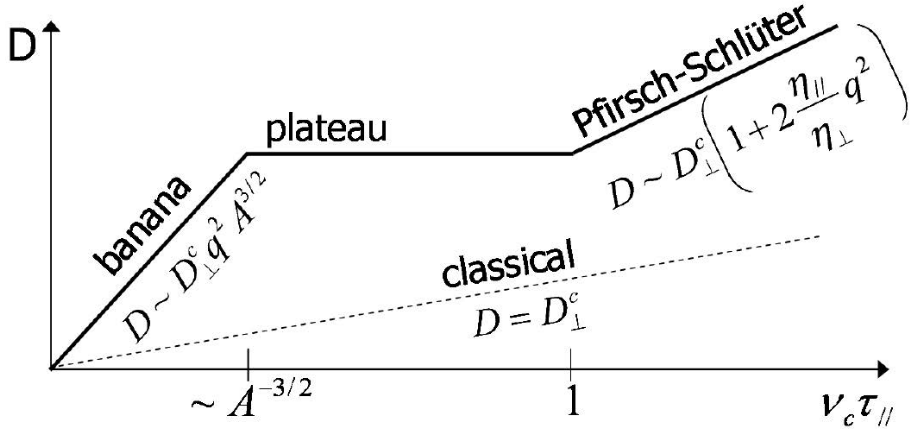

Figure 2.2: *Classical and neoclassical diffusion coefficient as a function of the collision rate.*

2.2.2 Plasma facing materials

In a fusion reactor, we can find several components facing the plasma directly. The largest surface consists of the first wall which surrounds the bulk region of the plasma torus. The plasma shape may be restricted by additional limiters to protect the vessel wall or equipment like antennas for radio-frequency heating or optics of some diagnostic systems which cannot withstand excessive heat loads. Within this work we will deal very often with the limiters that protect heating antennas on both its sides. Our interest lies with the fact that our diagnostic, a reciprocating Langmuir probe, is magnetically connected to one of the antenna side limiters. Finally, a very important part of the plasma facing components in current and future fusion devices are the divertor target plates. In a diverted plasma configuration these plates provide the main plasma-surface interaction zone. The fraction of the fusion power carried by the produced α-particles is coupled out to a large extent through these areas.

Magnetic field lines which lie on a flux surface that never makes contact with a solid surface are called closed, while those which pass through a solid surface are termed open (for our particular case, it is the antenna protection limiter which we are interested in). The border of the confined region is known as the last closed flux surface. In the case of divertor configuration, it is common to use the term 'separatrix'. By definition, the last closed flux surface and separatrix are not the same, but the former is located infinitesimally inside the latter. The term scrape-off layer then stands for a narrow region of width of only a few cm, outside this border. The SOL may be imagined as the region where the plasma is essentially scraped off from the core plasma (Fig. 2.3). The width of the SOL can be then defined as the mean radial distance that a particle moves during the parallel time of flight along one connection length. There are two ways by which the last closed field line can be limited, see Figure 2.4. In the simplest solution, the confined region is 'limited' by inserting a barrier into the plasma. This is called a limiter. Large impurity fluxes from sputtered limiter material prevented the achievement of hot, clean plasmas. Therefore, to overcome these difficulties, another configuration had to be considered. This new conception is based on divergence of magnetic field lines of the SOL

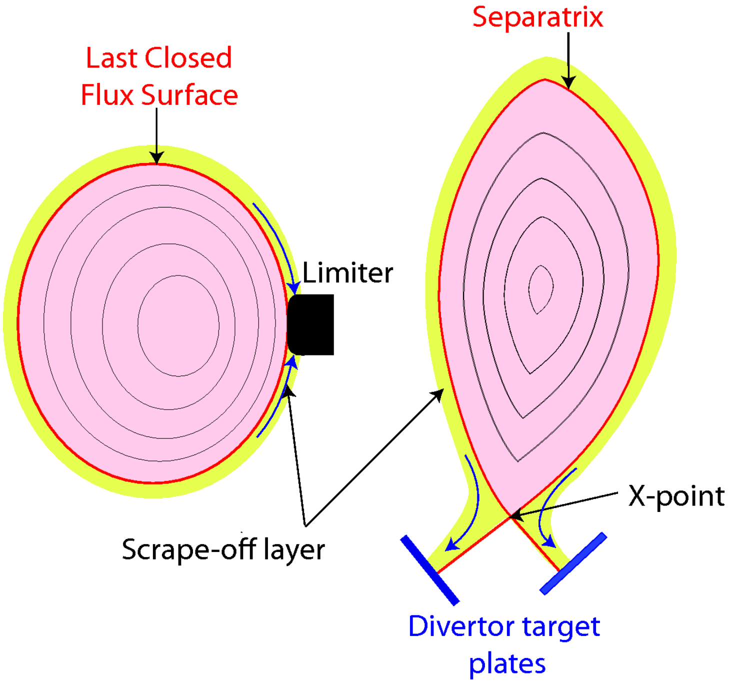

Figure 2.3: *Limiter and divertor configurations.*

to a dedicated region inside the vessel where they intersect with a special target plates. This configuration, called a divertor, has proved in experiments to be significantly more advantageous, because it reduced significantly the direct line-of-sight contamination of the core plasma by sputtered impurity atoms. It also allows to reach the H-mode with a characteristic edge transport barrier leading to enhanced energy confinement [Wagner 82]. The next section describes in more detail limiter configurations[1].

2.2.3 Limiter

A limiter is a solid surface inserted in the tokamak chamber which defines the last closed flux surface. Limiters take various geometrical forms as illustrated in Fig. 2.4. The simplest concept is a circular hole in a diaphragm normal to the toroidal field. This is known as a poloidal limiter. Despite the fact that magnetic field lines in a tokamak form closed surfaces, it does not necessary mean that even a local insertion of limiter will define a boundary. Experiments performed on Tore Supra suggest that to obtain a narrow simple SOL, more than one poloidal limiter is required [Kubič 12]. In either case there will be a decreasing plasma density radially outside the limiting surface, due to parallel losses of plasma which flows along magnetic field lines to be neutralized on the limiter. In the case of a complete poloidal limiter the connection length L will be approximately the circumference of the torus, $2\pi R$. In the case of the toroidal limiter the connection length L is longer, as the particles need to go around the chamber several times before hitting the solid surface. The connection length depends on the pitch angle via the safety factor q defined by Eq. (1.17) and it can be expressed as $L \approx 2\pi Rq$. A limiter plays a number of roles in tokamak operation. It serves mainly as a wall protection from the plasma (disruption, runaway electrons or other instabilities). It also serves as a protection

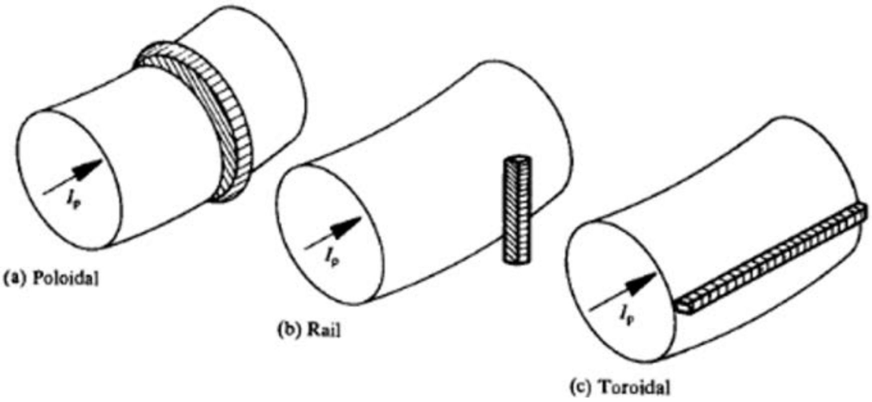

Figure 2.4: *Schematic representation of different types of limiter.*

---

[1] Divertor configuration is not presented due to the fact that in this thesis we will deal on with Tore Supra tokamak.

of heating antennas. For this reason it is commonly made of a refractory material, such as carbon, molybdenum or tungsten, capable of withstanding high heat loads. Moreover, in order to decrease the thermal stress of plasma facing materials, they are actively cooled by series of pipes with flowing water at high pressure inside the materials. For instance, the first wall in Tore Supra tokamak is cooled at temperature of 120°C. Secondly, the limiter localizes the plasma-surface interaction. The high power and particle density at the limiter's surface cause rapid removal of absorbed gas and other impurities via processes described earlier of this chapter. A higher neutral density and more radiation are observed in the region near the limiter than at other positions around the torus. [Wesson 04]. The Tore Supra tokamak is equipped with one toroidal pump limiter (Figure 2.5 - left) and one main 'antenna protection limiter' (Figure 2.5 - middle). In addition, TS disposes of 5 heating antennas, which can be used to limit plasma as well (Figure 2.5 - right). In a typical Tore Supra discharge, the plasma contacts the bottom limiter and leans on a main antenna protection limiter, while the rest of them are retracted behind. Nevertheless, experiments with a special plasma configuration have been made in order to investigate ramp up phase in ITER start-up experiments with a plasma leaning either on the inboard [Gunn 10] or on the outboard side of the vessel [Kubič 12].

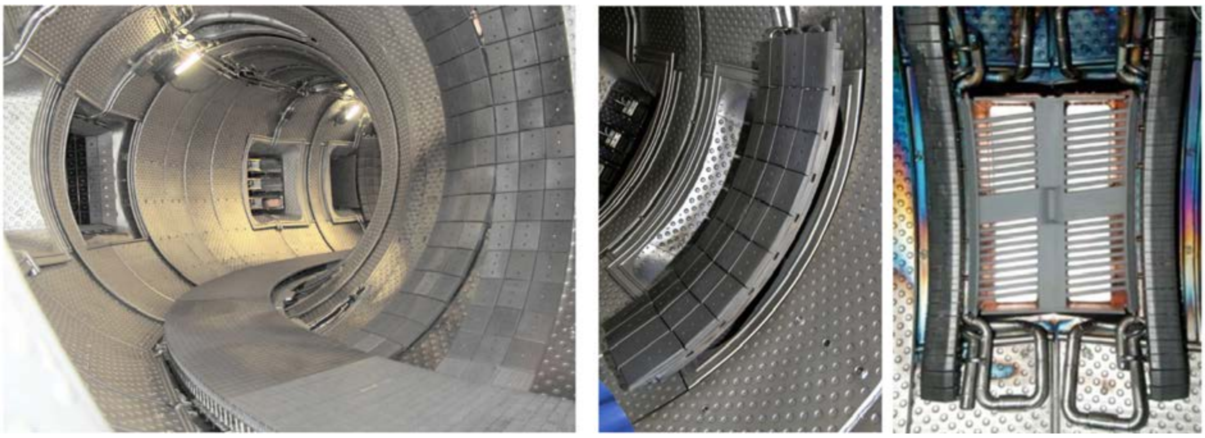

Figure 2.5: *Toroidal pumped limiter of the Tore Supra tokamak placed at the bottom of the chamber (left) and modular limiter placed at the midplane (right).*

2.3 The scrape-off layer

As shown on Figure 2.3 the boundary between the plasma core and the plasma edge in magnetically confined plasma is either defined by a material limiter or, in the case of a diverted plasma, by a magnetic separatrix. Inside the boundary, the magnetic surfaces are closed while in the region between the LCFS and the wall surface, the field lines intersect material components. These connections play a crucial role in edge plasma physics. The particle exhaust and the α-particle fraction of the produced power (as well as the additional heating power during start-up) are coupled out to a large extent through this region and transferred to the limiters or divertor plates. In the following pages are derived some of the main SOL properties together with the sheath theory which serves as basis for all probe applications.

2.3.1 Simple SOL model

Any wall element which comes into the contact with the striking magnetic field line serves as an ideal plasma sink and imposes a flow that is directed along the field lines. The flux tubes terminating on wall elements are filled with plasma by perpendicular transport from the confined plasma (collisional diffusion, drifts and turbulent transport). It was mentioned in previous pages that the particle transport across the magnetic field lines is quite complex and not yet fully understood. Simulations based on diffusive model in 2D codes rely on empirically adjusted diffusion coefficient $D(r, \theta)$ to make code results agree with experimental observations, but still with limited success. Moreover, for reasons of economy and plasma performance, confined magnetic flux surfaces are shaped to occupy as much of the vacuum chamber volume as possible. In addition, all tokamaks have secondary limiters (poloidal limiters, antenna protection limiters - Figure 2.5) which can play an important role especially if antennas are active. Hence a significant interaction with the SOL plasma can occur such as enhanced sputtering or impurity production from material surfaces. This is the case when using the ICRH antennas to heat the plasma which are usually placed 1cm behind the main poloidal limiter. In the case of the Tore Supra tokamak, up to three ICRH antennas can be used. The simple SOL structure thus can be disturbed leading to the formation of a complex SOL. The best approach would be then to use a 3D code with self consistent turbulent transport, but they are strongly non-linear and require massive parallel processing that are still years away from being feasible. Therefore, to understand basic scrape-off layer features, there is still a case to be made for using a simple heuristic model.

In the following part will be described some of the main properties of the scrape-off layer, such as the density variation along the radial direction in the SOL, or the SOL width [Unterberg 06, Stangeby 00]. An essential aspect of the simple SOL is that the radial distance between the LCFS and the first wall is sufficiently large that the plasma density decays naturally to zero. In the other words, all charged particles hit the main limiter or divertor plates, none hit the first wall. Due to the symmetry of tokamak devices, both equipped with a limiter or a divertor, the situation can be simplified into a 2D case by assuming no variations in toroidal direction. We will consider the diffusion processes in radial direction (coordinate x) and the plasma flow along the field line (coordinate z). The situation is schematically shown on Figure 2.6. Considering radial thickness of the SOL

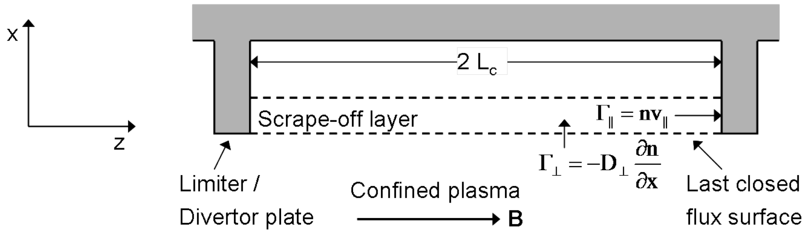

Figure 2.6: *The simple SOL model*

being about few cm that is negligible in comparison with the plasma minor radius (0.7m for TS), a plane geometry can be applied. To obtain an estimate of the SOL characteristic width, we assume particles moving in parallel direction with a typical speed of the order of ion sound speed c_s (proof will be provided later in this chapter) along the flux tubes with connection length 2L, where $L = \pi q R$, with q being the safety factor and R plasma major radius. The SOL thickness λ can be estimated from Fick's law:

$$\lambda^2 = D_{\perp}\tau_{||} \tag{2.4}$$

Essentially the SOL thickness is given by the mean radial distance that an ion can traverse under a random walk process during the characteristic time $\tau_{||} = L/c_s$ which it takes to propagate along field lines towards the target. The expression for the SOL thickness then yields

$$\lambda = \sqrt{\frac{D_{\perp}L}{c_s}} \tag{2.5}$$

For typical values of Tore Supra edge plasma: $D_{\perp} = 1m^2s^{-1}$, $L = 40m$ and $c_s = 5 \cdot 10^4 ms^{-1}$, the SOL width of the Tore Supra is of the order of $\lambda \approx 3cm$. Despite the fact that $D_{\perp}$ is an empirical result based on SOL measurements of λ, L, and c_s, there is no first-principle derivation of it. The main constraint with the evaluation of $D_{\perp}$, associated with the turbulent transport using neoclassical values, lies in the fact that such evaluations are still not in the good agreement with experimental observations. Equation (2.5) provides just an estimate. It has to be kept in mind, that there is a temperature dependence hidden in the definition of ion sound speed [Stangeby 00]. Sometimes, it is more convenient to express the SOL thickness as a function of the magnetic field. To obtain such a relation, we can simply use the definition of safety factor (Equation (1.17)):

$$\lambda \sim a\sqrt{\frac{B_T}{B_p}} \tag{2.6}$$

Having now an estimate of the SOL thickness, it would be convenient to know how does the density vary across the SOL. In order to do that, one has to consider a law of mass conservation along the flux tube (flux tube model, [Stangeby 00])

$$\frac{\partial}{\partial z}(nv_{||}) = \frac{\partial}{\partial x} D_{\perp} \frac{\partial n}{\partial x} \tag{2.7}$$

Assuming that radial diffusion coefficient is constant, together with $\partial n/\partial x = const.$ along z, we can write $\partial/\partial z(nv_{||}) = nv_{||}/L$ leading to differential equation of following form

$$\frac{\partial^2 n}{\partial x^2} - \frac{c_s}{LD_{\perp}} n = 0 \tag{2.8}$$

The solution is then given by

$$n(x) = n(0) \cdot e^{-x/\lambda} \tag{2.9}$$

This equation suggests that the density varies exponentially inside the scrape-off layer. The characteristic length λ of the decay is provided by Equation (2.5). Here, $n(0)$ denotes the density at the LCFS. It is important to recall that the characteristic length λ is not constant across the scrape-off layer but varies with the plasma temperature. In general, temperature decreases radially in the SOL as well, but in manner slower than exponential. The slope of the density decay depends on many factors, such as particle source spatial distribution or even, as will be shown later, on the performance of a powered ICRH antenna, and varies poloidally.

2.3.2 Parallel flow in the SOL

In the following, we would like to investigate the parallel flow in the scrape-off layer. In order to do that we will assume the simple SOL defined in previous section. We consider the flow as one-dimensional with no heat sinks or sources inside the SOL. The only source S_p considered here is the diffusive cross field transport constant all along the magnetic field (idea of homogeneous source is very idealistic here, in the real case, the source is rather heterogeneous with the source located at one place) - Figure 2.7.

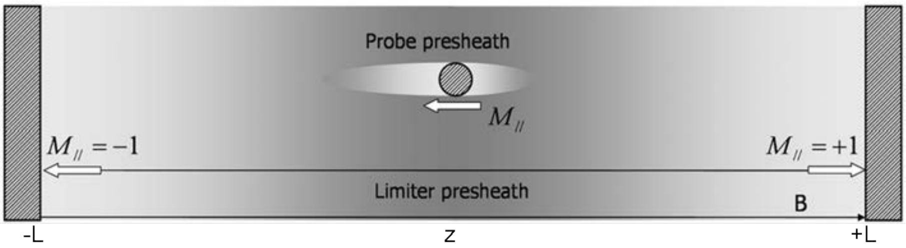

Figure 2.7: *Picture of the plasma equilibrium along the pre-sheath of limiters and probes.*

The continuity equation yields

$$\frac{\partial}{\partial z}(nu_{||}) = S_p = \frac{\partial}{\partial x} D_{\perp} \frac{\partial n}{\partial x} \approx \frac{D_{\perp} n}{\lambda^2} \tag{2.10}$$

The second equation is given by the momentum conservation

$$m_i n u_{||} \frac{\partial u_{||}}{\partial z} = -\frac{\partial p_i}{\partial z} + enE - m_i u_{||} S_p \tag{2.11}$$

The next step would be to derive the energy conservation equation. However, for demonstrating the basis of the plasma flow along the SOL, it is sufficient to assume the isothermal condition. The unknowns are the density n and the velocity v with T as a parameter that has to be derived from other considerations. If we consider the definition of electric field given by $E = -d\phi/dx$ and the Boltzmann relation for electron density $n = n_0 exp(e\phi/kT_e)$, the first two terms on the RHS of above equation transform to

$$-\frac{\partial p_i}{\partial z} + enE = -\frac{\partial n}{\partial z}\left(\frac{k(T_e + T_i)}{m_i}\right)$$

where we also used isothermal condition for ions when neglecting the term $\partial T_i/\partial z$. The plasma momentum equation then gives

$$n u_{||} \frac{\partial u_{||}}{\partial z} = -c_s^2 \frac{\partial n}{\partial z} - m_i u_{||} S_p \tag{2.12}$$

At this point, it is convenient to define parallel Mach number $M = u_{||}/c_s$. The combination of Equations (2.10) and (2.12) then provides equations which describe the variation of the density and the Mach number:

$$\begin{aligned} \frac{\partial n}{\partial z} &= -\frac{n D_\perp}{c_s \lambda^2} \frac{2M}{1-M^2} \\ \frac{\partial M}{\partial z} &= \frac{D_\perp}{c_s \lambda^2} \frac{1+M^2}{1-M^2} \end{aligned} \tag{2.13}$$

These equations give rise the Bohm criterion since they define the boundary condition of the flow at the sheath entrance which is determined by the singularity for M = ±1. Concerning the density profile along the field line, the previous conservation equation allows us to evaluate its dependence with the local flow strength. Since the Mach number is defined at the field lines boundaries by the Bohm criterion : $M(-L)$ = -1 and $M(L)$ = +1, the flow continuity condition necessary implies position along the field line where the flow is stagnant $M_0 = 0$ - the stagnation point. The local density along the field line is thus linked to the local flow velocity via the relation:

$$\frac{\partial n}{\partial M} = n \frac{2M}{1+M^2} \tag{2.14}$$

which after integration with following substitution $y = 1 + M^2$ provides

$$n(z) = \frac{n_0}{1 + M(z)^2} \tag{2.15}$$

with n_0 being the density in the stagnation plane where $M(z = 0) = 0$. It is worth to note that there is no dependence of particle source S_p. One can also note that the density variation is weak. The density drops from the stagnation point to the sheath entrance only by half of its value. The particle flux density at the sheath edge Γ_{se} is therefore

$$\Gamma_{se} = n(0)v_{se} = \frac{1}{2}n_0 c_s \tag{2.16}$$

The source distribution along the field line can be defined by using a new parallel coordinate s [Gunn 07b]

$$s(z) = \frac{\int_{-L}^{z} S_p dz}{\int_{-L}^{L} S_p dz} \tag{2.17}$$

This parallel coordinate s describes the source fraction collected along the field line from an origin to a given position. Based on the Bohm sheath criterion Eq. (2.29) this formalism allows to determine the position where the velocity of the particles is zero if the source distribution is known. Integrating the mass conservation equation from a field line boundary to a given position yields a flow expression function of the source coordinate s assuming $M(s = 0) = -1$ and $M(s = 1) = +1$:

$$\frac{M}{1 + M^2} = s - \frac{1}{2} \tag{2.18}$$

For instance, this formula says that the flow is stagnant at the position where the source is equally distributed on each side of that position $s = 1/2$.

2.3.3 The Sheath

In previous sections we described main properties of the tokamak scrape-off layer. But, there is also another region which plays an important role in edge plasma physics - the sheath. The sheath is defined as a thin region that appears between the plasma and the material boundary. Let us now consider simple 1D case with a plasma flowing to a neutral isolating surface. Because the velocity of electrons is much greater than ions due to a large difference in their masses, the surface receives an electron flux higher than the ion flux. This in turn perturbs the ambipolarity condition (same amount of negative and positive charge arrives to the surface) imposed by the surface at the equilibrium. The surface is charged negatively due to electron accumulation which at some point leads to repulsion of incoming electrons and to attraction of ions. In order to preserve the ambipolarity, an electrostatic potential is formed due to negative charge accumulation on the surface. Therefore, the sheath is defined as the plasma volume over which the charge separation occurs. In our particular case, we have a grounded metallic plate representing a probe at one end, while on the other side of the flux tube is an oscillating sheath generating a rectified sheath potential. We will see later that biasing one of either plates has a crucial effect of the sheath potential formation. To obtain the estimation of the sheath thickness, that is determined by the Debye length, one has to solve Poisson equation.

Within the sheath, the quasi-neutrality condition is no longer fulfilled, $n_e < n_i$, where n_e and n_i are electron and ion densities, respectively. Moreover, we assume that the initial ion temperature at the upstream side of the sheath edge is zero and the electrostatic potential is then given by

$$\frac{d^2\phi}{dx^2} = -\frac{e}{\epsilon_0}(n_i - n_e) \tag{2.19}$$

For the further purposes we define a reference position at the sheath entrance, labelled as s.e., where quasi-neutrality still holds but begins to diverge when moving inside the sheath. We further assume that in this potential, electrons can be described by Boltzmann equilibrium

$$n_e(x) = n_{se}\, exp\left[\frac{e(\phi - \phi_{se})}{kT_e}\right] \tag{2.20}$$

where $n_{se,e} = n_{se,i} = n_{se}$ is the density at the sheath entrance. This potential distribution contains a barrier for the electrons ($\phi < 0$), which is a representation of a limiter or divertor surface that has initially been charged negatively by the electrons. Here we are taking the reference potential to be $\phi = 0$ at a location in the plasma far away from the sheath edge. ϕ_{se} describes the potential drop which occurs in the plasma itself, i.e. in the pre-sheath. The electric field resulting from the exponential decay of the potential gives rise to a strong acceleration of ions towards the surface. Our goal is to solve Equation (2.19) and find out the plasma exit velocity. In our further procedure, we will assume ion temperature to be zero, $T_i = 0$[2]. In addition we will assume that all the ions are reaching the sheath edge from a single location which allows us to write

$$\frac{1}{2}m_i v_{se}^2 = -e\Delta\phi_{pre-sheath} = -e\phi_{se} \tag{2.21}$$

Inside the sheath, the energy conservation yields

$$\frac{1}{2}m_i v_i^2 = -e\phi \tag{2.22}$$

The assumption we made about the ion source being concentrated into a single location is convenient because in such case we can close our system of equations by equation for particle conservation to preserve the quasineutrality

$$\Gamma = n_i v_i = n_{se} v_{se} \tag{2.23}$$

By combining all three above equations, we can write

$$n_i = n_{se}\frac{\phi_{se}}{\phi} \tag{2.24}$$

---

[2] although it is obvious this does not correspond to reality where ion temperature usually exceeds the electron temperature

Now having both n_e and n_i as function of n_{se}, ϕ_{se} and ϕ, we can substitute for them in Poisson equation leading to

$$\frac{d^2\phi}{dx^2} = -\frac{e}{\epsilon_0} n_{se} \left[\left(\frac{\phi_{se}}{\phi} \right)^{1/2} - exp[\frac{e(\phi - \phi_{se})}{kT_e}] \right] \tag{2.25}$$

To solve this equation analytically, we will use a perturbation approach based on the Taylor expansion of the right hand side of the differential equation. We define a region just inside the sheath where $\Delta \equiv \phi_{se} - \phi > 0$ with the condition $\Delta \ll \phi$. The both terms in square brackets of the Equation (2.25) can be now rewritten to

$$\left(\frac{\phi_{se}}{\phi} \right)^{1/2} \approx 1 - \frac{1}{2} \frac{\Delta}{\phi_{se}} \tag{2.26}$$

$$exp[e(\phi - \phi_{se})/kT_e] \approx 1 - \frac{e\Delta}{kT_e} \tag{2.27}$$

and substitute to Equation (2.25) giving

$$\frac{d^2\Delta}{dx^2} \approx \frac{en_{se}\Delta}{\epsilon_0} \left(\frac{e}{kT_e} - \frac{1}{2\phi_{se}} \right) \tag{2.28}$$

The theory of single, second-order differential equations says that the solution is non-oscillatory if the RHS is > 0. Therefore, we obtain

$$\begin{aligned} \frac{e}{kT_e} &\geq \frac{1}{2\phi_{se}} \\ m_i v_{se}^2 &\geq kT_e \\ v_{se} &\geq c_s \end{aligned} \tag{2.29}$$

where the last inequality is again the Bohm criterion for the plasma exit velocity, but in the case of pre-sheath we obtain $v_{se} \leq c_s$. Hence to satisfy both condition an the sheath entrance, it directly implies $v_{se} = c_s$. In order to obtain a characteristic scale length of the sheath, we can replace the second derivative in the Equation (2.28) by the sheath thickness L_{sheath}

$$\frac{\Delta}{L_{sheath}^2} \approx \frac{en_{se}\Delta}{\epsilon_0} \frac{e}{kT_e} \tag{2.30}$$

yielding in

$$L_{sheath} \approx \left(\frac{\epsilon_0 kT_e}{e^2 n} \right)^{1/2} \equiv \lambda_D \tag{2.31}$$

where λ_D is Debye length which defines distance over which the electrostatic potentials are shielded out. Considering standard edge plasma conditions, $n_e = 10^{19}$ m^{-3}, $T_e =$ 20eV, the characteristic scale length of the sheath width is of the order $\lambda_D \approx 10\mu m$.

2.3.4 Potential drop across the sheath

In the frame of the topic of this work, we are interested in knowing the potential drop, $\Delta\phi$, that spontaneously arises between a plasma and a solid surface in contact with it which is electrically isolated - floating. The quantity $\Delta\phi$ is important for determining the ion sputtering rate of the solid surface and the heat flux to the solid surface (corresponding formulas can be found in [Stangeby 00]). Having the total flow in the sheath that satisfies $\Gamma^e = \Gamma^i$, we can derive the potential drop across the sheath. From the above defined Bohm criterion, we can describe the ion flux density to the target as the parallel flux density at the sheath entrance. From previous derivations we have an ion flux density at the sheath edge given by Equation (2.16)

$$\Gamma^i_{target} = n_{se}c_s = \frac{1}{2}n(0)\sqrt{\frac{k(T_i+T_e)}{m_i}} \tag{2.32}$$

If we consider that electrons are characterized by a Maxwellian distribution, together with the assumption of no secondary electron emission from the surface, the electron flux to the target yields [Stangeby 00]

$$\Gamma^e_{target} = n_{se}\bar{c}_s = \frac{1}{4}n_{se}\, exp(\frac{e\Delta\phi}{kT_e})\sqrt{\frac{8kT_e}{\pi m_e}} \tag{2.33}$$

By combining two previous equations we can obtain the potential drop between the sheath edge and the electrically floating surface defined as

$$\frac{e\Delta\phi}{kT_e} = 0.5\, ln\left[2\pi\frac{m_e}{m_i}(1+\frac{T_i}{T_e})\right] \tag{2.34}$$

It is worth noticing that there is no dependence on plasma density in Equation (2.34). Magnitude of $\Delta\phi$ decreases with the increase of ion-to-electron temperature ratio and with the decrease of ion mass. For a deuterium plasma with $T_e = T_i$, the potential drop across the sheath is $\Delta\phi \approx -2.3\frac{kT_e}{e}$. In order to get total potential drop, we have to add the drop that occurs in the pre-sheath. For that purpose we use Equation (2.15) describing the density variation as a function of Mach number, together with the Boltzmann equation for electron density

$$\left.\begin{array}{l} n(z) = \frac{n_0}{1+M(z)^2} \\ n = n_{se}exp(e\phi/kT_e) \end{array}\right\} \quad \phi z = -\frac{kT_e}{e}ln[1+M(z)^2] \tag{2.35}$$

Therefore, at the sheath edge one obtains

$$\phi_{se} \equiv \phi(L) = -\frac{kT_e}{e}ln2 \approx -0.69\frac{kT_e}{e} \tag{2.36}$$

Hence, the total potential drop across the pre-sheath and the sheath is $\approx \mathbf{3T_e}$. This is a very important value for the thesis purposes and we will refer to it many times later during the analysis of RF-SOL induced modifications. As we will see later, the sheath properties change dramatically when RF potentials are introduced due to the fact that the effective electron flux is modified by the present RF field near a powered ICRH antenna. Corresponding model will be described in the chapter 4.

Chapter 3

Probes

3.1 Introduction

After providing a general introduction to nuclear fusion and to the basis of edge plasma physics in previous chapters, this chapter is related to the description of Langmuir probes. Langmuir probes play a key role in this work since they are used as a main diagnostic tool for the study of RF-SOL interactions. This chapter is structured as follows. At first, basic principles of the Langmuir probe measurement technique are explained followed by presentation and detailed description of the operational principles of two main probes used on Tore Supra, the tunnel probe and the retarding field analyzer. Because most of the probes used on Tore Supra are built as bi-directional, a Mach probe theory described with 1D fluid model is presented to derive a useful tool for probe data interpretation. Namely, it will be discussed how to evaluate the measured plasma density or parallel flow in the scrape-off layer. The applicability of Mach probe theory is then practically demonstrated by comparing data evaluated with aid of Mach probe theory, and standard data treatment. Finally, the description of the operational principles and technical aspects of using the probes on Tore Supra is provided with the emphasis on different modes of their operation. Considerable attention is given also to the feedback system whose proper functionality is necessary for the measurement of RF-induced SOL modifications.

3.2 Langmuir probe description

Probes are active plasma diagnostics that come in direct contact with the plasma. Therefore, they can only be applied at the plasma edge where the plasma flux does not lead to destruction of the probe due to excessive heating, or perturbation of the confined plasma due to the release of sputtered impurities. The most well known kind of probe is the *Langmuir probe* [Mott-Smith 26], which typically consists of a small metal electrode - cylindrical, spherical or in the shape of a disk - inserted into the plasma [Hutchinson 02]. The main principle of the Langmuir probe is to measure the current collected by the probe as a function of the applied voltage to the probe. The current dependence on the varying voltage is generally called an I-V characteristic. An example of an ideal I-V characteristic of such a single probe is shown in Figure 3.1. By the ideal I-V characteristic shown here, we mean a characteristic obtained by a small probe placed in highly ionized, weakly collisional, unmagnetized plasma. In such a case, the perturbations are localized to a few Debye lengths around the probe due to Debye shielding. If we assume that the current drawn by the probe from the plasma is negative, when the probe bias V is very negative with respect to the plasma potential, V_p, the electric field around the probe will prevent all but the most energetic electrons from reaching the probe, effectively reducing the electron current to zero. The current collected by the probe will then be entirely due to positive ions, since these encounter only an attracting field. This current is called the 'ion-saturation current' I_{is}. As the probe bias is increased, the number of electrons which are able to overcome the repulsive electric field, and contribute to a current, increases exponentially (if we assume Boltzmann distribution). Eventually the electron current collected is equal to -I_{is}, so that the total current is zero. At this point the floating potential V_f is defined. It is the natural electric potential of a conducting object immersed in the plasma with no electrical connection to the outside world. Examples of such objects could be small dust particles in industrial or fusion plasmas, or spacecraft moving through the ionosphere. The floating potential can be accurately measured by connecting a probe to the tokamak wall through a very large resistor which impedes the flow of current to microscopic values, and measuring the voltage drop across the resistor. Further increase of the probe bias to V_p allows the electron current to dominate over the ion current. At V_p, electrons are unrestricted from being collected by the probe. Any further increase

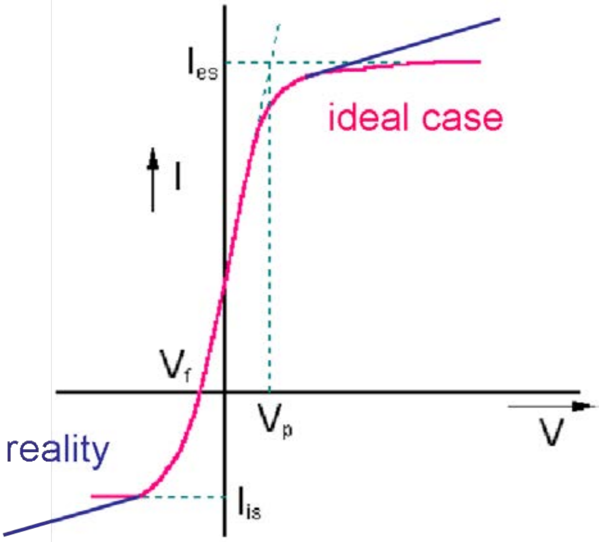

Figure 3.1: *I-V characteristic of an idealized Langmuir probe.*

in bias will simply add energy to the electrons, not the current drawn. No additional current is collected stabilizing at 'electron-saturation current' I_{es}. Note that this is the ideal I-V characteristic, ignoring the disturbing processes such as bombardment of the probe by high energy electrons, emission of secondary electrons from the probe, and the probe etching away. Moreover, many probes operating in the edge plasmas of fusion devices, which is a magnetized plasma, are not biased to large positive voltages in order to avoid the electron saturation part and hence prevent the probe from overheating. Collecting the electron saturation current in dense tokamak plasmas is often limited by the maximum current specification of the power supplies and it is possible only at very far scrape-off layer where electron current density is low. In magnetized plasma, the particles remain tied to the magnetic field lines. In the magnetic field, it is necessary to take into account also the cross-field transport of the particles. Transport of particles across the magnetic field leads to generation of dc currents. Understanding of the flow of these currents (mainly inertia, viscous and friction) has been a subject of various modellings [Rozhansky 99, Carlson 01, Faudot 13] and we will deal with the simulation of some of these currents in the chapter 6. The non-saturation of the electron part of the I-V characteristic is then caused by the electron density depletion in the probe's flux tube due to high cross-field currents.

To describe quantitatively the current-voltage dependence for voltages more negative than the floating potential, we refer to Equations. (2.61)-(2.71) in [Stangeby 00] defining a current to an electrically biased surface inserted into the plasma in the following form:

$$I = I_{sat}\left(1 - exp(\frac{V - V_f}{T_e})\right), where\ \ I_{sat} = en_e c_s A_{col} \tag{3.1}$$

where I is the current collected on the probe head, V is the applied bias voltage, I_{sat} is the ion saturation current and A_{col} is the probe collecting area. The electron temperature T_e is then obtained by a least-squares fit of the exponential part of the I-V characteristic. The electron density can be obtained directly from the ion saturation current, assuming the T_e is known:

$$n_e = \frac{I_{sat}}{ec_s A_{col}},\ where\ \ c_s = \sqrt{\frac{k(T_e + T_i)}{m_i}} \tag{3.2}$$

Typical ion-to-electron temperature ratio in the SOL of ohmically heated discharges is $\tau = \dfrac{T_i}{T_e} \approx 2$, but it can increase up to $\tau \sim 10$ in discharges with strong RF heating [Kočan 08].

Since the current is collected over the whole surface of the probe, we can divide I_{sat} by the probe's effective collecting area A_{col} yielding the ion saturation current density J_{sat}. Unfortunately, measurements of J_{sat} are often subject of uncertainty due to the fact that the effective collecting area is not always well known. Let us define A_{geo} as the geometrical projection of the electrode along the magnetic field **B**. If the Debye length λ_D as well as the Larmor radius are sufficiently smaller compared to probe dimension (in the direction perpendicular to **B**), $A_{col} \doteq A_{geo}$. Langmuir probes used in their simplest form for measurements in tokamak plasma, consist of thin cylindrical pins with a diameter of few mm. That implies, considering the fact that typical r_L of ions in the scrape-off layer is in the range of $0.1 < r_L < 1$mm, the probe collects the fluxes larger than the flux of the ion guiding centres on A_{geo}. The size of the electrode is effectively increased in all directions by the sheath thickness. This is caused by an electric field in the magnetic pre-sheath which deflects the ions towards the probe surface and hence to an increase of the current collected by the probe [Dejarnac 07]. This phenomena is known as 'sheath expansion' and causes the J_{sat} to be very often overestimated. Moreover, it scales with the local plasma parameters making its analytical description difficult. To investigate this phenomenon, one has to use 3D kinetic simulations. The effect of the sheath expansion on the probe measurement can be eliminated by building a concave probe. One of such is routinely used on Tore Supra and is described in detail in section 3.2.1 of this chapter [Gunn 02].

In the following, various types of probes used on Tore Supra will be presented. Two kinds of probes were intensively used in order to study RF-SOL interactions. Namely, they are the tunnel probe which can provide well calibrated measurements of parallel ion current density at the sheath edge, and the retarding field analyzer which is able to measure ion temperature and sheath potential. Descriptions of both probes are given in the following subsections.

3.2.1 Tunnel probe

The tunnel probe is a kind of electrostatic probe used for the scrape-off layer measurements [Gunn 02]. It provides simultaneous measurements of electron temperature, floating potential and parallel ion current density. The tunnel probe used in these experiments consists of a hollow stainless steel tunnel 3 mm in diameter and 5 mm deep that is closed at one end by an electrically isolated graphite back plate as is shown on Figure 3.2. The conductors are mounted in an insulating boron nitride head and biased negatively with respect to the tokamak chamber to collect ions and repel electrons. The tunnel axis is not exactly parallel to the magnetic field but can be misaligned up to ≈ 5° depending on field line pitch angle. Plasma flows into the open orifice and the ion flux is distributed between the tunnel and the back plate [Gunn 08].

The main advantage of tunnel probe is its concave shape. The concave tunnel probe yields more accurate measurements of T_e and $J_{\parallel,i}$ than conventional convex probes due to the fact that its sheath electric field is entirely contained inside the probe and does

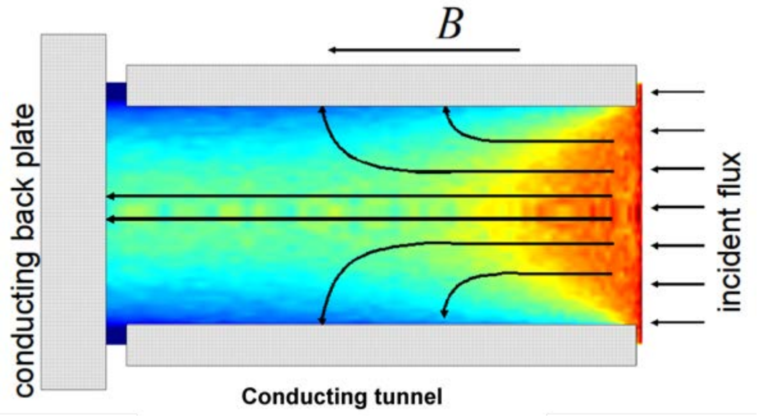

Figure 3.2: *Schematic view of tunnel probe. The current collected by each of the three conductors is monitored separately. The ion guiding center trajectories are shown by black arrows.*

not expand into the plasma to perturb the incoming ion orbits. In order to correctly measure the ion current density, the effective collecting area of any probe must be known precisely. For example, the effective area of a small cylindrical pin is larger than its geometrical projection along the field lines due to expansion of the magnetized sheath around the probe. This expanding electric field increases the effective collecting area, i.e. ions whose orbits would not intersect the probe in the absence of electric fields are deflected towards the probe and collected. Therefore, the ion current does not saturate for a convex probe, whereas it saturates perfectly for the tunnel probe. The sheath in this case does not perturb the incoming ion orbits, and the effective collecting area of probe is almost exactly equal to its geometric projection along the field lines, i.e. the effective collecting area is given by the cross section of the orifice $A_{geo} = \pi r_{orifice}$. [Gunn 06].

3.2.2 Retarding Field Analyzer

In principle, a retarding field analyzer can directly measure the sheath potential V_{sh} in the scrape-off layer, in contrast to Langmuir probes which only measure floating potential [Guo 96]. We will show later in chapter 7 that RFAs cannot measure the rectified DC sheath potential correctly. A RFA consists of a slit plate, two biasing grids and a collector (see Figure 3.3). The slit plate is biased negatively to repel most of the thermal electrons. Ions that are transmitted through the slit plate are retarded in the electric field created by a swept positive voltage applied to grid 1, V_{g1}. The collector should collect only ions. Therefore, it is necessary to repel all remaining fast electrons that passed through the slit plate or those released by secondary emission inside the analyzer, by applying a negative voltage on grid 2, V_{g2}. To obtain an I-V characteristic of the probe, one can simply plot collector current I_{col} against sweeping voltage on grid 1. If V_{g1} is low, I_{col} remains constant due to the potential drop in the Debye sheath that shifts all incident ions towards higher energies. Once the V_{g1} overcomes the sheath potential, the signal on the collector starts to decrease exponentially.

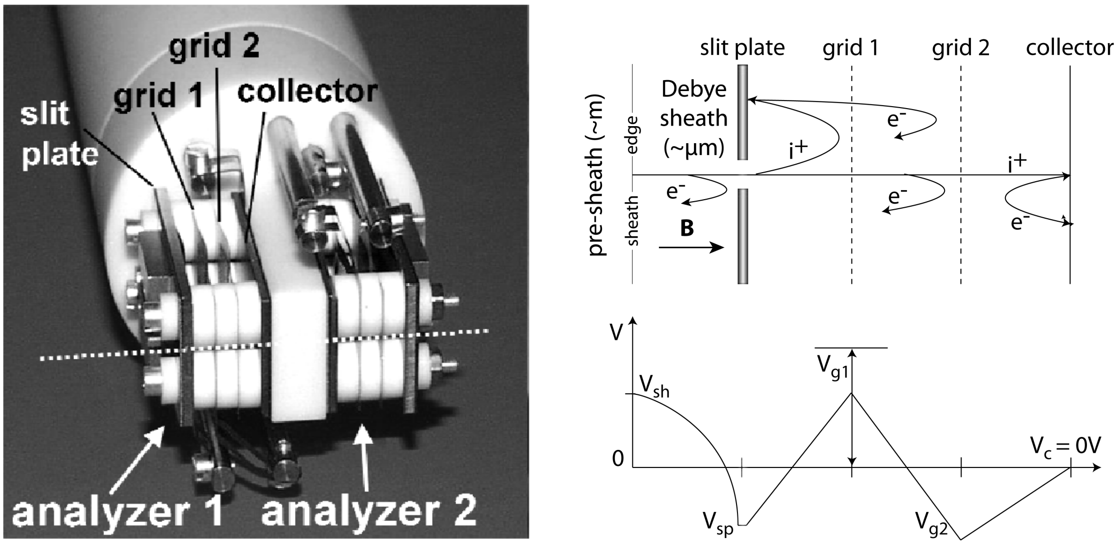

(a) (b)

Figure 3.3: *Schematic view of the main RFA components and the typical biasing scheme used for T_i and V_{sh} measurements.*

An example of an I-V characteristic obtained by the RFA is shown in Figure 3.4. It should be pointed out that sometimes it is difficult to distinguish V_{sh} exactly due to a gradual change from saturation to the decaying part of I-V characteristic. This effect is caused by the fact that the distribution of incoming ions is not a shifted half Maxwellian as sometimes assumed, but contains a population of low energy ions that diffuse into the flux tube in a continuous way all along the pre-sheath [Valsaque 02]. The typical error bar of sheath potential in ohmic plasma is ± 20V, or in the terms of electron temperature $\pm T_e$ with a typical electron temperature in the SOL of Tore Supra being $\approx$ 20eV. According to the basic sheath theory derived in Equation (2.34), the potential drop between the sheath edge and the floating metallic wall in an unperturbed plasma should be equal to $\sim 3T_e$ [Stangeby 00]. On the other hand, when the probe is connected to a powered antenna, we might expect a time-averaged sheath potential $\langle V_{sh} \rangle$ of the order of several hundred volts [Perkins 89]. To avoid inaccuracies in the sheath potential evaluation, we introduce a new variable, V_{half}, which is defined as a potential corresponding to the half of the ion saturation current, I_0, and it will serve as an upper bound of the sheath potential. Although the V_{half} is robustly defined due to the sharp decay of the ion repelling part of the I-V characteristic, it should be kept in mind that it still depends on the ion temperature.

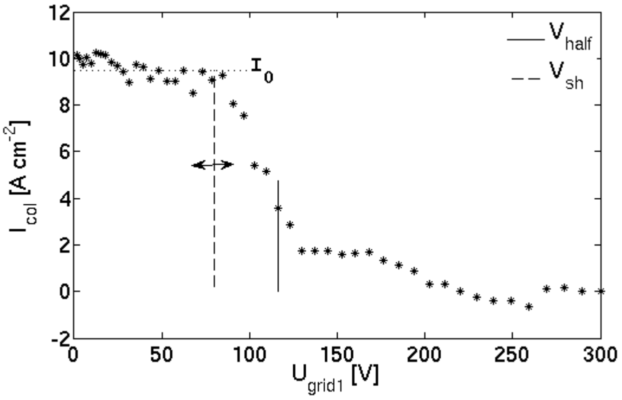

Figure 3.4: *Example of an I-V characteristic measured by the RFA.*

Besides the sheath potential and ion temperature, the RFA can provide also information about the plasma density, electron temperature and floating potential. This is provided by a sweeping voltage applied to the slit plate which then operates as a Langmuir probe. On the other hand, the RFA measurement of ion current density is less accurate in comparison with the tunnel probe due to uncertainty in the effective collecting area of the slit plate. The RFA head is protected by a carbon fiber composite housing of diameter of 40mm. The thickness of the housing is 5mm. Plasma is transmitted to the slit plate located behind a 19mm^2 orifice drilled into the CFC housing. Consequently, due to the loss of ions on the walls of these holes, the effective collecting area of the slit plates is reduced with respect to the geometrical cross section of the orifice projected along the field lines. In order to preserve biasing scheme for V_{sh} and T_i measurement, the slit plate voltage varies only during the phase where the grid 1 voltage is constant. Once the slit plate voltage is negative enough to repel most of the thermal electrons (typically -70 → -150 V depending on plasma conditions), the voltage on grid 1 starts to increase up to maximal value. The time evolution of the RFA biasing scheme together with the currents collected on the slit plate and collector, is shown on Figure 3.5.

3.2.3 Mach probe

Mach probes consist of two collectors mounted back-to-back which allows to collect charged particle fluxes separately along field lines on both sides of the probe head. The probe heads used in this thesis consist either of back-to-back tunnel probe collectors, or back-to-back retarding field analyzers whose slit plates can be biased as standard Langmuir probes. Therefore, in addition to the various novel measurements they are capable of making, both probe heads can be used as simple Mach probes.

We define the side of the probe facing the magnetic field as ‘B-side’ (generally known as the ion side or upstream side), whereas the other side will be referred as ‘A-side’ (electron

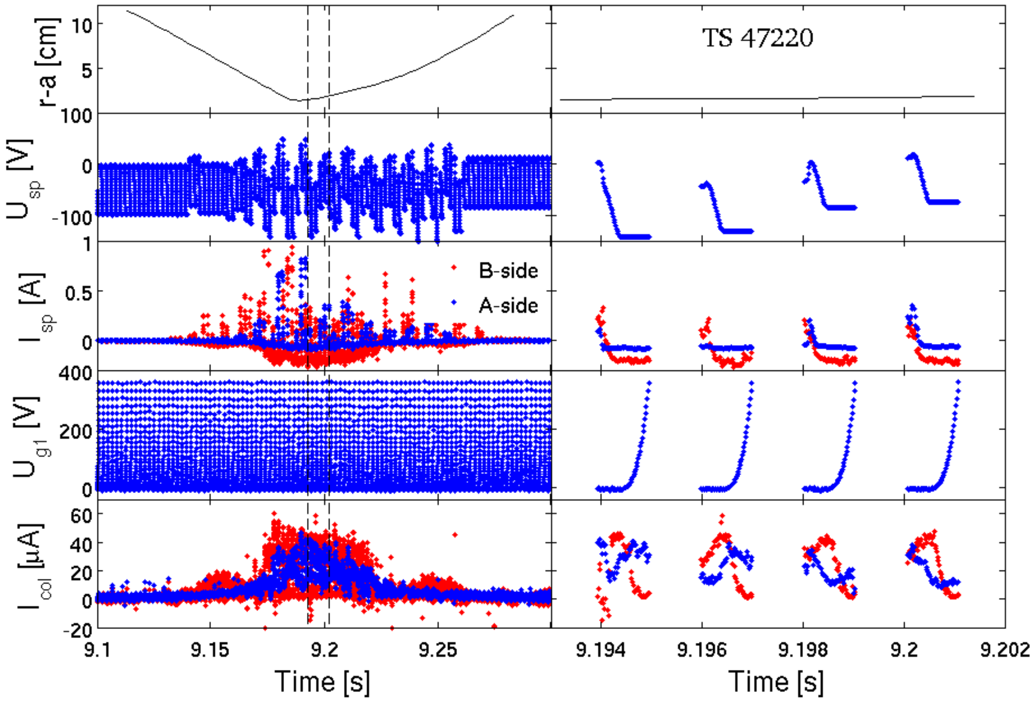

Figure 3.5: *Left: RFA signals measured during one probe reciprocation. From top to bottom: vertical distance from the LCFS, bias voltage applied to the slit plate, slit plate current, bias voltage applied to grid 1 and the collector current. Time slice of the signal defined by vertical dashed lines is shown on the right.*

side or downstream side)[1].

By using a Mach probe theory, one can deduce a parallel flow in the SOL. In the following section is given a basic overview of the Mach probe theory and its practical applications on probe data analysis. Although Mach probes are commonly used, the theory is not always correctly applied to data interpretation. Instead, crude simplifications are used. In the following, we shall quantify the errors that can be incurred.

3.3 Mach probe theory

If a Mach probe is immersed into a flowing plasma, then the parallel ion current density measured on each side of the probe will be different. The current measured on the upstream side will be larger than that on the downstream side. Mach probe theory, either fluid [Hutchinson 87] or kinetic [Chung 88], provides a simple relation between the ratio of ion currents collected on opposite sides of the probe and the parallel flow velocity.

---

[1] Notation of A-side and B-side is just our simplification as it is used on Tore Supra.

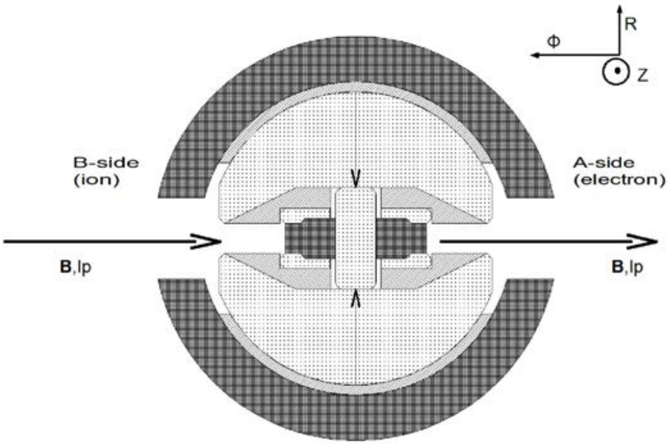

Figure 3.6: *Schematic top view of Mach probe arrangement. The ion side and electron side collectors are tunnel probes.*

3.3.1 1D Fluid model

The principal approximation used in 1-dimensional models is that the ion density n_i, velocity v_i and plasma potential ϕ at any parallel position x can be regarded as given by single function of x, representing a mean value of the parameter over the perpendicular extent of the collection region. The radius of the collection region is taken to be equal to the probe radius. The cross-field diffusion of ions into the collection region may be represented by a source S in the ion equations which determine the parallel extent of the collection region.

Probe theory is very similar to the theory of the scrape-off layer (see section 2.3.1). From the SOL model we know that the connection length is fixed by magnetic geometry, and the SOL width is determined by the radial distance that ions can diffuse during their short time-of-flight along field lines to the limiter. On the contrary, the plasma is considered to be infinite and uniform in probe theory. The width of the collection region is then given by the probe dimensions perpendicular to the field. The collection length is the parallel distance that an ion will travel in the time it takes to diffuse across the width of the collection region. The collection region of a probe is equivalent to the SOL. The same equations can be applied, only the boundary conditions of the model are different. The SOL width is determined by the connection length whereas the probe collection length is determined by the probe width. In both cases the equilibrium solution is determined by the diffusion coefficient.

The model presented here was proposed by Hutchinson more than 20 years ago [Hutchinson 87]. The pre-sheath is modelled as a one-dimensional, two-fluid plasma, which is quasineutral (see Figure 3.7). Under these conditions, we can replace Poisson's equation by the quasineutrality equation $Zn_i = n_e$ (Z denotes the ion charge). We further suppose that

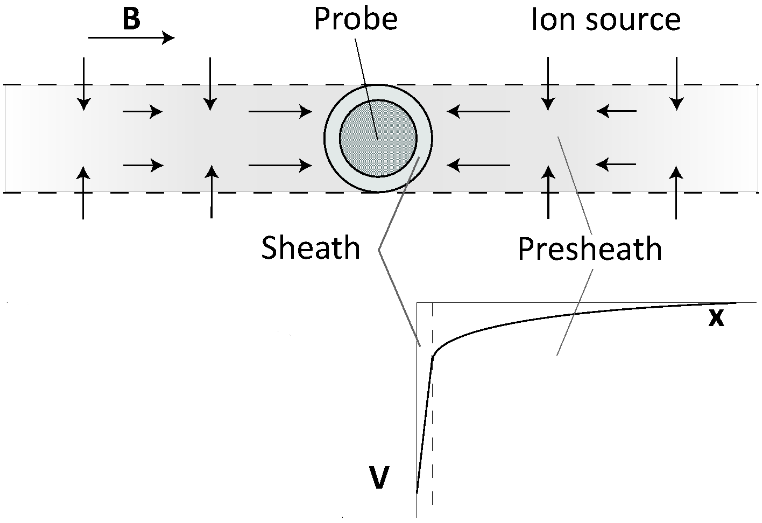

Figure 3.7: *Schematic illustration of the geometry of ion collection in a strong magnetic field. Image courtesy [Hutchinson 87].*

ions and electrons are produced at the same rate. The case in which the majority of electrons are reflected because the probe is sufficiently negative is considered. This allows to use for the electron density a Boltzmann equation[2]

$$n_e = Zn_\infty exp(e\phi/T_e) \tag{3.3}$$

Subscript ∞ here denotes quantities in the outer plasma, far away from the collection region, where the potential is taken $\phi = \phi_\infty$ to be zero. The electron temperature T_e is expressed in eV. In the following we consider that the diffusive exchange of ions between the collection region and the outer plasma is given with the frequency Ω. That is, the rate of loss of particles per unit length is $\Omega n_i(x)$ and the rate of gain is Ωn_∞. We can approximate Ω by $D_\perp/a^2$, the diffusive inverse time constant of the collection region for perpendicular diffusion coefficient $D_\perp$. The Boltzmann kinetic equation can be written as

$$\frac{\partial f}{\partial t} + (\vec{\mathbf{v}} \cdot \nabla_x)f + \frac{1}{m}(\vec{\mathbf{F}} \cdot \nabla_{\mathbf{v}})f = \Omega(f_\infty - f) \tag{3.4}$$

Our goal now is to switch from kinetic description to continuum. Equations are firstly derived in general vector form and then a transition to one-dimensional case is made. Before we start to integrate Equation (3.4) to obtain continuity equation and momentum conservation, we simplify our further calculations by multiplying Equation (3.4) with

---

[2] From the quasineutrality and one-dimensional ambipolarity assumption it yields that the electron and ion fluid velocities are equal. As a consequence, electrons cannot actually be in perfect force balance along B. However, it can be found in [Stangeby 00] that the electron + ion fluid velocity is smaller compared to the electron thermal speed, and that the electron force balance is almost exact.

invariant parameter Ψ. Now we can integrate over the velocities and obtain:

$$\int \Psi(\vec{\mathbf{v}} \cdot \nabla_x) f d^3\mathbf{v} + \int \frac{\Psi}{m}(\vec{\mathbf{F}} \cdot \nabla_{\mathbf{v}}) f d^3\mathbf{v} = \int \Psi\Omega(f_\infty - f) \tag{3.5}$$

First term on the left hand side (LHS) yields

$$\int \Psi(\mathbf{v}) v_k \frac{\partial f}{\partial x_k} d^3\mathbf{v} = \frac{\partial}{\partial x_k} \int \Psi(\mathbf{v}) v_k f d^3\mathbf{v} = \frac{\partial}{\partial x_k} \langle n\Psi v_k \rangle_{\mathbf{v}} \tag{3.6}$$

and the second term gives

$$\int \frac{\Psi}{m} F_k(t, \vec{\mathbf{x}}, \vec{\mathbf{v}}) \frac{\partial f}{\partial v_k} d^3\mathbf{v} \overset{p.p.}{=} \left[\frac{\Psi F_k f}{m}\right]_{\partial\mathcal{G}} - \frac{1}{m} \int \frac{\partial}{\partial v_k} \left[\Psi F_k\right] f d^3\mathbf{v} = -\frac{1}{m} \langle n \frac{\partial}{\partial \mathbf{v}} (\Psi \vec{\mathbf{F}}) \rangle_{\mathbf{v}} \tag{3.7}$$

We integrated per parts assuming that zero probability at the boundary $\mathcal{G}$. By combining all three above equations we obtain transfer equation in the form of

$$\frac{\partial}{\partial x_i} \langle n\Psi v_i \rangle_{\mathbf{v}} - \frac{1}{m} \langle n \frac{\partial}{\partial \mathbf{v}} (\Psi \vec{\mathbf{F}}) \rangle_{\mathbf{v}} = \int \Psi\Omega(f_\infty - f) \tag{3.8}$$

For the force $\vec{\mathbf{F}}$ we will consider only contribution of electric field neglecting the magnetic one, $\vec{\mathbf{F}} = Q\vec{\mathbf{E}}$:

$$\nabla_{\mathbf{x}} \cdot \langle n\Psi \vec{\mathbf{v}} \rangle_{\mathbf{v}} - \frac{Q}{m} \langle n\vec{\mathbf{E}} \cdot \frac{\partial \Psi}{\partial v} \rangle_{\mathbf{v}} = \int \Psi\Omega(f_\infty - f) \tag{3.9}$$

In order to obtain the one-dimensional continuity equation we put $\Psi = 1$:

$$\frac{d}{dx}(n_i u_i) = \Omega(n_\infty - n_i) \tag{3.10}$$

where $\vec{\mathbf{u}} = \langle \vec{\mathbf{v}} \rangle$. Similarly, to derive the momentum equation, we put $\Psi = mv$:

$$\frac{\partial}{\partial x_x}(nm\langle v_l v_k \rangle_{\mathbf{v}}) = nQ\vec{\mathbf{E}}_{\mathbf{l}} + \int m v_l \Omega(f_\infty - f) d^3\mathbf{v} \tag{3.11}$$

Defining the chaotic (thermal) velocity as $\vec{\mathbf{w}} \equiv \vec{\mathbf{v}} + \vec{\mathbf{u}}$, Equation (3.11) yields:

$$\frac{\partial}{\partial x_x} T_{lk} = nQ\vec{\mathbf{E}}_{\mathbf{l}} + \int m v_l \Omega(f_\infty - f) d^3\mathbf{v} \tag{3.12}$$

where tensor T_{lk} consits of two parts - dynamic pressure D_{lk} and pressure tensor P_{lk}:

$$T_{lk} = nmu_l u_k + nm\langle w_l w_k \rangle_{\mathbf{v}}$$

For the one-dimensional case we can write

$$\frac{d}{dx}(n_i m_i u_i u_i) = n_i QE - \frac{dp_i}{dx} + m_i\Omega(n_\infty u_\infty - n_i u_i) \tag{3.13}$$

The derivative of the first term on the LHS can be rewritten as:

$$\frac{d}{dx}(n_i m_i u_i u_i) = m_i n_i u_i \frac{du_i}{dx} + m_i u_i \frac{d}{dx}(n_i u_i) \tag{3.14}$$

We can now substitute for the derivative of the second term on the RHS from continuity equation (3.10) and obtain

$$m_i n_i u_i \frac{du_i}{dx} + m_i u_i \Omega (n_\infty - n_i) = n_i Q E - \frac{dp_i}{dx} + m_i \Omega (n_\infty u_\infty - n_i u_i) \tag{3.15}$$

To be able to solve our equations, it is necessary to eliminate the pressure from above equation. This can be achieved if we consider definition of electric field $E = -d\phi/dx$ and substitute it from Equation (3.3):

$$\frac{d\phi}{dx} = \frac{T_e}{e n_i} \frac{dn_i}{dx}$$

Now we can write:

$$\frac{n_i Q E}{m} - \frac{dp_i}{dx} = \frac{-n_i Z e}{m_i} \frac{d\phi}{dx} - \frac{T_i}{m_i} \frac{dn_i}{dx} - \frac{n_i}{m_i} \frac{dT_i}{dx} = -\frac{dn_i}{dx} \left(\frac{Z T_e + T_i}{m_i} \right)$$

Finally, the momentum equation can be written as:

$$n_i u_i \frac{du_i}{dx} = -c_s^2 \frac{dn_i}{dx} + \Omega n_\infty (u_\infty - u_i) \tag{3.16}$$

In order to close the system of equations, we ignored term dT_i/dx arising from dp_i/dx during the derivation of this equation. This assumption does not of course represent reality where $dT_i/dx \neq 0$. However, it was shown that a full kinetic model [Chung 88] gives nearly exactly the same result as the simple isothermal fluid model [Hutchinson 87], indicating that ion temperature gradients play a negligible role in presheath dynamics.

The sound speed c_s corresponding to this approximation is given by

$$c_s^2 = \left(\frac{Z T_e + T_i}{m_i} \right) \tag{3.17}$$

Equations (3.10) and (3.16) are the pre-sheath equations we want to solve. It is worth to notice that if we write the equations (3.10) and (3.16) in matrix form

$$\begin{pmatrix} u_i & n_i \\ c_s^2 & n_i u_i \end{pmatrix} \begin{pmatrix} n' \\ u' \end{pmatrix} = \begin{pmatrix} \Omega (n_\infty - n_i) \\ \Omega n_\infty (u_\infty - u_i) \end{pmatrix} \tag{3.18}$$

the determinant of the coefficient matrix provides the Bohm criterion:

$$det \begin{pmatrix} u_i & n_i \\ c_s^2 & n_i u_i \end{pmatrix} = n_i (u_i^2 - c_s^2) \tag{3.19}$$

To solve Equations (3.10) and (3.16) we adopt Hutchinson's non-dimensionalizing transformation

$$n = \frac{n_i}{n_\infty} \, , M = \frac{u_i}{c_s} \, , y = \int_0^x \frac{\Omega}{c_s} dx' \tag{3.20}$$

which leads to the final equation of solution in the following form

$$\frac{dn}{dM} = n \cdot \frac{(1-n)M - (M_\infty - M)}{(M_\infty - M)M - (1-n)} \tag{3.21}$$

Applying boundary conditions appropriate to the unperturbed plasma density and flow speed far from the probe, Equation (3.21) is integrated numerically from infinity to the probe surface where the Mach number attains the value M = 1, as given by the Bohm criterion.

3.3.2 Application of Mach probe theory

Within this section, we will use the above described Mach probe theory and apply it to our probe data treatment. The parallel ion current density is calculated by dividing the ion saturation current by the geometrical projection A_{geo} of the probe along the magnetic field lines [Gunn 08]:

$$J_i = \frac{I_{sat,i}}{A_{geo}} \tag{3.22}$$

The quantities J_i, T_e and V_f are measured by each probe, then the values on both side of the probe are used to calculate the density and Mach number. The total saturation current collected by both sides of the Mach probe can be expressed as:

$$\frac{I_{sat}}{A_{geo}} = \beta_u n_\infty c_s + \beta_d n_\infty c_s \tag{3.23}$$

where coefficient $\beta = \beta_u + \beta_d$ needs to be found, and the total current density consists of an upstream and a downstream component: $\frac{I_{sat}}{A_{geo}} = J_i = J_i^u + J_i^d$. Both components have to be considered, because the source location responsible for the parallel flow causes unequal redistribution of the current density on both sides of the probe. In order to find out what relation between the both sides of the probe is the most convenient, we have to solve the Equation (3.21). The Equation (3.21) is solved for n as a function of Mach number M, with given condition M_∞ by using a Runge-Kutta method. The solution is plotted in Figure 3.8. Each line corresponds to a different value of M_∞. Each curve starts at the point $n = 1$, $M = M_\infty$ and ends at $M = 1$. The initial values give the information about the external flow field, where negative M_∞ represents the downstream side of the probe and M_∞ positive corresponds to the upstream side of the probe, while the end points provide the value of the density at the sheath edge. As was shown above, the velocity at the sheath edge is equal to the sound speed, the density also gives the ion flux into the sheath and hence to the probe.

The solution of our problem is shown on Figure 3.9, where is plotted the sheath edge current density normalized to $n_\infty c_s$ as a function of M_∞. As can be seen, the optimal value found by Hutchinson for parameter β is 0.35 whereas Stangeby's model predicts 0.5

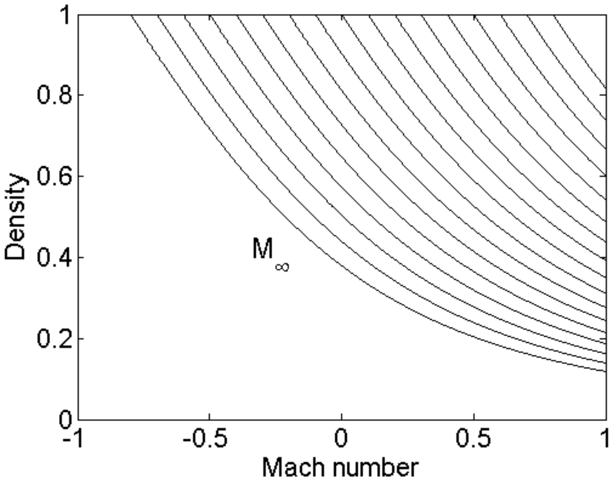

Figure 3.8: *Solution of the density as a function of Mach number in the pre-sheath of a Mach probe. Each curve corresponds to a different value of* M_∞ *starting at the point* $n = 1$, $M = M_\infty$ *and ending at* $M = 1$. *The initial values give the information about the external flow field.*

[Stangeby 00]. In the frame of data analysis, the most commonly used method among Mach probe users is to take an average of the currents collected on the both sides of the probe as was advocated by Hutchinson himself in his seminal paper. This case is represented on Figure 3.9 by red line. As can be seen, this approach is sufficiently accurate for small flows, $|M_\infty| < 0.2$. But for higher flows the difference from the solution could be more than 15%. A better way is to use a square root of the product of $J_i^u J_i^d$ (shown by green curve) which provide more accurate data representation with only small deviation for large flows.

The electron density calculated by taking into account the ion flow is then [Hutchinson 87]:

$$n_e = \frac{\sqrt{J_i^u J_i^d}}{0.35 e c_s} \tag{3.24}$$

where ion sound speed c_s is defined as

$$c_s = \frac{\sqrt{e(T_e + T_i)}}{m_i} \tag{3.25}$$

The T_e and T_i are the electron and ion temperature, respectively. It is important to say, that in real measurements an average value of temperature measured on both sides of the probe is used. The parallel Mach number can be derived from the Hutchinson model [Hutchinson 88] according to the following formula:

$$M_{||} = 0.4\, ln\left(\frac{J_i^u}{J_i^d}\right) \tag{3.26}$$

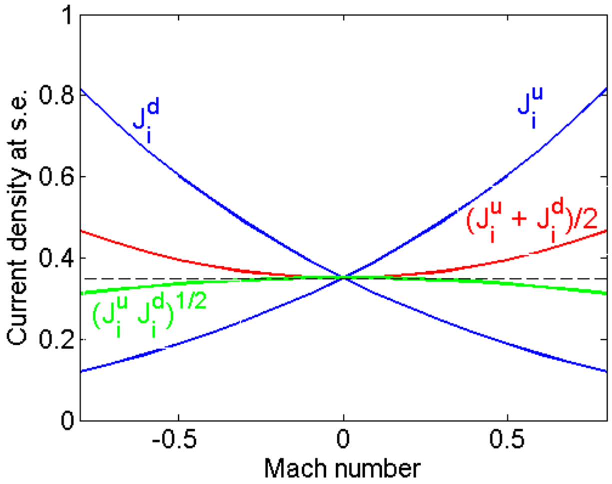

Figure 3.9: *Normalized sheath edge current density as a function of external flow Mach number.*

3.3.3 Practical demonstration

Although Mach probes are widely applied for SOL measurements, the majority of researchers use the simple approximate formula for $J_{sat} = en_ec_s$ (sometimes with the factor 1/2 of Stangeby [Stangeby 00]). In reality, the sheath edge current density depends on the unperturbed flow speed of the plasma far away from the probe (outside the pre-sheath). It will be shown below how neglecting the corrections to J_{sat} imposed by the flow can lead to erroneous interpretation of probe data (for example structures in density profiles can be deduced where in fact none exist if the Mach probe theory was correctly applied).

Let us now demonstrate one of the advantages of the Mach probe which turns to be very important for RF-induced SOL modifications study. If the probe is magnetically connected to a powered ICRH antenna, the radial profile of parallel ion saturation current density $J_{||}$ exhibits structures in the perturbed zone and is no longer monotonically decreasing as during the ohmic phase. The observed structures on $J_{||}$ are fairly different on the two sides of the probe (see Figure 3.10). If the density was evaluated only by using $J_{||}$ from one side of the probe, the resulting density profile would be characterized by a hole or a bump depending on chosen probe side. To correctly unfold the influence of this effect, it is necessary to combine the measurements of $J_{||}$ from both sides of the probe as defined by Equation (3.24).

It is important to emphasize the meaning of these curves. The ion saturation current collected by one side of a Mach probe is given by the product of the ion sound speed and the sheath-edge density. The latter quantity depends on the potential drop in the pre-sheath via the Boltzmann relation, and the precise magnitude of the potential drop is determined by the Mach number of the unperturbed parallel flow, as outlined earlier

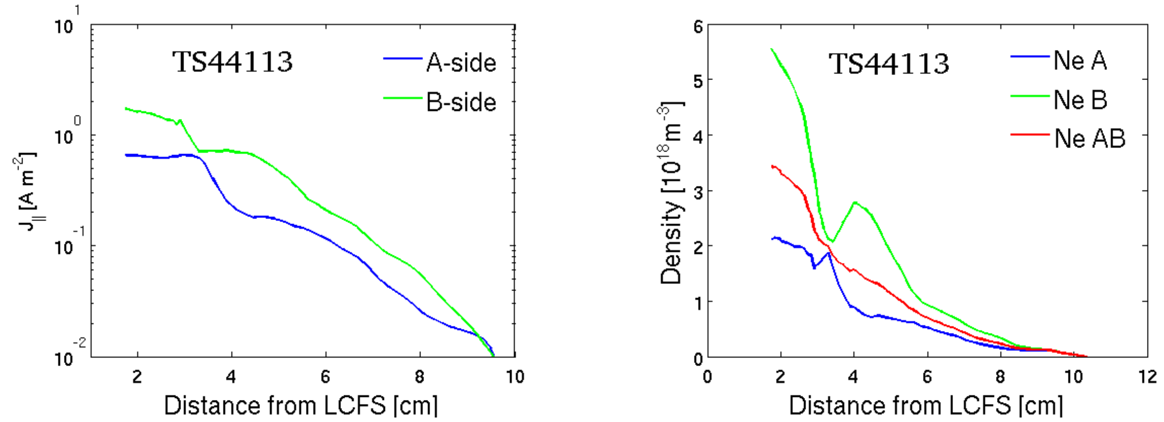

(a) Current

(b) Density

Figure 3.10: *(a) Radial profile of parallel ion saturation current density $J_{||}$ measured on both sides of the probe equipped with tunnel probe collectors. (b) Resulting density calculated either by using only one side on the probe (blue, green) or by combining both sides (red) with the correct application of Hutchinson's Mach probe theory.*

in Section 3.3.1. Therefore, the structures observed on the ion current profiles are due to radial variations of both density and flow. When the data are analyzed using Mach probe theory, the resulting density profile is monotonic compensating perturbations observed individually on each side of the probe.

The ratio of the ion currents measured on both sides of the probe is seen to vary significantly. This indicates that there are strong radial variations of parallel flow which are responsible for the structures observed on each side of the probe. These flow variations are a new observation with potentially important consequences. They will be discussed in more detail in Section 5.3. It should be stressed that there is a priori no reason to exclude the possibility of stationary radial structures of plasma density. The point here is to demonstrate how important it is to carefully consider all aspects of the measured data. Mach probe theory is applied here for the simple reason that there is no other theory available, and there is a wide body of experimental evidence that supports its validity. While it is intuitively satisfying to find a monotonic density profile, it is certainly possible that Mach probe theory is not valid, in which case one would have to find an explanation for the existence of such improbable structures. Not only would one need to identify a mechanism where coherent, stationary structures are formed near the antenna, but they would have to survive propagation 12m along the field lines from the antenna to the probe. Both perpendicular ion transport (the same transport that is responsible for the formation of the SOL) and magnetic shear would act to smear out any stationary structures.

3.4 Operation of the probes at Tore Supra

Tore Supra is equipped with two reciprocating probe drives located in top ports of the vessel situated at 40° and 160° toroidally. They make vertical strokes along the cord R = 2.53m. The maximum plunge depth is 0.46m below its resting point. Probe is immersed into the SOL with speed $1.5 m \cdot s^{-1}$ which is sufficiently fast enough to prevent the probe from overheating due to the strong energy accumulation. To help to protect the probe, a dedicated feedback system is routinely used allowing probe operation even in high power discharges [Gunn 11b].

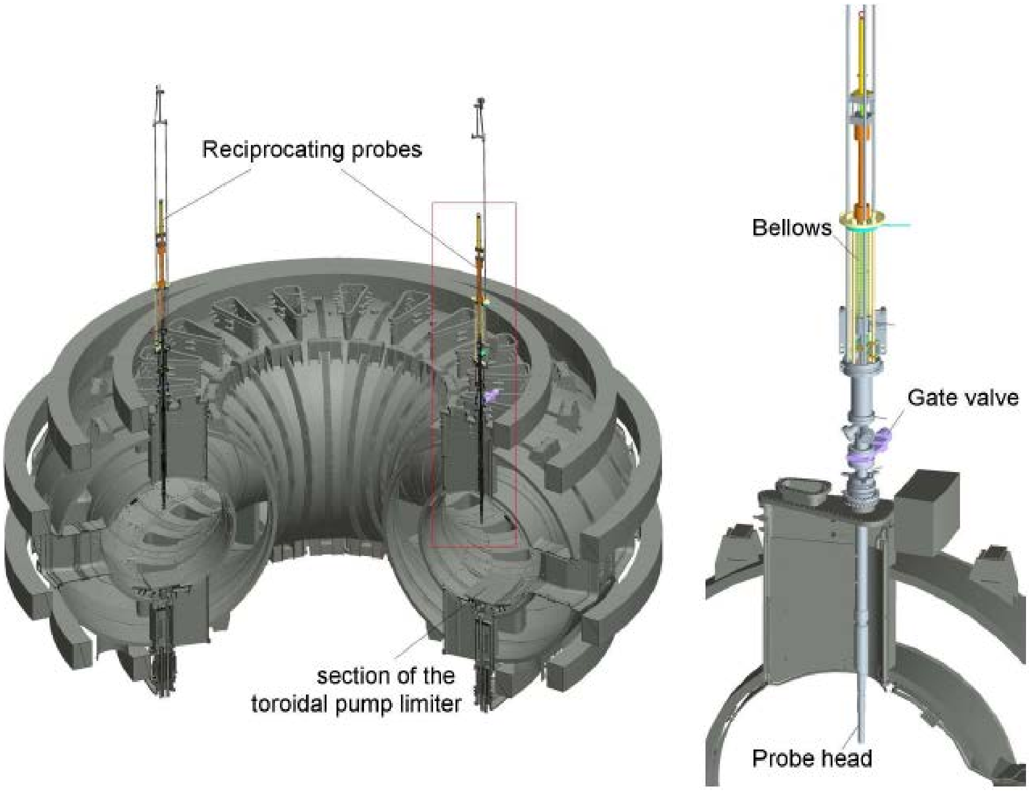

Figure 3.11: *Drawing of the Tore Supra chamber and magnetic coils system with locations of two reciprocating probe drives.*

Measurement of the high potentials that are induced by a powered ICRH antenna to which the probe might be magnetically connected, is possible only due to a usage of a reliable real-time feedback system. For the proper probe operation, there is a necessity to control in real-time the probe movement with high accuracy. That is to say, the feedback system has to react merely immediately to the changes of plasma position. In most cases the plasma position is pre-programmed by a tokamak operator, so the depth of the probe plunge can be adjust accordingly. However, if an unexpected event occurs during the probe plunge, the control of the absolute probe position relies purely on the feedback system. In the following paragraphs we will describe how the feedback system works and how are TS probes operated.

The probe operation is controlled by two dedicated computer systems. The first, called ‘DLANG’, is responsible for data acquisition and control of power supplies and it is the main system that is fully adjustable by a probe operator. The second one controls the motion of the probe holder via a hydraulic piston and is called ‘DPOLO’ that serves for magnetic field diagnostics [Moreau 09]. To run an experiment with probes, the probe operator is obliged to set in the main control software (called ‘Top’) time triggers at which the probe should be inserted into the plasma. Due to the superconducting coils allowing TS to perform long discharges, several plunges can be attained. In addition, it is necessary to specify the desired depth of given probe reciprocation (which can differ from plunge to plunge). The depth is not given in absolute values, but as a relative position to the last closed flux surface in accordance with the projected discharge scenario. This has to be done before the discharge and an example will be demonstrated later on when describing a mapping experiment - section 5.3.1. Once discharge starts, the probe position is measured instantaneously by DLANG at a frequency rate of 2kHz and shared by a network memory where DPOLO can read it in order to control in real-time feedback loop of the probe movement. When a pre-programmed trigger time is reached, DLANG sends a signal to start probe reciprocation process upon which DPOLO immediately launches the probe towards the plasma to a given distance with respect to LCFS. The whole process of reciprocation is very fast. The typical exposed time that probe spends in the plasma is < 200ms as a precaution of excessive heating. If DPOLO detects during the probe movement any suspicious event that could end up the discharge in unexpected way, it sends a signal to abort probe reciprocation and push it back to its resting position as soon as possible. An extensive overview of the probe system on Tore Supra is given in [Gunn 11b].

3.4.1 Feedback system

If the probe is magnetically connected to a powered ICRH antenna, the measured floating potential increases to values up to 200V depending on the poloidal magnetic connection and antenna power (chapter 5). On the other hand, the floating potential on the other side of the probe which is connected via the high field side to the bottom toroidal limiter, remains unchanged. Therefore, the biasing scheme of each side of the probe has to be done separately. By default, the biasing range of the applied voltage varies from -200V to 20V. The voltage ramp has a non-linear waveform in order to provide maximal resolution near the anticipated floating potential. The bias voltage waveforms are adapted separately by real-time analysis of the I-V characteristics. If the feedback system detects a difference between two following characteristics, it adds an offset to upcoming bias waveform in order to keep the floating potential in the biased range. The limits set for the feedback system is in the range of -1.5 $< I/I_{sat} <$ -0.5. An example of the functionality of the feedback system is demonstrated on Figure 3.12. The graph shows time evolution of the applied bias voltage over one plunge (top). The time evolution of the measured floating potential, as well as the probe position, is shown on the bottom. Variation of ramp up voltage is plotted on the right. As can be seen, the feedback reaction time on V_{float} modulation is very fast, $t_f \approx 5ms$. If the time variation of the V_{float} is fast enough, then the feedback response is insufficient and information about the floating potential is lost. In that case one can switch the probe into a 'floating' mode without necessity of sweeping and measure it instantaneously.

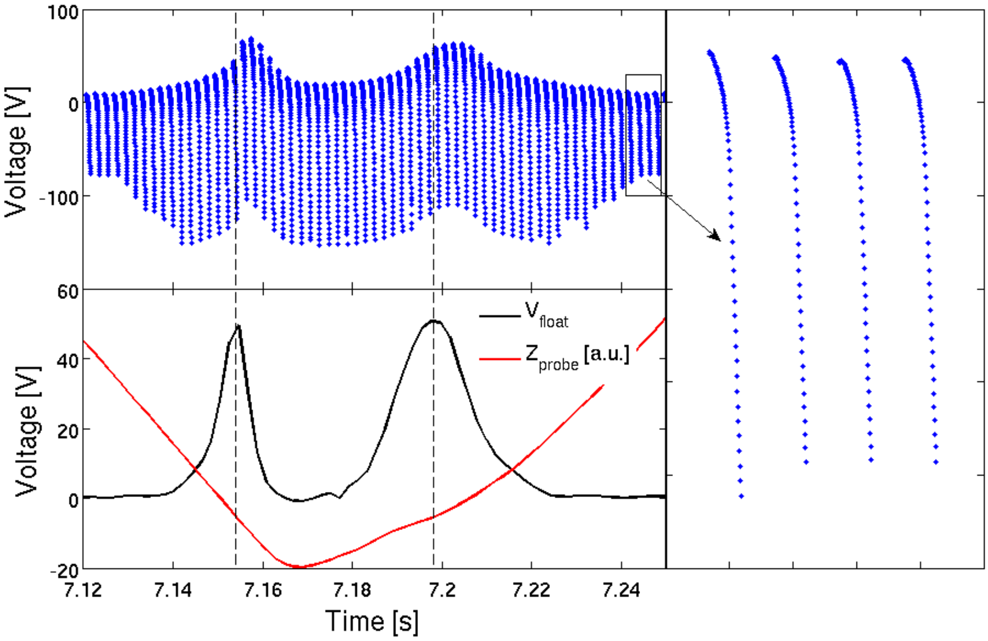

Figure 3.12: *Time evolution of applied bias voltage on the B-side (electron) of the probe during a discharge with a powered ICRH antenna to which the probe is magnetically connected to (top). Corresponding measurement of the floating potential is plotted on the bottom - black curve. The probe position is then plotted by red curve and an example of few voltage ramps is shown on the right.*

3.4.2 Modes of operation

In general, any of the Langmuir probes, whether they be tunnel probes or RFA slit plates, can operate in three different regimes depending on the acquisition mode:

- **sweeping mode:** The potential applied to the collector is swept in time in order to obtain a current-voltage characteristic. Exponential part of the I-V characteristic provides information about electron temperature and floating potential of the probe. Plasma density can be derived directly form the ion saturation part of the curve with a degree of uncertainty that depends on the type of collector being used (RFA or tunnel probe).

- **floating mode:** The collected current is fixed to zero so that the probe potential is imposed by the ambipolar interaction with the plasma to give the measure of the floating potential.

- **saturation mode:** The probe voltage is fixed to a strongly negative value (-200V) to collect only current that is equalled to the ion saturation current.

For standard TS measurements, without a need of high temporal data resolution, sweeping mode is sufficient with a sampling rate of 2kHz. On the other hand, for turbulence or fluctuation studies, it is more convenient to switch the probe either to floating or saturation mode depending of the topic of interest.

During the 2011 experimental campaign, probe measurements obtained during the ICRH discharges on flux tubes that are magnetically connected to powered antenna showed that the radial gradients of the measured floating potential V_{float} are so steep that the standard sweeping mode cannot provide measurements of the V_{float} in the perturbed zones due to the probe motion through the structures (about 1 mm / ms). For that reason, it was decided to connect the probe, for the last week of the experimental campaign (25.-29.8.2011), to the fast data acquisition system running at 1MHz (DTURB) in order to obtain better temporal resolution of the measured signal [Fedorczak 10]. During that week, probe was operating only in saturation and floating modes. In that case, the reconstruction of the I-V characteristic is not possible and the information about T_e as well as n_e is lost. To get an estimate about plasma density, one can use Hutchinson formula - Equation 3.26 while assuming a reasonable value for T_e. Measurements performed on TS with retarding field analyser [Kočan 08] showed that for typical ohmic TS discharge the ion temperature can be estimated as $T_i = 2T_e$ with electron temperature being typically $T_e \sim 20$eV. T_e measured during the RF heated discharges increases up to $T_e \sim 40$eV.

The estimate of the uncertainty of the density evaluation is shown on Figure 3.13. Radial profiles of the n_e calculated according to Equation 3.24 for different values of T_e are plotted on the Figure 3.13. As can be seen, the density dependence on T_e, T_i is rather strong close to the LCFS and error-bar can reach up to 30% considering higher ion temperatures, $\tau = 2 \rightarrow 4$.

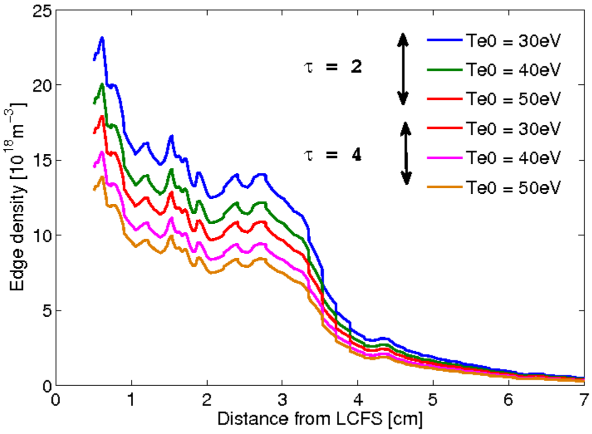

Figure 3.13: *Variation of the edge density for different values of* T_e *and ion-to-electron ratio* τ.

Summary

This chapter was devoted to the description of Langmuir probes. It is important to note that all measurements presented in this work were obtained from Mach probe either consisting of two tunnel probes (labelled from now as tunnel/Mach probe) or two RFAs (labelled as RFA/Mach probe). Among the main advantages of the tunnel probe is its capability to measure correctly the parallel ion current density. This is attained by its unique concave shape that ensures the immunity of the probe to sheath expansion effects and hence leads to exact knowledge of the effective collecting area of the tunnel probe. The positive aspect of the RFA is its ability to provide, in addition to the tunnel probe, information about ion temperature and sheath potential. While the tunnel probe appears to be a very robust, well-calibrated probe, the RFA's main weakness (and we will show later in chapter 7 that this is not the only one) lies with the housing of the RFA inside CFC head causing incorrect estimation of effective collecting area due to ion collection of the housing walls as they pass it towards the RFA slit plate. In order to be able to study plasma flows in the SOL together with correct data interpretation, both kinds of probes are exclusively used in the Mach probe arrangement. Mach probes, in contrast to conventional probes that collect charges simultaneously from both directions along the magnetic field lines, have directional sensitivity. In their simplest form, Mach probes consist of two Langmuir probes mounted back-to-back on either side of an insulator so as to monitor separately the charged particle fluxes that approach the probe along field lines. When connected to an active antenna, the ion saturation current to the two sides of a Mach probe exhibit stationary radial structures (peaks on one side and troughs on the other). Within the context of Mach probe theory, such structures could be due to radial variations of parallel flow rather than density.

Chapter 4

Ion Cyclotron Resonant Heating

4.1 Introduction

The basic principle of plasma heating in the ion cyclotron range of frequencies was briefly described in the section 1.6.1. Here, a detailed look will be given with an emphasis on heating scenarios, various designs of Faraday screen used on Tore Supra and most importantly, on the effects of the active antenna on surrounding plasma and objects which are magnetically connected to it.

For rf heating method, several different conditions have to be fulfilled in order to reach an efficient plasma heating by wave in the ion cyclotron range of frequencies. First of all, a good plasma-antenna coupling with a minimization of spurious effects has to be ensured. In addition, it is not only necessary to launch the waves, but the waves must also propagate into the plasma to a specific target location, be absorbed there and transfer its energy to plasma particles. In the ion cyclotron range of frequencies, two types of cold plasma waves can propagate and carry energy from plasma edge to the bulk core: the *slow* wave and the *fast* wave [Stix 92]. The interesting characteristic for our work of the slow wave is that the slow wave exhibits an electric field parallel to magnetic field, which permits to evaluate the RF potential driving the sheath effects. The role of the fast wave is to transfer the energy into the plasma with a quasi perpendicular propagation - Figure 4.1. The wave is launched from the antenna strap at the low field side far from the absorption zone. In order to describe the propagation of both fast and slow waves, a cold plasma approximation can be used. The approach is valid when the phase velocities of the waves are larger then the thermal velocity of the background plasma. In this approximation thermal effects can be neglected. This is quite sufficient for a wide range of wave phenomena. Under this assumption, the wave dispersion relation can be written as:

$$An_{\perp}^4 - Bn_{\perp}^2 + C = 0 \tag{4.1}$$

where $A = S$, $B = RL + PS - n_{//}^2(P + S)$ and $C = P(R - n_{//}^2)(L - n_{//}^2)$. where R, L, S,

P are all part of a dielectric tensor. For the purposes of this thesis, the most important is the parallel component of the dielectric tensor P that is associated with rf sheaths effects.

$$\varepsilon_{||} = P = 1 - \frac{\omega_{pi}^2}{\omega_0^2} \tag{4.2}$$

Every solution of dispersion relations gives two roots - fast and slow wave. Considering typical densities in the core of tokamak plasmas, $\omega_{pi} \gg \omega_{ci}$, elements of dielectric tensor can be simplified as

$$\begin{aligned}
R &= \frac{\omega_{pi}^2}{\omega_{ci}^2(1 + \omega_0/\omega_{ci})} \gg 1 \\
L &= \frac{\omega_{pi}^2}{\omega_{ci}^2(1 - \omega_0/\omega_{ci})} \ll -1 \\
S &= \frac{\omega_{pi}^2}{\omega_{ci}^2(1 + \omega_0^2/\omega_{ci}^2)} \ll -1 \\
D &= -\frac{\omega_0}{\omega_{ci}} S \gg 1
\end{aligned} \tag{4.3}$$

Assuming $|n_{\perp F}^2| < P$ and $|n_{\perp S}^2| \sim P$, solution of dispersion relation (Eq. 4.1) in the ion cyclotron range of frequencies gives:

$$Fast\,wave\ :\ \ n_{\perp F}^2 = (R - n_{//}^2)(L - n_{//}^2)(S - n_{//}^2) = (S - n_{//}^2) - D^2/(S - n_{//}^2) \tag{4.4}$$

$$Slow\,wave\ :\ \ n_{\perp S}^2 = P(1 - n_{//}^2/S) \tag{4.5}$$

Because the squared transverse refractive index of the FW is negative, the wave remains evanescent until it reaches the cut-off, $n_{//}^2 = R$. This evanescent layer imposes strong technological constraints on ICRH antenna due to the necessity of antennas being placed very close to plasma leading to issues with PWI mainly associated with the generation of the electric field by slow wave component. The wave transmission depends strongly on the plasma density which determines the coupling efficiency. If the density is too low, the power transmission from the wave to plasma is weak. Once the cut-off layer is reached, the wave can then propagate freely towards the plasma core where the wave is dumped on resonant particles. That is to say on particles with the same oscillating frequency (including Doppler effect that cause broadening of the particle oscillation frequency with respect to its movement) as the wave frequency (Equation 4.6) and its energy is further redistributed through particles collisions to the bulk plasma.

Over the years, a few approaches have been developed to obtain absorption on the ions such as: heating of minority species, higher ion cyclotron harmonic damping or direct coupling to the electrons parallel motion. Assuming a plane wave with a harmonic

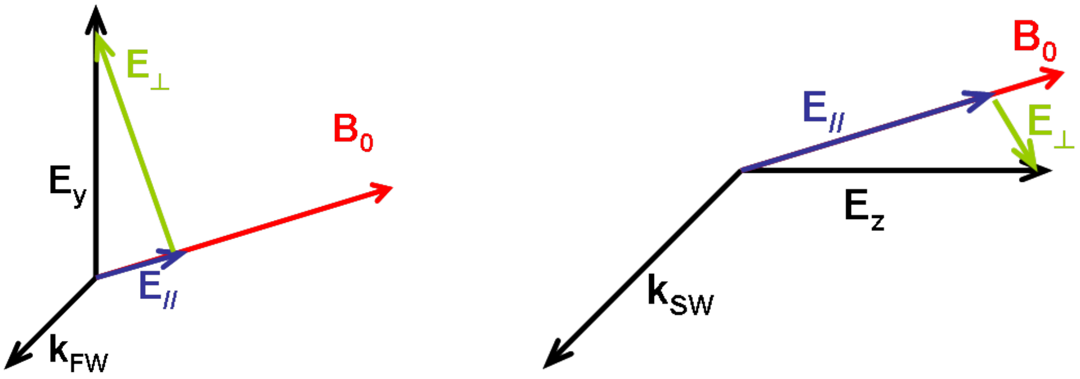

(a) Fast wave (b) Slow wave

Figure 4.1: *Direction of the electric field components of the FW and SW with respect to magnetic field and wave vector.*

oscillations in form of $exp(-i\omega_0 t + i\mathbf{k}\cdot\mathbf{r})$, the resonance condition for a particles of mass m_i, charge q and constant parallel velocity $v_{||i}$ is given by

$$\omega_0 - p\omega_{cs} - k_{||}v_{||s} = 0 \tag{4.6}$$

where $\omega_{cs} = Q_s B_0/m_i$ is the cyclotron frequency of specie s and the integer p is the cyclotron harmonic number. Heating at higher harmonics occurs for $p > 0$ and dumping on electron for $p = 0$. Last term in the Equation (4.6) is the Doppler shift. For present tokamaks, the wave frequency f_0 is in the range of 25-130MHz (precisely 15.25MHz per Tesla for hydrogen ions). The wave can match the local ion cyclotron frequency on the so-called ion cyclotron resonant layer which radial position can be defined as: $R_{ci} = pR_0 q_i B_0/m\omega$, where magnetic field contains only toroidal component, poloidal field is neglected. In a tokamak the toroidal magnetic field decreases radially as 1/R. Thus the resonant zones can be easily adjusted by changing either the magnetic field strength or the wave frequency.

It turns out that heating by ion cyclotron waves is not efficient for single species plasma. However, situation can be modified by adding a small concentration of resonant ions. The polarization is set by the majority component, so the wave has partially correct polarization for the resonant ions and can be absorbed. Hot minority ions thermalize either on bulk ions or electrons, depending on their energy [Bécoulet 96]. This method is called minority heating scenario. The common mixture on TS is the hydrogen-deuterium with hydrogen as a minority element. The concentration of hydrogen atoms varies at TS from 2 - 20%. The resonance of such a mixture occurs on so-called ‘two-ion hybrid’ layer, located between ω_{cH} and ω_{cD}:

$$\omega_{ii}^2 = \omega_{cH}\omega_{cD}\frac{n_H\omega_{cD} + n_D\omega_{cH}}{n_H\omega_{cH} + n_D\omega_{cD}} \tag{4.7}$$

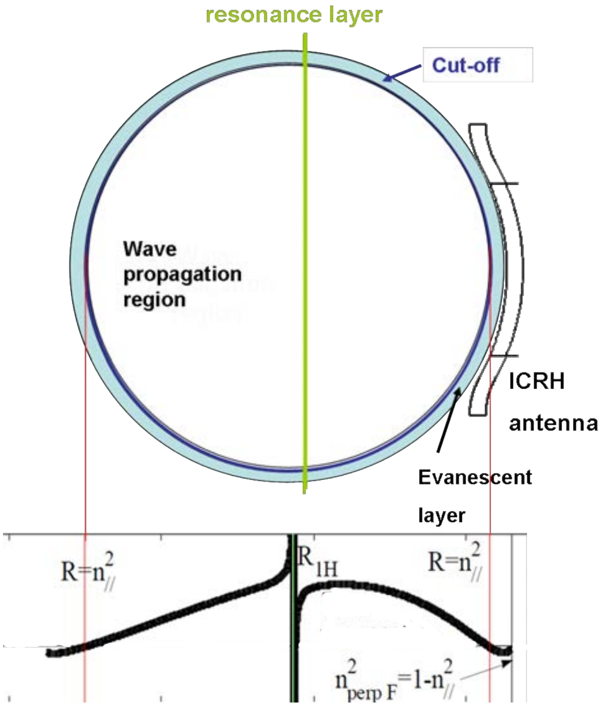

Figure 4.2: *Fast wave propagation domain and the resonance layer in a tokamak plasma.*

where n_H and n_D is hydrogen and deuterium density, respectively. This is the most used heating technique in the ion cyclotron range of frequencies and some TS records were achieved during this scenario, e.g. 4MW injected by a single antenna or 10.4MW by the whole ICRH system. As the concentration of the minority species increases, the polarization becomes less favourable for the resonant ions. Nevertheless, if the concentrations of both mixtures are comparable, the fast magneto-sonic wave can be converted to a short wavelength ion Bernstein wave (IBW). The IBW is then absorbed by electron via Landau damping. Plasma heating is also possible at higher harmonics. Main advantage here is that there is no screening effect on the cyclotron layer, allowing the wave to damp even in the single-ion plasma. The overview of above mentioned heating scenarios can be found in [Bécoulet 96]. An introduction to the ICRH system used on Tore Supra is given in the next section.

4.2 ICRH system on Tore Supra

The TS tokamak is equipped with three ICRF antennas. As it will be shown later, one of these antennas is equipped with the new type of Faraday screen. They are placed in horizontal ports Q1B, Q2B and Q5B (at 40°, 100° and 280° toroidally - Figure 4.3a). Position of each antenna plays an important role because it defines the connection length between the antenna and the probe. The maximum heating power of each antenna is

4MW. Typical plasma mixture consists of deuterium with a small amount of hydrogen (2 - 20% in TS). Most common heating method used on TS is the minority heating scenario. The antennas consist of phased arrays of 2 straps. The phasing between the two straps is usually chosen $\phi = 180°$ but can be varied. The vertical strap extension is 260mm above and below the equatorial plane of the torus. Each strap is embedded in a metallic box, partially closed on the plasma side by a Faraday screen. The vertical box extension is 300mm on either side of the equatorial plane. The antenna box is protected from the plasma scrape-off layer on both sides by actively cooled limiters.

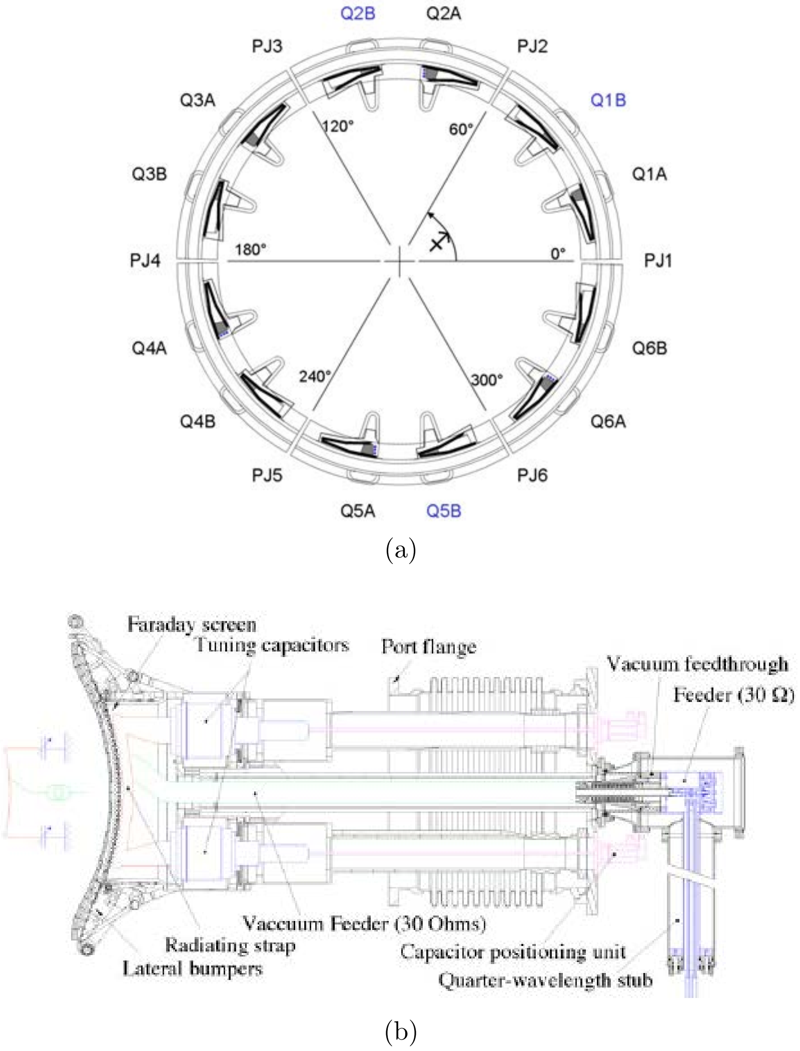

(a)

(b)

Figure 4.3: *(a) Schematic of the position of ICRH antennas (marked by blue color) in the mid-plane port plugs of the TS tokamak. (b) Cutaway view of the main components of RDL antenna used on Tore Supra.*

The vertical limiter extensions are about 550mm on both sides of the equatorial plane. Favourable position of the antennas with respect to the probes allows us to choose such a magnetic configuration that permits the probe to be magnetically connected to the whole poloidal structure of an antenna. The whole antenna structure, including side limiters, is mounted on a radially movable arm capable of a stoke of 300mm inside the chamber. Each of the antenna launcher is fed by two transmission lines connected to rf generator (one per antenna strap). Antenna front parts of each launcher are actively cooled in accordance with TS operational requirements. All antennas installed during the 2011 experimental campaign are based on RDL concept (Figure 4.3b) - technical specifications of the complete ICRF facility on TS can be found in [Colas 09].

The TS ICRH system allows to operate in five main frequency bands, centred at $f_0 =$ 42, 48, 57, 63, or 76 MHz, each with a width of 2 MHz. The choice of both frequency and magnetic field allows many different kinds of scenario, which are described on Figure 4.4. The minority heating scenario (used during the experiments presented in this work) is represented by grey boxes, the fast wave electron heating (FWEH) scenario corresponds to dark grey boxes, the FWEH scenario without any layer inside the plasma or the ^{3}He minority scenario is marked by light grey color, and finally the second harmonic hydrogen scenario is coloured in black. The white boxes are scenarios that are not yet explored.

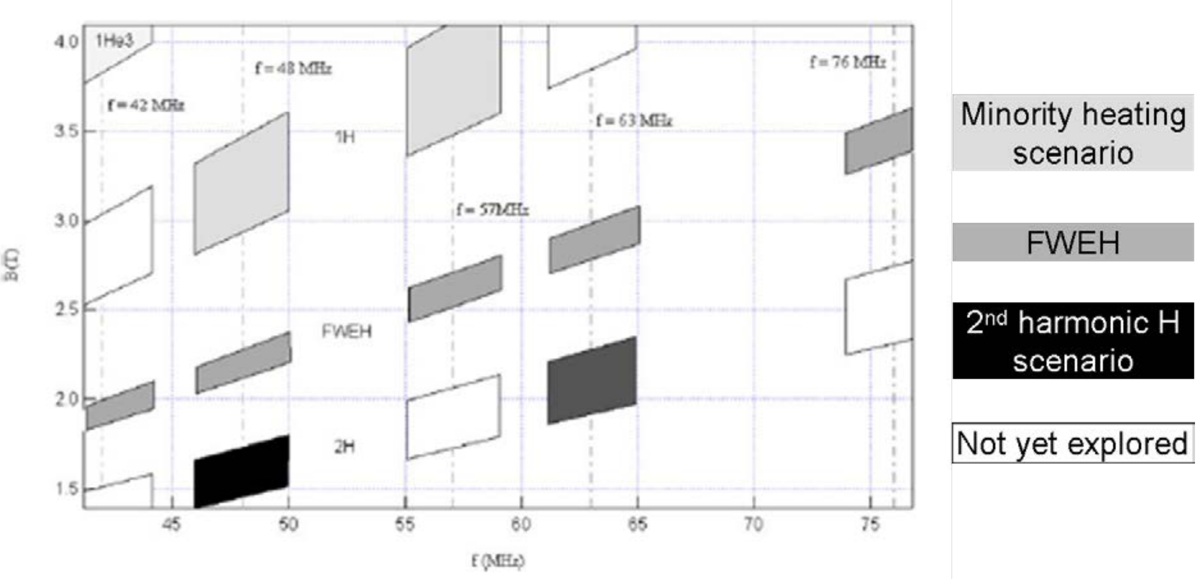

Figure 4.4: *Main available heating schemes using ICRH on TS. The five frequencies bands with widths of 2MHz are represented by the dashed lines. The limit of the domain in the magnetic field is because of the radial location of the resonance layer.*

Unfortunately, the presence of a powered ICRH antenna inside the tokamak vessel does not always yield positive effects. There exist also side effects that are mainly associated with the formation of RF sheaths. In the following section, we will give an introduction to the RF sheaths physics and emphasize main consequences connected with it.

4.3 RF sheaths

We showed in chapter 2 that there is a thin layer between the plasma and material surface that bounds it, called the sheath, which maintains the balance between the outflow of ions and electrons by biasing positively plasma with respect to wall. Now, we would like to study the sheath when it is subject to rf biasing. These rf potentials might come from a RF biasing electrode or more importantly, from an existing parallel electric field emitted by the RF antenna, which can be associated to the slow wave.

Antennas operating in the ion cyclotron range of frequency provide a useful tool for plasma heating (specifically to the ions) in many tokamaks and are foreseen to play an important role in ITER [ITER 12]. However, in addition to the desired ion heating in the core plasma, spurious interactions with the plasma and material boundary are known to occur. Many of these deleterious effects are caused by the formation of rf sheaths. Presence of the powered antenna can lead to unwanted interactions with the scrape-off layer associated mainly with the generation of the slow wave, such as enhanced sputtering and impurity generation [Colas 07b, D'Ippolito 91], convective transport [Bobkov 10], and localized high heat fluxes at the field line extremities [Bécoulet 02] (Figure 4.5 red circles).

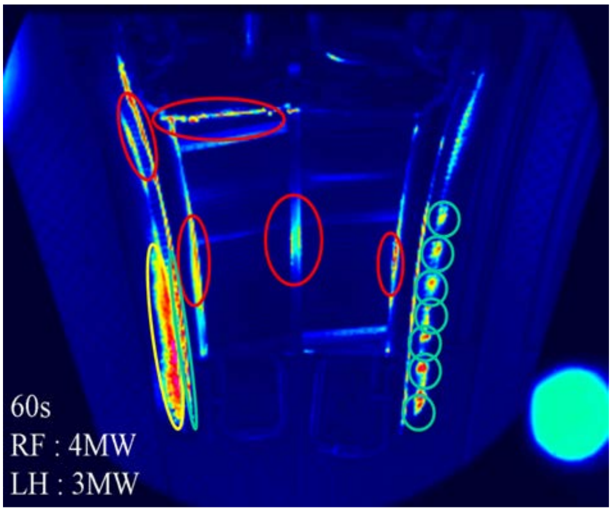

Figure 4.5: *Infra-red image of one of the TS ICRH antenna demonstrating in red circles the side effects associated with the rf sheaths.*

The parallel electric field $E_{||}$ of the slow wave (parallel component of the FW is negligible with respect to SW and it is further assumed that the Faraday screen bars are aligned with the magnetic field lines) then drives an oscillating RF potential between the extremities of open magnetic flux tubes defined as

$$V = \int E_{||} ds \tag{4.8}$$

where the $E_{||}$ is calculated from antenna codes and the integral is taken between the two contact points of the magnetic field with the conducting boundary (usually antenna bumpers). This potential can reach up to several hundred volts, according to the 1D modelling [Perkins 89]. Natural reaction of the sheath due to its diode-like I-V characteristic, is to rectify the oscillating RF voltage by suppressing its negative component due to the difference in the mobility of ions and electrons, and producing a dc potential (see Figure 4.7). This physical effect is induced by the mass difference of ions and electrons. In consequence, more energetic ions accelerated across this high dc potential then cause deleterious antenna-edge interactions whose are mentioned above.

Until recently, rf sheaths effects were mainly studied in the vicinity of the antenna, and they were estimated using the vacuum field approximation to the sheath voltage according to Equation (4.8), where the integral is taken between the two contact points of the magnetic field line with the conducting boundary (usually antenna bumpers). Each magnetic field line intercepted by metallic surface can be considered as a flux tube along which the potential oscillates at rf frequency and is longitudinally constant. Two cases can be distinguished. First is related to the antenna private region near the screen, between the limiters, where a symmetric situation exists. This is modelled by two rf sources referenced to ground, with bias voltage phased by $\pi/2$ (see Figure 4.6a). In the second case, outside the antenna, it is an asymmetric situation. Bias voltage is entirely applied to one wall, while the other is grounded. Only the second case allows the DC currents to flow (see Figure 4.6). In such case, negative (net electron) current is collected on the powered ICRF antenna, while positive (net ion) current is collected by magnetically connected Langmuir probe as is observed experimentally on TS. The rectification of rf potential due to asymmetrical inertia of ions and electrons in sheaths and parallel dynamic of rf sheaths has been studied in previous works. Some of the approaches using 2D fluid models have considered transverse currents, either purely from rf component [Ngadjeu 11], or with the contributions of the inertia and viscosity currents [Faudot 10].

The problem of RF sheaths is quite complex since dynamics of all plasma particles in perpendicular and parallel directions to the magnetic field must be taken into account. This problem was investigated more often in the cold plasmas, where measurements are more easily accessible, compared to fusion plasmas. Studies by Riemann [Riemann 92] have shown that the Bohm criterion is still applicable in the case of RF sheaths which allows to consider models derived in previous chapters. In tokamaks, the plasma frequency is higher then the antenna frequency, e.g. the ion cyclotron frequency of the deuterium ion in the plasma edge is $\approx 6\times$ higher then the antenna frequency set for minority heating of the hydrogen. Several models have been proposed to simulate the rf sheath either in low frequency mode [Pointu 86] or for near antenna frequency range [Metze 86] considering capacitive effects of the sheath.

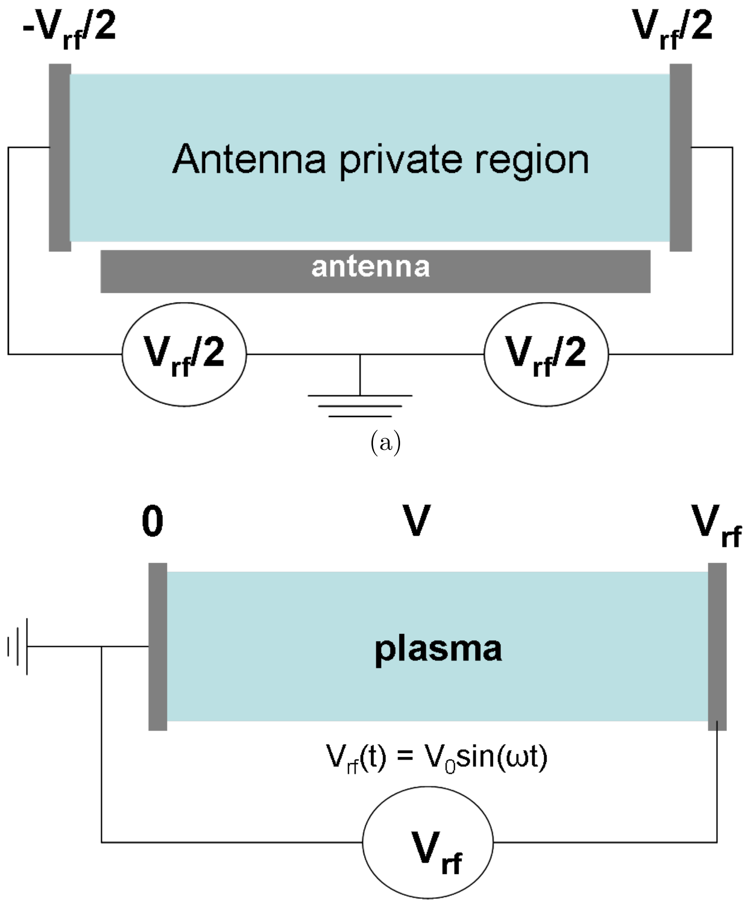

(a)

(b)

Figure 4.6: *(a) Symmetric case: scheme of the flux tube embedded by two electrodes biased in opposite phase. (b) Asymmetric case: scheme of the flux tube embedded on its one end by a grounded electrode white the other end is biased by rf electrode.*

To demonstrate the effect of rectification of the rf potential, we can use a simple analytical model. It should be recalled that the rectification is associated with the diode-like I-V characteristic of the sheath. Hence, both ion and electron parts of the I-V characteristic can be associated with equations similar to Equation (3.1). It is common to model the rectification process as a circuit with two electrodes. Electrodes can be biased symmetrically (Figure 4.6a) or asymmetrically (Figure 4.6b), where one of them is grounded and the other one is biased with an rf oscillating voltage. We assume that the rf frequency is small compared to the ion plasma frequency (as it is in the case of deuterium during minority heating scenario of hydrogen), i.g. no parallel capacitive effects occur. In addition, all transverse dynamics are neglected (see Figure 4.6), and plasma density is assumed to be constant and electrons follow the Boltzmann law. From the current conservation law integrated over the flux tube yields [Ngadjeu 10]:

$$j^i_{sat} - j^e_{sat} exp\left(-\frac{e(V-V_{rf})}{kT_e}\right) + j^i_{sat} - j^e_{sat} exp\left(-\frac{eV)}{kT_e}\right) = 0 \tag{4.9}$$

Now we can express the plasma potential as

$$V = \frac{kT_e}{e}\left[ln\left(\frac{j^e_{sat}}{j^i_{sat}}\right) - ln2 - ln\left(1 + exp\frac{eV_{rf}}{kT_e}\right)\right] = V_{fl} + \frac{kT_e}{e}\left[-ln2 - ln\left(1 + exp\frac{eV_{rf}}{kT_e}\right)\right] \tag{4.10}$$

Compared to Equation (2.34), two additional terms appear causing truncation of the negative component V_{rf}. The resulting rectified potential is plotted on Figure 4.7 and it depends on both the floating potential V_{fl} and rf potential V_{rf}. In the case of ICRH antennas, the V_{rf} is the rf potential resulting from the integration of the parallel electric field along open magnetic lines in front of antenna according to Equation (4.8). The minimal value of rectified potential, V_{rectif}, is given by $V_{fl} - (kT_e/e)ln2$ and it reaches its maximum for $V_{fl} + (kT_e/e)(-ln2 + ln(1 + exp(eV_0/kT_e)))$. To obtain averaged dc potential one has to integrate V_{rectif} over one rf cycle. Assuming $V_0 \ll (kT_e/e)ln2$, the dc potentials is given by $V_{fl} + V_0/\pi - (kT_e/e)ln2$ [Godyak 90].

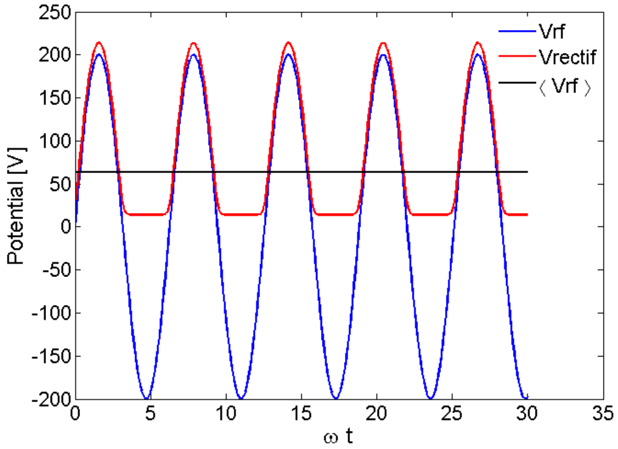

Figure 4.7: *Temporal evolution of the applied rf potential (blue) and resulting rectified potential (red).*

It was mentioned that formation of rf sheaths can lead to spurious interaction such as enhanced sputtering, impurity generation or localized heat fluxes on the walls ($Q = \gamma_{bohm}V_{rectif}$). In addition, the distribution of the rectified potential in front of the antenna creates an electric field which generates convection cells leading to plasma transport. All these effects are results of extremely high rectified potentials generated by a powered antenna. Therefore, a decision has been made to design a completely new type of Faraday screen for one of Tore Supra ICRH antenna, that would significantly reduce these high potentials and limit rf sheaths effect. A brief description of this new design is presented in the next section in comparison with a conventional Faraday screen design used on Tore Supra.

4.4 Faraday screen design

The design of conventional Faraday screen consists of a set of parallel bars tilted by 7° to be aligned with pitch of the magnetic field in order to reduce rf sheaths effects. The bars are connected to an actively cooled septum and, in addition, are also angled inward to follow the external shape of the plasma. The primary motivation of the Faraday screen improvement was to reduce localized heat fluxes that arise especially during the combination of LH and ICRH operation leading to hot spots on the FS frame (Figure 4.5 - green circles). Among other motivations of manufacturing new FS were to increase heat exhaust capability in order to reduce thermal loads and prolong fatigue cycle to withstand high power long discharge operation [Bécoulet 02, Corre 11]. Further motivation was to reduce the source of the RF potentials on open field lines and and qualify qualify new screen suitable for ITER. In order to fulfill all requirements, following modifications has been made in the FS design:

- FS bars are disconnected from the vertical septum.
- FS bars are aligned perpendicular to the side wall - no tilting.
- shark tooth opening at the top and bottom of the screen to reduce parallel current flow.

In comparison with the conventional FS, gaps between rods are larger, rods are broader and no more aligned with tilted field lines. The new FS was successfully installed in spring 2011 on one of the three ICRH antennas. Design of both screens is shown on Figure 4.8. Main design differences for both screens are summarized in Table 4.1. More detailed specifications of the technical and mechanical aspects concerning the design of the new FS can be found in [Vulliez 09, Mendes 09]. According to the simplest model of RF sheaths rectification [Perkins 89], the rectified potential is defined by the integral of the parallel electric field $E_{||}$ along open field line $V_{rf} = \int E_{||} \mathrm{d}l$. As mentioned above, the RF sheath effects are associated with the formation of the slow wave, which arises if the FS elements are not precisely aligned with magnetic field lines, and thereby increasing the electric fields to an appreciable fraction of the gap voltage (see Figure 4.9).

On long open field lines with large toroidal extension on both sides of the antenna, this rectified voltage is excited by parallel RF current $j_{||}$ flowing on the antenna structure. Results based on TOPICA (TOrino Polytechnic Ion Cyclotron Antenna)[Lancellotti 06,

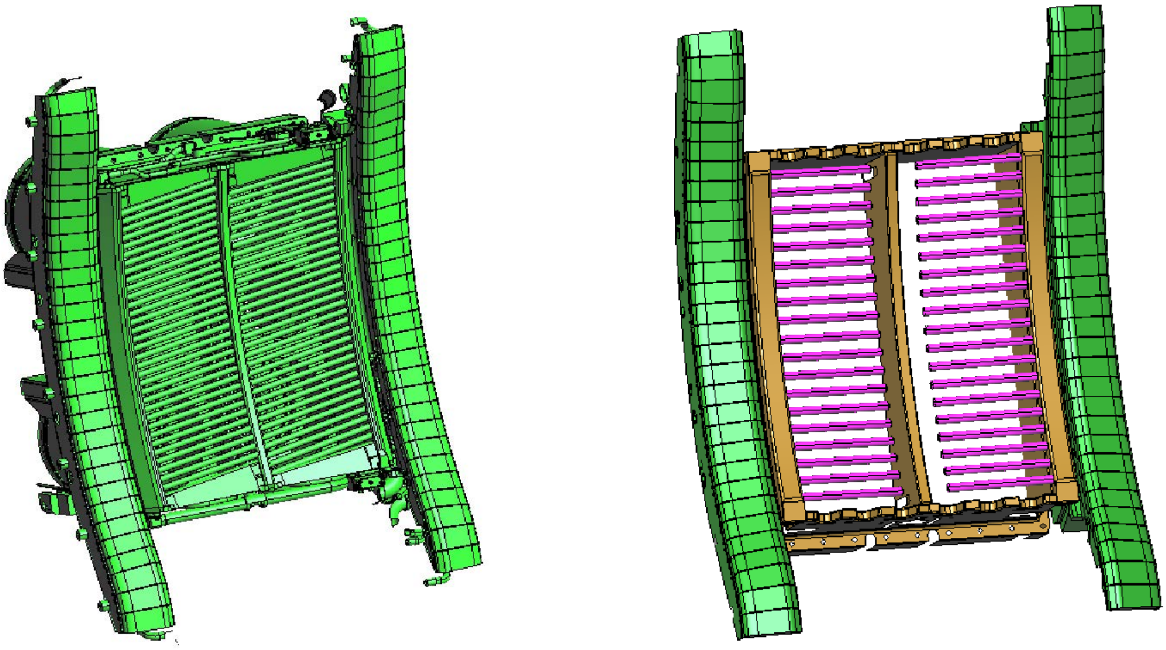

(a) Old Faraday screen (b) New Faraday screen

Figure 4.8: *Schematic of the old and new Faraday screen.*

Mendes 09] simulations suggest that the new innovative design with cantilevered bars[1] and shark tooth openings at the top and bottom of the screen dramatically changes the current flow pattern on the front face of the antenna [Vulliez 09]. Near field simulations on TS geometry predict that the major contribution to the RF potential is the circulation of $j_{||}$ on the horizontal parts of the frame and on the FS bars. As a result of simulations, the RF potential (∼300V for 1MW of coupled power) and RF parallel electric field (which contributes to generating RF sheaths) are reduced. Generation of potentials by both

---

[1] i.e. bars not connected to central vertical septum

	Conventional FS	**New FS**
number of slots	35	20
gap width	0.5mm	1.5mm
bar length	80mm	75mm
material thickness	1.5mm	0.5mm
bar width	6.0mm	7.5mm
tilt angle	7°	0°
gap voltage for V_{strap}=30kV	850V	1.5kV

Table 4.1: Main design differences between conventional and new FS design.

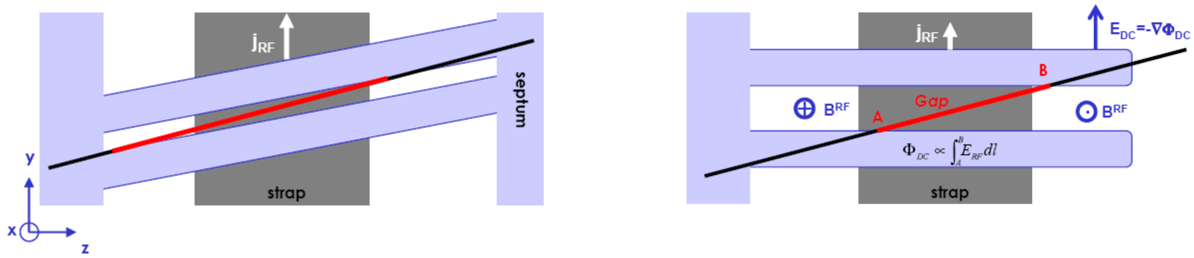

(a) Tilted bars

(b) Horizontal cantilevered bars

Figure 4.9: *Schematic of the magnetic connections in the gap between FS bars for (a) tilted and (b) not titled case. Coordinates x, y, z are the radial, vertical and toroidal directions, respectively.*

screens are studied experimentally by means of Langmuir probes in chapter 5 where will be shown that these initial simulations are not in good agreement with experimental observations. Moreover, it will be demonstrated that the new FS design can even lead to the generation of much higher potentials compared to conventional FS concept [2].

4.4.1 Probe-screen interaction

During the plasma operation, protection of plasma facing components inside the vessel relies basically on two criteria: surface temperature (monitored by infra-red thermography system) and material impurities (measured with a high resolution vacuum ultra-violet spectrometer) [Corre 12]. Each of TS ICRH antenna is therefore monitored by an IR camera to control its surface temperature which can increase rapidly especially due to hot spots. The IR system operates at frequency 50Hz with an average spatial resolution of approximately 2mm [Guilhem 05]. The surface temperature varies strongly, from 200 - over 500°C (in space) depending on localized heat loads - caused for instance by fast electrons generated by LH grill. Moreover, it was found out in this thesis when analysing the IR images, that the antenna structure interacts with the probe as well. Although the probe is not magnetically connected directly to the Faraday screen, because it is shielded by the guard limiter on antenna side, one can notice by analysing IR images that the screen can actually 'see' the probe which is situated 12m away along the field lines. Tools used for calculation of magnetic field connections are summarized in the Appendix A. Such a probe-screen interaction is evinced by the change of the FS surface temperature (see Figure 4.11). The probe is not magnetically connected to the screen itself. The field lines just pass ≈ 1cm in front of the FS structure (bars n°8 and n°9 in this particular case - Figure 4.10) and terminate at the bottom toroidal limiter of the vessel.

---

[2] June 2013: This problem is now understood and comes from an oversimplified modelling of the new Faraday screen.

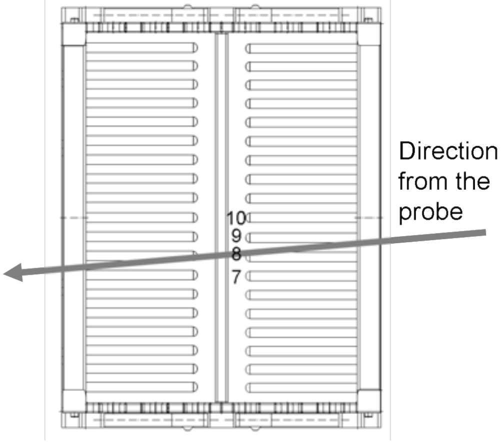

Figure 4.10: *Front view of the new FS and field lines emerging from the probe passing in front of the screen.*

As can be seen from Figure 4.10, when the probe is immersed into the plasma, the surface temperature of the bars changes nearly immediately (not only of the bars near which the probe is passing along, but also neighbouring ones). The change of the antenna surface temperature is about 4% (20°C degrees change for the bar temperature of 500°C). One can also notice that the surface temperature increases for bars n°8-10, while for the bar n°7 decreases. It should be also pointed out that the same phenomena were observed also on the side limiter to which the probe is magnetically connected. In addition, these observations were made also at different poloidal locations of the antenna structure. But what is the mechanism behind this phenomenon? How is it possible that the presence of the probe can affect surface temperature of an object to which it is clearly not connected to? And why is the change of the antenna surface temperature positive in one case and negative in other one? The probe itself houses in grounded tube and only a small part of it (orifice of diameter of 3mm) is biased. One of the possible explanations of this observation could be as follows. The differential biasing of nearby flux tubes caused by RF sheaths, gives rise to perpendicular electric field inducing $\mathbf{E} \times \mathbf{B}$ particle convection. This particle convection is not only in poloidal direction (see section 5.3.1) but also transversely to magnetic flux surfaces. The $\mathbf{E} \times \mathbf{B}$ particle transport is therefore directed towards or away from the FS according to the orientation of the rectified potential gradients (see Figure 4.12). As a consequence of particle transport in the vicinity of the antenna, the averaged density in front it, is changed poloidally [Bécoulet 02] and we will discuss it in detail in section 5.3.1. Concerning detailed investigation of the thermal heat loads on the new FS, the operation also revealed that the new design does not reduce the RF-induced heat loads as expected.

A factor of about 5 higher is even found locally (in the mid-plan region) between conventional and new screen for similar plasma conditions. The enhanced heat flux observed with the new Faraday screen qualitatively agree with the two interplaying mechanisms: enhanced RF sheath effect leading to higher rectified potential (see chapter 5) and subsequently enhanced $\mathbf{E} \times \mathbf{B}$ particle convection driving the particles in the equatorial midplane. The full investigation of thermal heat loads of new FS is summarized in [Corre 12].

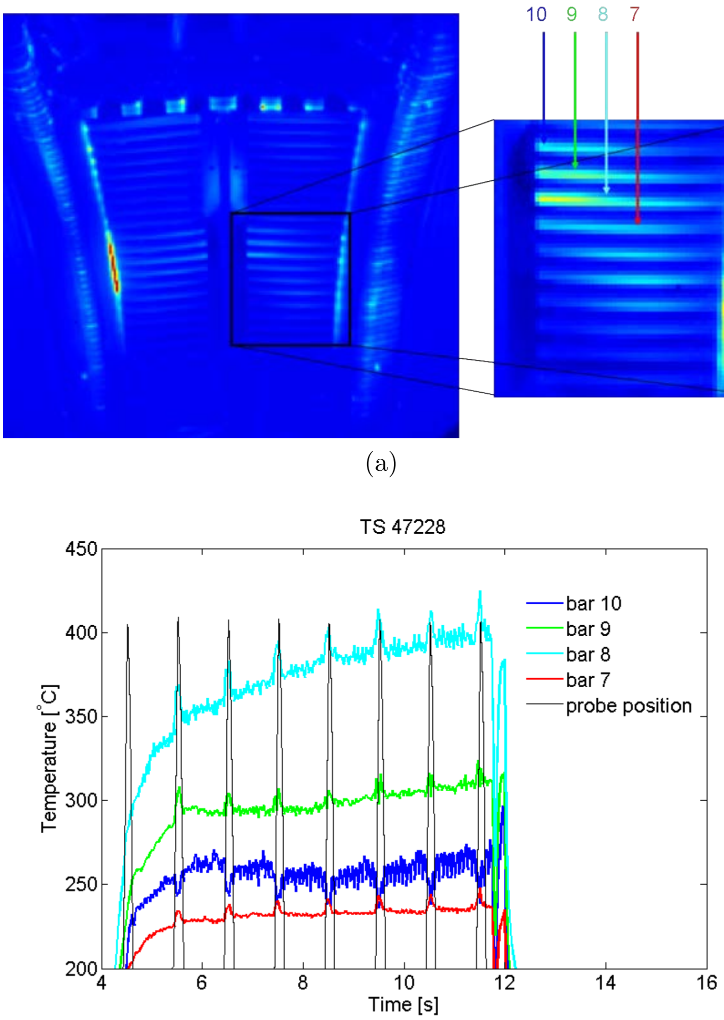

(a)

(b)

Figure 4.11: *(a) Infra-red image of ICRH antenna equipped with the new type of FS. (b) Temporal evolution of the surface temperature measured on selected bars located in the bottom right quarter. The probe is not connected to the bars, it just passes ≈1cm in front of them. By black color is superimposed the probe position.*

As is mentioned above, the infra-red images give an indication of the power fluxes to different parts of the antenna. The deposited power on the wall or antenna structure is due to photon irradiation from the plasma, and also direct particle fluxes onto surfaces, where the higher fluxes are first due to the increase of the DC sheath potential and due to some local increases of the local density induced by the convection cells associated to E×B convection. The observed coincidence between probe reciprocations and the redistribution of power flux to the Faraday screen has important implications. It suggests that the probe perturbation (its wake) extends long distances along magnetic field lines (here the connection length is 12m). This perturbation could involve any combination of the local plasma density, temperature, electric fields, or parallel current flow, which could conceivably be sufficient to modify the 3D pattern of time-averaged electric field in front of the antenna, and hence affect the $\mathbf{E} \times \mathbf{B}$ convective flows. It also implies that measurements made with such a (necessarily) large probe might not be fully representative of the plasma parameters that would arise in the absence of the probe. The observation of direct perturbation of the IR images by the probe is in line with the observations discussed earlier, namely the presence of large DC potentials on the downstream side of the probe which faces away from the antenna [Gunn 08]. To fully understand how the probe interacts with the rf biased flux tubes it would be necessary to perform sophisticated 2D modelling that includes both parallel and radial effects undergoing on biased flux tubes. Nonetheless, the qualitative results presented here are valuable in that they highlight important phenomena that need to be explained, and will thus guide future research in this field.

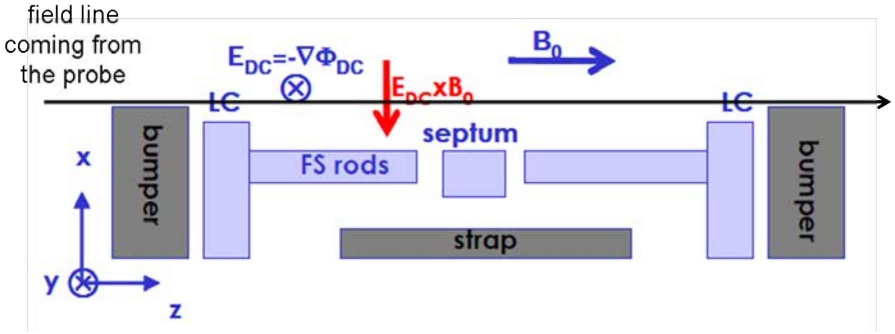

(a) Top view

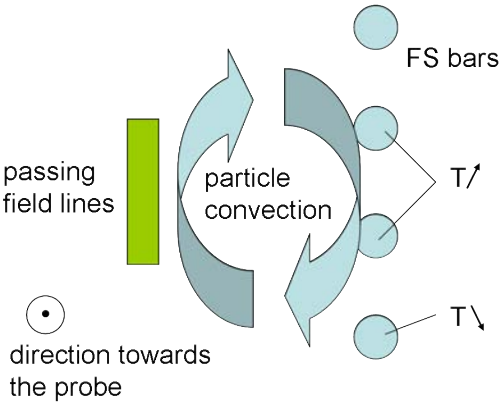

(b) Poloidal projection

Figure 4.12: *(a) Top view and (b) poloidal projection of the simplified cross-section of the new FS in its private region illustrating the* $\mathbf{E} \times \mathbf{B}$ *particle convection toward the screen (outward if the electric filed is opposite.*

Summary

This chapter completes the description of the ion cyclotron resonance heating techniques that were briefly introduced at the end of the first chapter. It was also mentioned that usage of ICRH in tokamaks is not only associated with favorable effect of the plasma heating, but some unwanted phenomena can occur as well, e.g. localized heat fluxes, enhanced sputtering and impurities production. The cause of these effects lies in the formation of rf sheath whose natural behavior is to rectify the oscillating potentials to high values (up to several hundred of volts). In order to reduce these high potential, a new concept of Fadaray screen has been designed. Main features of this new type of FS are shark tooth opening at the top and the bottom of the screen, and bars disconnected from the central septum. Such a configuration should significantly reduce current flows on the antenna structure. Main objective of the following chapter is to compare, by means of reciprocating probes data, consequences of induced RF-SOL interactions during the operation of conventional and new type of FS design. We remind that all measurements presented in next chapter were obtained by a tunnel/Mach probe containing two tunnel collectors mounted back-to-back.

Chapter 5

RF-induced SOL modifications

5.1 Introduction

In this chapter, we will focus on experimental observations that were made in order to characterize the RF-induced SOL modifications with emphasis on their spatial structures and the effects of the various plasma and antenna configurations on them. Most of the results presented here were carried out during the 2011 TS experimental campaign during which over ∼100 ICRH discharges were performed with a tunnel/Mach probe measurements. These data, obtained during the new FS type operation are compared to earlier measurements performed in 2009 with the conventional FS. Several sessions dedicated to different aspects of antenna-SOL interactions were made such as:

- Detailed 2D radial-poloidal mapping
- Old vs. new Faraday screen
- Density scan
- Power scan
- Scan of strap power imbalance

The chapter is structured as follows. Firstly, principles of the magnetic field line tracing technique are given followed by the description of the experimental procedure. The main body of the chapter is devoted to the data analysis of each particular session. We start with the description of the general features of the RF-SOL interaction followed by more specific and particular cased that were observed. In the last part, main results are summarized and suggestions for possible future experiments are given. We recall the data presented in this chapter were obtained by the tunnel/Mach probe.

5.2 Experimental setup

In 2009, the tunnel/Mach probe was mounted in top port Q3B at 160° toroidally to be magnetically connected to the Q1 antenna at 40° with a conventional Faraday screen. For the 2011 experimental campaign, the probe was moved to port Q1B at 40° with magnetic connections to antenna Q5 at 280° toroidal position where the new FS was installed. In both cases, the toroidal angle between the probe and the antenna is 240°, which corresponds to a magnetic connection length of 12 m. Both configurations are summarized in Table 5.1. During the discharge, the probe is reciprocated into the SOL several times. In 2009, the probe was operating in swept mode, while for the 2011 data presented here, the dc floating or saturation mode was chosen in order to increase temporal resolution and to avoid failure of the real time feedback system in the presence of strong radial gradients of floating potential. The heating power varies from 1-3MW depending on the experimental session for both screens. Magnetic connections of the probe to the antenna are shown in Figure 5.1. Scanning the safety factor q from 3 to 7.5 allows magnetic connections to the whole poloidal projection of the antenna structure. The plasma configuration for each dedicated session is described in the corresponding section.

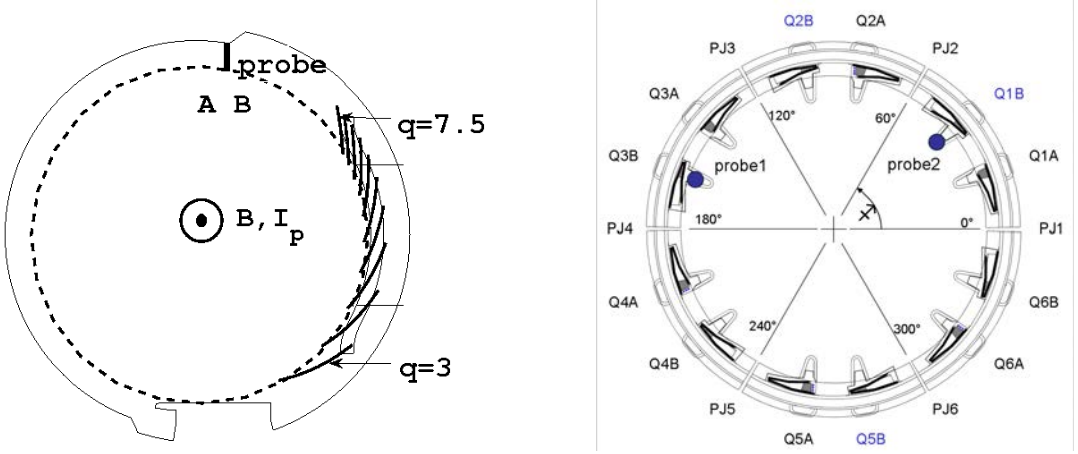

(a) (b)

Figure 5.1: *(a) Magnetic connections of the probe to the poloidal plane at the antenna for different values of the safety factor q. Both A-side and B-side of the probe are labelled. (b) Layout of the antennas and probes position. ICRH antennas are located in Q1B, Q2B and Q5B ports.*

It is also important to recall here the notation we will use in the following pages. Since the probe is built in the Mach probe arrangement, we will distinguish the 'A-side' (electron side) and the 'B-side' (ion side) of the probe. The A-side is magnetically connected to the limiter on the HFS while the B-side can be connected to a powered antenna on the

Year	**Probe**	**Probe location**	**Antenna**	**Screen**
2009	STP	Q3B	Q1	old
2011	TP	Q1B	Q5	new

Table 5.1: *Experimental setup for 2009 and 2011 experimental campaigns.*

outboard mid-plane. The situation is schematically shown on Figure 3.6. In comparison to [Colas 07a], special attention will be also paid to data measured on both sides of the probe.

5.3 Experimental observations

Typical local modifications of the basic SOL parameters induced by a powered ICRH antenna are shown on Figure 5.2. These particular measurements were made by the tunnel/Mach probe connected to the Q5 antenna with new Faraday screen in 2011. For this experiment the probe was operated in DC mode, measuring either ion saturation current or floating potential. To calculate the edge density we use Equation (3.24) with fixed electron temperature $T_e = 20eV$ and $T_i = 2T_e$. Two reciprocations from consecutive ICRH discharges are compared. In both of them, the probe is magnetically connected to Q5 antenna. In the first case, the Q5 antenna is inactive, but Q2 antenna is injecting 2MW of power (red line). The Q2 antenna is located at 100° toroidally and the probe is not magnetically connected to it. No perturbations are observed on radial profile of the floating potential which is nearly identical to measurements that are typically observed during the ohmic discharges, i.e. floating potential around 0V. The second case is opposite. Q5 antenna is powered while Q2 antenna is off ($P_{Q5} = 2MW$ and $P_{Q2} = 0MW$). It that case, the profile of the floating potential (as well as other SOL parameters) is no longer monotonic but is characterized by the strong perturbation (blue line). It appears only on the flux tubes connected directly to a powered antenna. One can see that for the unconnected case, the floating potential remains roughly constant around $V_{float} = 0V$ while for the connected case there is a radially localized structure with floating potential nearly up to 200V with a radial width of $\Delta r \approx 4cm$. A very sharp gradient of V_{float} appearing at $d_{lcfs} = 1.5$cm demonstrates the necessity of the floating mode utilization. The probe moves quite fast ($\sim$ 1m/s) which would cause difficulties for the feedback system to react adequately for such a sharp V_{float} variation. This implies that RF-induced SOL modification is a local effect and it was already observed on Tore Supra [Colas 07a]. Therefore, special attention will be paid to 2D maps of floating potential that bring completely new experimental observations.

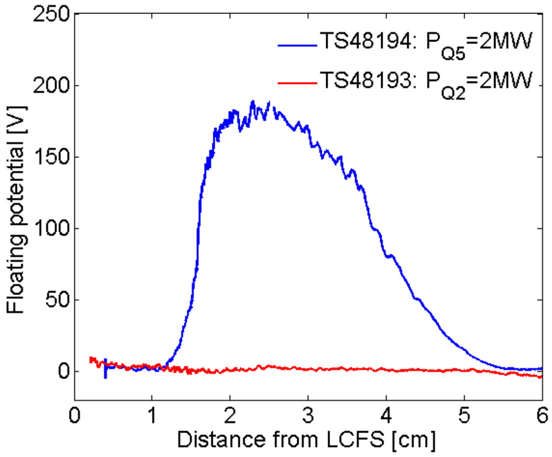

Figure 5.2: *Radial profile of the floating potential measured by the probe in Q1B magnetically connected only to Q5 antenna*

5.3.1 2D mapping of V_{float}

This section is devoted to the 2D mapping of the floating potential. In order to obtain full 2D map of the new type of Faraday screen, the probe was reciprocated several times into the SOL - 42 times in 6 shots (TS48271, TS48272, TS48274, TS48277, TS48278 and TS48280). Based on the results obtained earlier in the campaign, it was decided to keep the injected power from the Q5 antenna equipped with the new FS only at P_{Q5} = 1MW. In contrast to the old FS, probe measurements showed that for higher antenna power ($P >$ 2MW), the floating potential measured at the mid-plane is already high, $V_{float} \approx 100V$. And typically at ±10cm above and below the mid-plane, the V_{float} exceeded the maximal range for measured voltage and saturated at ~220V. The antenna was operating in a dipole phasing configuration, i.e. the currents flowing along the strap are in opposite phase. Moreover, for better strap-to-strap balance, it was necessary to set the strap power ratio to left/right = 43/57. The possible reason of that was revealed after the examination of the antenna when the campaign was over. The imbalance of the coupling between two straps was most likely caused by the relative misalignment of about 4mm between the positions of the bars on left side of the FS with respect to the right side. Nevertheless, no other experiments were done since that time and to confirm this hypothesis, one has to wait until the next Tore Supra experimental campaign. As it will be shown later, the relative misalignment of bars plays a minority role for the probe measurements presented here. As usually in TS discharges, the antenna was retracted 1cm behind the main antenna protection limiter. The full 2D map of V_{float} is shown on Figure 5.3b. Scan of the bottom extension of the lateral limiter could not been done due to requirement of $q < 4$, for which the antenna coupling became difficult. Such a mapping picture corresponds very well to results obtained in earlier TS experiments [Colas 07a].

There are two lobes located around the top and the bottom corners of the antenna strap and are shifted little bit up with respect to the mid-plane. As can be seen from Figure 5.3a, the poloidal position of the two lobes of floating potential is well correlated with the two peaks on the poloidal profile of the edge density in front of the powered Q5 antenna. There is an asymmetry in the poloidal position of both peaks with respect to the mid-plane. The upper peak, characterized by higher density value, is located at ∼0.3m above the mid-plane which corresponds with the top edge of the FS structure. On the other hand, the bottom peak of a smaller intensity is located approximately 0.1m below the

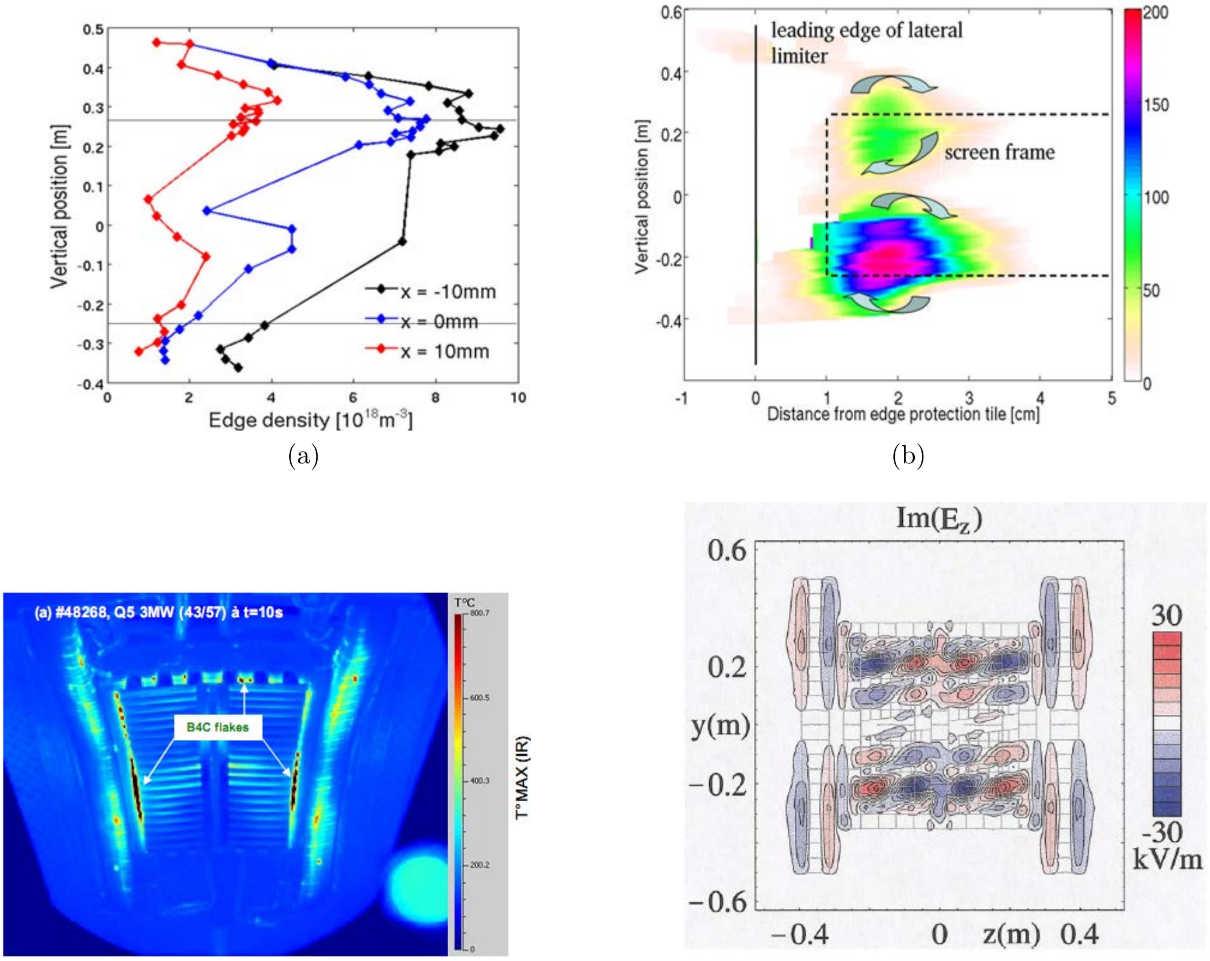

(a) (b) (c) (d)

Figure 5.3: *(a) Poloidal variations of the density measured by the tunnel probe connected to the antenna equipped with the new type of FS. Profiles are mapped to the antenna and plotted at given distance with respect to the position of the antenna lateral limiter. Distance is negative when mapped in front of the antenna. (b) 2D map of floating potential together with schematic of the* $\mathbf{E} \times \mathbf{B}$ *particle cells convection. (c) Infra-red image of a powered ICRH antenna equipped with the new FS. (d) Contour lines of the z-component of the electric field at the distance of 0.5cm from the screen, for a two-strap structure similar to the Tore-Supra antenna.*

mid-plane. Regarding the link of the density peaks with the position of the two potential lobes, one can notice that the poloidal position of the density peaks corresponds well to the upper edge of bottom/top lobe where strong potential gradients appear and give rise to particle transport via $\mathbf{E} \times \mathbf{B}$ convection.

Moreover, these two peaks in the density profile are also well visible on the images from infra-red camera facing towards the antenna (Figure 5.3c). As can be seen, there is a strong heating of the antenna structure located on upper shark tooth openings while almost no heating is observed on the bottom part of the FS. In addition, and as we showed at the end of previous chapter, increased heating is also observed on the bars located just below the mid-plane. But in the scope of this section, most important are two localized heated zones located on the both lateral limiters adjacent to the FS. Moreover, the enhanced heated zones on the upper shark tooth openings are located in the antenna private region that is inaccessible for our probe measurements because is shadowed by the side limiter.

Concerning the explanation of the poloidal density profiles, one has to be careful. It is important to recall here that profiles shown on Figure 5.3a were not measured during single discharge with constant plasma parameters but were created from data combination of several different shots. As was mentioned earlier, in order to obtain various magnetic connections of the probe to a powered antenna, it is necessary to vary the plasma current. But as the plasma current changes, other parameters change as well such as β and consequently also the edge plasma density. Therefore, it cannot be surely said that there is a poloidal variation of the density profile in front of a powered ICRH antenna. To prove that, several simultaneous measurements at different poloidal positions would have to be made. However, if we assume that density modifications caused due to variation of plasma current are negligible, poloidal variation of the plasma density in front of a powered antenna can be explained as follows. Due to the differential biasing of nearby flux tubes by sheath rectification process, intense localized gradients of the plasma potential can arise leading to particle transport via $\mathbf{E} \times \mathbf{B}$ convection in the vicinity of the antenna. These so called convection cells are illustrated on Figure 5.3b by arrows. Their location is similar to the appearance of the zones with high potentials. Due to the spatial variation of the electric field (with stronger on the bottom), the particles are driven by $\mathbf{E} \times \mathbf{B}$ drift towards the upper part of the antenna where the electric field is weaker. As a consequence, the averaged density in front of the antenna is changed poloidally. As can be seen, the density asymmetry is higher above the mid-plane compared to the bottom part of the antenna structure with a local minimum around the mid-plane. Hence we can conclude that poloidally asymmetric power deposition is in good agreement with the poloidal density variations. This observation is in an agreement with numerical simulations made in [Bécoulet 02], which showed that the two-dimensional density pattern is also poloidally inhomogeneous. Simulations performed in [Bécoulet 02] show particle depletion above and in front of the FS, and an over density below the antenna mid-plane. The opposite density pattern compared to our measurements has purely technical aspects. At the time the simulations were made, Tore Supra was operating with reverse magnetic field and hence the $\mathbf{E} \times \mathbf{B}$ transport of particles was pointing downwards.

The poloidal double structure that we observe on Figure 5.3b is reminiscent of ICANT calculations of the parallel electric field (Figure 5.3d [Pécoul 02]). One can observe two poloidally extended lobes on the exterior sides of the bumpers. However, these lobes correspond to the slow wave (although polarization of the wave was not checked, it is assumed that $E_{||}$ of the FW is negligible) launched by image currents in the antenna structure, and in the particular case shown here, the radial position is 5 mm in front of the leading edge. Our measurements are several centimeters behind the leading edge. We were unable during the course of this thesis work to learn whether such structures were ever predicted by past antenna code calculations, nor whether they are anticipated by experts. We suggest that given the clarity of the results, it is important to look into this question. Undoubtedly, there is a source of rf rectification outside of the antenna box, on surfaces that are not magnetically connected to the straps. Perhaps the observed structures could be driven by oscillating surface charge density due to image currents in the bumpers.

5.3.2 Old vs. new Faraday screen

In this section we will deal with the comparison between the both old and new Faraday screens are compared here. Only SOL parameters measured by the probe are addressed. It was shown in previous section that quantitatively both screens are very similar. In both cases, two characteristic potential lobes were measured located poloidaly around the FS top and bottom corners. Nevertheless, there are also some substantial differences and will be discussed them below.

Main difference between our measurements (new FS) and those made in [Colas 07a] (old FS), is related to the radial position on the lobes. As can be seen from Figure 5.4a, the zone of increased floating potential is shifted behind the leading edge of the antenna lateral limiter (TS44105, TS44106, TS44108-TS44110). On the other hand, the radial extent of the perturbed zone is in the order of the uncertainty given by the magnetic reconstruction. Therefore, it is difficult to state whether the potential lobes are induced on lateral limiter or in the volume in front of the antenna. This is an important issue because all of the modelling done until now assumes that the observed potential structures originate from the evanescent slow wave in front of the antenna. In the absence of cross-field currents, the potential structure should have a radial width given by the skin depth (a few mm in

Tore Supra) [Faudot 10]. Radial currents predict possible broadening of the structure, but it should still be located on flux tubes that pass very near the front face of the antenna. On the contrary, in the case of new FS (Figure 5.4b), zones of high V_{float} are shifted in outboard direction from the leading edge of the lateral limiter. Typical radial extent of the perturbation zone is ∼3cm, but in contrast with [Colas 07a], they are located ∼2cm behind the front edge of the LL. Therefore, there can be no doubt that the structures indeed originate on the LL. Recently, similar simulations were made using 2D SSWICH code (Self-consistent Sheaths and Waves for Ion Cyclotron Heating) with implementation of TOPICA results of near field simulations (Figure 5.4c). These new simulations give better description of the near field and on the sheath boundary conditions. But the full RF current distribution on the antenna structure is reduced because the side limiters were

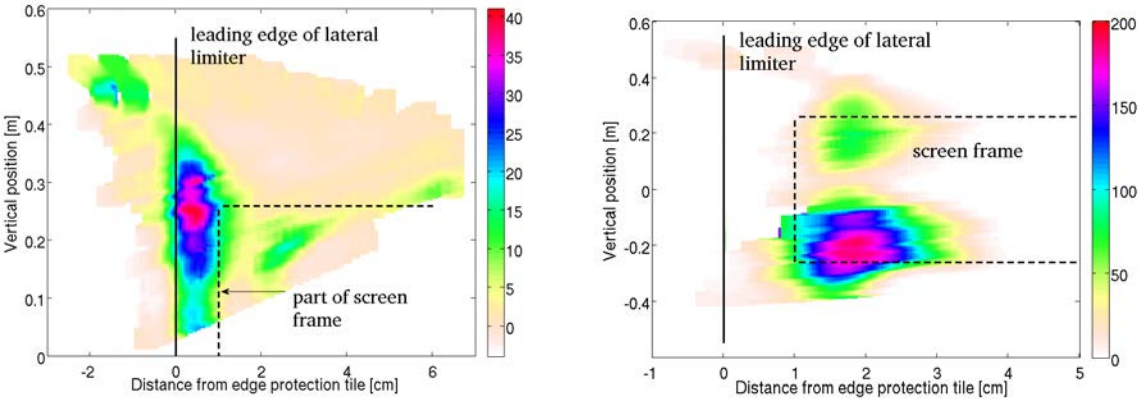

(a) Old screen. P_{ICRH}=2MW.

(b) New screen. P_{ICRH}=1MW.

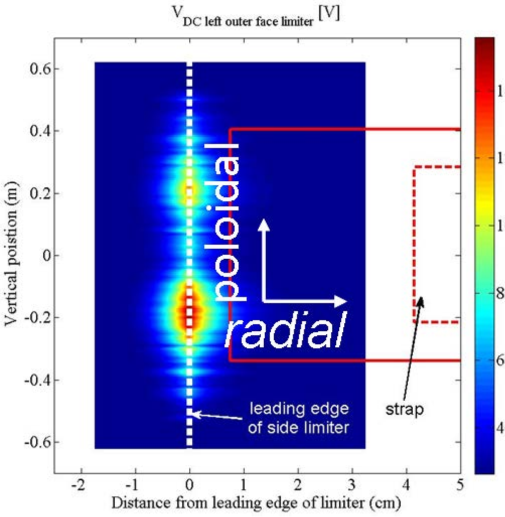

(c) SSWICH simulations

Figure 5.4: *Detailed 2D map of floating potential measured on flux tubes connected to powered ICRH antenna equipped with (a) conventional FS and (b) new type of FS. (c) SSWICH simulations of the new FS, but side limiters are not included*

not included into the calculations. That is the reason why the potential computed stays in front the antenna. Moreover, the structures predicted by the modelling are narrow, of about 1cm in the width. Therefore, to improve our understanding, a 3D description in needed.

Looking closer on Figure 5.4, one can notice that in contrast to [Colas 07a], there is a clear up and down asymmetry in the amplitude of V_{float} where higher values (by factor of 2) are located around the bottom corner of the FS. The comparison of the old and new FS by means of floating potential measurements is shown on Figure 5.5. Measurements with the old screen are on the upper graph and with the new screen on the bottom graph. Corresponding magnetic connections are plotted on the right. Measurements compared here were performed for almost identical plasmas for four different magnetic connections. Due to coupling difficulties with the new FS, it was necessary to increase the line-averaged density from $\overline{n}_e = 5.0 \cdot 10^{19} m^{-2}$ to $\overline{n}_e = 5.5 \cdot 10^{19} m^{-2}$, and move the plasma 1cm inward. While V_{float} measured on flux tubes connected to the old screen is small ($<$ 40V for 1MW of coupled power), potentials measured in presence of new FS are up to 5 times higher. This result is rather unexpected considering the fact that one of the main purpose of the new FS is to reduce these high potentials [Vulliez 09].

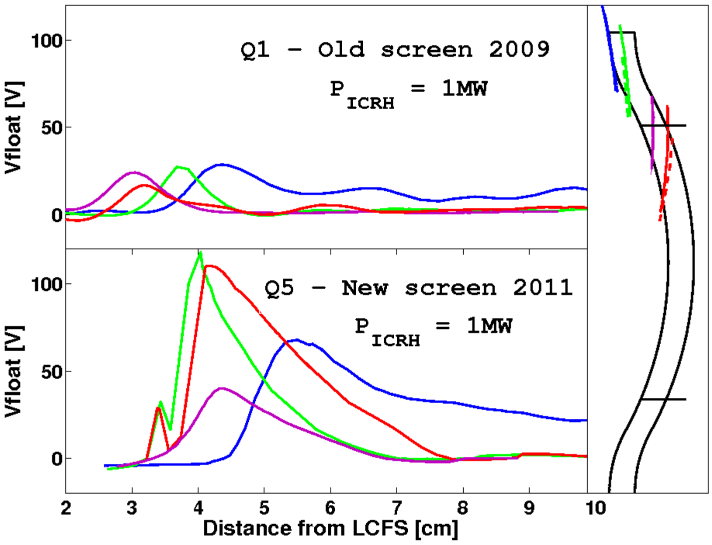

Figure 5.5: *Comparison of the V_{float} measured during the old (top) and the new (bottom) screen operation. Magnetic connections to the antenna are plotted on the right.*

5.3.3 E × B shearing rate

Significant difference between old and new FS is also observed on parallel flow signal. For typical ohmic discharge, parallel flow measured by the probe at the top of the vessel is negative, $M_{\|} \sim -0.5$[1] and increases moderately in radial direction [Gunn 07a]. Same behaviour was observed with the old FS, except at low density ($\bar{n_e} = 4.0 \cdot 10^{19} m^{-2}$ typically [Kubič 11]). On the contrary, the situation is changed drastically in the presence of new screen. The radial profile of $M_{\|}$ is no longer monotonic, but it is strongly sheared (see Figure 5.6). For the deepest position of the probe plunge, the parallel flow is the same for both antennas, $M_{\|} \approx -0.4$. Moving away from the LCFS, parallel flow decreases to zero followed by a steep increase back to negative values. This sudden drop is observed within a thin layer of width < 5mm. In contrast to the old FS, such profiles are observed for a wide range of densities (up to $\bar{n_e} = 7.0 \cdot 10^{19} m^{-2}$).

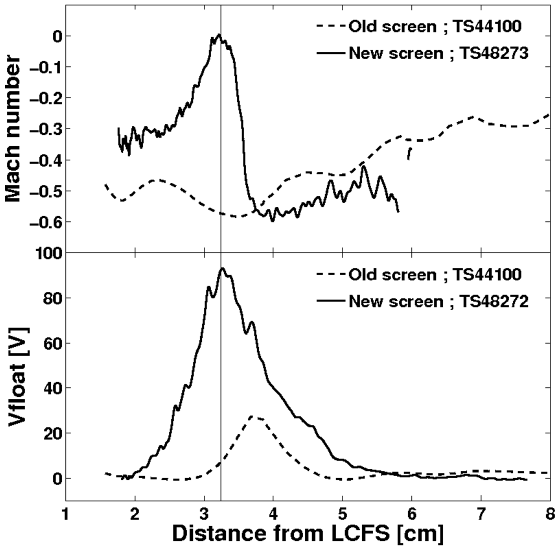

Figure 5.6: *Comparison of the $M_{\|}$ measured during the old (dashed) and the new (solid) screen operation. Radial profiles measured in the presence of new FS are strongly sheared. Profiles of floating potential are on the bottom figure.*

The fact that the parallel flow is characterized by a strong shear in the presence of a powered ICRH antenna has an important consequence for the SOL properties. It is commonly known that having a region with strongly varying radial electric field in the plasma is favourable situation. If the shear is sufficiently large, any turbulent structure that is moving radially outward from the plasma is essentially destroyed and a transport barrier is formed leading to enhanced particle and energy confinement. The particle source for the SOL is concentrated on LFS. This source is believed to be provided by ballooning instabilities that release plasma filaments into the SOL. These filaments, initially of finite parallel length, expand along field lines at the same time as they propagate radially outwards. The free parallel expansion gives rise to the mean parallel flow observed on top

---

[1] $M_{\|}$ is negative because the flow is driven from the LFS to the HFS, i.e. particle source is on LFS flowing in negative toroidal direction

of the torus. The reduction of the flow in the shear layer might be an indication that the blobs are in fact suppressed by the E × B shear.

Let us now calculate the E × B shearing rate arising from the formation of large potential structures induced by a powered antenna. Let us consider floating potential profile shown on Figure 5.6 - TS48272. Let us further consider for this particular case that floating potential is equal to the plasma potential ϕ_p. Because we are going to need to calculate the gradient of the measured signal, it is more convenient to fit the profile with Gaussian curve in order to avoid noise from signal fluctuations. Fit is done for the Gaussian curve defined as $F(x) = a \cdot exp(\frac{(x-b)^2}{2c^2})$, where $a = 95$, $b = 0.033$, and $c = 0.005$.

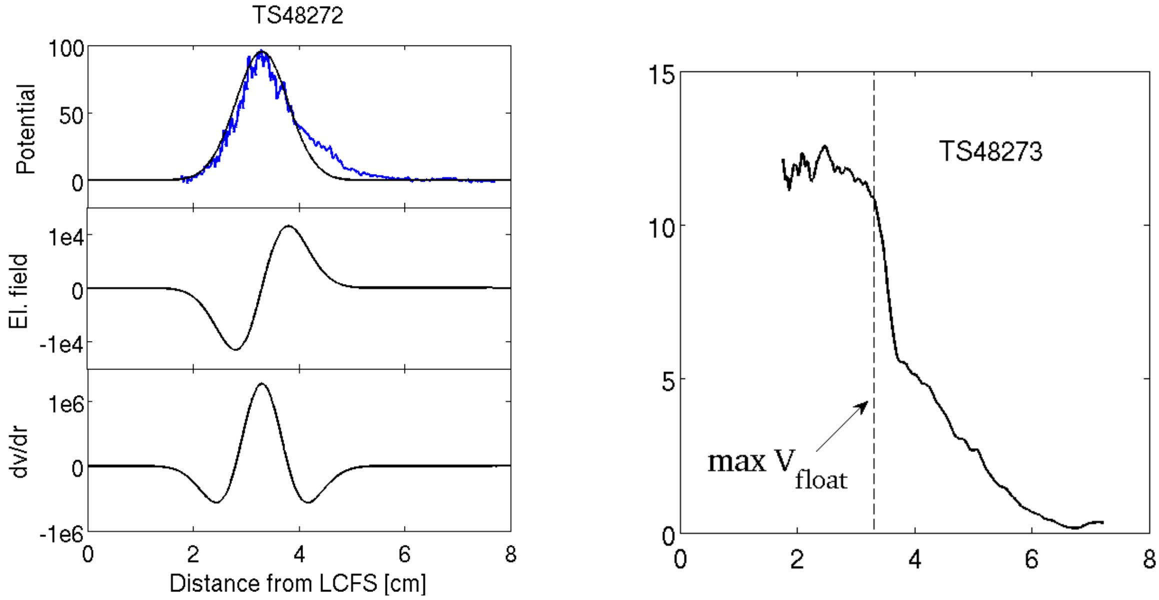

(a)

(b)

Figure 5.7: *(a) Estimation of the E × B shearing frequency. (b) Edge density profile showing the presence of the transport barrier due to the large radial electric fields.*

Associated radial electric field E_r and the E × B shearing frequency $\omega_s = \frac{dv_{E\times B}}{dr} = \frac{d}{dr}\frac{E_r}{B}$ are plotted on Figure 5.7a. Here we take the magnetic field at the plasma edge of 3T. For our potential profile with the amplitude of ≈100V, the shearing frequency is about $1.6 \cdot 10^6 \mathrm{s}^{-1}$. If we consider typical blob velocity $v_b = 1000 m/s$, the time that is necessary for blob to travel the distance of 1cm is equal to 10^{-5}s. This is about 10 times slower than the shearing frequency rate. This simple comparison suggests that the shear induced by the strong electric field generated by an active ICRH antenna can actually destroy the blob. The evidence of the formation of a small transport barrier due to a flux tube biasing to large potentials can be seen on the edge density profile - Figure 5.7b[2].

---

[2] Shots TS48272 and TS48273 are identical, but for the first one the probe was operating in the floating

Instead of continuous exponential decay, the edge density profile is characterized by a sharp decrease (factor of 2 over 5mm) indicating the formation of transport barrier. The effect of the transport barrier formation achieved by the biasing of narrow poloidal rings of the wall components was modelled in [Ghendrih 03]. This has an beneficial effect on the tokamak chamber which is protected from the energetic bursts. Our observations provide experimental evidence of a reduction of radial turbulent transport by localized SOL biasing. It is important to note that the observation of the sharp density drop was observed many times for various plasma conditions. In the shot presented here, the probe is connected to the upper part of the antenna structure. But the same profiles were measured also when the probe was connected to the middle of antenna where the maximal floating potential reaches only less than 30V (see Figure 5.14). It has to be taken into the account that floating potential measured by the probe is lower bound of the true plasma potential which can be several times higher which will be discussed in chapter 7.

5.3.4 Density scan

It was shown above that there is a link between the poloidal position of the peaks in density profile and the position of the two potential lobes. The main goal addressed here is to answer to following question: could be the asymmetry of the up and down intensity of the measured potential consistently explained by a poloidal density modification in front of the powered ICRH antenna?

Recent experiments show that perturbations of V_{float} are strongly affected by plasma density [Kubič 11]. For a given machine configuration and constant ICRH power the amplitude of floating potential decreases with increasing density (see Figure 5.8). This effect appears to be independent on plasma current, heating power or type of Faraday screen.

- **old screen:** The density scan was performed in four shots. Moreover, to eliminate the possibility of poloidal dependence, a scan of plasma current was done for three of the shots, each with 8 probe reciprocations. The Q1 antenna was firing at constant power of 2MW. The case compared here is characterized with $I_p = 0.75$MA and safety factor $q = 6.35$.
- **new screen:** All shots were performed for plasma current $I_p = 1.1MA$ yielding the safety factor $q = 4.35$. For that configuration, probe is connected to antenna ∼10cm below the mid-plane. Two ICRH antennas were firing together with the total input ICRH power of 2MW each.

---

mode while in the second in the saturation mode.

Let us consider two limit cases obtained during the new FS operation. First with the minimal, and the second with the maximal density. When the density is high ($\overline{n}_e = 7.0 \cdot 10^{19} m^{-2}$), measured V_{fl} reaches up to ~95V. By decreasing the density to $\overline{n}_e = 5.6 \cdot 10^{19} m^{-2}$, floating potential increases rapidly up to ~190V. This implies that for a 20% change of plasma density, V_{fl} changes by factor of 2. The result is comparable with the conventional screen observations. Although, the amplitude of the V_{fl} and heating power are different, the relative change of the floating potential yields factor of 2 for 20% change of the density.

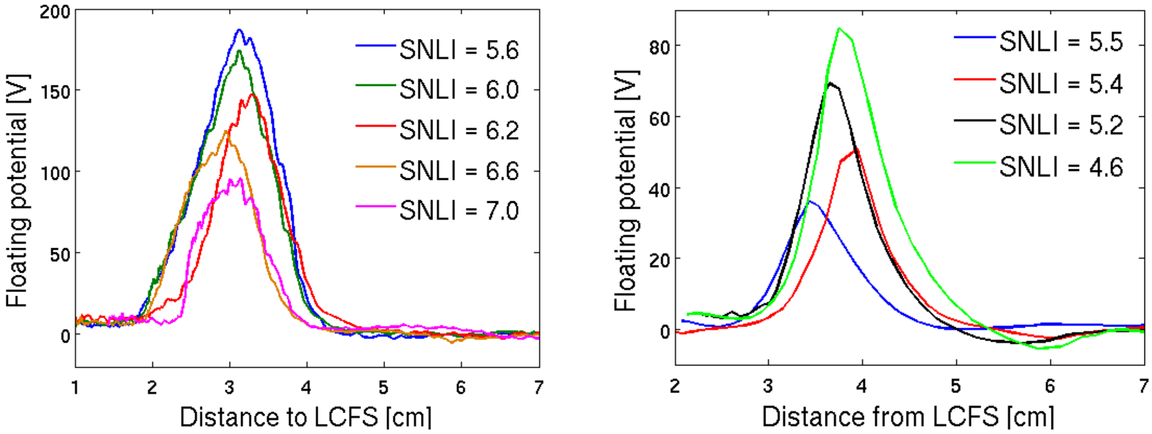

(a) New screen (b) Old screen

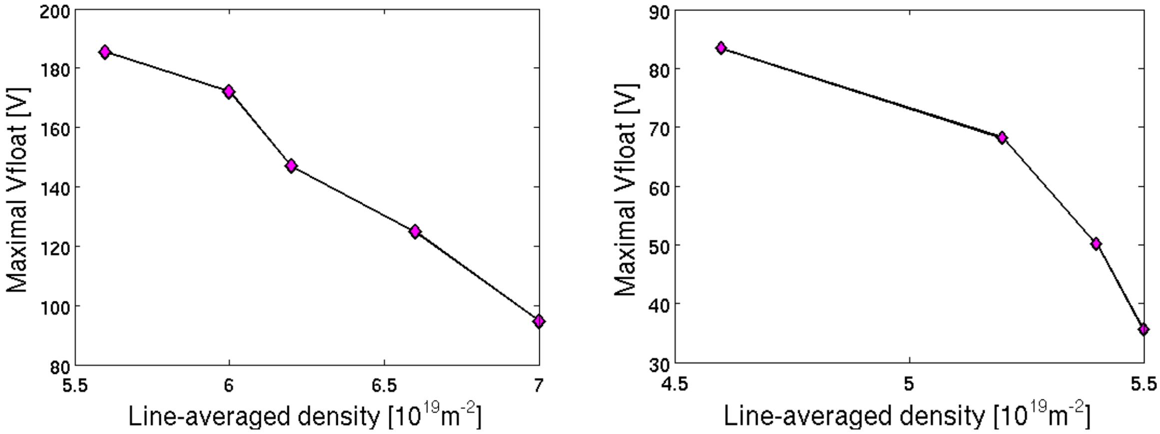

(c) New screen (d) Old screen

Figure 5.8: *Radial profile of the floating potential measured by the probe connected to Q5 antenna as a function of plasma line-averaged density for (a) new and (b) old Faraday screen. (c) and (d) Maximal values of the* V_{float} *as a function of plasma line-averaged density for both screens.*

In order to obtain the same ICRH power for different values of plasma density it is necessary to vary the voltage on the antenna straps accordingly. Each strap is equipped with 2 RF probes located at the top and the bottom of the strap that measure applied voltage, V_{strap}. The strap voltage increases with decreasing density. Time evolution of the V_{strap} measured on the new FS for the lowest (left) and highest (right) density case is shown on Figure 5.9.

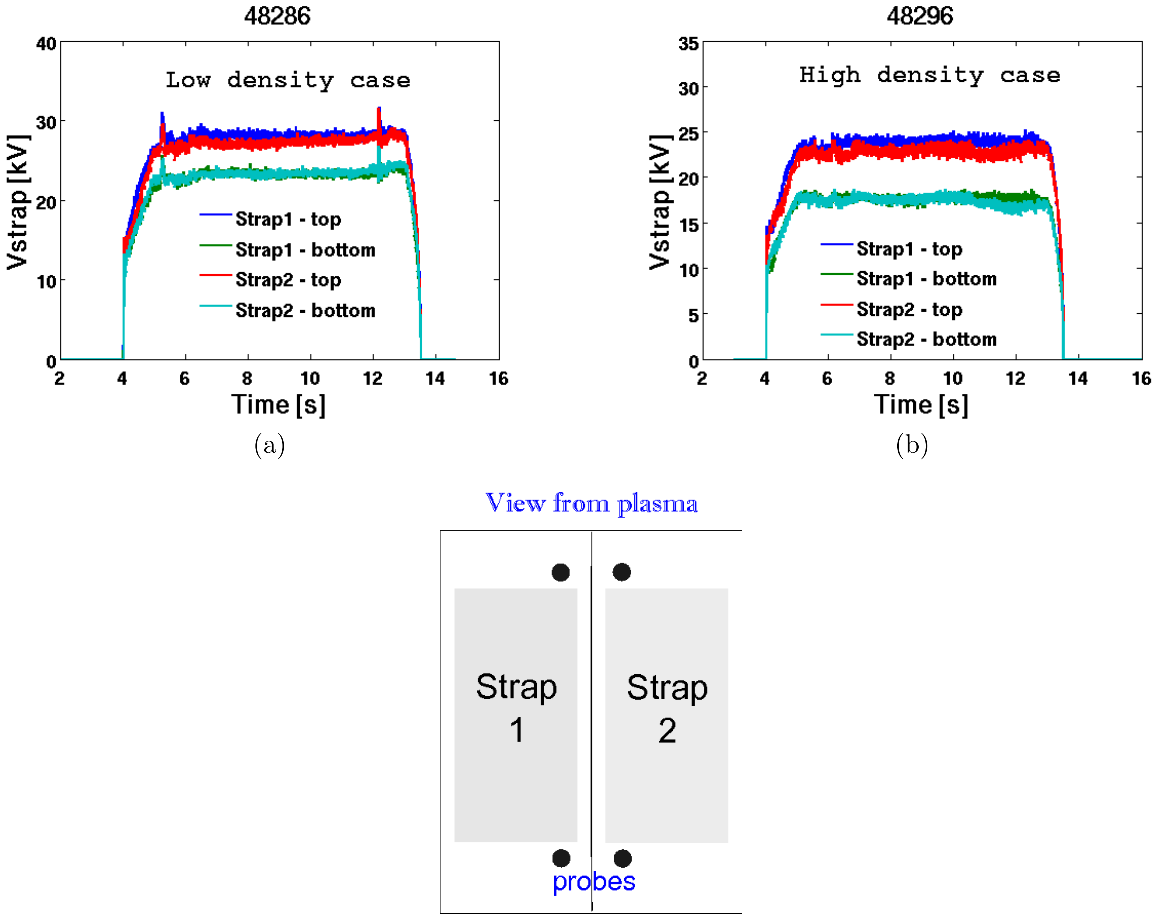

(a) (b)

(c)

Figure 5.9: *Time evolution of the voltage applied to antenna straps (new screen) for minimal (left) and maximal density (left). Location of the probes is schematically drawn in the middle.*

As can be seen, voltage measured at the top of the straps is by ∼5kV higher compared to the bottom. This discrepancy has pure technical reason. The capacitors are not fed symmetrically and the difference of ∼5kV is measured independently on plasma density and even in vacuum. For further purposes, an averaged value from all four capacitors is used.

One can also calculate the skin depth which defines evanescent layer. A general attenuation formula is used for the skin depth calculation in the following form:

$$V(x) = V_{strap} \cdot exp\left(-\int_{0}^{x} \frac{\omega_{pe}}{c} \mathrm{d}x \right) \tag{5.1}$$

where ω_{pe} is the local plasma frequency. To obtain distance from the antenna x, the probe position is mapped to the poloidal plane of the antenna, and the radial distance between the probe and the antenna lateral limiter is calculated. We assume that the voltage applied to the strap is constant and the density values are taken from real measurements by the probe. We further assume that there are zero gradients parallel to the magnetic field. Let us now consider data obtained during the conventional screen operation. The edge density, attenuated voltage and floating potential profiles are plotted on Figure 5.10. All figures are drawn for the 'limit' cases, i.e. lowest and highest values of $\bar{n}_e$.

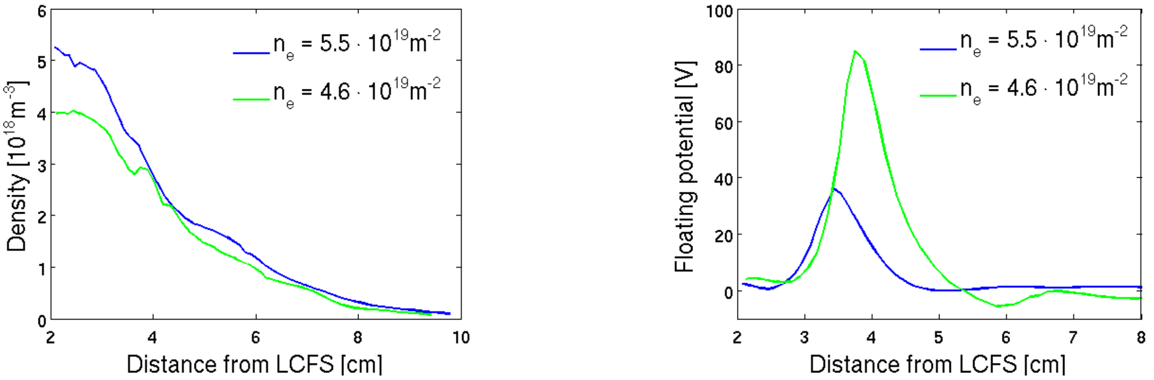

(a) Density (b) Floating potential

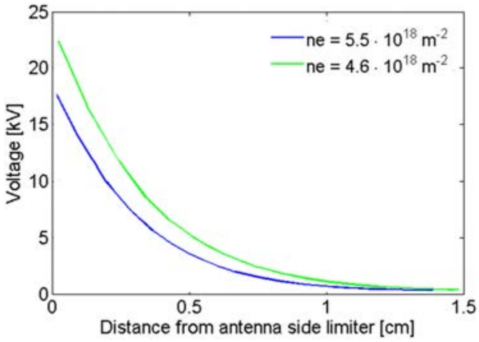

(c) Voltage

Figure 5.10: *Radial profile od density (a) and floating potential (b) for minimal and maximal density case in density scan experiment during conventional screen operation. (c) Voltage as a function of distance from the antenna side limiter. Skin depth is defines as an e-folding length of the profile.*

Values of key parameters are listed in the Tab. 5.2: the line-averaged density $\overline{n}_e$, maximum of floating potential V_{fmax}, the mean voltage on antenna strap V_{strap} and the skin depth λ_{skin} which characterizes how far into the plasma the evanescent wave is transmitted from the strap.

The density and V_{strap} change by ~20% as well as the skin depth and the floating

Shot	$\mathbf{\bar{n}_e}$ $[10^{19}m^{-2}]$	$\mathbf{Vf_{max}}$ [V]	$\mathbf{V_{strap}}$ [kV]	$(\omega_{\mathbf{pe}}/\mathbf{c})^{-\mathbf{1}}$ [mm]
		Old screen		
44105	5.5	36	17.5	29
44109	5.4	50	17.4	34
44112	5.2	69	19.4	27
44113	4.6	85	22.2	31
		New screen		
48286	5.6	190	25.4	5.0
48290	6.0	175	23.9	5.0
48291	6.2	150	22.7	4.0
48295	6.6	125	21.4	3.6
48296	7.0	95	20.4	3.6

Table 5.2: *List of main parameters in density scan experiment.*

potential changes by a factor of 2. Simple 1D modelling predicts that potentials induced by antenna should be linearly proportional to the strap voltage. Therefore, such a small variation cannot cause such strong modulations of floating potential and the key factor is hence plasma density. These results indicate that control of edge density might provide a means to attenuate RF sheath effects in ICRH-heated tokamaks. More sophisticated 2D modelling is needed including self-consistency between the potential structure and radial currents [Faudot 10]. These measurements might provide clues about the radial conductivity of the plasma.

5.3.5 Power scan

The effect of different input ICRH power on SOL parameters was studied for the following plasma configurations: heating power was injected from two ICRH antennas (Q2, Q5) with total power of 3MW but various antenna-to-antenna power ratio (see Tab. 5.3). Plasma current was kept constant at 1MA. For that current, the reciprocating probe is magnetically connected to the mid-plane in the poloidal projection of Q5 antenna position. As was mentioned earlier, mid-plane is a region where potentials are minimal. Here, for the first time, a special attention will be paid not only to the B-side of the probe that is magnetically connected to a powered antenna, but also to the other unconnected side of the probe. Radial profiles of V_{float} for both sides of the probe are plotted on Figure 5.11.

Let us first describe measurements on B-side of the probe which is magnetically connected to powered Q5 antenna. As naturally expected, V_{float} increases with increasing

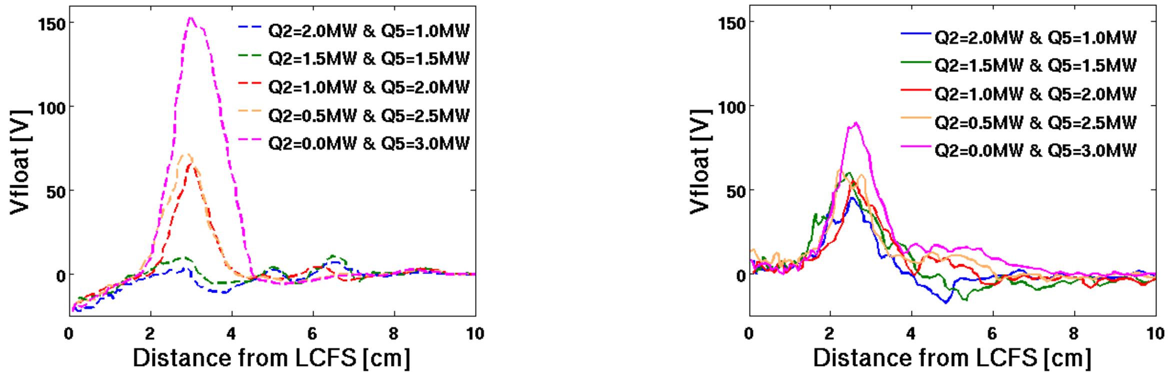

(a) A-side (b) B-side

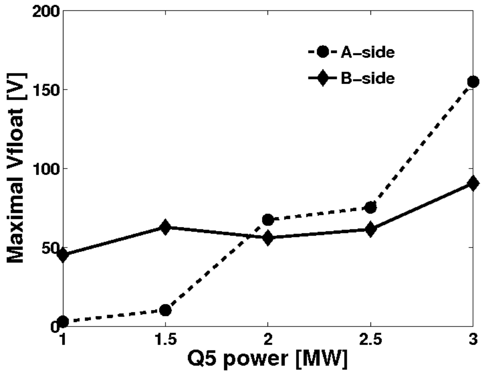

(c) Maximal V_{float}

Figure 5.11: *Measurements of the floating potential on both sides of the probe for various antenna-to-antenna power ratio: (a) A-side, (b) B-side and (c) for maximal floating potential.*

power injected by Q5 antenna, P_{Q5}. Change of V_{float} is very moderate for power going from 1MW up to 2.5MW. In that region of input power by Q5 antenna, V_{float} increases from 40V up to ∼60V. The saturation of the measured potential with the low power (<1.5MW) was reported in [Colas 07a]. Here, we can extend the power limit up to 2.5MW. In the last case when Q2 antenna is turned off and Q5 is firing at 3MW, steep increase of V_{float} by ∼30V is observed reaching maximum of about 90V. Comparing to lowest input power by Q5 (1MW), an increase of the amplitude of V_{float} is greater than factor of 2. More interesting are measurements provided on the other side of the probe. A-side of the probe is not directly connected to an antenna but mostly via high field side to the inner wall or the toroidal pump limiter located at the bottom of the vessel. Despite the above mentioned facts, floating potential increases linearly with the power injected by Q5 antenna and does not saturate. Moreover, perturbations of V_{float} are more intense compared to B-side reaching ∼160V for 3MW coupled power from Q5. This is 2x higher in comparison with the B-side. It is not yet clear why the potential measured on the

A-side is much higher compared to B-side. Same effect is observed for a field lines passing near the bottom of antenna strap [Gunn 08].

Shot	**P**$_{Q2}$ [MW]	**P**$_{Q5}$ [MW]	**VfA**$_{\mathbf{max}}$ [V]	**VfB**$_{\mathbf{max}}$ [V]
48270	2	1	3	45
48264	1.5	1.5	10	63
48265	1	2	68	55
48267	0.5	2.5	75	61
48268	0	3	155	91

Table 5.3: *List of main parameters of power scan experiments.*

Such a difference between V_{float} measurements on both sides of the probe is quite surprising. Basic Mach probe theory assumes that size of the probe can be neglected compared to the dimension of the SOL. Therefore, probe can be considered as a single point situated in the space. But why do we measure a different potential on both sides of the probe? Does it mean that the size of the probe (Δ = 4cm, which is a maximal width of perturbed zones) cannot be ignored and plasma perturbations caused by the probe presence have to be taken into account? According to [Dejarnac 07], the difference between the floating potential measured on both sides of the probe can be expressed as:

$$\Delta V_{float} = V_{float}^{B} - V_{float}^{A} = \bar{T}_e \, ln \left(\frac{J_i^B}{J_i^A} \right) + \Delta T_e \, ln \frac{\sqrt{J_i^A J_i^B}}{\bar{J}_e} \tag{5.2}$$

where $\bar{T}_e = (T_e + T_i)/2$ and $\Delta T_e = T_i - T_e$. This expression shows that ion flux asymmetries and electron temperature asymmetries can contribute to a difference in floating potential. The first term on the RHS is proportional to the parallel ion flow while the logarithm in the second term of Equation (5.2) is practically constant for fixed plasma density, independent of the ion flow speed. However, if we look on Figure 5.6, radial position of minimal flow corresponds to the maximum of V_{float}, whereas Equation (5.2), based on Mach probe theory, predicts ΔV_{float} to be zero for no parallel flow in the SOL. By comparing measurements shown on Figure 5.11, no clear correlation with Equation (5.2) is observed. This could mean that the standard Mach probe theory is not sufficient for the description of biased flux tubes in the scrape-off layer. As mentioned earlier, these observations could imply that the probe size plays an important role. Perhaps the downstream side of the probe should be regarded as a private SOL into which the rf rectified potential might not be able to systematically penetrate, depending on plasma conditions.

Similarly to B-side, one can create a 2D image of the floating potential measured on the A-side of the probe (Figure 5.12a). As can be seen, general pattern is similar for both sides of the probe. Despite the fact that the intensity of induced potentials is lower by ≈100V on the A-side of the probe, it can still reach 100V in the lower part of the antenna structure. It is important to recall that these mapping images were obtained from shots characterized by ICRH injected power of 1MW. In order to understand the discrepancy of V_{float} measurement on both sides, a full mapping for higher power needs to be done. Based on these unexpected measurements, one can naturally ask if the floating potential is really a measure of the plasma potential. Answer to this question will be treated in the next chapter by use of modelling.

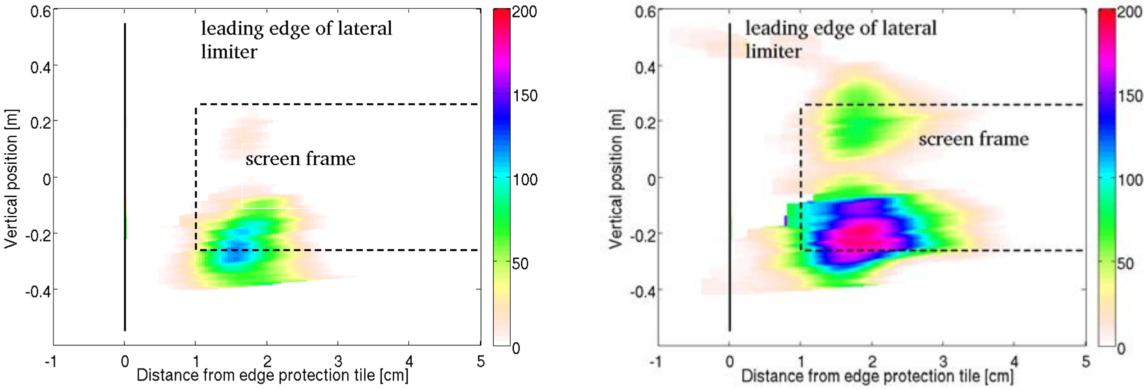

(a) A-side

(b) B-side

Figure 5.12: *Detailed 2D map of floating potential measured on flux tubes unconnected (a) and connected (b) to powered ICRH antenna equipped with the new FS.*

5.3.6 Current driven to a powered ICRH antenna

Having a detailed map of the SOL parameters along the antenna structure allows us not only to know the location of the most perturbed zones, but it could be also helpful in providing an idea about the current driven by the antenna. This large electron current was already measured on the TEXTOR tokamak and it was shown that this DC current (up to 400A) extends toroidally all around the circumference of the machine and returns to the wall via conducting objects which are electrically connected to the wall [Nieuwenhove 92].

Let us consider the mapping data obtained with the old Faraday screen. The reason why we choose older data despite the fact that we do not have the full map of the antenna is simply because these data were obtained with a probe running in the swept mode. Thus, we can use the I-V characteristics and deduce the current which is collected by the probe for the zero applied voltage to the probe - short-circuit current. For such

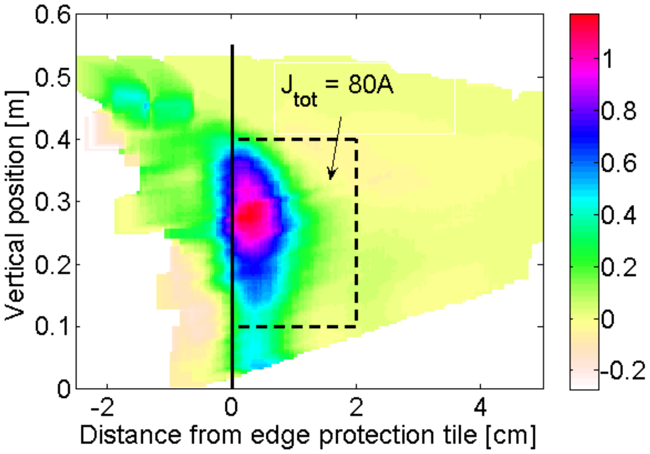

Figure 5.13: *2D map of short-circuit current collected by the probe. The current driven by an active antenna is calculated in the frame surrounded by dashed lines.*

condition we assume the probe to be completely grounded and the current collected by the probe comes directly from the antenna. Resulting map of short-circuit current is shown of Figure 5.13. The current driven by the active antenna was calculated for a small rectangular box enclosing only the zone with high V_{float} perturbation (drawn by dashed lines). The total current integrated across the selected region is about 80A. If we assume the same value around the bottom corner plus the rest of the antenna surface, the total current driven by the whole antenna structure could be estimated up to 200A which is in good agreement with the TEXTOR measurements. One could also remark that a theoretical basis for parallel DC currents was proposed [Ngadjeu 11]. Such currents were predicted to be driven by the perpendicular exchange of rf polarization currents between asymmetrically biased flux tubes (i.e. one end biased with rf voltage and the other end, the probe, grounded). That model was based on the flute assumption (potentials are assumed to be constant along open magnetic field lines, except in the sheaths), which is valid over about 50cm for Tore Supra parameters. That parallel currents are observed over connection lengths greater than 10m is doubtlessly an important finding in this respect.

5.3.7 Strap power imbalance

One of the sessions dedicated to the study of the new FS performance was devoted to investigation of imbalanced strap power ratio. Left-to-right strap power ratio was changed in a series of shots. Notation is shown on Figure 5.14c. Looking from plasma, 'Left' strap is located on the right hand side, and 'right' strap is on the left hand side. For all discharges only Q5 antenna was firing with 1MW of input power. Line averaged density was kept constant at $\bar{n}_e = 5.5{\cdot}10^{18}m^{-2}$. Radial profiles of edge density and parallel Mach number for various strap power ratios are shown on Figure 5.14. No effect of strap power imbalance is observed on edge density profiles. Therefore, we can conclude that only aspect affecting edge density profile measured by Langmuir probe is the presence of power ICRH antenna itself. Redistribution of injected power is not important in sense of density measurements.

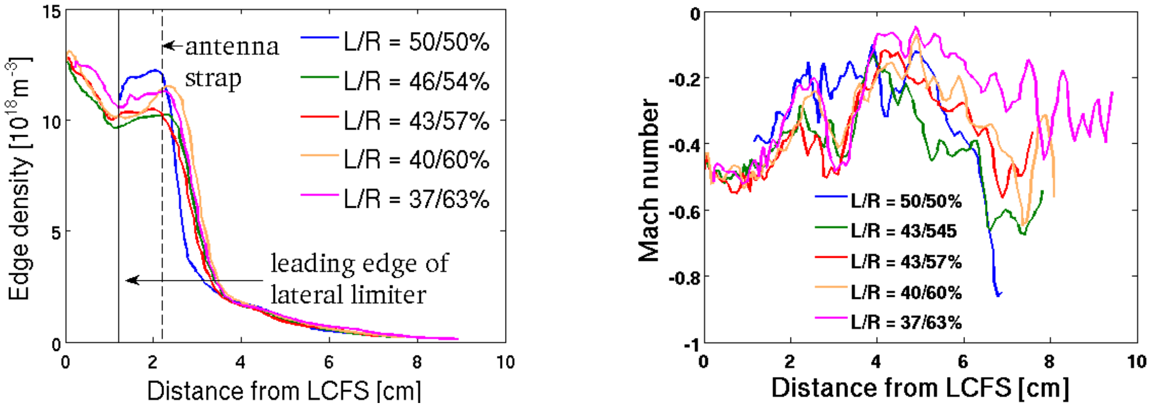

(a) Density (b) Mach no.

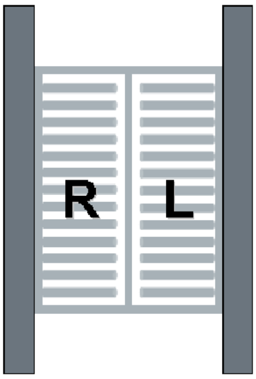

(c) Notation

Figure 5.14: *Effect of different strap power ration on (a) edge density and (b) parallel flow measurements. No variations are observed. (c) Notation.*

Measurements of V_{float} are plotted on Fig. 5.15. As can be seen, no particular effect of strap power imbalance is observed on the A-side of the probe. That is quite expected because A-side of the probe is not magnetically connected to powered ICRH antenna and, as shown on Fig 5.11, potentials measured there are low for 1MW of input power. Let us then take a look more closely on the B-side of the probe. As mentioned above, B-side of the probe is magnetically connected mostly to adjacent limiter on antenna. If probe plunge is sufficiently deep, field lines connected to probe pass up to ~2cm in front of the leading edge of lateral limiter, depending on plasma size and antenna position with respect to outboard limiter. As reported above, flux tubes passing in front of the antenna are not biased to high potential and the most affected are those flux tubes connected to adjacent limiter on RHS of the antenna. However, density radial profiles exhibits a sharp decrease starting approximately 1cm behind the leading edge of the LL. The zone over which the density decrease occurs, corresponds radially to the highly perturbed zones. Moreover, such a steep drop is observed only on profiles connected to the antenna equipped with the new type of FS (one can compare with Figure 5.10a).

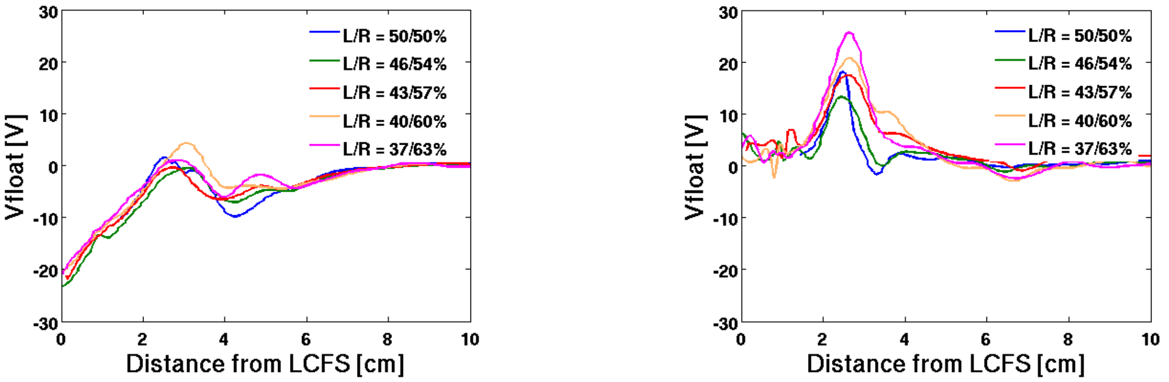

(a) A-side (b) B-side

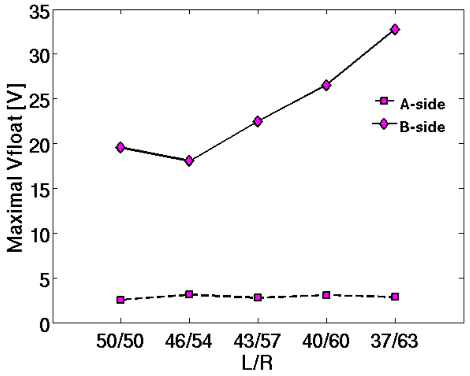

(c) Maximal V^{B}_{float}

Figure 5.15: *Floating potential measurement during strap power imbalance ratio experiment.*

Level of V_{float} perturbation is small and does not exceed 40V, which appears to be a typical value for $I_p = 1MA$. Perturbation of V_{float} varies as the L/R power ratio changes (Tab. 5.4). It is worth noticing that the potentials increase with the decreasing L/R strap power ratio (i.e. less power is injected from the 'left' strap). But the probe is connected to the right hand side of the antenna where 'left' strap is placed. As naturally expected and as was shown above, induced potentials increase with increasing power. But in this case, total input power does not change, it is only non-equally redistributed. It provides also evidence that flow of image currents on antenna structure is complex and requires a full 3D electromagnetic calculations.

Shot	**Left** [%]	**Right** [%]	$\mathbf{V_{fmax}^{A}}$ [V]	$\mathbf{V_{fmax}^{B}}$ [V]
48257	50	50	2.6	19
48258	46	54	3.2	18
48259	43	57	2.9	22
48260	40	60	3.1	26
48261	37	63	2.3	32

Table 5.4: *List of main parameters of strap power imbalance ratio experiment.*

Summary

RF-induced SOL modifications are investigated by means of tunnel/Mach probe with the emphasis on the comparison of the new design of the FS with the old conventional one. In general, lobes pattern is similar to previous observations. However, with the new magnetic reconstruction method that uses EFIT calculations, these high potentials appear to be induced on the lateral limiters in the case of new FS and not in front of the antenna as is usually predicted by modelling. Therefore, in order to explain disagreement with the model, side limiters cannot be neglected. In addition, measured potentials induced by the new screen are several times higher reaching up to 200V with typical radial width of 4cm. Another significant observation is the increased radial width of the structures associated with the new FS. Fluid modelling predicted that the radial width of the structure could be enhanced by radial currents, depending on the effective parallel length over which radial currents are exchanged between neighbouring flux tubes. In [Faudot 10], it was concluded that widths of 1 cm which were observed on the old screen implied that the effective parallel flute length was shorter than the magnetic connection length to the probe. Now with the new screen, wider structures are observed. Does it mean that something has changed, and that now the effective parallel length has increased? It should be noted that if the effective parallel flute length for radial current exchange is comparable to the connection length, then the radial width can increase from the skin depth (a few mm) up to 10cm for Tore Supra conditions (this was explicitly stated in [Faudot 10]). However, again, we remark that the structures do not originate from the front of the antenna, but from the sides of the bumpers. Therefore, the notion of broadening of a source due to the evanescent slow wave in front of the antenna is obviously questionable. Is the radial width we observe an indication of broadening of a narrow source of rf potential, or is it a direct measurement of a source which is already very wide? The up and down asymmetry of the intensity of the measured floating potential seems to be consistent with the poloidal density pattern with lower density below the mid-plane and the fact, the measured potential is a strong function of plasma density. According to experimental observations, either with old or new FS, 20% change in the plasma density causes the floating potential to vary by factor of two. Parallel flow is modified as well during ICRH operation. The flow, which is driven by blobs, changes monotonically in radial direction in ohmic phase while during the ICRH phase is strongly sheared. In the contrary to the old screen, the shear does not vanish for high densities. It was also shown that this effect leads to reduction of radial transport in RF-biased flux tubes. Difference in floating potential measurements on both sides of the probe is interesting especially from simple Mach probe theory point of view. Our measurements suggest that probe acts like a small limiter and its size cannot be neglected. To fully understand this observation an advanced modelling is needed. Large potentials do not have to appear strictly only on the connected side of the probe. For certain configurations, a huge floating potential is measured also on the unconnected side of the probe. First case happens when the probe is connected to the bottom of the strap, where potentials are high (observed for both screens). The other case was observed for large injected power from one ICRH antenna. In both cases, the floating potential is 150V and the width of the peak becomes comparable with the radial dimension of the probe holder. I would like to mention here that this work I presented on 20^{th} International Conference on Nuclear Engineering was awarded by the best paper in ‘Student paper competition’ section.

Chapter 6

Modelling of biased flux tubes

6.1 Introduction

Models used to simulate a probe, or any other object, that is magnetically connected to an active antenna are generally described as flux tubes that are bounded at each end by an electrode. Each magnetic field line intercepted by a metallic surface can be considered as a flux tube along which the potential oscillates at the rf frequency. In the case of plasma facing components far away from the antenna but still magnetically connected to it, negative (net electron) DC current is collected on the powered ICRF antenna, while positive (net ion) DC current is collected by a magnetically connected Langmuir probe as is observed experimentally in TEXTOR [Nieuwenhove 92], Tore Supra [Gunn 08] and ASDEX Upgrade [Bobkov 10]. To achieve this in modelling, one has to allow exchange of rf and dc current between the active flux tube and neighbouring passive flux tubes. If no transverse currents are taken into account, no parallel currents arise and the wall remains floating. Some of the approaches using 2D fluid models have considered transverse rf currents able to modify the rectified potential [Faudot 06] and to drive net parallel dc current through the sheath [Ngadjeu 11]. The total sheath potential consists, with respect to tokamak ground, of nonambipolar and ambipolar parts V_{fl} and V_{amb}, respectively. The ambipolar part refers here to a potential allowing ambipolarity for zero ion current to the wall. For concreteness, imagine a small probe embedded in a grounded wall. If the probe draws zero net current when biased to zero volts with respect to the surrounding wall, it (and the wall) are said to be naturally floating. The expected potential drop in the sheath is then the famous -3T$_e$ from classical sheath theory, which we refer to as V_{amb}. In the more general situation, it is possible that electric currents flow to the wall. These currents can be measured directly when the probe is biased to zero volts with respect to the grounded wall. The voltage to which the probe must be biased in order to obtain zero net current is the floating potential V_{float}. The sheath potential with respect to the grounded wall is therefore $V_{sh} = V_{float} + V_{amb}$.

In a typical double probe model, one of the electrodes is biased with an ac potential modulated at the rf frequency and represents the antenna, while the other electrode representing a probe is biased to constant dc potential. It is generally known that it is the more positive electrode that defines the final potential on the flux tube (see Figure 6.1). This directly implies a following question: if we bias a probe, what do we really measure? Can we still consider our measurements to be passive? Only a probe biased at 0V can be considered as non-perturbing (if we neglect the dimension of the probe). For any positive biasing, a modelling is needed. Modelling presented in this chapter uses a 1D fluid code based on the idea of exchanging rf and dc currents between neighbouring flux tubes working under the assumption of flute hypothesis. The simulated dimension is the cross-field direction. Parallel gradients are assumed to be negligible. Firstly, a model description is given. The second part is then devoted to the discussion of the obtained results and their possible links to our probe measurements.

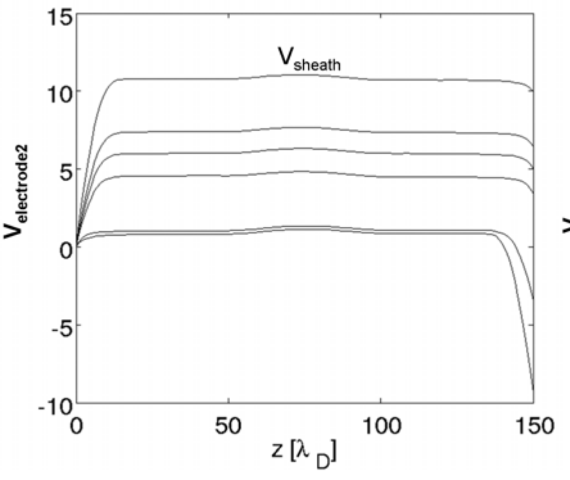

Figure 6.1: *In the double probe model, it is the positive electrode that defines the final potential on the flux tube.*

6.2 1D fluid modelling

The biasing of a flux tube is able to induce many effects like local convection, particle acceleration in the sheath and around the biased flux tube, and especially sensitive currents (dc or rf) can be driven and flow along and across the magnetic field. This effect can help us to understand the current measurements from Langmuir probes, especially when the probe is magnetically connected to a powered ICRH antenna. Each magnetic field line intercepted by metallic surface can be considered as a flux tube along which the potential oscillates at rf frequency and is longitudinally constant. Such a situation is equivalent to a double probe model. The model presented here takes into account the effect of both rf and dc transverse currents. Namely, it is the inertia and viscous current. Recent improvement of the model presented here has been made and takes into account also the friction term [Faudot 13]. The rectification of the rf potential due to asymmetrical inertia of ions and electrons in sheaths and parallel dynamic of rf sheaths has been studied in previous works. Some of the approaches using fluid models have considered transverse currents due to collisions both in the case of Langmuir probes [Rozhansky 99, Günther 94] and in the case of edge plasmas in tokamaks [Rozhansky 01]. Other studies deal with rf sheaths driven by ICRH and use fluid model including transverse currents with the contributions of the rf polarization currents [Faudot 06]. Previous works considering only rf polarization currents have shown that while the time average of the transverse currents is zero, they are able to induce a parallel current [Ngadjeu 11].

6.2.1 Model description

A schematic of the simulated region is shown on Figure 6.2. Open magnetic field lines (OMFL) are enclosed at each end by a biased electrode perpendicular to magnetic field. One of the electrodes is biased with a rf oscillating voltage V_{rf} representing an active ICRH antenna. The other electrode is considered to be a probe biased at constant voltage V_{dc}. Potentials are assumed to be constant along OMFLs (flute hypothesis), except in the sheaths. The active flux tube can exchange transverse currents (both rf and dc) with neighbouring passive tubes whose both extremities are grounded. The parallel current is calculated from the ion flux determined by the Bohm criterion and for massless electrons (Boltzmann law). This is a simplified model of a real situation in which the probe sits between the two electrodes where one of the is biased with rf voltage while the second one is grounded (chamber wall).

The analytical model proposed here solves self-consistently rf and dc transverse current and plasma potential. Here, we focus mainly on the outputs of the code, so a basic description of the code is given. More detailed code description with the code implementation and validation can be found in [Faudot 11a]. By applying the current conservation law $\nabla \cdot (j_{\parallel} + j_{\perp}) = 0$ with a double probe model including transverse currents and integrating over one flux tube embedded by two electrodes using a 'flute hypothesis' we obtain

$$j_i - j_e\, exp(-\Phi + \Phi_{rf}) + j_i - j_e\, exp(-\Phi + \Phi_{dc}) = L_{\parallel} \nabla_{\perp} \cdot [j_{\perp}^{rf} + j_{\perp}^{dc}] \tag{6.1}$$

where j_i and j_e are ion and electron saturation current, respectively, with j_e being defined as $j_e(\Phi) = j_e exp(-\Phi)$, where $\Phi = \frac{eV}{kT_e}$. $L_{\parallel}$ is a parallel magnetic length of the flux tube, $j_{\perp}^{rf}$ and $j_{\perp}^{dc}$ are rf and dc perpendicular currents, respectively. The rf perpendicular current is defined as follows

$$j_{\perp}^{rf} = L_{\parallel}^{eff} \nabla_{\perp} \cdot \left(\frac{\partial}{\partial t} \nabla_{\perp} \Phi \right) \; , \qquad L_{\parallel}^{eff} = \frac{C_s m_i}{2\omega m_e} \tag{6.2}$$

with $L_{\parallel}^{eff}$ being a parallel effective length for a valid flute hypothesis [Günther 94]. The dc part is represented by the inertia current j^{in} caused by convective flux crossing potential structure and the viscous current j^{vis} created by a shear around the structure.

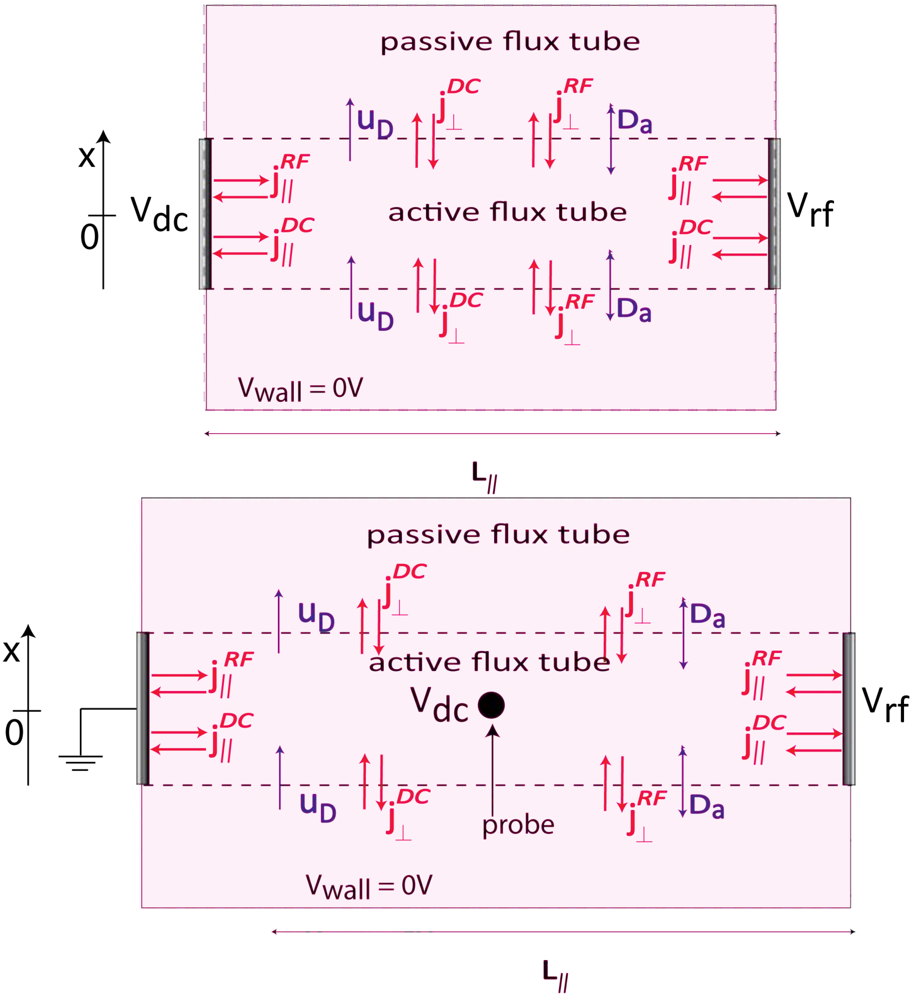

Figure 6.2: *(top) Schematic of the simulated plasma box. Active flux tubes are bounded on each side by biased electrode. Probe is located on the left side while antenna on the right side. The extend of potential structure on the probe and the antenna is different. Transverse rf and dc currents are considered contributing to parallel current driven by sheath. (bottom) Schematic of the real situation.*

The inertia and the viscous current are defined as in [Rozhansky 99]

$$j_\perp^{in} = -\frac{nm_i}{B^2}u_d\nabla_\perp^2\Phi \qquad ,and \qquad j_\perp^{vis} = \frac{nm_i}{B^2}\mu_a\nabla_\perp(\Delta_\perp\Phi) \tag{6.3}$$

where u_d is a drift velocity in the direction of local electric field with a typical value in the range of $c_s/10 < u_d < cs$ [Carlson 01], and μ_a is the anomalous viscous coefficient assumed to be of the order of the anomalous diffusion coefficient D_a. Then, we can rewrite

Eq. 6.1 into

$$1 - \frac{1}{2}[exp(-\Phi + \Phi_{rf} + \Phi_{fl}) - exp(-\Phi + \Phi_{dc} + \Phi_{fl})] \\ = \frac{L_{\|}\rho_s}{2\Omega_{ci}} \nabla_{\perp} \cdot [\partial_t \nabla_{\perp}\Phi - u_d \nabla_{\perp}^2 \Phi + \mu_a \nabla_{\perp}(\Delta_{\perp}\Phi)] \tag{6.4}$$

where $\Phi_{fl} = ln(j_e/j_i)$, ρ_s is the Larmor radius and Ω_{ci} is the ion cyclotron frequency.

The density is calculated from the mass continuity equation. The flow in the continuity equation for mass can be divided into two terms: contribution from the currents and the diffusion part:

$$\nabla \cdot (\Gamma_{curr} + \Gamma_{diff}) = S - L \tag{6.5}$$

where S denotes the source and L stands for the loss term. Considering the assumption of zero parallel gradients $\nabla_{\|} \equiv 0$, Eg. 6.5 gives

$$\frac{1}{e}\nabla_{\perp}\left[\langle j_{\perp}^{rf}\rangle + \langle j_{\perp}^{in}\rangle + \langle j_{\perp}^{vis}\rangle\right] + \nabla_{\perp}(D_a \nabla_{\perp} n) = S - L \tag{6.6}$$

The first term on the left hand side of the Eg. 6.6 equals to zero and hence we obtain

$$\frac{m_i T_e}{eB^2}\nabla_{\perp}\left[-n u_d \nabla_{\perp}^2 \Phi + n\mu_a \nabla_{\perp}(\Delta_{\perp}\Phi\right] + \nabla_{\perp}(D_a \nabla_{\perp} n) = S - L \tag{6.7}$$

Compared to previous models working with the constant density in the whole system, our model defines density with an exponential profile in radial direction to approach conditions in the tokamak scrape-off layer.

6.2.2 Numerical simulations

The shape of the imposed potentials used in our simulations is defined by following formula:

$$\Phi(x) = \Phi_0 \left(tanh\left[\frac{x + x_0}{x_0}\right] + tanh\left[\frac{-x + x_0}{x_0}\right]\right) \tag{6.8}$$

where x is a radial direction and x_0 defines a half width of the structure. Example of such a potential structure is on Figure 6.3. The half width of the potential structure on dc electrode was chosen, with respect to dimension of the probe, $x_0^{pr} = 1.5mm$. To define the half width of the rf structure we use $x_0^{rf} = 5mm$, which corresponds to a typical radial extension of measured rf-induced SOL perturbations as was shown in previous chapter. The radial width of an electrode is 60mm. It is important to point out that previous models considered identical potential structures on both electrodes. Such a shape of potential structure was chosen in order to avoid a singularity at the transition between the biased and non-biased parts of an electrode. Equations (6.6) and (6.7) are solved for a wide range of probe bias voltage Φ_{dc} in order to reconstruct I-V characteristics and hence determine the floating potential. The amplitude of applied rf potential is set to 10, and

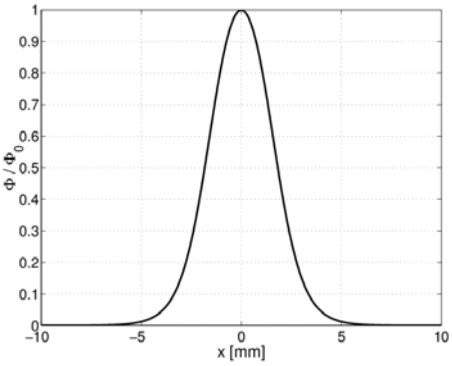

Figure 6.3: *Shape of the potential structure used in the simulations.*

the probe bias voltage is varied in the range of -5 to 13. Both Φ_{rf} and Φ_{dc} are normalized to electron temperature $T_e = 15eV$. The density profile in the simulating box is defined in radial direction as

$$n = n_0 \cdot e^{\frac{-x + x_{lim}}{\lambda_n}} \tag{6.9}$$

where x_{lim} defines half width of the box and λ_n is density decay length.

The code is based on a semi-implicit scheme. The space component is solved through an implicit scheme (matrix inversion) while the time is solved explicitly by a converging method. The rf current term plays this role and make the potential converge up to its stationary value if the driving potential is purely dc.

6.2.3 V_{float} and V_{sheath} evaluation

An example of the current profile as a function of the dc biased potential applied on the probe is plotted on Figure 6.4a. In this studied case, both rf structure and the theoretical probe are centered in the middle of a simulation box. To extract a single characteristic (time-averaged), we simply take one flux tube in the middle of the theoretical probe (x = 0). One of such a resulting double probe I-V characteristic is shown on Figure 6.4b. The floating potential is defined for zero net current to the probe. One could also consider the current collected over the whole probe surface as it is in the real measurement, and make an average of it. To avoid large uncertainty in the estimation of the floating potential due to a low resolution of Φ_{dc} (step of 15V), a linear interpolation method is used to achieve higher resolution and hence increase the accuracy.

The sheath potential is calculated instantaneously for every radial position in the middle of the simulating box. Similarly as in previous case, we can plot the V_{sh} profile as a function of Φ_{dc} (see Figure 6.5a). One can note that for negative probe voltages, the sheath potential is saturated to a value determined by the rf electrode. However, as the probe voltage increases above floating potential, the flux tube connected to the probe becomes positively biased. This is the usual behaviour of a 1D double probe system: the

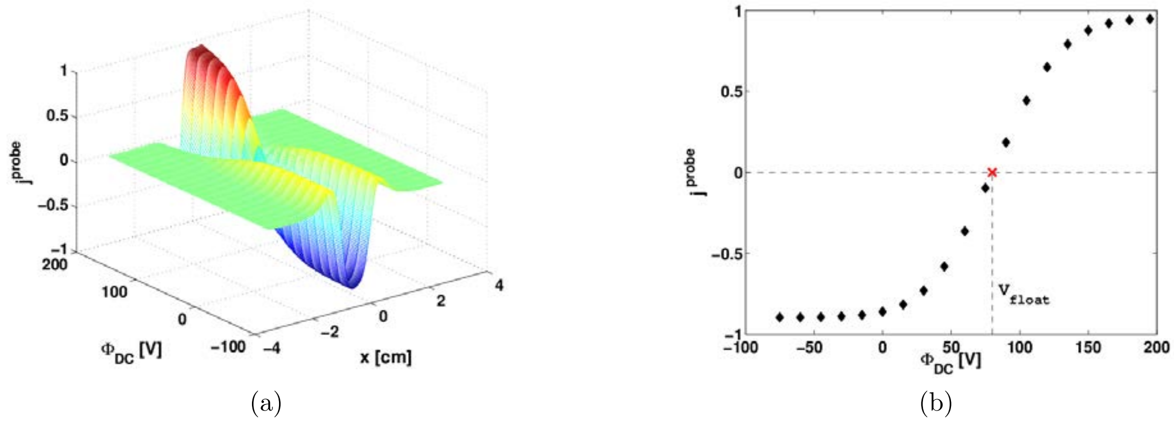

Figure 6.4: *(a) Time-averaged current profile collected on the theoretical probe for various dc probe potential applied. The probe is centred on x=0. (b) Example of the double probe characteristic in the middle of the theoretical probe.*

anode determines the plasma potential. Since the floating potential is already known, the V_{sh} can be simply obtained by finding corresponding value for $x = 0$ and given V_{float} - Figure 6.5b. As can be seen, the floating potential $V_{float} = 80V$ and the sheath potential $V_{sh} = 125V$ - giving the difference exactly equals to $3T_e$ as is predicted by the sheath theory [Stangeby 90], but for unperturbed plasma. It is also a proof that the numerics is correct in the code. More detailed validation of the code numerics can be found in [Faudot 11b]. It thus seems that even though the rf electrode does create a large positive rectified sheath potential, a small Langmuir probe inserted into that structure still floats to voltages about 3T$_e$ below that value. This behaviour is very similar to what we observe experimentally using a RFA (see chapter 7).

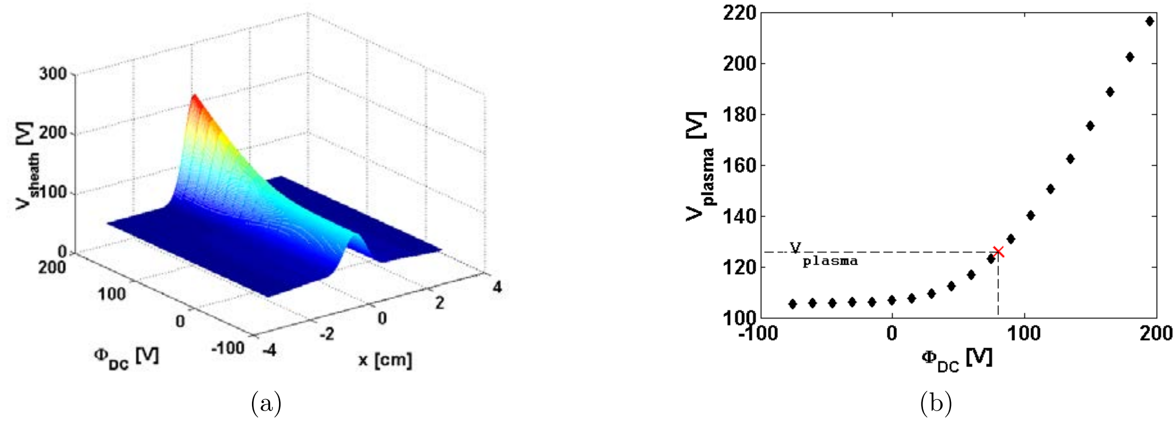

Figure 6.5: *(a) Radial profile of the time-averaged sheath potential in the middle of the box for various Φ_{dc}. (b) Once the floating potential is known, its corresponding sheath potential can be derived easily.*

6.2.4 Effect of rf width structure

Before we proceed to the study of parametric dependencies of the sheath potential, we have to define properly imposed structures on biasing plates. The dimension of the theoretical probe is given and its value is fixed in all simulations, $x_0^{pr} = 1.5mm$. Based on experimental observations, the width of the measured potential structure can vary from 10 - 30mm. Several simulations were done for various half width of the rf structure for $1 < x_0^{rf} < 20mm$. The anomalous diffusion coefficient $D_a = \mu_a = 1$ and the drift velocity $u_d = 100m/s$ to minimize their effect. Both rf and dc electrodes are aligned radially in the middle of the simulating box. As can be seen from Figure 6.6, the dependence of the potentials on the widths of rf structure cannot be neglected. This can be explained as follows. In the case of a large rf structure, which is characterized by a small gradient, the induced radial dc currents are small and hence the parallel dc currents collected on the probe come mainly from the rf radial current yielding in small floating and sheath potential. In that case the current collected on the probe saturates at j_{sat}. On the contrary, when the gradients are large (small structure), the $j_{\perp}^{dc}$ becomes dominating causing increase of the floating and sheath potential. For further purposes, the half width of the rf structure is set to $x_0^{rf} = 15mm$ which corresponds to the profile shown on Figure 6.3. It is important to mention only the current collected in the middle of the theoretical probe is taken into account.

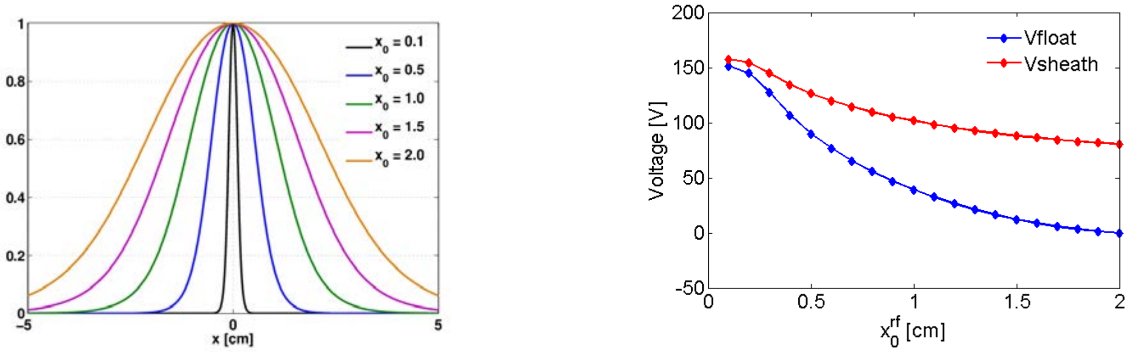

(a) (b)

Figure 6.6: *(a) rf potential structures for various* x_0. *(b) Evolution of the potentials in the middle of the box as a function of* x_0^{rf}. *The currents are driven by the potential gradient of a given structure.*

6.2.5 Scan of parameters

In order to study sheath potential in the flux tubes magnetically connected to powered ICRH antenna, we ran a scan for different transverse current values. The anomalous diffusion coefficient, as well as μ_a, was changed in the range of $1 < D_a < 5$, and the drift velocity $0 < u_d < 5000$m/s. In all simulations we consider $D_a = \mu_a$. The rest of the parameters was kept constant and the list of them is summarized in Tab. 6.1. It should be recalled that the transport at the plasma edge is governed mainly by turbulence. Nevertheless, in the scope of the problem, the diffusive approximation can be used accounting for values similar to those that are measured experimentally.

Parameter	Value	Explanation
dx	10^{-4}m	space step
dt	$2 \cdot 10^{-10}$s	time step
tfin	$4 \cdot 10^{-7}$s	final time
x_0^{dc}	1.5mm	half width of dc structure
x_0^{rf}	5mm	half width of rf structure
Φ_{dc}	[-5:13]	swept probe voltage
Φ_{rf}	10	applied rf voltage
x_{lim}	0.03m	half width of the box
ω_{rf}	$2\pi \cdot 50$	rf frequency
$L_{\parallel}$	12m	parallel length of the box
T_e	15eV	electron temperature
λ_n	0.05m	density decay length

Table 6.1: *List of fixed parameters used in simulations.*

Results of the parametric scan are shown on Figure 6.7. Dependencies of the sheath potential on the diffusion coefficient D_a and on the drift velocity u_d are plotted on Figure 6.7a and Figure 6.7b, respectively. As can be seen, the sheath potential decreases with increasing radial currents. Let us first describe Figure 6.7a. Simulations show that to achieve the same value of the sheath potential as measured in experiments, it is necessary to consider turbulent plasma. For drift velocity $u_d > 4000m/s$, where the sound speed $c_s \sim 4500m/s$, the sheath potential remains $< 1T_e$ independently on D_a, μ_a. On the other hand, to avoid convergence problems for high u_d, higher values of D_a and u_d might be needed [Faudot 11b].

6.2.6 Radial profiles of the potentials

Simulations described in previous section suggest to increase radial dc currents to obtain small the difference between the sheath and floating potential. By varying the radial position of the theoretical probe across the simulation box, we can obtain radial profile of both considered potentials, V_{float}, and V_{sh}. Both zero and non-zero radial dc current cases are compared on Figure 6.8. When no transverse dc currents are considered, the sheath potential is of the order of 3-4T_e above the floating potential with the maximum in the middle of the perturbed zone which is in agreement with Stangeby's prediction.

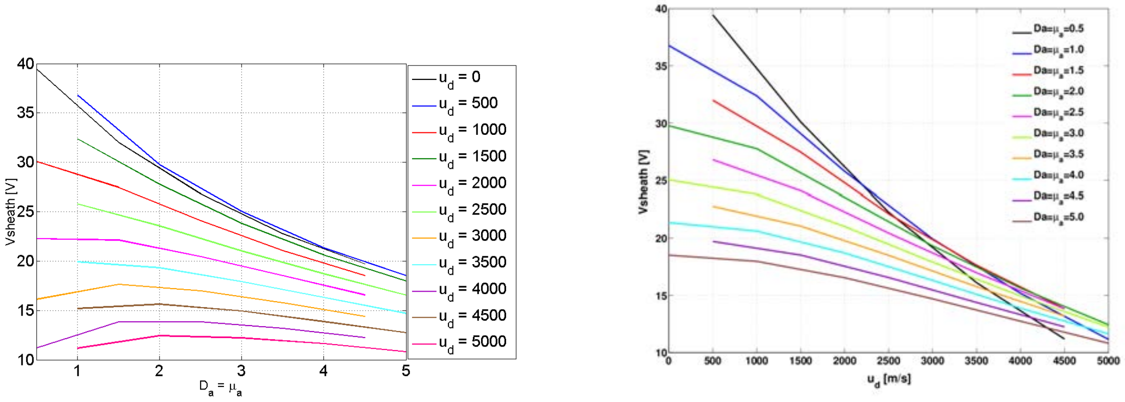

(a) Scan of D_a (b) Scan of u_d

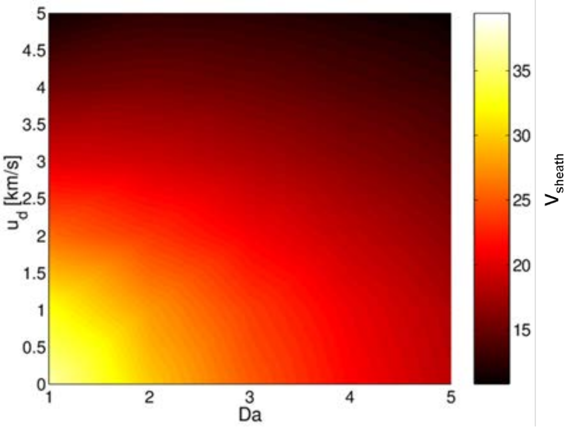

(c) Scan of D_a & u_d

Figure 6.7: *Parametric study of the sheath potential dependence on (a)* D_a*, (b)* u_d*, (c)* D_a *and* u_d*.*

But we are more interested in the case with currents flowing. Let us therefore pay more attention to simulations including non-zero radial currents. The code was run for the following parameters: anomalous diffusion coefficient $D_a = \mu_a = 1$, drift velocity $u_d = 4000m/s$, with the density e-folding length being $\lambda_n = 3cm$. In order to obtain radial profiles of the density similar to what is observed experimentally in the SOL (that is exponentially decreasing profile with the decay length of few cm), the D_a is kept to low values due to the fact that it tends to increase numerically the density decay length by decreasing the density gradient. This effect will be discussed in more detail in the next section. Resulting profiles are plotted on Figure 6.8b. The sheath potential does not change over the whole profile. On the other hand, outside the perturbed zone, the V_{float} decreases rapidly. These holes in the V_{float} profile suggest existence of a return negative current collected on the probe driven by the presence of transverse currents. Moreover, this current is quite large. The saturation of the floating potential for the $0.5 < x < 1$cm is due to the fact that V_{float} exceeds the range of applied dc voltage on the probe yielding

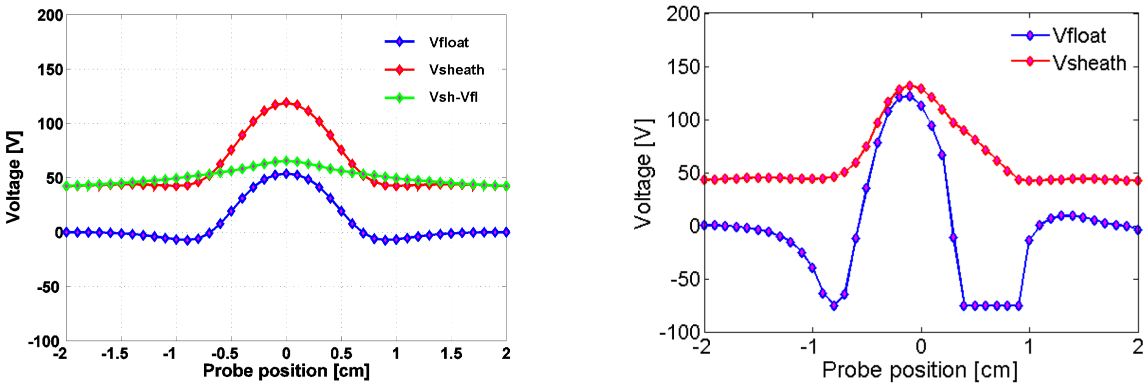

(a) Zero dc currents (b) Non-zero dc currents

Figure 6.8: *Radial profiles of simulated potentials for (a) zero dc currets and (b) non-zero dc currents.*

even lower V_{float} with the amplitude comparable in the center of the structure. Presence of these negative currents is in disagreement with experimental measurements.

One of the ideas how to explain these negative holes in the V_{float} profiles is to change the shape of the imposed structures on the biased electrodes. In general, the shape in simulations is defined by Eq. 6.8. In detailed look on Figure 6.6a, one can notice that negative holes appear at the radial position corresponding to the point where the first derivative of $\Phi(x)$ changes its sign. This in turn can have an effect on currents collected on the theoretical probe. To investigate this hypothesis, we replaced the Gaussian-like shape of the structures by parabolic one (first derivative does not change the sign). Nevertheless, simulations show no difference in the floating potential profile.

Among other factors that might have an influence on the dc currents is the density gradient which appears in Eg. 6.7. In the previous case, we assumed the density decay length being $\lambda_n = 3cm$. To decrease transverse currents, one has to increase the density gradient by defining shorter λ_n. Output of the simulations for $\lambda_n = 1cm$ is plotted on Figure 6.9. The situation is changed drastically compared to the case with $\lambda_n = 3cm$. While the negative hole on the LHS of the peak is suppressed only by $\sim 1T_e$ reaching still nearly -50V, the RHS hole is gone completely and the floating potential is back at zero level. This is caused due to a relatively high difference in density in both sides of the structure imposed by short λ_n. Since currents are proportional to the local density, smaller correction of floating potential is made for the case of low density, due to the fact that driven transverse currents are smaller as well. Even if $\lambda = 1cm$ appears to be not a typical experimental value, we will demonstrate in the next section that such a short decay length might be actually a very good choice.

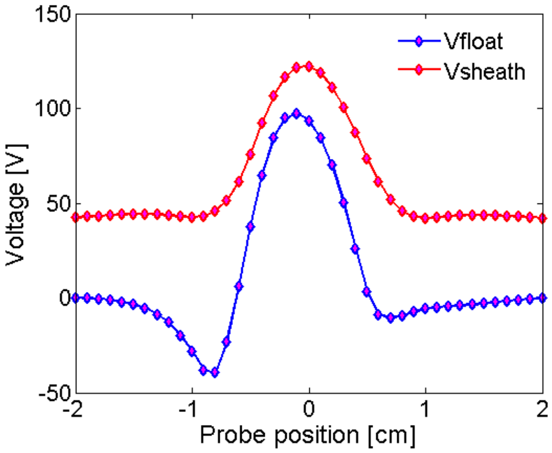

Figure 6.9: *Radial profiles of simulated potentials for* $D_a = 1$, $u_d = 4000m/s$, *and the density decay length* $\lambda = 1cm$.

6.2.7 Density profiles

Simulation results show that the reduction of the difference between the sheath and floating potential of the order of $1T_e$ can be achieved for a wide range of anomalous diffusion coefficient $D_a > 3$ and drift velocity $u_d > 2/3c_s$. In this section we will narrow this range by matching the simulation results with the density profiles measured by the probe. Example of the radial profile of the edge density measured by the RFA is shown on Figure 6.10. It is the same plunge as used for potential profiles on Figure 7.2b. Compared to ohmic or not connected case, the profile is no longer monotonic but is characterized by a hole/bump in the perturbed zone which we already attributed to the presence of the shear layer in the SOL (see subsection 5.3.3).

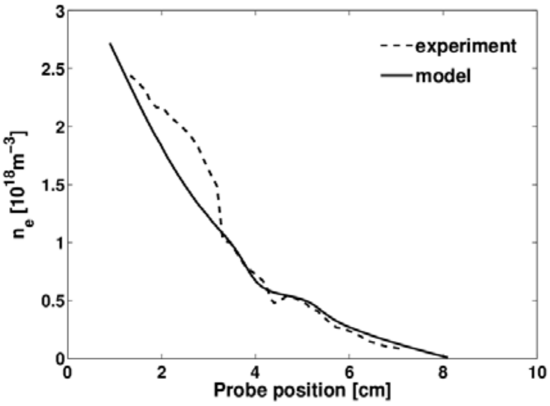

Figure 6.10: *Comparison of the experimental and theoretical density profile.*

To fit simulation data with experimental measurements, it is necessary to adjust the radial position of the probe properly and to scale the density amplitude. The hole/bump in the density profile is attained by increasing the drift velocity u_d. On the other hand, increase of the diffusion coefficients leads to smoothing of the profile and to complete vanishing of the structures for $D_a > 3$. Same configuration is used here as for the potential profiles in previous section, e.g. $D_a = \mu_a = 1$ and $u_d = 4000 m/s$. Despite the fact, the density decay length was chosen $\lambda = 1cm$ as an input, the decay length of the resulting profile increased to $\lambda \sim 3.6cm$ which agrees with experimental observations in the TS scrape-off layer.

Summary

A 1D fluid model including both rf and dc (viscosity and inertia) transverse currents is presented. Simulations show that low V_{sh} can be reached if we consider turbulent plasma by increasing the inertia current by the drift velocity similar to the ion sound speed (4500m/s). Moreover, such a condition yields significant match in density profile. On the other hand, the floating potential exhibits highly negative peaks as well, resulting from the presence of negative currents. This can be suppressed by assuming high density gradients across the system. In addition, simulations clearly showed that biasing of a very small probe (3mm in diameter) affects flux tube over long distances. This implies that the best possible measurements we can make with the probe is when the probe is biased at 0V. On the other hand, to measure RF-induced SOL modifications, probe needs to be biased to very high potentials. In order to overcome the effect of positively biased perturbing probe, one can use the retarding field analyzer which is biased negatively and hence it appears as non-perturbing object (if we neglect the probe head of 4cm in diameter in which the RFA houses). Measurements of the sheath potential with the RFA are presented in the next chapter.

Chapter 7

Sheath potential: modelling vs. experiment

7.1 Introduction

In the chapter 5 we were dealing with the measurements of the scrape-off layer parameters such as plasma density, electron temperature, Mach number and floating potential, affected by a powered ICRH antenna. However, the floating potential is rather a property of the measuring probe itself than plasma. Moreover, it serves only as a lower estimate of the sheath potential in which we are more interested. In addition, it was shown in previous chapter that a positively biased probe acts as a perturbing object and if the probe voltage is superior to the actual rf voltage, it is the probe that defines the potential on the flux tube even if the probe is much smaller (3mm) compared to the rf structure (2cm.) From the overview of the probes given in chapter 3, we know that for sheath potential measurement in plasmas without rf sources, one can use a retarding field analyzer. The advantage of the RFA is that its plate is biased negatively, hence the effect of flux tube biasing does not play a role. The goal addressed here is to present experimental measurements of the sheath potential using a RFA. In addition, a reliability study of the RFA is presented by using a 1D particle-in-cell (PIC) code which will allow us to recover the I-V characteristics that RFA would measure. In this case it is the parallel direction that is simulated. In this second part, we will be dealing with the question of whether is it possible to obtain direct information about the rectified sheath potential using a RFA (i.e. $V_{sh}^{RFA} = V_{float} + V_{amb}$).

7.2 Experimental setup

The sheath potential V_{sh}^{RFA} is mapped in 2D to one of the Tore Supra ICRH antenna by using the RFA/Mach probe mounted on the reciprocating drive situated on the top of the torus. The mapping was done in four shots, with 7 probe plunges each, for the plasma current in the range of $0.78 < I_p < 1.24$MA. Or, in the terms of the edge safety factor, $6.5 < q < 3.8$. There was only one ICRH antenna firing during the whole mapping experiment with the heating power $P_{Q1} = 2$MW. This antenna is equipped with the old type of Faraday screen. The RFA/Mach probe is placed 160° and the antenna is located at 40° toroidally. The connection length is from symmetry same as in previous case with the tunnel probe and Q5 antenna, i.e. $L_{\|} \sim 12m$. Connections for all 28 probe plunges to the antenna are plotted on Figure 7.1.

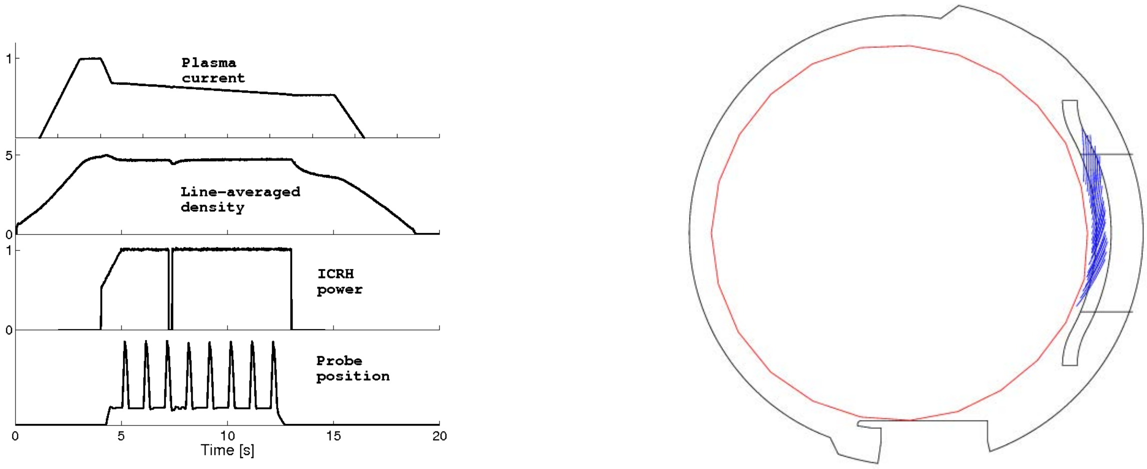

(a) (b)

Figure 7.1: *(a) Time history of the main plasma parameters. Plasma current changes progressively in little steps to obtain different magnetic connections of the probe to the antenna. Probe is plunged into the SOL during the flat stages of I_p profile. (b) Magnetic connections of the probe to powered ICRH antenna during the mapping experiment - full set.*

Plasma density (line averaged[1]) was kept constant at $\bar{n}_e = 5.3 \cdot 10^{19} m^{-2}$. Corresponding values of the plasma current and the safety factor for each shot are listed in Tab. 7.1.

Shot	Ip	q
47219	$1 \rightarrow 0.88$	$4.8 \rightarrow 5.5$
47220	$0.90 \rightarrow 0.78$	$5.4 \rightarrow 6.5$
47223	$1 \rightarrow 1.12$	$4.8 \rightarrow 4.3$
47224	$1.12 \rightarrow 1.24$	$4.3 \rightarrow 3.8$

Table 7.1: *List of the plasma current and associated safety factor for given shots.*

---

[1] SNLI signal

7.2.1 Experimental observation

In the following, we shall compare floating potentials using the RFA slit plate made as a Langmuir probe, with sheath potentials obtained from the RFA collector characteristics. It is important to recall that the two measurements are not obtained simultaneously. During each measurement cycle, the slit plate voltage is ramped down to negative values while the grid voltage is held at 0V. During this phase, the floating potential is extracted from the slit plate I-V characteristic. Once the slit plate voltage saturates at a sufficiently negative value to repel all incident electrons, the grid voltage is ramped up to obtain the RFA collector characteristic from which V_{sh} and T_i are obtained. (See Figure 3.5 for the biasing waveforms).

It is known that in flux tubes magnetically connected to the powered ICRH antenna, strong modifications of SOL parameters are observed [Colas 07a]. The floating potential measurements on the slit plate of the RFA are up to 100V for 2MW coupled ICRH power, which is well comparable to other probe measurements on Tore Supra [Gunn 08]. As mentioned earlier, RFA can also provide information about the sheath edge potential. According to the basic sheath theory, which is derived in chapter 2, the potential drop between the sheath edge and the floating metallic wall in unperturbed plasma, should be equal to $V_{amb} = 3T_e$ [Stangeby 00]. Radial profiles of the potentials for both ohmic and ICRH cases are shown on Figure 7.2. As can be seen, when the antenna is inactive, the measured floating potential is near zero similarly to the tunnel/Mach probe measurements presented in chapter 5. The measured sheath potential decreases with increasing distance from the LCFS. This would be consistent with decreasing electron temperature. However, the magnitude of the sheath potential is less than the expected 3T$_e$. This observation could be consistent with a large coefficient of secondary electron emission from the slit plate (∼0.8), which was measured directly using the tunnel probe [Gunn 12b] and deduced in order to obtain SOL power balance using probes [Gunn 12a]. Situation changes dramatically when antenna is turned on. Both sheath and floating potential are no longer monotonic and rise by several tens of volts depending on magnetic connection of the probe to antenna.It is important to recall that similarly to previous case with the tunnel/Mach probe, modifications occur only on flux tubes directly connected to a powered ICRH antenna. One can notice that the peaks of V_{sh}^{RFA} and V_{float} are not always in phase. Nevertheless, the amplitude of resulting sheath potential is still close to the measured floating potential. Strong variations are also observed on the electron temperature profiles - Figure 7.2c. While the T_e profile is rather constant in ohmic plasmas, strong variations occur in ICRH case. In such case, I-V characteristic is perturbed (even when using sophisticated smoothing routine) and fit to its exponential part becomes inaccurate. This is an opposite effect to the sheath rectification that one would expect.

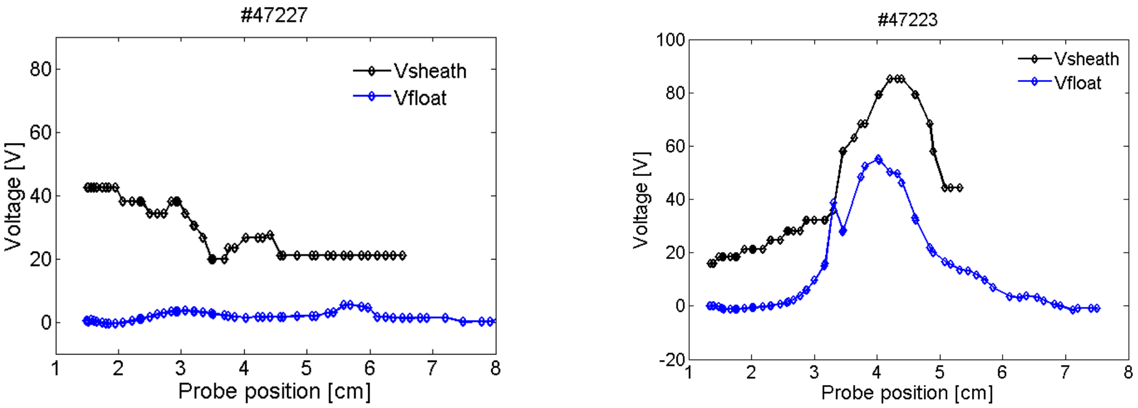

(a) Ohmic plasma (b) ICRH plasma

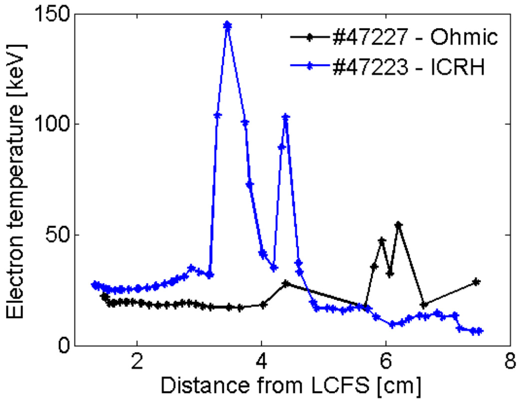

(c) Electron temperature

Figure 7.2: *Radial profiles of* V_{sh} *and* V_{float}*, in the (a) ohmic and (b) ICRH plasma. (c) Corresponding profiles of electron temperature measured on slit plate of the RFA.*

Instead of analysing data from individual probe plunges, we can also choose a global approach by compiling a large number of probe data from several discharges. For simplicity, we consider data only from the mapping experiment (28 probe plunges in total). The advantage here is that all the shots were performed for the same plasma density (by which we can avoid the effect of strong potential dependence on density as described in [Kubič 11]). On the other hand, poloidal connection of the probe varies shot-by-shot. Sheath potential as a function of the floating potential for whole data set is plotted on Figure 7.4a. As can be seen, the difference between measured sheath and floating potential is merely contained in the range of $0 < V_{amb} < 40$V.

To eliminate the poloidal variation of the analysed data, one could normalize the sheath potential to electron temperature measured on the entrance slit. It should be pointed out that scatter of T_e data occurs very often, especially for the probe position passing through the perturbed zone and in the far SOL where the measured current signals are very small. However, if we do so, the resulting normalized sheath potential measured in the flux tubes connected to powered ICRH antenna fluctuates around the constant

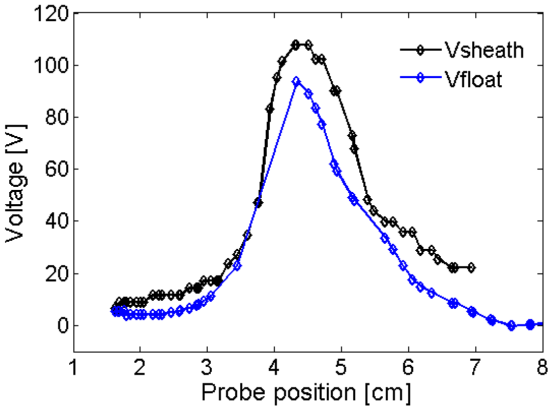

Figure 7.3: *Radial profile of both potentials in the highly perturbed zone. In the limit case, the amplitude of the floating potential is of the same order as the maximum of the sheath potential.*

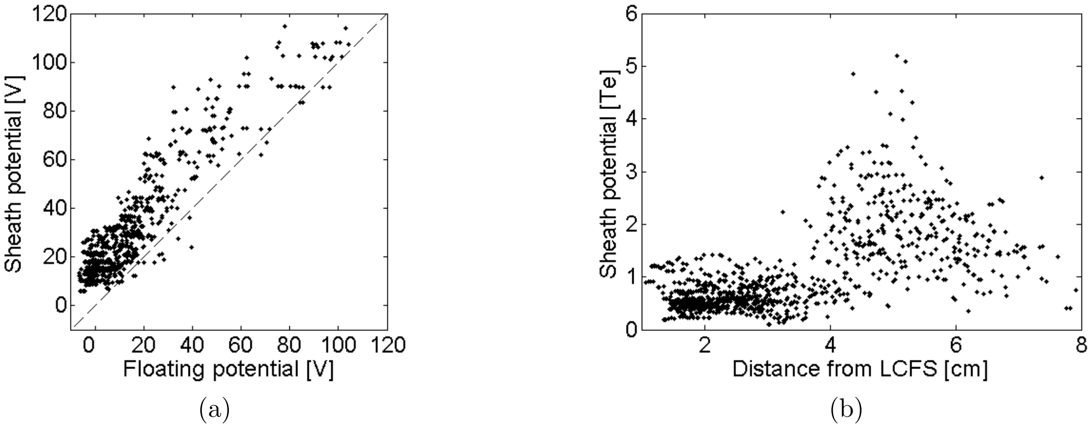

(a)

(b)

Figure 7.4: *(a) Sheath potential as a function of the floating potential containing whole data set. (b) Normalized V_{sheath} to the T_e on the slit plate.*

value for a wide range of radial probe position between 0 and 4cm away from LCFS, and does not exceed $1T_e$ - Figure 7.4b. After that, the normalized V_{sh}^{RFA} increases due to the presence of the peak in the potential structure reaching in some cases up to $5T_e$ but in this region the errors on Te and V_{sh}^{RFA} are both very large.

To complete the analysis of our measurements, we can create mapping images. The full 2D map of V_{sh}^{RFA} and V_{float} is plotted on Figure 7.5. Such a mapping corresponds well to results we obtained in chapter 5. The most intense zones are located around the top and the bottom corners of the antenna strap. The typical radial extent of the perturbation zone is ~1.5cm. This implies that the floating potential measurements performed on the entrance slit of RFA are in good agreement with those obtained by the tunnel probe. One can notice from Figure 7.5 that while the most intense zone of V_{float} is located around the bottom corner of antenna structure, the sheath potential exhibits an opposite pattern.

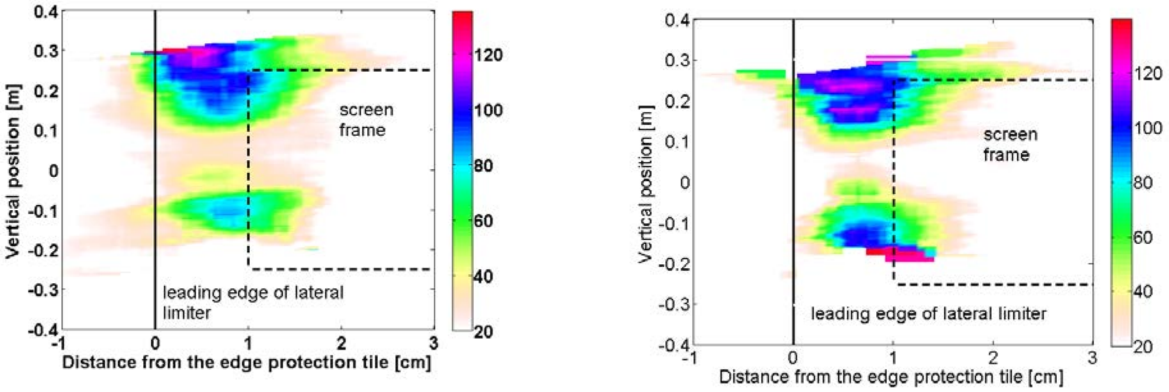

(a) Sheath potential (b) Floating potential

Figure 7.5: *Detailed 2D of plasma and floating potential measured on flux tubes connected to powered ICRH antenna.*

We explained the up and down asymmetry of floating potential by the possible poloidal variation of edge density. But what about the sheath potential case. Can we apply the same hypothesis? In fact, to answer these questions is rather difficult. As can be seen, the map is done up to 0.3m above the mid-plane and only less then 0.2m below the mid-plane. Since the strongest variation of potential is observed in the area below -0.2m, we cannot provide a clear answer. On the other hand, inverse poloidal distribution of the amplitudes of V_{float} and V_{sh}^{RFA} is consistent with observations mentioned above, i.e. the higher the measured floating potential is, the smaller is the difference between V_{float} and V_{sh}^{RFA}. That corresponds well with simulations presented in previous chapter, that is to say, there is sheath rectification, but there is also non-ambipolar current flow from the grounded wall to the antenna.

Although simulations made in the previous chapter gave us some ideas about the effect of transverse currents on the sheath and floating potential, we still do not have an answer to the following question: why is the sheath potential measured by the RFA relatively low ($\sim$100V) and not several hundred of volts? One of the possibilities could simply be that rf potential on the lateral limiters is low compared to the antenna private region where the probe cannot measure. Hence, it is possible that the potential we measure on the LL is some residual voltage due to image currents flowing in the structures that surround the straps. In that case, rf voltage inside the antenna private region can be really in the order of hundreds volts. Or, the second option explaining measured low sheath potential simply relies on the RFA measuring capabilities and RFA cannot measure the sheath potential properly on flux tubes magnetically connected to a powered ICRH antenna. In the following pages, I will try to give an answer by using particle-in-cell simulations.

7.3 Particle-in-cell code

A one-dimensional particle-in-cell (PIC) code is used to model the effect of RF sheaths on RFA measurements. The code simulates the interaction of plasma bound by conducting walls, in the presence of a strong uniform magnetic field. The magnetic field is normal to the boundary and there are no gradients in directions parallel to the target surface. All the quantities vary in the normal direction only. One of the walls, representing the tokamak vessel or a probe, is electrically grounded. The other wall, representing an excited antenna, is also grounded but behaves as if its potential was oscillating with respect to the 'ground'. The applied voltage on the rf electrode varies as $V = V_{rf} \cdot cos(\omega_{rf} t)$, where ω_{rf} is frequency of rf waves and the input amplitude of oscillations is set to $V_{rf} = 20T_e$, where T_e is the equilibrium electron temperature calculated by the code. Therefore, particles can be subject only to the acceleration by parallel component of electric field, but the resonance effect in the perpendicular direction (parallel with the bounded walls) is neglected. The goal is to find the self-consistent, steady-state (although time-varying) sheath potential through which the ions are accelerated, together with the resulting charge distribution function that is responsible for maintaining the potential. The basic equations and normalization system are adopted from [Gunn 97]. The potential is found by solving Poisson's equation

$$\nabla^2 \Phi = -\frac{e}{\epsilon_0}(n_i - n_e) \tag{7.1}$$

where n_i and n_e stand for the local ion and electron densities, respectively. One of the advantages of using PIC simulations is in the normalization system, which allows to interpret the results for wide scale of plasma parameters. The normalized quantities used in the code are listed in Table 7.2. In addition to them, we also define the following nondimensional quantities: $\tau = T_i/T_e$ (ion-to-electron temperature ratio; $\mu = m_i/m_e$ (ion-to-electron mass ratio) and $\xi = r_L/\lambda_D$ with $r_L = c_e/\omega_{ci}$ being the ion Larmor radius at the cold ion sound speed - $c_e^2 = eT_e/m_i$, where T_e is expressed in volts). The parameter ξ is called 'magnetization parameter' and determines the relative importance of the Lorentz force compared with the electric force. However, for the purposes needed here, it is more convenient to express the magnetization parameter as a function of plasma and ion cyclotron frequency:

$$\xi = \frac{r_L}{\lambda_D} = \frac{c_e}{\omega_{ci}} \cdot \sqrt{\frac{n_e e^2}{\epsilon_0 T_e}} = \frac{1}{\omega_{ci}} \cdot \sqrt{\frac{T_e}{m_i}} \cdot \sqrt{\frac{n_e e^2}{\epsilon_0 T_e}} = \frac{\omega_{pi}}{\omega_{ci}} \tag{7.2}$$

All charges that strike the probe wall are removed from the system and their energy is recorded so the distribution function can be obtained. With the knowledge of the ion distribution function, we can construct the time-averaged I-V characteristic that a theoretical RFA would measure if such a distribution was collected inside a real RFA.

Physical quantity	**Normalized by**	**Symbols**
Time	Ion cyclotron time	$t \to t\omega_{ci}$
Distance	Debye length	$(x, z) \to (x, z)/\lambda_D$
Velocity	Debye length/ion gyroperiod	$u_{x,z} \to u_{x,z}/(\omega_{ci}\lambda_D)$
Potential	Electron temperature	$\Phi \to \Phi/kT_e$
Electric field	Typical potential drop on Debye scale	$E \to E/(kT_e/e\lambda_D)$
Density	Bulk plasma density far from target	$n_{i,e} \to n_{i,e}/n_0$

Table 7.2: *List of nondimensional variables used in the PIC code.*

The code is run for deuterium plasma with collisionality $\nu^\star = 10$. The ion-to-electron temperature ratio equals 2 and the length of the simulating box is 200 Debye lengths.

Particles, both ions and electrons are exchanged between the simulation region and a uniform source plasma using a Monte Carlo method. This simulates particle diffusion between an open flux tube and a neighbouring flux tube of much greater connection length, but not the plasma transverse rf conductivity.

7.3.1 Ion distribution function

In order to investigate the behavior of the RFA for a wide range of possible rf regimes, we run a scan of ω_{pi}/ω_{rf}, where ω_{pi} is the ion plasma frequency. Three main frequency domains can be considered:

- Low-frequency domain $\omega_{rf} < \omega_{pi}$
- Intermediate-frequency domain $\omega_{rf} \approx \omega_{pi}$
- High-frequency domain $\omega_{rf} > \omega_{pi}$

The frequency domain plays an important role in ions dynamics in the sheath. For example, when the sheath potential fluctuates slower then the ion plasma frequency, it is important to consider the effect of the ion transit time and the phase at which an ion approaches the space charge region. It can be easily derived that the ion transit time (i.e. time that an ion would need to pass over one Debye length) equals $\tau_i = \omega_{pi}^{-1}$. Under these conditions some of the ions will fall into the sheath when it has a relatively small but fast growing potential across it. Other ions, having entered the sheath when the potential difference was rising more slowly close to its highest, may then be overtaken by the plasma boundary during the phase when the sheath width decreases. These latter ions then re-enter the sheath when the potential difference is lower. This situation is illustrated on Figure 7.6a. Thus, their final energies depend strongly on the phase of the rf cycle in which ions enter the sheath. As a result, the ion energy distribution (IED) function is broad and bimodal. The two peaks in the distribution correspond to the minimum and maximum sheath drops. Such bimodal shape of IED function can be derived analytically within a very simple model. Let us for simplicity consider first the case of mono-energetic ions crossing into a sheath, across which there is a large sinusoidal modulation of potential. The shape of this idealized distribution is derived as follows. Ions arrive at the plasma boundary at a steady rate dN/dt. The potential difference across the sheath is assumed to consist of a steady component, V_0 and a sinusoidal component with amplitude $V_1 \leq V_0$:

$$E = e(V_0 + V_1 sin(\omega t)) + \frac{1}{2} m_i c_s^2 \tag{7.3}$$

Then, defining the ion energy distribution function at any energy E as the number of ions with energy in the range E to E + dE we obtain:

$$f(E) = \frac{dN}{dE} = \frac{dN}{dt}\frac{dt}{dE} = \frac{dN}{dt} \cdot \frac{1}{eV_1 \omega cos(\omega t)} \tag{7.4}$$

The normalized ion energy distribution function at a surface that is biased 100V below the potential of the plasma and modulated with a 50V amplitude sinusoidal potential is shown on Figure 7.6b. No collisions are considered here. On the other hand, for higher rf frequencies, the ions take many rf cycles to cross the sheath and can no longer respond to the instantaneous sheath voltage. Instead, the ions react only to an averaged sheath voltage and the phase they enter the sheath becomes unimportant, resulting in narrower ion energy distribution function. An overview of ion energy distribution functions in the rf sheath can be found in [Kawamura 99]. Now we would like to use the PIC code to obtain ion distribution functions for various ion to plasma frequency ratios and link their consequences to RFA measurement technique.

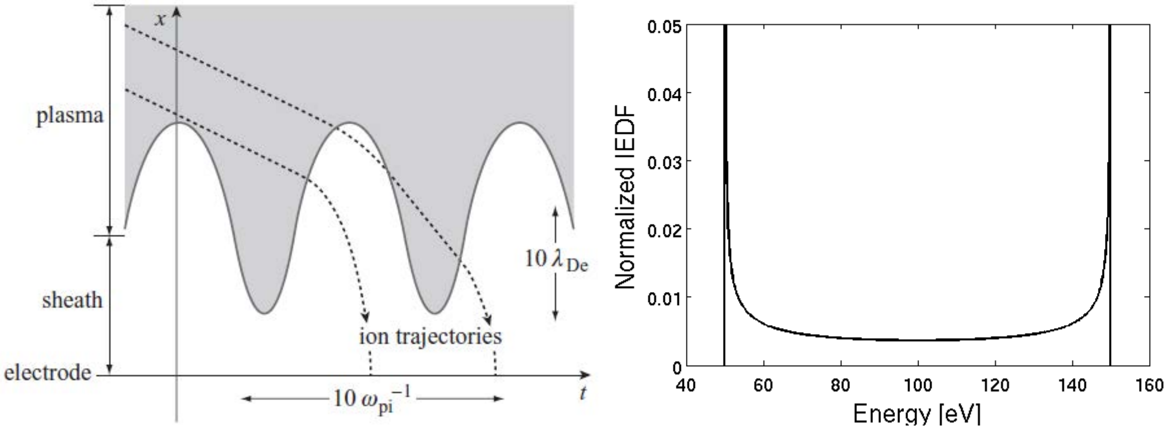

(a) (b)

Figure 7.6: *(a) Schematic of ion trajectories in a temporally modulated sheath ($\omega_{rf} \leq \omega_{pi}$). (b) As a result, ion energy distribution function is bimodal and broad.*

7.3.2 Simulation results

The ion distribution function is simulated using above mentioned PIC code for both low and intermediate frequency domains. In the case of Tore Supra, the wave frequency in minority heating scenario of hydrogen is 57MHz and the typical SOL density equals $n_e = 5 \cdot 10^{18} m^{-3}$, giving the $\omega_{pi}/\omega_{fr} \approx 6$. The resulting ion distribution functions are plotted on Figure 7.7. As can be seen, the ion distribution functions obtained at the target are in good agreement with other theoretical predictions. The asymmetry of the shape of the distribution function compared to that shown on Figure 7.6b is caused by two factors. First is the fact of using Maxwell-Boltzmann distribution of ions entering the sheath boundary and secondly, by presence of collisions that scatter some ions down to lower energies.

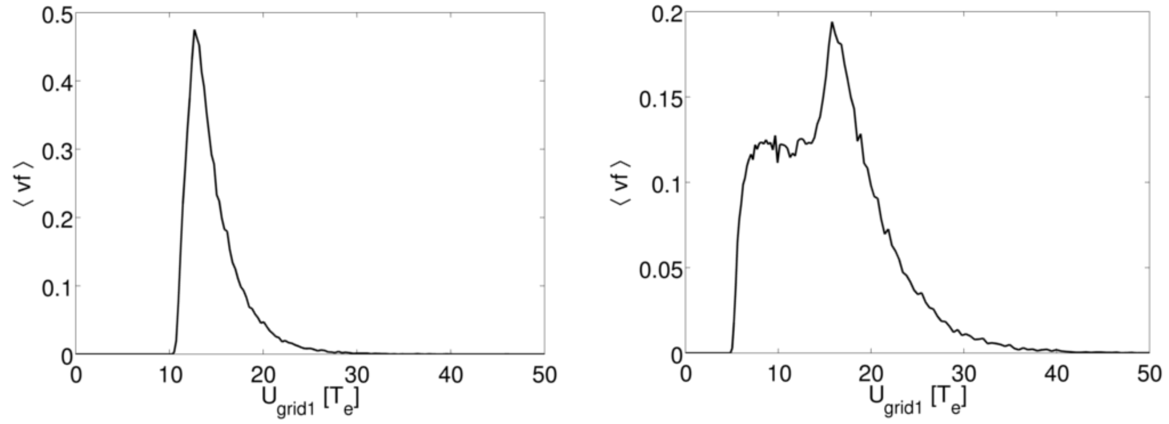

(a) $\omega_{pi}/\omega_{fr} = 1$ (b) $\omega_{pi}/\omega_{fr} = 6$

Figure 7.7: *Example of time-averaged ion distribution functions for (a) intermediate-frequency domain and (b) low-frequency domain. The ion distribution function (IDF) is plotted against the grid 1 voltage which is normalized to local* T_e.

Now having the distribution function, we can use standard RFA analysis techniques to obtain I-V characteristics that would RFA measure if such distributed ions were entering the RFA. To obtain the current that is recorded on the collector, one can just integrate

$$I = \int_{v_c}^{\infty} v f \mathrm{d}v \tag{7.5}$$

and obtain I-V characteristics that are shown on Figure 7.8. The effect of the IDF broadening on the RFA data analysis is now obvious, resulting in the change of the apparent sheath potential measured by RFA, V_{sh}^{RFA} (red lines). While for the rf frequencies close to ion plasma frequency, the measured sheath potential is close to the real sheath potential as it is in the system, V_{sh}, for real conditions in TS scrape-off layer, the predicted potential that would RFA measure is much smaller compared to V_{sh}.

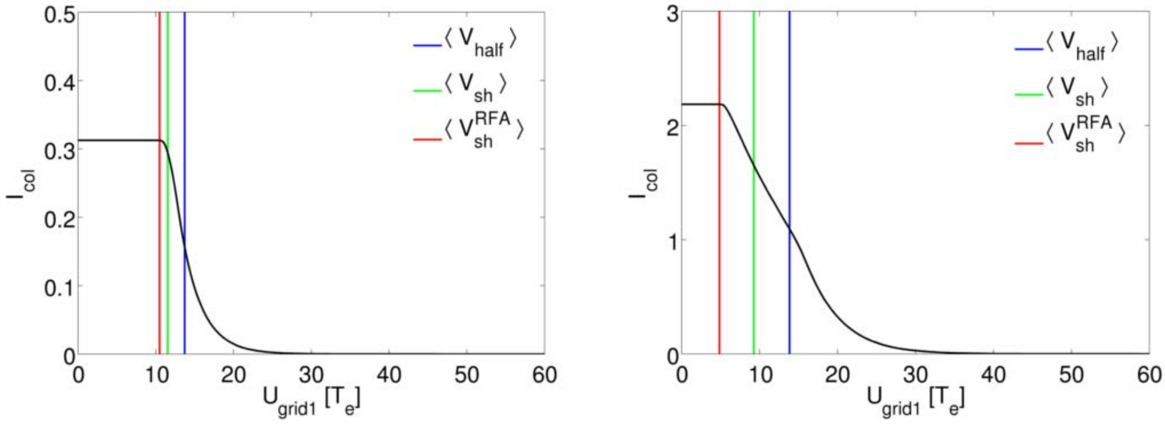

(a) $\omega_{pi}/\omega_{fr} = 1$ (b) $\omega_{pi}/\omega_{fr} = 6$

Figure 7.8: *Current-voltage characteristics for (a) intermediate-frequency domain and (b) low-frequency domain.*

Finer scan of ω_{pi}/ω_{fr} for both resulting time-averaged sheath potentials, as calculated in the system, V_{sh}, and as seen by the RFA, V_{sh}^{RFA} using standard analysis of the time-averaged collector characteristic, is shown on Figure 7.9. The simulations show that there

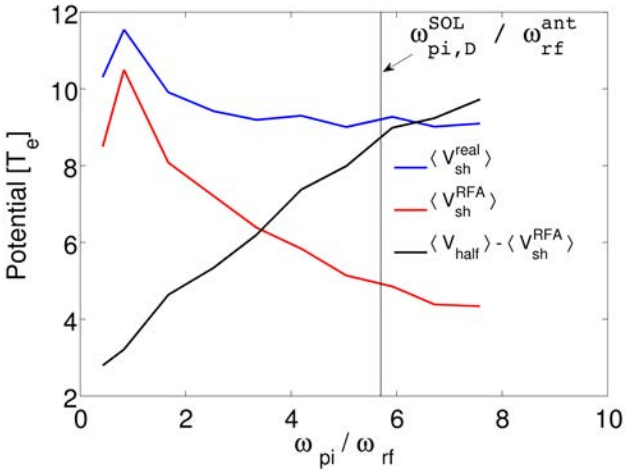

Figure 7.9: *Time-averaged sheath potential versus ω_{pi}/ω_{rf} calculated by the PIC code (solid) and apparent sheath potential seen by the RFA.*

is an evolution of the difference between the real sheath potential and that which the RFA would measure. Let us first consider the case where plasma and wave frequencies are of the same order. In that case, as is mentioned above, the oscillations of the sheath electric field are so fast that the ions cannot react to them. They feel only the time-averaged sheath potential. The ion inertia dominates, and the RFA can measure the rectified sheath potential correctly. Nevertheless, this regime is hardly attainable in real conditions. But for the real TS conditions, the $\langle V_{sh}\rangle$ remains constant at ~ 10 while the $\langle V_{sh}^{RFA}\rangle$ decreases and is underestimated by factor of 2 in this studied case. What does it mean for the RFA measurements? Can the RFA still be used to measure the effects of sheath rectification?

Now, we will extend these studies with respect to experimental observations. It is worth to mention that this dependence on ω_{pi}/ω_{rf} can be also seen in the rf simulations made by Perkins [Perkins 89]. The prediction of low apparent sheath potential complicates the analysis of the sheath rectification effects. Since we cannot measure it directly, we have to use an alternative approach. One possible method is to use relative difference between the V_{half} and the V_{sh}^{RFA} as an indication of the broadening of the ion distribution function and thus the presence of rf oscillations of the sheath at the probe side, as is shown of Figuge 7.9. We define $\Delta V = V_{half} - V_{sh}^{RFA}$. The V_{half} is very well defined from section 3.2.2 and the V_{sh}^{RFA} is measured within the accuracy of $1T_e$. Based on the simulation results, one should expect an increase of the ΔV as the probe is passing through the rf perturbed zone, while for unconnected case, the ΔV should remain low.

Let us first demonstrate RFA measurements on one particular plunge. As I already showed, during the ohmic phase, the measured sheath potential is low, while when antenna is active and the probe is magnetically connected to it, situation changes drastically (see Figure 7.10). Nevertheless the change of V_{sh}^{RFA} (mostly dominated by V_{float} rather than V_{amb}), is still small compared to theoretical predictions [Perkins 89]. This suggests two

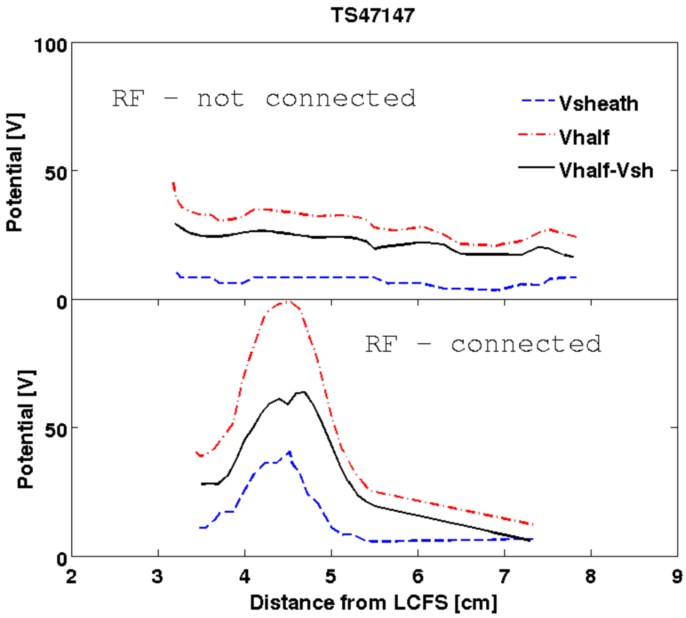

Figure 7.10: *Radial profiles of V_{sh} and V_{half} for the probe unconnected (top) and connected (bottom) to powered ICRF antenna.*

main possibilities. Firstly, rf potential induced on the antenna structure, to which the probe is connected to, is low and the sheath rectification effect is weak. It should be reminded that the probe is connected to the leading edge of lateral limiter that protects the antenna (see Figure 5.4). Even if the rf potentials are lower on the LLs compared to the screen itself, as modelled from $V_{sh}^{RFA} = \int E_{//} \mathrm{d}s$ using rf fields from ICANT code [Pécoul 02], they can still reach hundreds of volts. The second possibility is that the RFA measurements are underestimated exactly as predicted by the PIC code. It can be nicely seen that the ΔV increases in the perturbed zones, implying, if the PIC modelling is applicable to the real experimental conditions, that rf oscillations are present in sheaths located far away along magnetic field lines (12m in this case). In addition, 2D map of the ΔV is plotted on Figure 7.11. Such a mapping corresponds well to results obtained in previous chapter with the mapping of the floating potential. As can be seen, a noticeable increase of ΔV is obtained supporting our idea of indirect indication about the presence of rf sheaths effects in the biased flux tubes.

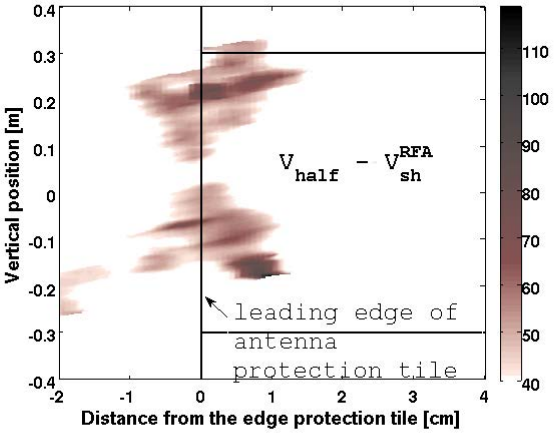

Figure 7.11: *Detailed 2D map of* $\langle V_{half} - V_{sh}^{RFA} \rangle$ *measured on flux tubes connected to a powered ICRF antenna. The data are truncated below 40V to highlight the local broadening of the distribution function.*

Summary

Sheath potential measurements were made on Tore Supra tokamak by using the RFA/Mach probe which was magnetically connected to powered ICRH antenna. Measured floating potential structures in the perturbed zones are similar to those obtained with the tunnel/Mach probe earlier: maximal $V_{float} \sim 120V$ with a typical width up to $\Delta = 3cm$. The value of the sheath potential measured by the RFA is similar to V_{float} measurements as predicted by the modelling presented in previous chapter (i.e. $V_{amb} \sim T_e$), although we have to remember that by measuring V_{float} with the probe, we are also perturbing V_{sh} due to the probe changing current patterns in the flux tube and acting as an anode. Therefore we can make the hypothesis that the RF excitation on the side limiters is ∼100V or (200 V for the new screen). It might be also natural to expect lower values than predicted in the private region where we cannot measure. Moreover, outside the perturbed zone, where the sheath potential is expected to be of the order of $3T_e$, nearly zero value is measured. In addition, 1D particle-in-cell code is used to simulate RFA in the rf environment. It should be recall, that the 1D PIC model (parallel direction) does not include radial currents. However, it does allow to see the effect of rectified voltages on the RFA characteristics. Simulations suggest, that the sheath potential that would a theoretical RFA measure, is strongly underestimated. The misbehaviour of the RFA in the rf environment can be explained by an apparent widening of ion distribution function across the sheath, which is a well known effect in rf sheath physics. Since the RFA measures the lowest voltage in the system, the apparent sheath potential measured by the RFA is necessary below the real value. Although the 1D model used here allows to calculate rf effects only over short distances, it turns out to be a powerful tool to evaluate IDF consistent with other theoretical approaches and hence to be suitable for the studies for RFA data interpretation. Moreover, alternative indirect method is proposed to study the rf sheaths effect based on the increase of ΔV.

General conclusions and future perspective

The goal of this thesis was to investigate, mainly experimentally, the interaction between the scrape-off layer and a powered ICRH antenna. These RF-induced SOL modifications are investigated by means of Langmuir probes. The emphasis is taken to examine modifications of scrape-off layer parameters (plasma density, electron temperature, sheath potential and parallel flow) due to a presence of an active antenna.

Special attention was given to the comparison of the SOL influence of two different designs of the Faraday screens. Experiments showed very clearly, in contrast to theoretical predictions, that the new type of the Faraday screen with cantilevered bars and shark tooth openings at the top and bottom of the screen, significantly increases the magnitude of induced potential. Measured potentials induced by the new screen are typically 5x higher compared with the old screen. It is worth to mention that for 2MW of antenna power, the measured potentials can exceed 200V even on the mid-plane where the local minimum is usually observed. This disagreement points out that our understanding of the rf potentials generation is not yet fully developed. The key point which might be responsible for this discrepancy lies in the evaluation of the rf potentials. Simulations of the new type of Faraday screen performed by the code TOPICA [Mendes 09] that calculates the potential simply as an integral of the electric field along the field line, are evidently false. More perspective simulations are currently undergoing using finite element analysis package COMSOL and the SSWICH (Self-consistent Sheaths and Waves for Ion Cyclotron Heating) [Jacquot 11] taking into account the sheath boundary condition. Preliminary simulations exhibit good agreement with our measurements.

Furthermore, we presented that with the magnetic reconstruction method that uses EFIT calculations, these high potential appear to be induced poloidally near the antenna corners but radially on the lateral limiters. With the new Faraday screen, the most intense zones are located ≈2cm behind the leading edge of lateral limiter, while for the old screen these zones appear radially at around the leading edge of lateral limiter. This difference in radial position is attributed to the current flowing on the FS screen structure and their associated image currents. Therefore, in order to explain this disagreement, side limiters cannot be neglected from the model, as they were in the TOPICA simulations [Mendes 09].

Another interesting observation made, which might have a direct consequence for radial particle transport, is the strong variation of the parallel flow in the flux tubes connected to a powered antenna. The flow, which is driven by blobs, changes monotonically in radial direction in ohmic phase while during the ICRH phase is strongly sheared. In the contrary to the old screen, the shear does not vanish for high densities and is observed at different poloidal locations. We showed with a simple estimate that even a 100V of the voltage amplitude could be sufficient to destroy turbulent structures across the SOL at the fraction of ion sound speed. The formation of local 'transport barrier' was observed clearly on the edge density profiles characterized by a sharp drop (factor of 2 over 5mm). On the other hand, such a decrease is not observed in the case of the old screen even if parallel flow is strongly sheared as well. That might imply a tool to reduce a radial transport in RF-biased flux tubes consisting for instance from a biased poloidal ring attached to the wall. On the contrary, feasibility of such implementation could be a bit of challenge because having a biased ring at the grounded wall would necessary lead also to enhanced particle acceleration to the walls causing sputtering, heat loads etc. as it happens with ICRH antenna itself. However, it would be interesting to calculate if the reduction of radial transport dominated over the side effects of biased ring.

As was mentioned earlier, the data collected by our probes are evaluated with the Mach probe theory. Although Mach probe theory has been proven to provide qualitatively sufficient base for the usage in most of the plasma scenarios, its validity in the presence of biased flux tubes emerging from a powered antenna towards the probe is at least questionable. According to the Mach probe theory, where the probe is considered as a single point in space, one would expect to measure same potential on the both sides of the probe. But we showed that the difference between the upstream-to-downstream potentials can vary from 100V to -100V. First case happens when the probe is connected to the bottom of the strap, where potentials are high (observed for both screens). The other case was observed for large injected power from one ICRH antenna. Therefore, our measurements suggest that the probe acts like a small limiter and its size cannot be neglected. This phenomena is associated with the complex pattern of radial current, both dc and rf, exchanging between neighbouring flux tubes. Simulations taking into account contribution of these transverse currents are based on double probe model [Faudot 10] where one boundary potential is oscillating (antenna) while the other is floating (probe). However, in the scope of our problem, a model with a probe situated in the middle of the simulation region between two boundaries would be more appropriate, but probably difficult to implement

Concerning the edge density measurements, we observed an up and down asymmetry with higher density above the mid-plane. Nevertheless, to confirm this statement, several simultaneous measurements would have to be performed at various poloidal location. However, if we assume the existence of poloidally variable density profile, we can link this poloidal variation of density to the E×B convective cells which is in good agreement with theoretical prediction [Bécoulet 02]. In addition to poloidal density distribution, these convective cells act also in radial direction. This was confirmed by the analysis of IR images of the FS components. If the probe is inserted into the SOL, a sudden increase/decrease of the temperature of FS bars, along which the field line passes, was observed. But the screen itself is protected by side limiters and hidden 1cm behind their leading edge, so the field line does not hit the screen structure directly, but interacts via the E×B convective cells. Moreover, the intensity of measured floating potential seems to be consistent with the poloidal density pattern with lower density below the mid-plane and the fact, the measured potential is a strong function of plasma density. According to experimental observations, either with old or new FS, 20% change in the plasma density causes the floating potential to vary by factor of two, implying a tool to reduce these high potentials.

In the last two chapters, we studied both theoretically and experimentally aspects of RF sheaths effects on the RFA sheath potential measurements. Although the retarding field analyzer is routinely used to measure ion temperature in the SOL or suprathermal electrons generated by low hybrid grill, its assessment in RF environment is still needed. Simulations I made with the 1D fluid code provided a clue how transverse rf and dc currents affects probe measurements. Moreover, to recover experimental observations, one has to consider a turbulent plasma, that is to say with strong radial current. In addition, we showed with 1D PIC simulations that the RFA cannot measure the rectified sheath potential directly, but it can provide indirect indication about RF sheaths due to apparent widening of the distribution function. The RFA measurements are in a good agreement with the theoretical prediction, which was observed by increase of the ΔV inside the perturbed zones, while the apparent sheath potential measured by the RFA is still way below the real time averaged sheath potential. This implies that RF potentials can propagate over long distances from antenna. It should be pointed out that the dimension of the simulated domain in the PIC code is negligible compared to 12m of real connection length of the probe to powered ICRF antenna, which also demonstrate the power of the code. Nevertheless, more detailed evaluation of the ΔV magnitude is needed to confirm whether it is consistent with RF voltage on the lateral limiters as predicted by antenna calculations.

Concerning future perspective in the field of the framework of this thesis, we showed that our understanding of the RF-induced SOL modifications is still limited in certain ways. Especially in the scope how are the rf potentials generated. We can conclude that the rf excitation does originate from the side limiters, but their value is limited to ∼100V in the case of the old Faraday screen and about 200V for the new FS. We believe that potential oscillations on the surface of the side limiters are not caused due to the slow wave. To fully understand this phenomenon, a full 3D calculation of the electric field distribution around the antenna with appropriate boundary condition, and including side limiters, is required. Regarding the experimental point of view, an advanced model of the RFA measurements in the biased flux tubes is needed as well in order to link the widening of the ion distribution function with the real sheath potential. Since the Tore Supra tokamak is going to be upgraded to a tokamak with a divertor, it will be important to repeat some of the experiments presented here to compare the effects of RF-induced SOL modification in the case of different edge plasma conditions such as a presence of ELMs or possible formation of edge transport barrier.

Appendix A

Magnetic reconstruction

Magnetic connection of either probe to any of the three powered antennas is possible for a wide range of magnetic configurations. To be able to compute the connection points of the flux tubes emerging from the probe in the poloidal plane of the antenna, it is necessary to know the magnetic equilibrium of the discharge. The plasma position and shape is on TS calculated from a set of magnetic flux loops measuring the radial and the poloidal magnetic field and by toroidal flux loops. There are 51 radial field coils and 51 poloidal field coils in total that are used to define the plasma shape and position. They are all placed on a ring which is situated at the same toroidal angle as one of the TF coils. This magnetic arrangement provides very good measurement of plasma position and shape only directly under the toroidal field coils. But for probe purposes, with respect to its location, it is necessary to know the magnetic field between the TF coils. The toroidal magnetic field in the SOL cannot be described as axisymmetric because it is strongly modulated by the spacing of the 18 superconducting toroidal field coils which are placed every 20° (ripple effect). In the following, an approximate method to estimate the magnetic field between the TF coils will be described.

EFIT reconstruction

EFIT reconstruction method is a generally known method for magnetic equilibrium calculations used at many tokamaks. It solves in real time the Grad-Shafranov equation for magnetic flux [Shafranov 66]. This equation is a two-dimensional, non-linear, elliptic partial differential equation obtained from the reduction of the ideal MHD equations to two dimensions for the case of toroidal axisymmetry.

$$\Delta^* \Psi = -\mu_0^2 R^2 \frac{dp}{d\Psi} - \frac{1}{2}\frac{dF^2}{d\Psi} \quad , where \quad \Delta^* \equiv R\frac{\partial}{\partial R}\frac{1}{R}\frac{\partial \Psi}{\partial R} + \frac{\partial^2 \Psi}{\partial Z^2} \tag{A.1}$$

The vacuum field generated by N toroidal field coils in cylindrical coordinates is defined as

$$\mathbf{B}^{vac} = B_0 R_0 \left(\frac{1}{R}(1 - \delta(R,Z)) cos N\phi \mathbf{e}_T + \frac{1}{N}\nabla\delta(R,Z) sin N\phi \right) \tag{A.2}$$

where δ describes the deviation from axisymmetry, and is calculated from the known geometry of the toroidal field coils. Its analytical form for Tore Supra is given in [Basiuk 94]. We assume that the total magnetic field is the sum of the poloidal field generated by the plasma Eq. (A.1) and the vacuum field generated by the toroidal field coils, including the toroidal ripple. The poloidal field is assumed to be axisymmetric. In principle, small corrections should be made due to the toroidal ripple [Zwingmann 05], but we find it sufficiently accurate to suppose that the poloidal field measured under the TF coils has no gradient in the toroidal direction. The assumption is reasonable because the plasma current profile is mostly concentrated near the magnetic axis where the ripple is zero.

To calculate a magnetic connection from the probe position to the poloidal plane of the ICRH antenna, one has to integrate the field line equations. For the small elements of the field line we can write

$$\frac{dl_x}{B_x} = \frac{dl_y}{B_y} = \frac{dl_z}{B_z} \tag{A.3}$$

But for tokamaks it is more convenient, with respect to the axisymmetry, to use a cylindrical coordinates in form:

$$\frac{dR}{B_R} = \frac{dZ}{B_Z} = \frac{Rd\phi}{B_\phi} \tag{A.4}$$

by rewriting into differential equations we obtain

$$\frac{dR}{d\phi} = \frac{RB_R}{B_\phi}, \quad \frac{dZ}{d\phi} = \frac{ZB_Z}{B_\phi} \tag{A.5}$$

To solve Equations A.5, we use a second order Runge-Kutta integration scheme, with linear interpolation of the magnetic field from the grid. This is sufficiently accurate for field lines that make less than one full poloidal turn in the SOL. On a Poincaré plot showing intersections of a given field line with poloidal planes situated under TF coils, it can be verified that the field line returns to a surface of constant poloidal flux within ±0.5mm radially after one poloidal turn.

The accuracy of the EFIT reconstruction method has shown to be sufficient which was supported by good agreement with experimental observations. RFA measurements of fast electrons generated by LH antenna showed that the beam of the fast electrons is generated ∼15mm in front of the grill (using older reconstruction method) [Gunn 08], while when using EFIT method the beam is generated only 5mm in front of the grill which corresponds much better with the theory that says the beam is excited directly in the vicinity of the antenna, i.e. 1-2mm in front of the grill. Moreover, another proof of the reliability of EFIT method was demonstrated on the conservation of the poloidal pressure measured at the mid-plane with the newly installed tunnel probes [Gunn 11a], and at the top of the torus. Therefore, the EFIT reconstruction method is used for all magnetic connection calculations presented in this chapter. The position of a magnetic flux surface calculated by EFIT is accurate to within 5 mm radially.

It should be pointed out that the EFIT reconstruction method, that I helped prove to be the most exact method with respect to experimental observations, has attained high level of interest among other colleagues at Tore Supra. I developed tools to predict detailed magnetic connections between arbitrary plasma facing components in the SOL. I was frequently asked to determine magnetic connections between probes and different antennas (ICRH or LH), other limiters, or gas injection valves for the study of impurity transport. The tools are user friendly Matlab routines that can even be run in real time between discharges to help optimize an experimental session.

List of abbreviations

APL	Antenna Protection Limiter
AUG	ASDEX-Upgrade
CKO	Cubic Kilometer of Oil
CMO	Cubic Mile of Oil
D-T	Deuterium-Tritium
DEMO	DEMOnstration Power Plant
ECRH	Electron Cyclotron Resonance Heating
FS	Faraday Screen
FW	Fast Wave
FWEH	Fast Wave Electron Heating
HFS	High Field Side
IBW	Ion Bernstein Wave
ICRH	Ion Cyclotron Resonance Heating
IDF	Ion Distribution Function
IEDF	Ion Energy Distribution Function
ITER	International Thermonuclear Experimental Reactor
ITW	Iter-Like Wall
JET	Joint European Torus
LCFS	Last Closed Flux Surface
LFS	Low Field Side

LHCD	Lower Hybrid Current Drive
LHS	Left Hand Side
LL	Lateral Limiter
LP	Langmuir probe
MHD	Magnethydrodynamic
NBI	Neutral Beam Injection
OECD	Organisation for Economic Co-operation and Development
PIC	Particle-In Cell
PWI	Plasma-Wall Interaction
RDL	Resonant Double Loop
RF	Radio-Frequency
RFA	Retarding Field Analyzer
RHS	Right Hand Side
SOL	Scrape-Off Layer
SW	Slow Wave
TF	Toroidal field
TOPICA	TOrino Polytechnic Ion Cyclotron Antenna
TP	Tunnel probe
TS	Tore Supra
WEST	W Environment in Steady-state Tokamak

Bibliography

[Atzeni 04] S. Atzeni & J. Meyer ter Vehn. The physics of inertial fusion. Oxford University Press, 2004.

[Basiuk 94] V. Basiuk. Fusion Technology, page 222, 1994.

[Bécoulet 96] A. Bécoulet. *Heating and current drive regimes in the ion cyclotron range of frequency.* Plasma Phys. Control. Fusion, vol. 38, pages A1–A11, 1996.

[Bécoulet 02] M. Bécoulet, L. Colas, S. Pécoul, J. Gunn, Ph. Ghendrih, A. Bécoulet & S. Heuraux. *Edge plasma density convection during ion cyclotron resonance heating on Tore Supra.* Physics of Plasmas, vol. 9, no. 6, pages 2619–2632, 2002.

[Berkner 75] K.H. Berkner, R.V Pyle & J.W Stearns. *Intense, mixed-energy hydrogen beams for CTR injection.* Nuclear Fusion, vol. 15, no. 2, page 249, 1975.

[Bobkov 10] Vl V Bobkov. *Assessment of compatibility of ICRF antenna operation with full W wall in ASDEX Upgrade.* Nuclear Fusion, vol. 50, no. 3, page 035004, 2010.

[Boeur 08] K S De Boeur & W Seggewiss. Stars and Stellar Evolution. EDP Sciences, 2008.

[BP 12] BP. BP Energy Outlook 2030, 2012.

[Braams 02] C. M. Braams & P. E. Stott. Nuclear fusion: half a century of magnetic confinement research. Institute of Physics Publishing, 2002.

[Bucalossi 10] J. Bucalossi & Tore Supra Team. *Feasibility study of an actively cooled tungsten divertor in Tore Supra.* Rapport technique, CEA, 2010.

[Carlson 01] A. Carlson. *Linearized magnetohydrodynamic theory of Langmuir probes with resistivity, friction, and polarization.* Physics of Plasmas, vol. 8, no. 11, pages 4732–4739, 2001.

[Carlson 10] C. R. Carlson. *Our Energy Challenge, In Cubic Miles Of Oil.* Forbes, 2010.

[Chung 88] K.S. Chung & I.H. Hutchinson. Phys. Rev. A, vol. 38, page 4721, 1988.

[Colas 07a] L. Colas. *2-D mapping of ICRF-induced SOL perturbations in Tore Supra tokamak.* Journal of Nuclear Materials, vol. 363-365, pages 555 – 559, 2007.

[Colas 07b] L Colas, A Ekedahl, M Goniche, J P Gunn, B Nold, Y Corre, V Bobkov, R Dux, F Braun, J-M Noterdaeme, M-L Mayoral, K Kirov, J Mailloux, S Heuraux, E Faudot, J Ongena, ASDEX Upgrade Team & JET-EFDA contributors. *Understanding the spatial structure of RF-induced SOL modifications.* Plasma Physics and Controlled Fusion, vol. 49, no. 12B, page B35, 2007.

[Colas 09] L. Colas, K. Vuilliez, V. Basiuk & Tore Supra Team. *Ion Cyclotron Resonant Heating in Tore Supra.* Fusion Science and Technology, vol. 56, 2009.

[Corre 11] Y. Corre, M. Lipa, G. Agarici, V. Basiuk, L. Colas, X. Courtois, G. Dunand, R. Dumont, A. Ekedahl, J.-L. Gardarein, C.C. Klepper, V. Martin, V. Moncada, C. Portafaix, F. Rigollet, R. Tawizgant, J.-M. Travére & K. Vulliez. *Heat flux calculation and problem of flaking of boron carbide coatings on the Faraday screen of the ICRH antennas during Tore Supra high power, long pulse operation.* Fusion Engineering and Design, vol. 86, pages 429 – 441, 2011.

[Corre 12] Y. Corre, M. Firdaouss, L. Colas, A. Argouarch, M. Chantant, F. Clairet, D. Guilhem, J. Gunn, C. Hamlyn-Harris, J. Jacquot, M. Kubic, X. Litaudon, M. Missirlian, M. Richou, G. Ritz, D. Serret & K. Vulliez. *Characterisation of heat flux generated by ICRH heating with cantilevered bars and slotted box Faraday screen.* in press, 2012.

[Crane 10] H. Crane, E. Kinderman & R. Malhotra. A Cubic Mile of Oil: Realities and Options for Averting the Looming Global Energy Crisis. Oxford University Press, 2010.

[Dejarnac 07] R Dejarnac, J P Gunn, J Stöckel, J Adámek, J Brotánková & C Ionita. *Study of ion sheath expansion and anisotropy of the electron parallel energy distribution in the CASTOR tokamak.* Plasma Physics and Controlled Fusion, vol. 49, no. 11, page 1791, 2007.

[D'Ippolito 91] D A D'Ippolito, J R Myra, M Bures & J Jacquinot. *A model of sheath-driven impurity production by ICRF antennas.* Plasma Physics and Controlled Fusion, vol. 33, no. 6, page 607, 1991.

[Faudot 06] E. Faudot, S. Heuraux & L. Colas. *Parametric study of two-dimensional potential structures induced by radio-frequency sheaths coupled with transverse currents in front of the Ion Cyclotron Resonance Heating antenna.* Physics of Plasmas, vol. 13, no. 4, page 042512, 2006.

[Faudot 10] E. Faudot, L. Colas, S. Heuraux & J. P. Gunn. *Broadening of rectified potential structures induced by rf currents in a magnetized plasma: Application to ITER scrape-off-layer.* Physics of Plasmas, vol. 17, no. 4, page 042503, 2010.

[Faudot 11a] E. Faudot. *Current distribution in a biased flux tube.* Rapport technique, University of Lorraine, 2011.

[Faudot 11b] E. Faudot. *Current distribution in a biased flux tube.* Rapport technique, University of Lorraine, 2011.

[Faudot 13] E. Faudot, S. Heuraux, M. Kubic, J. Gunn & L. Colas. *Fluid modeling of radio frequency and direct currents in a biased magnetized plasma.* Physics of Plasmas, vol. 20, no. 4, page 043514, 2013.

[Fedorczak 10] N. Fedorczak. *DTURB User guide.* Rapport technique, CEA/IRFM Cadarache, 2010.

[Freidberg 07] J.A. Freidberg. Plasma Physics and Fusion Energy. Cambridge University Press, 2007.

[Ghendrih 03] Ph. Ghendrih, Y. Sarazin, G. Attuel, S. Benkadda, P. Beyerand G. Falchetto, C. Figarella, X. Garbet, V. Grandgirard, & M. Ottaviani. *Theoretical analysis of the influence of external biasing on long range turbulent transport in the scrape-off layer.* Nuclear Fusion, vol. 43, 2003.

[Godyak 90] V.A. Godyak & N. Sternberg. *Dynamic model of the electrode sheaths in symmetrically driven rf discharges.* Physical Review A, vol. 42, page 2299, 1990.

[Grisolia 00] C. Grisolia. *Density control and plasma wall interaction in Tore Supra.* In Hydrogen Recycling at Plasma Facing Materials, volume 1, pages 1–8. 2000.

[Guilhem 05] D. Guilhem, J.L. Bondil, B. Bertrand, C. Desgranges, M. Lipa, P. Messina, M. Missirlian, C. Portafaix, R. Reichle, H. Roche & A. Saille. *Tore-Supra infrared thermography system, a real steady-state diagnostic.* Fusion Engineering and Design, vol. 74, no. 1â4, pages 879 – 883, 2005.

[Gunn 97] J. P. Gunn. *The influence of magnetization strength on the sheath: Implications for flush-mounted probes.* Physics of Plasmas, vol. 4, no. 12, pages 4435–4446, 1997.

[Gunn 02] J. Gunn, P. Devynck, J. Pascal, J. Adámek, I. Ďuran, M. Hron, J. Stöckel, F. Žáček, O. Bařina, R. Hrach, M. Vicher & G. Van Oost. *A DC probe diagnostics for fast electron temperature measurements in tokamak edge plasmas.* Czechoslovak Journal of Physics, vol. 52, pages 1107–1114, 2002.

[Gunn 06] J. P. Gunn, C. Boucher, M. Dionne, I. Ďuran, V. Fuchs, T. Loarer, R. Pánek, F. Saint-Laurent, J. Stöckel, J. Adámek, J. Bucalossi, R. Dejarnac, P. Devynck, P. Hertout, M. Hron, P. Moreau, I. Nanobashvili, F. Rimini & A. Sarkissian. *Scrape-off layer flows in the Tore Supra tokamak.* AIP Conference Proceedings, vol. 812, no. 1, pages 27–34, 2006.

[Gunn 07a] J P Gunn. *Mach probe interpretation in the presence of suprathermal electrons.* Phys. of Plasmas, vol. 14, no. 032502, 2007.

[Gunn 07b] J.P. Gunn, C. Boucher, M. Dionne, I. Ďuran, V. Fuchs, T. Loarer, I. Nanobashvili, R. Pánek, J.-Y. Pascal, F. Saint-Laurent, J. Stockel, T. Van Rompuy, R. Zagórski, J. Adámek, J. Bucalossi, R. Dejarnac, P. Devynck, P. Hertout, M. Hron, G. Lebrun, P. Moreau, F. Rimini, A. Sarkissian & G. Van Oost. *Evidence for a poloidally localized enhancement of radial transport in the scrape-off layer of the Tore Supra tokamak.* Journal of Nuclear Materials, vol. 363 365, pages 484 – 490, 2007.

[Gunn 08] J P Gunn. *Suprathermal electron beams and large sheath potentials generated by RF-antennas in the scrape-off layer of Tore Supra.* proc. 22nd IAEA Fusion Energy Conference Geneva, no. EX/P6-32, 2008.

[Gunn 10] J. P. Gunn, M. Kubič, N. Fedorczak & M. Kočan. *ITER limiter start-up experiments in Tore Supra.* In 3rd EFDA Transport Topical Group Meeting, Cordoba, Spain, 7th September 2010.

[Gunn 11a] J. P. Gunn & J.-Y. Pascal. *A magnetically driven reciprocating probe for tokamak scrape-off layer measurements.* Review of Scientific Instruments, vol. 82, no. 12, page 123505, 2011.

[Gunn 11b] J. P. Gunn, J.-Y. Pascal, F. Saint-Laurent & C. Gil. *Electric Probes in Tokamaks: Experience in Tore Supra.* Contributions to Plasma Physics, vol. 51, no. 2-3, pages 256–263, 2011.

[Gunn 12a] J. Gunn, R. Dejarnac, P. Devynck, N. Fedorczak, V. Fuchs, C. Gil, M. Kočan, M. Komm M. Kubič, T. Lunt, P. Monier-Garbet, J.-Y. Pascal & F. Saint-Laurent. *Scrape-off layer power flux measurements in the Tore Supra tokamak.* 2012. O8, 20th PSI Conference, Aachen, Germany.

[Gunn 12b] J.P. Gunn. *Evidence for strong secondary electron emission in the tokamak scrape-off layer.* Plasma Physics and Controlled Fusion, vol. 54, no. 8, page 085007, 2012.

[Günther 94] K. Günther & A. Carlson. *Fluid Theory of Langmuir Probes in a Magnetized Plasma with Open Flux Tubes.* Contributions to Plasma Physics, vol. 34, no. 2-3, pages 484–489, 1994.

[Guo 96] H. Y. Guo, G. F. Matthews, S. J. Davies, S. K. Erents, L. D. Horton, R. D. Monk & P. C. Stangeby. *Ion Temperature Measurements in JET Boundary Plasmas Using a Retarding Field Analyser.* Contributions to Plasma Physics, vol. 36, no. S1, pages 81–86, 1996.

[Hartmann 06] D.A. Hartmann. *Stellarators.* Fusion Science and Technology, vol. 49, no. T2, pages 43 – 55, 2006.

[Hawryluk 02] R. J. Hawryluk. *Review of D-T Experiments Relevant to Burning Plasma Issues.* J. Plasma Fusion Res. SERIES, vol. 5, pages 12–21, 2002.

[Hemsworth 09] R. Hemsworth, H. Decamps, J. Graceffa, B. Schunke, M. Tanaka, M. Dremel, A. Tanga, H.P.L. De Esch, F. Geli, J. Milnes, T. Inoue, D. Marcuzzi, P. Sonato & P. Zaccaria. *Status of the ITER heating neutral beam system.* Nuclear Fusion, vol. 49, no. 4, page 045006, 2009.

[Hoekzema 00] J. A. Hoekzema. *Electron Cyclotron Waves.* Transactions of Fusion Technology, vol. 37, pages 163–169, 2000.

[Hutchinson 87] I. H. Hutchinson. *A fluid theory of ion collection by probes in strong magnetic fields with plasma flow.* Physics of Fluids, vol. 30, no. 12, pages 3777–3781, 1987.

[Hutchinson 88] I.H. Hutchinson. *Ion collection by probes in strong magnetic fields with plasma flow.* Phys. Rev. A, vol. 37, no. 11, 1988.

[Hutchinson 02] I.H. Hutchinson. Principles of plasma diagnostics. Cambridge University Press, 2nd edition, 2002.

[ITER 12] ITER. www.iter.org, 2012.

[Jacquot 11] J. Jacquot, L. Colas, S. Heuraux, M. Kubič, J. P. Gunn, E. Faudot, J. Hillairet & M. Goniche. *Self-consistent non-linear radio-frequency wave propagation and peripheral plasma biasing.* AIP Conference Proceedings, vol. 1406, no. 1, pages 211–214, 2011.

[Kawamura 99] E. Kawamura, V. Vahedi, M.A. Liebermann & C.K. Birdsall. *Ion energy distributions in rf sheath; review, analysis and simulation.* Plasma Sources Sci. Technol., vol. 8, pages R45–R64, 1999.

[Kaye 98] A. Kaye & the JET Team. *Results of Recent Deuterium/Tritium Experiments in JET.* In 13th ANS Topical Meeting, Nashville USA, June 1998.

[Koch 00] R. Koch. *The Ion Cyclotron, Lower Hybrid and Alfeven Wave Heating Methods.* Transactions of Fusion Technology, vol. 37, pages 155–162, 2000.

[Kočan 08] M. Kočan, J. P. Gunn, M. Komm, J.-Y. Pascal, E. Gauthier & G. Bonhomme. *On the reliability of scrape-off layer ion temperature measurements by retarding field analyzers.* Review of Scientific Instruments, vol. 79, no. 7, page 073502, 2008.

[Kubič 11] M. Kubič, J. P. Gunn, L. Colas, S. Heuraux, E. Faudot & A. Ngadjeu. *Attenuation of ICRH-induced potentials in the SOL of Tore Supra.* AIP Conference Proceedings, vol. 1406, no. 1, pages 215–218, 2011.

[Kubič 12] M. Kubič. Experimental study of the edge plasma of the Tore Supra tokamak. Lambert Academic Publishing, 2012.

[Kulhánek 08] P. Kulhánek. *Lectures of Plasma theory.* Rapport technique, Czech Technical University in Prague, 2008.

[Lancellotti 06] V. Lancellotti, D. Milanesio, R. Maggiora, G. Vecchi & V. Kyrytsya. *TOPICA: an accurate and efficient numerical tool for analysis and design of ICRF antennas.* Nuclear Fusion, vol. 46, no. 7, page S476, 2006.

[Lawson 57] J.D. Lawson. *Proceedings of the Physical Society B.* vol. 70, page 6, 1957.

[Mendes 09] A. Mendes. *Reduction of RF sheaths potentials by compensation or suppression of parallel RF currents on ICRF antennae.* AIP Conference Proceedings, vol. 1187, no. 1, pages 141–144, 2009.

[Metze 86] A. Metze, D. W. Ernie & H. J. Oskam. *Application of the physics of plasma sheaths to the modeling of rf plasma reactors.* Journal of Applied Physics, vol. 60, no. 9, pages 3081–3087, 1986.

[Moreau 09] Ph. Moreau, S. Bremond, D. Douai, A. Geraud, P. Hertout, M. Lennholm, D. Mazon, F. Saint-Laurent & Tore Supra Team. *Plasma Control in Tore Supra.* Fusion Science and Technology, vol. 56, pages 1284–1299, 2009.

[Mott-Smith 26] H.M. Mott-Smith & I. Langmuir. *The Theory of Collectors in Gaseous Discharges.* Phys. Rev., vol. 28, pages 727–763, Oct 1926.

[Ngadjeu 10] A. Ngadjeu. *Etude des effets de gaine induites par une antenne de chauffage à la fréquence cyclotronique ionique (FCI, 30-80 MHz) et de leur impact sur les mesures par sondes dans les plasmas de fusion.* PhD thesis, Université Henri Poincaré, 2010.

[Ngadjeu 11] A. Ngadjeu, E. Faudot, L. Colas, S. Heuraux, J. Gunn & M. Kubič. *Generation of DC currents by ICRF near fields in the Scrape-off Layer.* Journal of Nuclear Materials, vol. 415, pages S1009 – S1012, 2011.

[Nieuwenhove 92] R Van Nieuwenhove & G Van Oost. *Experimental study of sheath currents in the scrape-off layer during ICRH on TEXTOR.* Plasma Physics and Controlled Fusion, vol. 34, no. 4, page 525, 1992.

[Pécoul 02] S. Pécoul, S. Heuraux, R. Koch & G. Leclert. *Numerical modeling of the coupling of an ICRH antenna with a plasma with self-consistent antenna currents.* Computer Physics Communications, vol. 146, no. 2, pages 166 – 187, 2002.

[Perkins 89] F.W. Perkins. *Radio-frequency sheaths and impurity generation by ICRF antennas.* Nuclear Fusion, vol. 29, page 583, 1989.

[Pointu 86] A. M. Pointu. *Double probe model of radio frequency capacitively coupled planar discharges.* Applied Physics Letters, vol. 48, no. 12, pages 762–763, 1986.

[Riemann 92] K.-U. Riemann. *The validity of Bohm's sheath criterion in rf discharges.* Physics of Fluids B: Plasma Physics, vol. 4, no. 9, pages 2693–2695, 1992.

[Rozhansky 99] V.A. Rozhansky, A.A. Ushakov & S.P. Voskoboynikov. *Electric fields and currents in front of a biased electrode (flush mounted probe) and the I - V characteristics of the electrode for various mechanisms of transverse conductivity.* Nuclear Fusion, vol. 39, no. 5, page 613, 1999.

[Rozhansky 01] V.A. Rozhansky, S.P. Voskoboynikov, E.G. Kaveeva, D.P. Coster & R. Schneider. *Simulation of tokamak edge plasma including self-consistent electric fields.* Nuclear Fusion, vol. 41, no. 4, page 387, 2001.

[Shafranov 66] V D Shafranov. *Plasma Equilibrium in a Magnetic Field.* Reviews of Plasma Physics, vol. 2, page 103, 1966.

[Stangeby 90] P.C. Stangeby & G.M. McCracken. Nucl. Fusion, vol. 30, no. 1225, 1990.

[Stangeby 00] P.C. Stangeby. The Plasma Boundary of Magnetic Fusion Devices. Institute of Physical Publishing Bristol and Philadelphia, 2000.

[Stix 92] T.H. Stix. Waves in plasmas. Springel-Verlag New York, 1992.

[Tanabe 12] T. Tanabe. *Tritium Fuel Cycle in ITER and DEMO.* In 20^{th} Plasma Surface Interaction Conference, Aachen, Germany, 2012.

[Tore Supra] Tore Supra Tore Supra. www.

[Unterberg 06] B. Unterberg. Fusion Science and Technology, vol. 49, no. T2, pages 215 –233, 2006.

[Valsaque 02] F. Valsaque, G. Manfredi, J. P. Gunn & E. Gauthier. *Kinetic simulations of ion temperature measurements from retarding field analyzers.* Physics of Plasmas, vol. 9, no. 5, pages 1806–1814, 2002.

[Vulliez 09] K. Vulliez. *A New Faraday Screen For Tore Supra ICRH Antenna.* AIP Conference Proceedings, vol. 1187, no. 1, pages 145–148, 2009.

[Wagner 82] F. Wagner. Phys. Rev. Lett., vol. 49, no. 1408, 1982.

[Wendelstein 7X] Max-Planck Institut Wendelstein 7X Greifswald. http://www.ipp.mpg.de/ippcms/de/for/projekte/w7x/.

[Wesson 04] J. Wesson. Tokamaks. Clarendon Press, Oxford, 3 edition, 2004.

[Weynants 06] R. R. Weynants. *Fusion Machines.* Fusion Science and Technology, vol. 49, no. T2, pages 36 –42, 2006.

[Zwingmann 05] W. Zwingmann. *Equilibrium recontruction of tokamak discharges with toroidal variation.* 32nd EPS Conference on Plasma Phys Tarragona, vol. 29C, pages P–2.044, 2005.